Solar Light Driven Photocatalysis for Hydrogen and Value-added Products Generation

by

Himanshu Bajpai
10CC17A26026

A thesis submitted to the
Academy of Scientific & Innovative Research
for the award of the degree of
DOCTOR OF PHILOSOPHY
in
SCIENCE

Under the supervision of
Dr. Chinnakonda S. Gopinath



CSIR-National Chemical Laboratory, Pune



Academy of Scientific and Innovative Research
AcSIR Headquarters, CSIR-HRDC campus
Sector 19, Kamla Nehru Nagar,
Ghaziabad, U.P. – 201 002, India

May, 2023

Certificate

This is to certify that the work incorporated in this Ph.D. thesis entitled, "*Solar Light Driven Photocatalysis for Hydrogen and Value-added Products Generation*", submitted by *Himanshu Bajpai* to the Academy of Scientific and Innovative Research (AcSIR), in partial fulfillment of the requirements for the award of the Degree of *Doctor of Philosophy in Science*, embodies original research work carried-out by the student. We further certify that this work has not been submitted to any other University or Institution in part or full for the award of any degree or diploma. Research material(s) obtained from other source(s) and used in this research work has/have been duly acknowledged in the thesis. Image(s), illustration(s), figure(s), table(s) etc., used in the thesis from other source(s), have also been duly cited and acknowledged.

Himansh. Bajpai 11/5/23
(Signature of Student)

Himanshu Bajpai

C.S. Gopi 11/5/23
(Signature of Supervisor)

Dr. C.S. Gopinath

STATEMENTS OF ACADEMIC INTEGRITY

I, Himanshu Bajpai, a Ph.D. student of the Academy of Scientific and Innovative Research (AcSIR) with Registration No. 10CC17A26026 hereby undertake that the thesis entitled "Solar Light Driven Photocatalysis for Hydrogen and Value-added Products Generation" has been prepared by me and that the document reports original work carried out by me and is free of any plagiarism in compliance with the UGC Regulations on *"Promotion of Academic Integrity and Prevention of Plagiarism in Higher Educational Institutions (2018)"* and the CSIR Guidelines for *"Ethics in Research and in Governance (2020)"*.

Himanshu Bajpai

Signature of the Student

Date: 1-5-2023

Place: Pune

It is hereby certified that the work done by the student, under my/our supervision, is plagiarism-free in accordance with the UGC Regulations on *"Promotion of Academic Integrity and Prevention of Plagiarism in Higher Educational Institutions (2018)"* and the CSIR Guidelines for *"Ethics in Research and in Governance (2020)"*.

C S Gopinath

Signature of the Supervisor

Name: Dr. C.S Gopinath

Date: May 01, 2023

Place: Pune

ACKNOWLEDGEMENTS

There are so many people whose support, inspiration, and encouragement are crucial to achieve meaningful goals in life, mainly if they include parts of realizing one's most cherished aspirations. This thesis is a significant goal to me, and I am grateful to many individuals for their encouragement and well wishes as I travel this path. I would like to use this opportunity to express my gratitude to everyone who helped make the scientific work outlined in this thesis possible, directly or indirectly. I thank God for how good my life is, for providing me with this opportunity, and for giving me the ability to succeed.

First and foremost, I would like to thank my research supervisor, Dr. Chinnakonda S. Gopinath, from the bottom of my heart for allowing me to work with him. He has been a tremendous help to me throughout my career as a Ph.D. student, and I want to thank him for that. His interest in science and holistic viewpoint has motivated me to work as a researcher. I have learned throughout the doctoral years from interactions with him on how to approach a subject from all possible directions and find a solution at the most fundamental level. He continuously stresses the need to develop critical thought habits while teaching us the do's and don'ts of science and daily life. Aside from this, I appreciate his teaching style since he makes every issue incredibly plain and straightforward by beginning at a basic level and working his way up. I was highly amazed by his depth of knowledge in many subjects. Being a member of his study team and affiliated with him makes me feel fortunate and privileged.

I also want to express my gratitude to the members of my doctoral advisory committee, Dr. Ashok P. Giri, Dr. Santhosh Babu Sukumaran, Dr. Shatabdi Porel Mukherjee for their time, helpful advice, and support. I owe my external expert Prof. Avinash S. Kumbhar, Department of Chemistry, Savitribai Phule Pune University, a great deal of respect and appreciation for assessing my work in my up-gradation meeting. I sincerely appreciate his time, insight, and conversation regarding my work. Additionally, I'd like to express my gratitude to Prof. Balasubramanian Viswanathan, for the orientation course at IITM.

I want to express my gratitude to Dr. Ashish Lele, the current director of the CSIR-NCL, and Prof. Ashwini Kumar Nangia, the previous director, for allowing me to work at this esteemed organization for providing the resources and infrastructure I needed. For their generous assistance throughout the course of my Ph.D., I am incredibly grateful to Dr. Shubhangi B. Umbarkar, Chairperson, Catalysis and Inorganic Chemistry Division, and Drs.

Chinnakonda S. Gopinath and Darbha Srinivas (former Chairpersons). Many thanks to the division staff members who assisted me with the many office tasks. I want to express my gratitude to the entire administrative and non-teaching personnel of CSIR-NCL for all of their help and support over the years.

I also want to express my gratitude to all the staff members at NCL's Center for Materials Characterization, who have helped me through their services over the years. I sincerely appreciate the prompt assistance provided by Mr. S. S. Deo, Mr. R. S. Gholap, Venkatesh, Sheetal, Chetan, Tushar, Medha, and Shurti for the XPS, TEM, HRTEM, FESEM, and SEM measurements. Special thanks to Medha and Chetan for providing me with urgent slots on request. Many thanks to Dr. Tejas, Mr. Ratnesh Jha for providing me with the XRD and UV-Vis's spectroscopy and BET slots.

I sincerely acknowledge for the UGC Fellowship given to me during my PhD research work at NCL.

I would also like to thank my lab's senior researchers, Dr. Kshirodra Kumar Patra, Dr. Naresh Nalajala, Dr. Pradnya Bharad, Dr. Manoj Kumar Ghosalya, Dr. Ruchi Jain, Dr. Kasala Prabhakar Reddy, Dr. P. Devaraji, Dr. Sadhu Kolekar, Dr. Abhaya Kumar Mishra. They have shared experiences with me that I will never forget, and I intend to keep in touch with them. I would like to thank all my labmates, Nitin, Ravi, Inderjeet, Kranti, Subhashree, Arindam, Niveditha, Dr. Priyabrata, Shinto Tom K S, Elsa Dais, Nashwa V P, Sayana, Sibo Chetry, Avadhi Trivedi, Sreeya Raj, Omkar Borade, Rahul Mendhe, Hamid P. Kanattil, Jyoti, Nikita, Dr. Mahendra Pawar, Akhila, Athira, Dr. Pranjal Saikia, Bibek, Sowjanya, Nayanjyothi, Layna, Maheswari, Vijay, Avani, Vasunthara Devi for their help and fostering a friendly and conducive work environment in the lab.

I thank to all my divisional friends Shiva, Aakash, Gorab, Shweta, Samuruddhi, Mayuri, Sheetal, Archana, Dr. Aswathi, Eishver Dr. Prabhu, Prabhu, Nittan, Dr, Govind, Sumanta, Dr. Yogita, Dr. Sharad, Mahesh, Anuradha, Pavan, Jyotsna, Betsy, Pooja, Sanket, Dr. Milan, Dr. Gargi. Dr. Rohit, Kritika, Vishal, Ajith, Kajal, Viplab, Kailash, Sonu, Manoj, Meera, Dr. Dhananjay, Ankit, Dr. Shunotra, Priyanka, Seema, Akshay, Vipul da, Jyoti, Akshay, Deepali, Dhreeendra bhai, Priya, Kalayani, Lavnya, Jyoti (Dhepe Sir), Tufeil, Susmita, Shrijith for their help.

My Special thanks to Tripathi bhai, Vikas Bhai, Pawan bhai, Mahendra bhai for all the fruitful discussion.

I'd want to thank all of my NCL Cricket's friends, including Manish, Rohit Sr. Sidharth, Akash, Anand, Dr. Arun, Dr. Ashish, Bharath, Bharath NCIM, Ashish NCIM Kundan, Dhermendra, Naaru bhai, Pinka bhai, Prashan Bhai, Nitin (polymer), Prashant (polymer), Priyam, Dr. Rahul Jagtaap, Sandy Bhai, Saumya, Umasharan, Yogesh, DJ, Bejosh, Rakesh, Nirshaad, Juned, Shabaaz Bhai.

I also want to thank Sangram, Akash, Sai, Pawan (Utpal Das Sir), Kiran, Visit, kakde bhai, Kale sir, Patil sir, Indronil, Vinita, Lakshmi, Mayur, Pooja (BLV sir), Shubham, Supriya, Monika, Monika ma'am, Amrita, Dr. Amrish, Chandan, Rajni, Soumya, Smita, Aishwerya, Surya, and Neha, Dr. Dipesh, Chandni, Sidhu, Tubai, Debjani, Pragya, Jesna, Hemant, Govardhan, Shivam, Dr. Anirban, Nikhil, Tushar, Chandrodaya, Amit, Ravi, Mayank, Mohit, Prem, Manoj, Prachi, Bandhu, Abhiraj, Spurti, Abha, Bhanu Bhai, Jagjeevan, Priyanka halder, Rejeshwari ma'am, Zenia ma'am, Shailendra, Suhag, Tahzeen, Sukhda, Bagyashree, Zenoy bhai, Ashvini, Neha, Arindam (Arooprath sir), Tanuja, Vineet (IITM), Inder (IISER for Characterization). Thanks, Sujeet and Chotu bhaiya, Subash, Bharat for giving me the best meals during the last four years. Thanks to my MSc friends Rakesh, Atul, Kuldeep, Kapil, Neelam, Ankita, Anil, Ashok, Deependra, Shashi, Dhanpal, Rana Sir, Subodh Sir, Rajat. I also want to extend my thanks to my IIP frriends Azeem bhai, Deepak bhai, Vivek, Neeraj, Vaishu, Jeetu bhai, Sattu bhai, Sonam, Chandrakala. Thanks to my friends from hometown Ravi, Ashok, Mohit, Santosh, Mayank, Puneet, Ravi II, Manish, Anuj, Vishal, Virendra, Bhaskar, Deepak, Deshdeepak for their support throughout this journey.

I want to sincerely thank my parents, for their unending love and unwavering support throughout my life. In every aspect of my life, you two have served as a consistent source of encouragement. I appreciate your believing in me and being patient with me. In addition, I want to thank my sisters (thanks for always supporting me and being with me), My Choti Bua, Badi Bua, Chacha, Dada, Badi mummy for their unwavering moral support, care, and love. I thank my brother-in-law for his encouragement, continued support over the years, and enthusiasm as I neared my goal.

Himanshu Bajpai



Dedicated to Lord Shiva

List of Abbreviations

QuAL	Quasi Artificial Leaf
XPS	X-ray Photoelectron Spectroscopy
LSPR	Localized Surface Plasmon Resonance
SPR	Surface Plasmon Resonance
SPP	Surface Plasmon Polarization
PEC	Photo-Electrochemical Measurement
CB	Conduction band
EDAX	Energy Dispersive Analysis of X-rays
VB	Valence band
GC	Gas Chromatography
HTEM	High-resolution transmission electron microscopy
BG	Band Gap
QD	Quantum Dot
SAED	Selected Area electron diffraction
PL	Photoluminescence
UV	UV-Visible Absoption
STEM	Scanning transmission electron microscopy
FESEM	Field emission scanning electron microscopy
GE	Gibbs free energy

Table Of Content

Chapter 1: Introduction

1.1 Photocatalysis: 2

1.2 History of photocatalysis 2

1.3 Fundamentals of Photocatalysis 3

1.4 Photocatalytic Applications 5

1.5 Photocatalytic water splitting 7

1.6 Strategy to Improve Photocatalytic activity 9

1.6.1 Role of Co-Catalyst 10

1.6.1.1 Factor Affecting the Co-Catalyst 12

1.6.2 Plasmons 13

1.6.3 Heterojunction 15

1.6.4 Artificial Photosynthesis 16

1.6.5 Role of Sacrificial Reagent 18

1.6.6 Role of Defects 20

1.7 Objective of Thesis 22

1.8 Outline of Thesis 22

1.9 References 24

Chapter 2: Synthesis and Experimental Methods

2.1 Synthesis and Experimental Methods 34

2.2 Synthesis of co-catalyst 34

2.2.1 Ni-Cu Alloy nanoparticles 34

2.2.2 Half-Monolayer Pt Integrated Ni-Cu ($0.5\theta_{Pt}$-NC) Bimetallic Nanoparticle 34

2.2.3 Synthesis of Au/TiO_2 composite 35

2.2.4 Synthesis of Cu/TiO_2 36

2.2.5 Synthesis of NiCu-bimetal Particles 36

2.2.5 NiCu@TiO_2 Composite 37

2.2.7 Synthesis of Defective TiO_2 37

2.3 Fabrication of Photochemical Device 37

2.4 Solar Hydrogen Production Measurement for TiO_2/ZnS/CdS/ZnS System 38

2.5 Photochemical Hydrogen Production Measurement 38

2.6 Photochemical Glycerol Oxidation Measurement 39

2.7 Photo-electrochemical measurement 39

2.8 Electrochemical measurement 40

2.9 Photocatalytic Ammonia Production Measurement 40

2.10 Structural Characterization Methods 40

2.11 References 46

Chapter3: Can Half-a-Monolayer of Pt Simulate Activity Like That of Bulk Pt? Solar Hydrogen Activity Demonstration with Quasi-artificial Leaf Device

3.1 Introduction 48

3.2 UV−Visible Absorption Spectroscopy 50

3.3 Photocatalytic Hydrogen Production 51

3.4 Elemental Mapping and Textural Properties of the Photoanode 55

3.5 Photoelectrochemical Measurement 58

3.6 Structural and Microscopy Analysis of Cocatalysts 59

3.7 XPS 62

3.8 Electrochemical Measurement 63

3.9 Mechanism 65

3.10 Conclusion 66

3.11 References 68

Chapter 4a: Biomass Components toward H_2 and Value-Added Products by Sunlight-Driven Photocatalysis with Electronically Integrated $Au\delta^-$–TiO_2: Concurrent Utilization of Electrons and Holes

4.1 Introduction 73

4.2 UV-visible absorption 75

4.3 Solar hydrogen production 75

4.4 Glycerol oxidation 82

4.5 Structural analysis and elemental mapping 85

4.6 X-ray photoelectron spectroscopy 88

4.7 Mechanism 91

4.8 Conclusions 93

4.9 Reference 94

Chapter 4b: Uniformly Integrated Sub-Nano Cu Particles over TiO_2; Concurrent Utilization of Electrons and Holes towards Efficient Photocatalytic Hydrogen Evolution and selective oxidation of Biomass.

4.10 Introduction 101

4.11 Structural Analysis 103

4.12 Photo-catalytic Water Splitting 107

4.13 Photocatalytic Glycerol Oxidation 109

4.14 UV-Visible Spectra 110

4.15 Raman Analysis 111

4.16 X-ray Photo-electron Spectroscopy 113

4.17 Mechanism 116

4.18 Conclusion 117

4.19 References 118

Chapter 4c: Optimizing Ni-Cu Bimetallic Nanoparticles Integrated with Titania for Efficient Hydrogen Production from Biomass: A Photocatalytic Study

4.20 Introduction 122

4.21 Solar Hydrogen Evolution 125

4.22 UV-Vis Absorption Spectra 128

4.23 Structural Characterization 129

4.24 Conclusion 131

4.25 References 132

Chapter 5: Enhancing Photocatalytic Nitrogen Fixation through Defective TiO_2 Composites: Optimization of Surface Defects

5.1 Introduction 136

5.2 XRD and UV-Vis Characterization 138

5.3 HRTEM analysis 140

5.4 Photocatalytic activity 141

5.5 XPS analysis 143

5.6 Photo-Luminescence (PL) studies 145

5.7 Raman analysis 146

5.8 Conclusion 148

5.9 References 149

Chapter 6: Conclusion

6.1 Conclusion and Future scope 159



Chapter 1

Introduction

1.1 Photocatalysis:

The carbon-based economy encourages more reliance on fossil fuels, which increases greenhouse gas emissions and has a negative impact on the environment.[1-3] The planet's temperature has risen over the past few years, which has greatly alarmed the scientific and political communities, and general population. 95 percent of the world's energy demand is currently met by petroleum and its equivalents.[4] The globe will eventually run out of fossil fuels since we are aware that they are not renewable. That means the globe should transition from relying on non-renewable fossil fuel energy sources to renewable ones before we confront a major energy crisis and global warming that could be fatal.[5,6] Thus, one of the most pressing problems facing academics today is the development of energy solutions that are safe, clean, and sustainable.[1] One of the most significant sources of pure, renewable energy on Earth is the solar energy; solar energy can be converted to electrical and/or chemical energy. For instance, solar water (H_2O) splitting can be used to provide a clean hydrogen (H_2) energy source. The world's environmental and energy challenges should thus be substantially solved by developing and utilising ecologically acceptable energy systems that use solar energy. One of the most significant developments in this area among the numerous energy technologies is photocatalysis, which utilises solar energy to power chemical and energy processes.

1.2 History of photocatalysis:

Photochemistry, often known as the study of how light influences chemical processes, was initiated in 1901 by the Italian scientist Giacomo Ciamician (Fig.1.1).[7,8] Despite his work on the effect of light on chemical processes, photocatalysts were not in use till the beginning of 20th century. In 1911, the word "photocatalysis" first appeared in scientific publications.[9] In 1932, it was revealed that TiO_2 and Nb_2O_5 are efficient photocatalysts for converting $AuCl_3$ and $AgNO_3$ to gold and silver, respectively.[10] In 1938, TiO_2 was utilised as a photosensitizer to bleach dyes. Nevertheless, scientists paid little attention to photocatalysis since it had few practical implications at that time.[11]

In the 1970s, scientists investigated alternate and renewable energy sources in response to the "oil crisis" and the detrimental environmental impacts of industrial operations.[12,13] Boddy noticed in 1968 that TiO_2 produced O_2 when exposed to UV light in an electrolytic cell.[14] Fujishima and Honda found in 1972 that when subjected to UV light,

photoelectrochemical water splitting on a TiO_2 electrode produces O_2 and H_2 on a platinum black electrode.[15] In an argon environment, it was discovered in 1977 that photocatalytic H_2O splitting on TiO_2 powder yields a 2:1 molar ratio of H_2 and O_2.[16] Kawai and Sakata discovered in 1980 that the sacrificial reagent methanol significantly increases photocatalytic H_2 generation from the CH_3OH-H_2O mixture.[17]

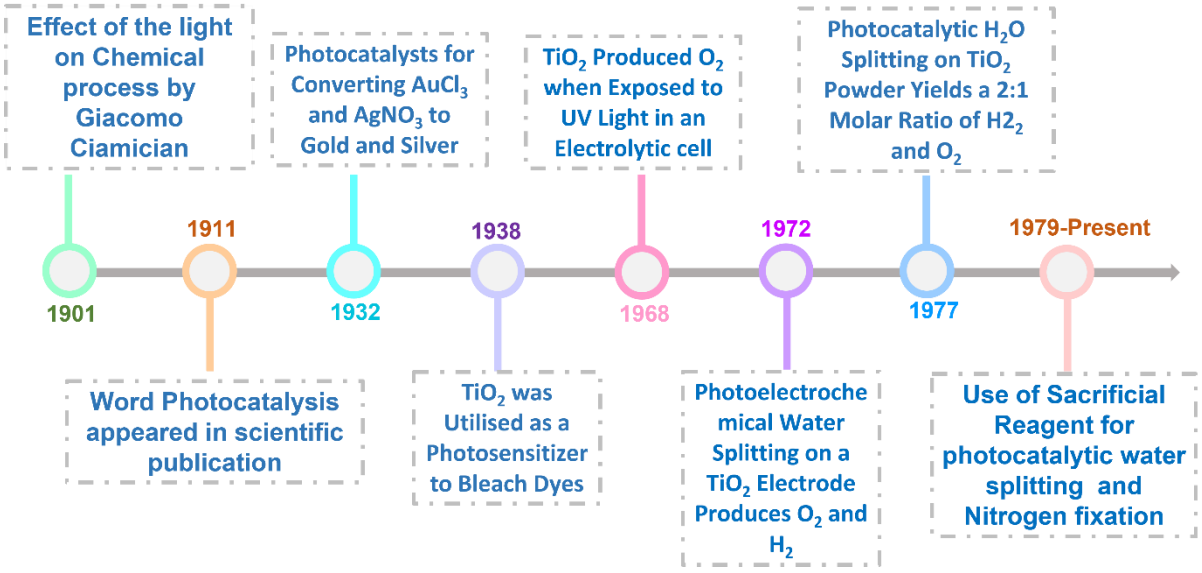


Figure 1.1 Evolution timeline of Photocatalysis over a century. Till date, R&D efforts of photocatalysis are largely in the laboratories and yet to reach significant applications.

These findings paved the way for the widespread application of photocatalysis in a variety of sectors, and for the past two decades, comparable techniques employing TiO_2 as a photocatalyst have attracted considerable scientific and R&D interests. Novel semiconductor materials, including $SrTiO_3$, $BiVO_4$, Ag_3PO_4, g-C_3N_4, CdS, and its nanoparticles, have also been utilised to directly employ solar energy for a variety of photocatalytic activities.[18-24]

1.3 Fundamentals of Photocatalysis:

The chemical process of photocatalysis involves the activation of a catalyst by light, which then causes a chemical reaction. According to the International Union of Pure and Applied Chemistry (IUPAC), photocatalysis is a catalytic process resulting from substrate-mediated light absorption.[25] When a semiconductor photocatalyst is exposed to light with photon energy exceeding its band gap energy, valence band (VB) electrons are stimulated into the conduction band (CB), leaving VB holes. In order for photocatalytic reactions to occur, photo-induced free charge carriers must diffuse onto the photocatalyst surface-active sites.[26]

Figure 1.2 demonstrates the simplified and/or general method employed in photocatalysis by predominant researchers.

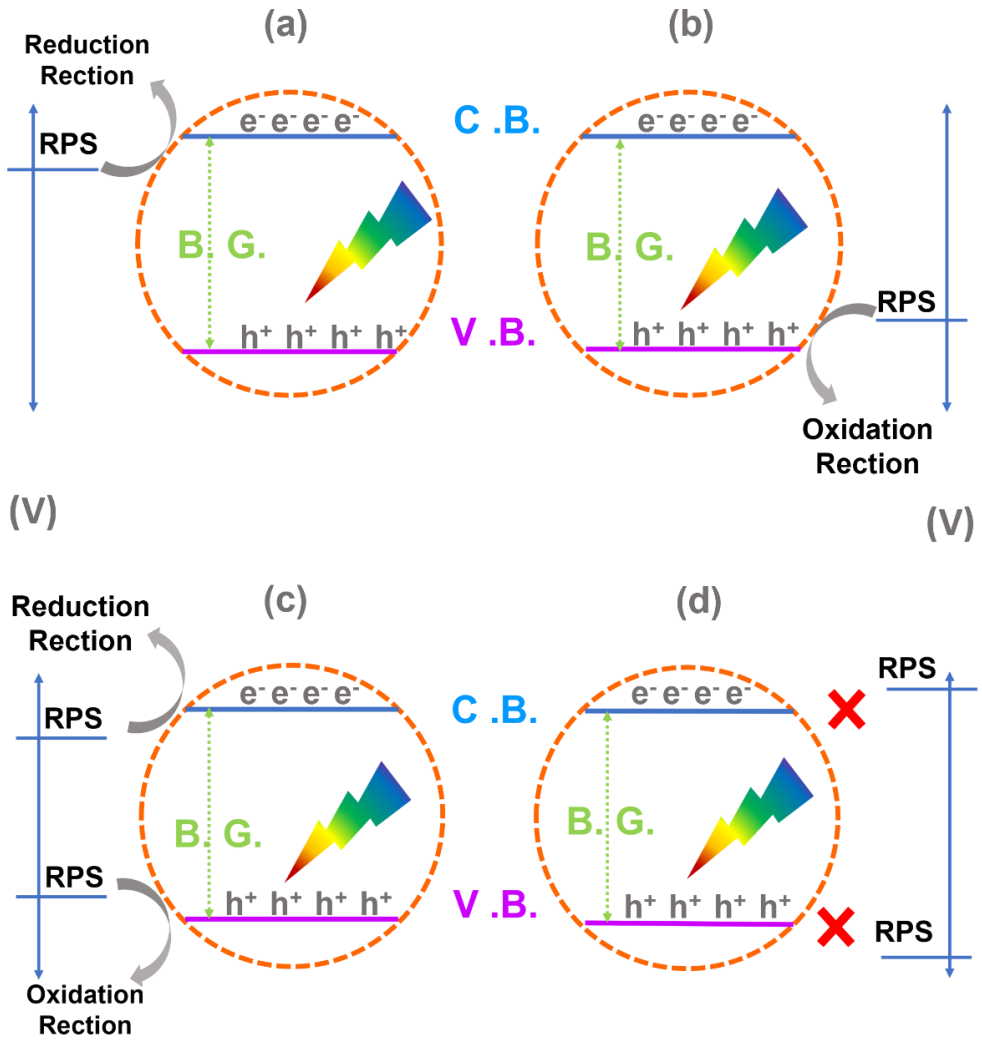


Figure 1.2 General schematic representation of photocatalysis process involving light absorption associated with electron excitation and redox reaction according to redox potential of substrate (RSP), where B.G. (bandgap).

The ability of a substrate to undertake chemical reactions on a semiconductor photocatalyst is contingent on the relative locations of the substrate's redox potentials and the band edges of the photocatalyst.[27,28] Four alternative outcomes exist:

- If the reduction potential of the substrate is less than the edge of the conduction band of the semiconductor photocatalyst, reductive reactions can occur (fig. 1.2a).
- The substrate can perform oxidative reactions if its oxidation potential is greater than the valence band edge of the semiconductor photocatalyst (fig. 1.2b).

- If the substrate's redox potential is greater than the valence band of the semiconductor photocatalyst and less than the conduction band edge, oxidative or reductive reactions can occur (fig. 1.2c).
- If the redox potential of the substrate is greater than the conduction band edge or less than the valence band of the semiconductor photocatalyst, it cannot undertake either reductive or oxidative reactions (fig. 1.2d).

Hence, the redox potential of the substrate is critical in determining the viability of photocatalytic processes on a semiconductor photocatalyst. By comprehending the redox potentials and band edges of photocatalysts and substrates, scientists may build more efficient and effective photocatalytic systems.

1.4 Photocatalytic Applications:

There are numerous applications of photocatalysis, however in this thesis we focus mainly on water splitting and nitrogen fixation with concurrent value-added products formation. Methane stream reforming and the Haber-Bosch process are commercially employed for the generation of hydrogen and ammonia, respectively.[29,30] Yet, flaws in both of these processes prevent chemistry from achieving its aims of being environmentally benign, sustainable, and energy-efficient. For example, the Haber-Bosch reaction requires hydrogen as an input, but the methane stream reforming method emits 10 kg of carbon dioxide for each kg of H_2 produced. In addition, each of the procedures requires high temperatures and pressures.[31]

In contrast, nature is able to achieve the splitting of water by chloroplasts and the fixing of nitrogen by nitrogenases, while keeping the same temperature and pressure by using solar light as an energy source. After being inspired by the natural process of photosynthesis, a number of academics have concentrated their research on solar water splitting and nitrogen fixation.[32-36] Solar energy is utilised in both of these processes, which turn water into hydrogen using a photocatalyst composed of semiconductor material, and nitrogen into ammonia using a nitrogen-fixing mechanism with in-situ generated protons.

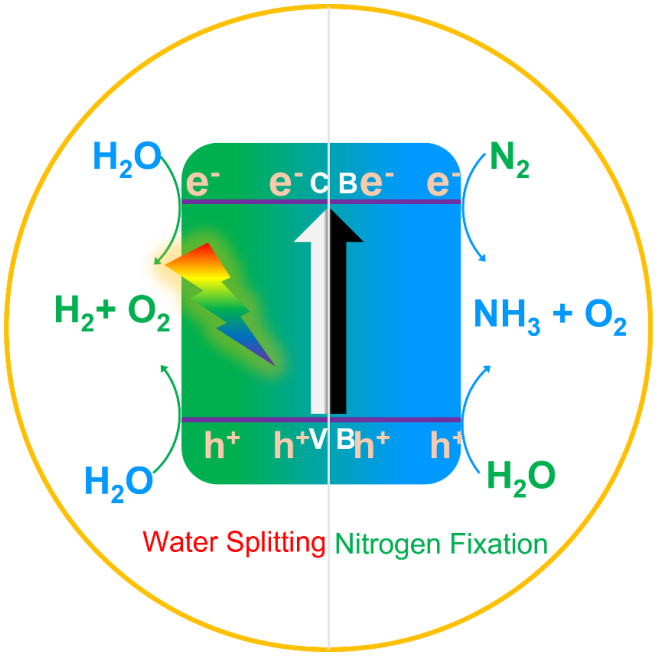


Figure 1.3 A schematic representation of photocatalytic water splitting and nitrogen fixation reactions.

At the initial phase of each of these artificial photosynthesis processes, known as photoexcitation, excitons are formed. Excitons could be defined as quasi-particles that form when Coulomb-interacting electrons and holes in semiconductors are bound into paired state. Excitons are very short-lived, and typical life time is in picosecond range. Throughout this phase, holes remain inside the VB, whilst stimulated electrons ascend to the CB. After the excitons are decomposed the electrons are liberated, from their confinement with the holes, and begin to circulate around the bulk and surface of the photocatalyst in an attempt to reach the reactive sites. The remaining electrons catalyse the conversion of the adsorbed H_2O (or N_2) to H_2 (or NH_3) (Fig. 1.3). In order to properly split water and fix nitrogen by using solar energy, it is necessary to employ a suitable photocatalyst with high activity. Detail mechanism is discussed in later sections.

TiO_2, g-C_3N_4, CdS, $SrTiO_3$, and $(Ga_{1x}Zn_x)(N_{1x}O_x)$ have all made considerable strides in the past four decades in the field of solar water splitting. Nevertheless, their functions are now hampered due to inadequate electron transmission from the bulk to the surface.[18-24] In addition, these photocatalysts typically exhibit weak nitrogen binding, resulting in a diminished solar nitrogen fixation efficiency. Many synthesis strategies, including crystalline facet tailoring, surface functionalization, co-catalyst, plasmonic modification, and

heterojunction creation, have been employed to improve photocatalytic activity.[37] By controlling photo absorption and accelerating electron transport on the photocatalysts' surfaces, these techniques aim to boost the efficiency of photocatalysts in solar water splitting and nitrogen fixation.

1.5 Photocatalytic water splitting:

Photocatalytic water splitting imitates the natural process of photosynthesis in plants and is frequently referred to as artificial photosynthesis.[38] Using photocatalytic processes and the solar energy that reaches the Earth's surface, it is feasible to create hydrogen from organic substances found in wastewater or water. This process includes the conversion of light energy to chemical energy, and the water splitting reaction contributes to the formation of Gibbs free energy (GE).[39] With this technique, there are two ways to create hydrogen: photocatalytic water splitting and photocatalytic organic reforming.[40-42] In the first and preferred method, water undergoes a redox reaction with electrons and holes to H_2 and O_2, respectively; whereas organic molecules gets oxidized to value added products as well as CO_2, and water undergoes reduction to form proton ions in the second technique. Using electrons, the photocatalyst enables the conversion of proton ions to H_2.

Figure 1.4[41] depicts the photocatalytic water splitting process for hydrogen generation, which consists of four primary photocatalytic processes: light absorption, charge excitation, charge separation and transfer, and surface catalytic reactions.[43] Light having energy equal to or more than the band gap energy (EBG) of the semiconductor photocatalyst initiates photocatalysis. A semiconductor photocatalyst typically exhibit a VB and a CB, which are separated by the EBG. When the proper photon excitation is present, photocatalysts undergo electronic transitions and form e/h pairs. Once the charges have been separated, the electrons are free to move around and available for reduction reaction; similarly, holes in the VB are available for oxidation reaction. Nonetheless, the chances of recombination of holes and electrons are really high, which deters the efficiency of photocatalytic process.

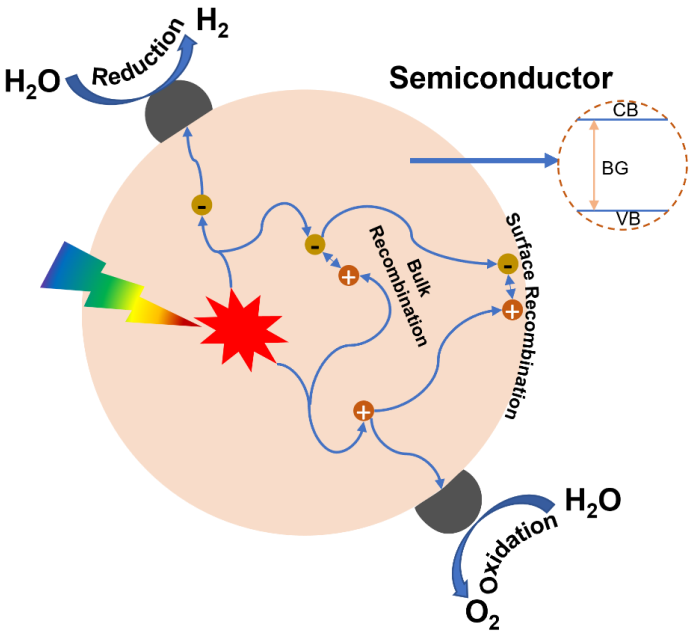


Figure 1.4 Photocatalytic water splitting mechanism and some of the recombination processes.

Both the reduction and oxidation processes involve water molecules; The oxidation reaction decomposes water into oxygen, whereas the reduction reaction reduce water into hydrogen gas. If the reduction and oxidation potentials are above and below the CB and VB levels, respectively, photocatalyst surface redox processes occur in a facile way.[40] Photo-excited holes (h^+) may oxidise both water and organic substances such as alcohols. With a photocatalyst and light energy, which is larger than the band gap, water can be split photo-catalytically at room temperature with the holes generated. Nevertheless, splitting water for H_2 production using photocatalysts is difficult due to the quick recombination of photo-generated charge carriers, which emits photon/heat and decreases the efficiency of H_2 production. While doing photocatalytic water splitting, methanol, ethanol, and glycerol are commonly utilised as sacrificial reagents and electrolytes to solve this issue.[43] The electrolytes are neither reduced nor oxidised by the CB electrons and VB holes. Electrolytes facilitate the flow of ions and the transfer of electrons to neighbouring semiconductors. Increasing the charge separation between VB and CB is crucial for boosting the effectiveness of photocatalytic water splitting events. This can be accomplished by combining VB with electron donors or sacrificial reagents.

Understanding thermodynamic analysis in terms of energy, band gap, and redox potential is vital for enhancing the maximum performance of photocatalytic activity. Limitations exist in the creation of H_2 from water, mainly due to high recombination of charge carriers and hence poor charge utilization. Consequently, it is important to enhance photocatalytic water splitting processes to enable the production of clean and sustainable energy/chemicals.

1.6 Strategy to Improve Photocatalytic activity:

In recent years, tremendous progress has been achieved in the field of photocatalysis; nevertheless, there are still various barriers to overcome before the technology can be extensively used in the real-world applications. To make photocatalysis practicable, a minimum efficiency of 10 percent is required. To achieve this level of efficiency, however, it is necessary to overcome various real-world obstacles, such as enhancing visible light absorption and decreasing charge recombination in the photocatalytic process.

Developing efficient photocatalysts for water splitting is complicated by the need to tailor both the bulk and surface characteristics of the material. Regulating the dependency between electrical, microstructural, and surface characteristics is required to build the optimal photocatalytic system. Several methods have been proposed to increase the efficiency of photocatalysts for water splitting, and nitrogen fixation; including sensitization, surface modification with co-catalysts to reduce the activation energy, minimizing defects, doping to tune the band gap and VB/CB edge energy, tuning the bandgap energy by various approaches for visible light absorption, and artificial leaves composed of multiple suitable semiconductors.

Tuning the bandgap energy is a typical strategy for increasing the efficiency of photocatalytic materials. By adjusting the energy of the bandgap to match that of visible light photons energy, more photons may be absorbed and utilised to increase the efficiency. The addition of co-catalysts to the surface of the photocatalyst reduces the activation energy required for reactions to occur. Sensitization is an additional intriguing method that includes affixing dye molecules to the photocatalyst's surface in order to boost light absorption and increase the system's efficiency.

One of the critical limiting factors in photocatalysis is the different time scales of photophysical and photochemical processes, which can lead to high charge recombination.

To address this, 2D-layered materials and quantum dots can be used to maximize charge carriers and improve diffusion. Another obstacle is the poor light absorption and high charge recombination when scaling up the photocatalyst amount. This can be overcome through the use of thin films or panels with enhanced hydrogen production. Additionally, it is important to perform experiments around neutral pH and explore cheaper and earth-abundant co-catalysts. The use of eco-friendly and/or biomass-derived agents as sacrificial agents can replace methanol.

The artificial leaf concept is an additional cutting-edge method for creating more efficient photocatalysts. Many appropriate semiconductors are used to create a system that replicates the photosynthesis mechanism in plants. By carefully managing the properties of the individual semiconductors, it is feasible to construct a system that successfully separates water into its constituent components using just sunlight.

Despite these promising ideas, there are still a large number of obstacles to overcome, before photocatalysis can be extensively used in the real world for applications. The high cost and limited durability of photocatalytic materials is a significant barrier. For the broad application of photocatalysis, the creation of more cost-effective and durable materials is essential. Another difficulty is the lack of consistency in photocatalytic testing techniques, which makes it impossible to evaluate the efficacy of various photocatalytic systems. In order to advance the field and facilitate the development of more efficient photocatalytic devices, it will be needed to establish uniform testing methodologies. Here we have discussed several strategies by which we can improve overall efficiency of the catalyst.

1.6.1 Role of Co-Catalyst:

Photocatalytic water splitting has long been projected as a possible method for the generation of hydrogen in a sustainable manner. Yet, the poor efficiency and stability of semiconductor photocatalysts continue to pose substantial obstacles to the practical deployment of this technology. Recent years have been devoted to the development of cocatalysts for increasing the activity and reliability of semiconductor photocatalysts. Cocatalyst may be defined as a substance/material that brings in catalysis in conjunction with one or more than one material; without the latter, co-catalyst cannot function independently. Critically the charge carriers are generated by the latter materials and supplied to the co-

catalysts; those charge carriers are critical for redox reactions to occur. Often the charge carrier generating materials cannot act as catalyst on its own or cannot act as efficient catalyst, and charge carriers are efficiently utilized by co-catalyst. In contrast, often co-catalyst cannot generate charge carriers on its own and hence it works best with its counterpart materials, which can generate charge carriers. In this section, the three essential roles of H_2 and O_2 evolution cocatalysts in photocatalytic water splitting has been described. (Fig. 1.5)

Cocatalysts minimise the activation energy or overpotential required for H_2 or O_2 evolution processes on semiconductor surfaces. While one molecule of H_2 formation requires only two electrons, four holes are concurrently required for the formation one O_2 molecule. In view of this O_2 evolution reaction is regarded as the most difficult step in the photocatalytic water splitting process. Consequently, cocatalysts with a low O_2 evolution overpotential can greatly improve the photocatalytic O_2 evolution reaction's efficiency.



Figure 1.5 Role of co-catalyst towards photocatalytic applications

Cocatalysts' second role is to facilitate the separation of electrons and holes at the cocatalyst/semiconductor interface. Holes on the photocatalyst's VB (rather electron transfer from co-catalyst to photocatalyst's VB) migrate to the O_2 evolution cocatalyst and oxidise H_2O to make O_2; while electrons on the photocatalyst's CB migrate to the H_2-evolution cocatalyst and reduce protons to H_2 molecules. The efficiency of charge separation and transfer from

the semiconductor to the cocatalyst is contingent upon the formation of an appropriate heterojunction between the two materials. The relative energy of CB/VB of photocatalyst and co-catalyst at the heterojunction interface impacts the direction and efficiency of carrier separation and transport. A heterostructure in close proximity to both the cocatalyst and the semiconductor can lower the required charge transfer distance, so significantly minimising bulk recombination and enhancing overall efficiency.

The third role of cocatalysts is to increase the stability of semiconductor photocatalysts and to inhibit photo-corrosion. Semiconductors that respond to visible light, such as (oxy)sulfides and (oxy)nitrides, are susceptible to oxidation via photogenerated holes, which results in their self-decomposition.[43] By removing the photogenerated holes for O_2 evolution, the loading of cocatalysts on these semiconductors can prevent their decomposition and improve their durability.

1.6.1.1 Factor Affecting the Co-Catalyst:

Photocatalytic water splitting based on semiconductors necessitates the employment of H_2 and O_2 evolution cocatalysts, which play a crucial role in boosting the activity and dependability of photocatalysts. The performance of these cocatalysts is controlled by a number of variables, such as the loading amount, particle size, and structure.

Research have revealed a volcano-like relationship between photocatalytic activity and the quantity of cocatalyst placed on the semiconductor, independent of synthesis process, photocatalyst type, and cocatalyst loading.[44] As the loading quantity of the cocatalyst on the semiconductor reaches the optimal value, the maximum inherent activity is realized. Nevertheless, beyond this limit, increasing the cocatalyst loading greatly lowers the photocatalytic activity. This decrease can be ascribed to a number of factors. High cocatalyst loading quantities may cover the surface-active sites of the semiconductor, preventing interaction with sacrificial agents or water molecules. Second, high cocatalyst loading on semiconductor surfaces may block incoming light, and hence preventing the formation of photogenerated electrons and holes. A considerable amount of the semiconductor's surface may be coated with cocatalysts, hence diminishing its photocatalytic activity.

The cocatalyst's particle size also plays an important influence in its catalytic activity. Cocatalyst with smaller particle size have a bigger surface area and more active sites at the

same loading level, resulting in enhanced catalytic activity.[45-47] Therefore, smaller cocatalyst particles have a reduced probability of charge carrier recombination than bigger ones. In some situations, smaller cocatalyst particles may have lower interfacial charge transfer barriers from semiconductors to cocatalysts (e.g. electron-tunnelling effect). Many studies have showed that the small size and wide dispersion of loaded cocatalysts result in a markedly enhanced photocatalytic efficiency. Man-made molecular cocatalysts with extremely tiny dimensions, such as $[Mo_3S_4]^{4+,}$ are composed only of surface atoms/edge sites and have the optimum number of active sites, which can considerably enhance the photocatalytic activity of semiconductors.[48]

Many cocatalysts, including the well-known core-shell Ni-NiO (NiO_x) and Rh-Cr_2O particles, are highly dependent on their structural features in order to attain high activity for overall photocatalytic water splitting, CO_2 reduction and photocatalytic nitrogen fixation.[49-56] The shells of these core-shell structures are capable of preventing corrosion of the metal core, reducing O_2 photoreduction and reverse reactions, and enhancing cocatalyst robustness. Understanding these sorts of structures might aid in the development of novel cocatalysts that are effective and dependable for photocatalytic water splitting.

1.6.2 Plasmons:

Michael Faraday discovered surface plasmons in 1857, although the scientific community at the time paid little attention to his findings.[57] Nevertheless, recent developments have demonstrated that surface plasmons are exploited in a number of sectors, including catalysis, imaging, sensing, solar cells, and electronics. Plasmonic effects cause molecules adsorbing on plasmonic metal surfaces to produce more pronounced Raman modes.[58,59] The photocatalytic splitting of water is one of the many applications for plasmonic nanostructures.

Surface plasmons refer to the coherent oscillation of CB electrons on the surface of a metal particle, which is triggered by the incident light's electromagnetic field. Surface plasmon resonance (SPR) employs metal nanostructures as antennas to convert light into localised electric fields at the metal-dielectric interface.[60] Surface plasmon polaritons (SPP) and localised surface plasmon resonance (LSPR) are two SPR different modes but dependent on the geometry of the metal surface (Fig 1.6).

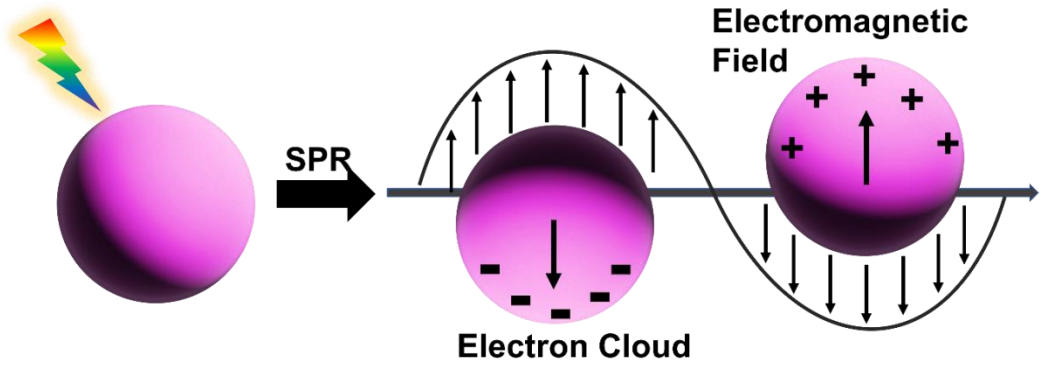


Figure 1.6 SPR effect in case of metal nanoparticles.

SPP takes place when metal nanostructures, such as nanowires and foil, are significantly larger than the wavelength of the incoming light, and this plasmon spreads hundreds of micrometres along the metal surface. LSPR arises when the size of metal nanostructures is substantially smaller than the incoming light wavelength. In the presence of an external electromagnetic field, the polarisation of the electron clouds in the CB of metal nanostructures causes them to oscillate at a certain frequency. When the frequency of an electron cloud's oscillation resonates with a specific frequency range of incoming light, a considerable electron oscillation will be seen. Hence, plasmonic surfaces absorb light. The LSPR of Au and Ag nanostructures occurs in the visible solar spectrum, and they have attracted a great deal of interest. Among the variables that determine the LSPR effect are the density of CB electrons, the index of refraction of the surrounding medium, and the size and shape of the metal nanostructure.[61]

By modifying the composition, shape, and size of the plasmonic nanostructure, it is possible to create plasmonic nanocomposites that absorb the maximum solar light from the UV, visible, and perhaps near-IR spectrums.[62] Unless otherwise specified, SPR typically refers to LSPR in applications involving plasmonic photocatalysis or solar light harvesting. The wavelength dependence of the photocatalytic activity of semiconductor/plasmonic nanostructure composites is a distinguishing characteristic.

Many experiments have been conducted in several semiconductors for the half-reactions of oxygen evolution and hydrogen evolution, and a boost in activity has been seen in the metal nanostructure SPR region. This indicates that SPR is crucial for boosting the photocatalytic reaction rate on neighbouring semiconductors. Cronin and colleagues

discovered that the photocurrent density was five times higher in an $AuTiO_2$ composite than in TiO_2 when illuminated by visible light. Metallic SPR boosts photocatalytic activity and increases charge carrier concentration in semiconductors by transferring energy associated with SPR to neighbouring semiconductors.[63]

The concentration of charge carriers on a semiconductor next to plasmonic nanostructures increases by three separate energy transfer mechanisms: (1) photon-induced hot electron transfer, (2) plasmon-induced resonance energy transfer, and (3) plasmon-induced charge separation.[64] Photon-induced hot electron transfer happens when the hot electrons created by plasmonic nanostructures transfer to the semiconductor owing to a high electric field close to the metal surface. Plasmon-induced resonance energy transfer takes place when the energy from the plasmon resonance is transmitted to the semiconductor, hence increasing the electron excitation state. Plasmon-induced charge separation takes place when the electric field close to the metal surface separates the photogenerated electrons and holes. Further, it is not necessary that only metal particle can induce LSPR effect; even oxides, such as MoO_{3-x} can induce LSPR.[65]

1.6.3 Heterojunction:

Materials that are capable of turning light into chemical energy are semiconductor photocatalysts. In recent years, these materials have gained considerable interest as a viable alternative for sustainable energy generation. A promising form of semiconductor photocatalyst is the heterojunction photocatalyst, which consists of two or more linked semiconductors. Virtual positions of the CB and VB of the semiconductors dictate the direction of charge transfer in a heterojunction photocatalyst.

Figure 1.7a, b, and c demonstrate three forms of heterojunction photocatalysts, known as type I, II, and III. In type I, electrons migrate to a material with a greater positive CB position, whereas in type II, holes migrate to a substance with a higher negative VB position.[66] In type III, electrons and holes move without spatial charge separation from one substance to another. The direct Z-scheme entails relocating the other semiconductor in a manner that induces spatial charge separation.

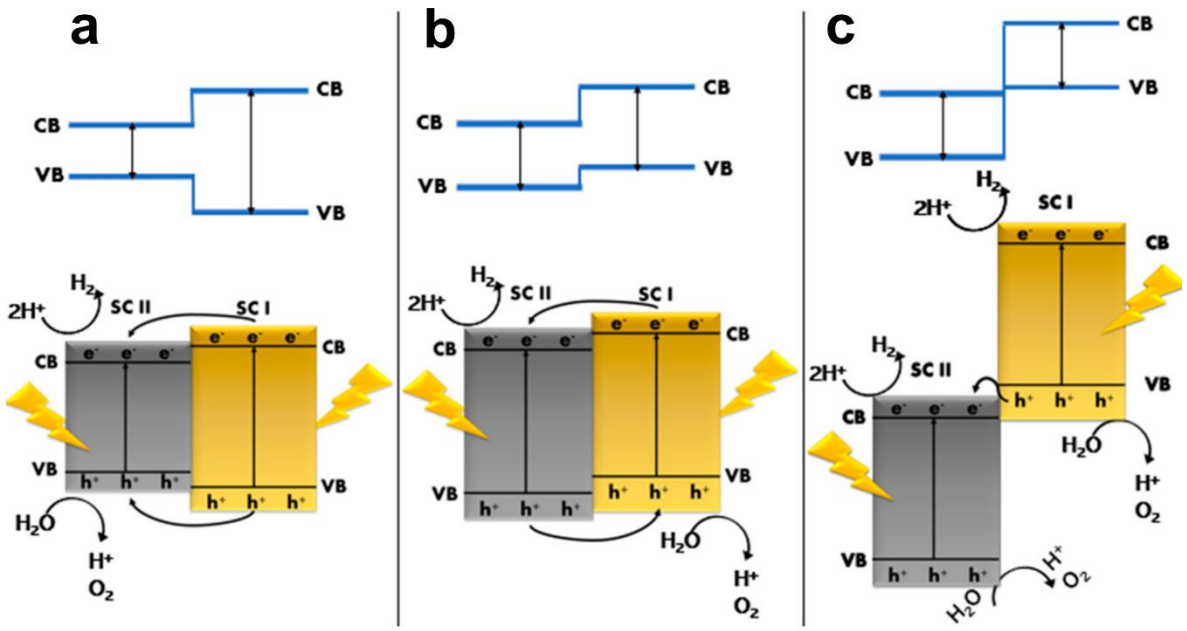


Figure 1.7 Band structures and charge transport in three different semiconductors combination systems (ref. 66)

CuO_x-TiO_2 is a well-known heterojunction photocatalyst that has been utilised well for photocatalytic H_2 production. It is unknown, however, which component of the composite is active. The CuO CB is placed below the TiO_2 CB, allowing photoexcited electrons to easily flow from the TiO_2 CB to the CuO CB. The CB edge (ECB) of CuO is +0.96 eV vs NHE, which cannot reduce water in principle. Hence, it is uncertain whether CuO is a cocatalyst or the active species for water splitting on TiO_2.[67]

To improve photocatalytic H_2 production activity, type I composites are utilised. The structure of Cu_2O enables TiO_2 to act as a cocatalyst in the charge separation process. Wu et al.[68] developed a number of CuO_x species supported on TiO_2 and studied their involvement in photocatalytic H_2 production. They discovered that the Cu(I) species promotes photocurrent and H_2 production, but the Cu(II) species suppresses these activities.

1.6.4 Artificial Photosynthesis:

Sensitizing them with semiconductor QDs that may be employed in QuAL devices for improved hydrogen generation is a potential technology.[69] Due to the fact that QDs have a high visible light absorption coefficient, they are effective in capturing photons from various regions of the sun spectrum.

Quantum size effect is a fundamental benefit of QDs, as it causes photon interactions with bulk semiconductor QDs to be comparatively weak compared to interactions with QDs of minute size. By adjusting the size of the QDs, it is possible to modify the optical band and provide new chances for collecting photons from various portions of the solar spectrum. As seen in Figure 1.8, when the size of the QDs decreases, the band gap dramatically increases, leading to a progressive shift in their associated colour. Its adjustable optical absorbance is simply one of the numerous advantages of utilising tiny QDs. In addition, electron transport to the semiconductor is achievable with QDs of minute size. The CB moves to a more negative potential as the size of the QDs decreases, enabling electron transport in the composite system.

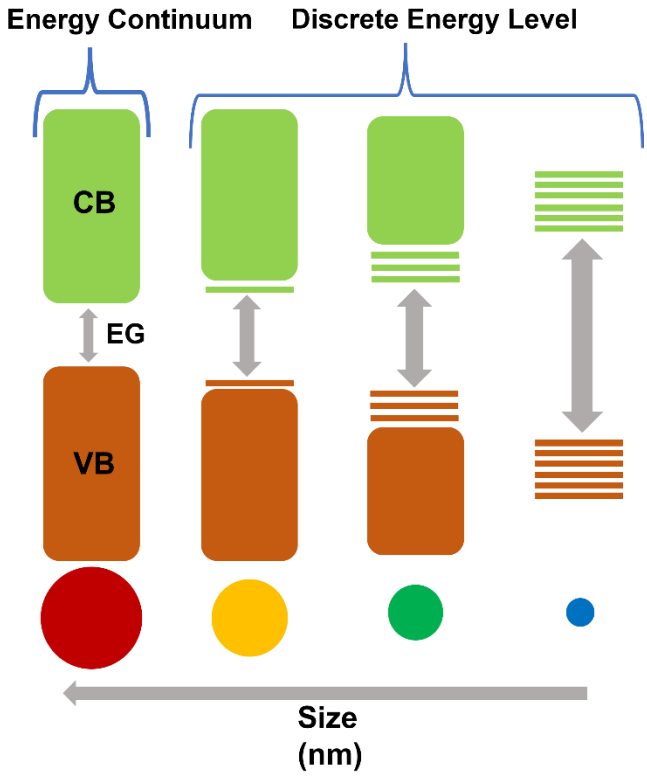


Figure 1.8 Discretization of the energy with respect to their size

Another important benefit of QDs is their capacity to separate charges. Charge transfer occurs in the quantum dot-sensitized semiconductor due to the hetero-junction produced at the QD and semiconductor interface. QDs absorb light and transport electrons to semiconductors through heterojunctions. This characteristic makes QDs suitable for solar water splitting. The significant negative potential associated with the CB (compared to hydrogen reduction potential) boosts hydrogen production even further.[70]

The process of sensitization by QDs is comparable to that of dye sensitized solar cell (DSSC). QDs have demonstrated excellent photon conversion efficiency at shorter wavelengths. This concept was utilised to develop a wireless photochemical cell, also known as a quasi-artificial leaf (QuAL), which generates hydrogen without the usage of electricity. By sensitising TiO_2 with QDs, the efficiency of QuAL devices may be increased, resulting to increased hydrogen generation. This strategy might lead to the creation of synthetic light-harvesting structures that generate solar fuels more efficiently.[43]

1.6.5 Role of Sacrificial Reagent:

In addition to studying mechanistic concerns and the function of sacrificial agents in optimising efficiency, substantial research has been devoted to improving the characteristics of photo-catalysts.[71] Methanol has been the most commonly employed sacrificial agent due to its high hydrogen concentration, its propensity to collect h^+ or low oxidizing potential, and its simple structure, which aids in the comprehension of reaction processes. Even though it possesses just one difficult-to-activate C-C bond, ethanol has also been widely studied since it is non-toxic and somewhat complicated than methanol. Bio-sources generated compounds such as ethanol, glycerol, and sugars generated from biological substrates or waste products are especially desirable for the Photocatalytic process. In the next part, we will cover some of the most prevalent organic sacrificial agents used in Photocatalysis for H_2 production.[71]

Due to its basic structure consisting of a single hydroxyl group and a single carbon atom, methanol is regarded as the one-of-the top standard molecules for photocatalytic H_2 production. Primarily methanol was utilised as the principal feedstock in the earliest the Photocatalytic experiments. Kawai and Sakata reported the production of H_2 using methanol oxidation in 1980 and presented a chemical pathway involving the synthesis of formaldehyde, its oxidation to formic acid as an intermediate, and its decomposition into CO_2 and H_2.[17] In a more recent study, Chiarello et al. investigated TiO_2 functionalized with several noble metals (Ag, Au, Pt) and discovered that the work function values and activity of the cocatalyst are strongly associated.[72,73]Similarly, Nalajala et al has shown the possibility of generating formaldehyde from methanol, while concurrent generation of hydrogen; this underscores the simultaneous utilisation of electrons and holes to generate H_2 and formaldehyde, respectively.[74]

Ethanol has attracted interest as a possible option for the synthesis of hydrogen via sacrificial-agent assisted photocatalysis due to its availability and its ability to be generate on a wide scale from renewable biomass like as cellulose or lingo-cellulose.[75] During the photo-oxidation of ethanol, acetaldehyde and acetic acid are produced concurrently with the reduction of H^+ to yield H_2.[76,77] These by-products may then undergo further oxidation, and although acetaldehyde is the primary by-product, other chemicals such as CH_4, CO_2, CO, C_2H_4, and C_2H_6 have been discovered in variable proportions.[77]

It has been claimed that acetaldehyde can also be formed by the spontaneous synthesis of ethoxide on the surface of TiO_2, which leads to the oxidation of H^+, or by the oxidation of ethanol by OH.[78] Complete ethanol oxidation over Pt/TiO_2 catalysts has been reported, displaying a 50% apparent quantum yield (AQY) of H_2 evolution at 365 nm based on the generated CO_2 and H_2.[79] In recent research, 1D brookite nanorods have been used to generate H_2 with a quantum yield of 65%. The dehydrogenation process produced acetaldehyde and 1,1-diethoxyethane, but no carbon dioxide was detected, suggesting that ethanol oxidation occurs more quickly than acetaldehyde oxidation.[80]

Research into the generation of hydrogen gas from renewable biomass sources like cellulose and lingo-cellulose has been spurred by the demand for sustainable fuel sources. Glucose, a saccharide derived from cellulose hydrolysis, has been utilised as a biomass model in a number of experiments for H_2 photoproduction capacity.[79,81] John et al. examined the photoreforming of glucose over a Pt/TiO_2 catalyst in 1983 and postulated that photogenerated h^+ transforms the OH and CHO terminal groups into oxides, which subsequently undergo decarboxylation with CO_2 evolution.[82] This process exhibits a negative Gibbs free energy shift, which makes it thermodynamically beneficial for H_2 production.[83]

Glycerol, a by-product of the biodiesel industry, has showed potential as a sacrificial agent for H_2 generation. Nanostructures based on TiO_2 have gained the greatest interest for glycerol photo-oxidation because they can function as both an H-source and an e-donor during the production of H_2.[84] When subjected to simulated solar light irradiation, Cu/TiO_2 nanocomposites with aqueous glycerol generate 1,3-dihydroxypropanone and hydroxyacetaldehyde in the liquid phase and CO_2 and H_2 in the gas phase. As the initial phases of glycerol oxidation, chemisorption, direct oxidation by h^+, and subsequent release of the ketone have been proposed.[85] Using a Pt/TiO_2 catalyst dispersed in aqueous solutions and

artificial sunlight, Kondarides and colleagues discovered that glycerol was completely converted to CO_2 and H_2.[79] By increasing glycerol concentration, the efficiency of light-to-chemical energy conversion increased, and high values (31%) were reached under UV light irradiation. It was discovered that the dissociation of adsorbed glycerol molecules on Pd/TiO_2 led to simultaneous CO and H_2 evolution, with photoactivated oxygen species travelling to the Pd and reacting with CO to convert it to CO_2.[86] During the photo reforming of glucose and glycerol, the formation of main by-products including ketones, alcohols, and acids has been documented in number of investigations. Copper oxide on titania nanotube was evaluated direct sunlight with aqueous glycerol and reported the maximum H_2 production of 99823 µmol h^{-1} g^{-1}.[87] Being a by-product of the biodiesel industry, the use of glycerol as a sacrificial agent offers the added benefit of decreasing waste and disposal expenses. TiO_2 nanostructures have demonstrated promise in glycerol photo reforming, with increased efficiency found with increasing glycerol concentration and UV light exposure.

Overall, these investigations demonstrate the viability of utilising renewable biomass sources as sacrificial agents for H_2 production, as well as the significance of catalyst design in optimising this process. While the use of glucose and glycerol as sacrificial agents has showed promise, further study is required to investigate the possibility of alternative renewable biomass sources, such as cellulose, lignocellulose, for H_2 generation as well as value added products formation. In addition, the optimization of catalysts and the reduction of major by-products will be essential for the development of sustainable and efficient H_2 generation systems utilising renewable biomass sources.

1.6.6 Role of Defects:

In the field of photocatalysis, the study of defects is a crucial area of study. Crystallographic defects are prevalent in photocatalytic materials, and these defects can have a significant effect on the materials' photocatalytic performance. In crystalline materials, these defects break the periodic arrangement of atoms in crystallographic lattice.[88] This inhibits the diffusion of photogenerated charge carriers by converting bulk defects into recombination sites for photoexcited electron-hole pairs.[88,89] Indeed passivation of defects are generally adopted, especially while fabrication various solar cells. It is also important to develop synthetic strategies to completely avoid or minimize the defects. Alternatively, surface defects might serve as adsorption sites. This permits photogenerated charge carriers

to diffuse to adsorbate species, hence accelerating the separation of charge carriers in photocatalysts.[90,91] In the scientific world, defects are widely utilised in the fields, such as, water splitting. Indeed caution is required to use the defects in a careful way, and it can be a double-edged sword. Defects may help to improve charge separation, surface reaction and enhancing the light absorption which is given as a schematic diagram in fig. 1.9. As a technique of classifying the numerous types of defects that may be encountered, numerous classification strategies have been provided.[92,93]

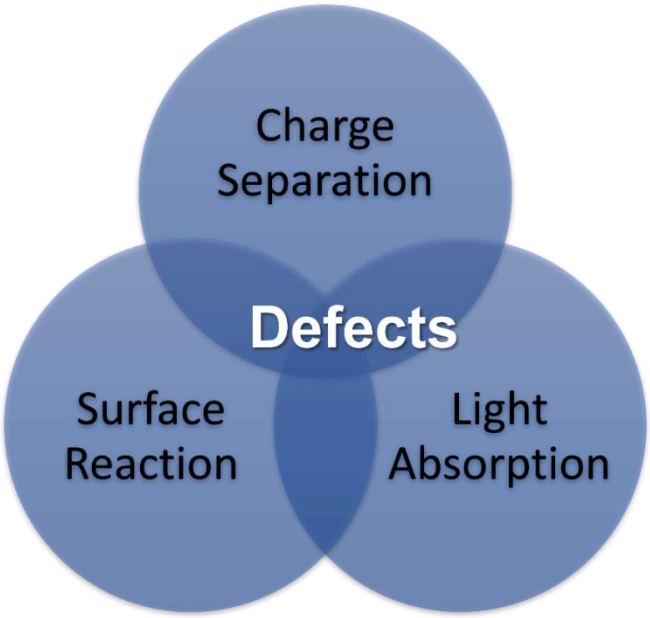


Figure 1.9 Role of defect for the photocatalytic applications

Dimensions are commonly used to classify issues and are one of the most prominent methods for doing so. This approach permits the classification of defects into four unique categories: zero-dimensional point defects, one-dimensional line defects, two-dimensional planar defects, and three-dimensional volume defects. Zero-dimensional point defects, such as vacancies and doping, play an essential role in photocatalytic nitrogen fixation.[94] In contrast, one-dimensional and higher-dimensional defects are rarely taken into account throughout this approach. The elemental composition of the point defects is an additional criterion for classification.[95] Many aspects associated with distinct defects each possess an own set of characteristics. Recent advances in photocatalytic nitrogen fixation, for instance, have led to the classification of diverse defects as nitrogen vacancies, oxygen vacancies, sulphur vacancies, and vacancies associated with other elements.

1.7 Objective of Thesis:

The fundamental objective of this thesis is to concentrate on photocatalytic hydrogen production and the concurrent creation of items with added value products through the efficient utilisation of electrons and holes. Combining several semiconductors with suitable bandgap and band edges, as well as incorporating a co-catalyst, is a viable strategy for photocatalytic solar water splitting. A photocatalyst should satisfy the following criteria: (i) The photoanode/photocatalytic composite/material should absorb UV and visible light to generate the maximum number of electron-hole pairs; (ii) efficient separation of electron and hole, and diffusion of them towards the redox sites; and (iii) efficient utilisation of electron and hole for the reduction and oxidation, respectively, of water at relevant cocatalyst sites. (iv) it is also very essential to electronically and structurally integrate the photocatalyst components, as it can enhance the charge separation and diffusion towards the redox sites. It may be reiterated that photocatalysis involves very short-lived charge carriers (time scale of ≤ns) and it is essential to separate electron-hole pairs and utilize them quickly. To boost light absorption, it is desired to employ QD; specifically, plasmonic material would be highly desired, as it can boost electron transfer or create local field effect. A high-quality heterojunction between quantum dots and semiconductors may effectively separate electrons and holes while minimising recombination. Co-catalysts can facilitate the utilisation of charge carriers, which serving as catalytic sites for the hydrogen and oxygen evolution. Whereas hydrogen evolution is a two-electron process, oxygen evolution is a four-electron process; the latter is known to be a rate-determining step that slows the total reaction rate. Yet, by employing holes for the oxidation of a sacrificed reagent, the kinetics of H2 evolution cay be maximized.

Important photocatalysis issues were investigated using a methodical and sequential methodology.

1.8 Outline of Thesis:

Chapter 1 start with a concise overview of the development of photocatalysis, then go on to the subject's core principles and the mechanism behind the process. In this chapter, we addressed many strategies that are described in the literature to increase photocatalytic activity while simultaneously decreasing charge recombination. To increase the effectiveness

of the catalyst, several factors, such as heterojunction and plasmonic effect, as well as the function of sacrificial reagent and usage of the defect, should be taken into consideration. In addition to that, the method of producing solar hydrogen using "quasi-artificial leaves" is covered in this chapter as well.

Chapter 2, discussed, the ways to produce photocatalysts based on TiO_2 and other materials used in the photocatalytic water splitting process. Particularly, we concentrated on TiO_2 photocatalysts. A facile photo-deposition process was utilised in order to prepare small clusters of anionic gold on titanium dioxide. The CuO_x/TiO_2 composite was also prepared using different methods, followed by the bimetal system and defective Titania, respectively. Chalcogenides and TiO_2 were utilised to construct a wireless cell using the successive ionic layer absorption and reaction (SILAR) technique. This chapter also includes a brief summary of the techniques employed, such as, UV-Visible spectroscopy transmission electron microscopy (TEM), UV-Visible spectroscopy, and Raman spectroscopy, N_2 adsorption-desorption isotherm. These are only a handful of the most common and significant analytical procedures employed extensively for the present thesis work.

Chapter 3 deals with study of an earth-abundant Ni-Cu co-catalyst is coated with half a monolayer of Pt ($0.5\theta_{Pt}$), which is then paired with a quasi-artificial leaf (QuAL) device (TiO2/ZnS/CdS) for efficient solar hydrogen production. Using the SILAR approach, ZnS and CdS quantum dots are used to sensitise TiO_2 in the QuAL. The $0.5\theta_{Pt}$ -coated Ni-Cu displays an onset potential of 0.05 V vs. the reversible hydrogen electrode for the hydrogen evolution process, which is nearly equal to that of commercial Pt/C. Incidentally, the photoactivity of the present QuAL device using either bulk Pt or a Ni-Cu cocatalyst with $0.5\theta_{Pt}$ coating is identical.

Chapter 4a The $Au@TiO_2$ material was prepared using a simple photo-deposition process, and it exhibits well-dispersed plasmonic gold that was electronically integrated with P25-TiO_2. Studies using XPS have shown that the fundamental nature of gold is electron-rich or anionic. This demonstrates strong electronic integration with titania and the possibility of charge transfer from oxygen-vacancy sites to gold. This, in turn, helps the simultaneous production of large amounts of H_2 (18 mmol/h.g.) and VAPs (glycolaldehyde, dihydroxyacetone, and formic acid) formation from glycerol under one sun condition or in direct sunlight.

Chapter 4b focuses on an in-depth analysis of the CuO_x/TiO_2 composite. The preparation of small copper clusters deposited over TiO_2 by creating surface oxygen vacancies at room temperature using a variety of different methods resulted in high photocatalytic hydrogen production by employing glycerol as a sacrificial reagent. XPS was employed to investigate the oxidation status of the material, before and after the reaction.

Chapter 4C present the study, to evaluate photocatalytic hydrogen generation along with VAP formation using biomass components. A NiCu bimetallic system impregnated over TiO_2 was employed as the photocatalyst. This part of thesis also demonstrates the exploitation of both charge carriers in a concurrent manner.

Chapter 5 Photocatalytic nitrogen fixation via defect engineering on TiO_2 has been carried out. The ratio between rutile and anatase was optimized to enhance the functional defects toward higher photocatalytic nitrogen fixation. Nitrogen activation is the rate-limiting step in nitrogen fixation; however, creating defects (especially oxygen vacancies) work as an active site for nitrogen activation, by reducing the bond order of nitrogen and resulting in ammonia formation with in-situ generated protons and electrons.

Chapter 6 includes the findings and conclusions that were derived from the observations that were made throughout the thesis work, described in the present thesis. In the end, we deliberate the potential depth and the breadth of possible future research directions in the field of solar water splitting.

1.9 References:

1. Morton, O. A New Day Dawning? Silicon Valley Sunrise. *Nature* **2006**, *443*, 19–22.
2. Barber, J. Photosynthetic Energy Conversion: Natural and Artificial. *Chem. Soc. Rev.* **2009**, *38*, 185–196.
3. Lewis, N. S. Toward Cost-Effective Solar Energy Use. *Science* **2007**, *315*, 798–801.
4. REN21. RENEWABLES 2019 GLOBAL STATUS REPORT https://www.ren21.net/gsr-2019.
5. Grätzel, M. Photoelectrochemical Cells. *Nature* **2001**, *414*, 338–344.
6. Erisman, J. W.; Sutton, M. A.; Galloway, J.; Klimont, Z.; Winiwarter, W. How a Century of Ammonia Synthesis Changed the World. *Nat. Geosci.* **2008**, *1*, 636–639.

7. Albini, A.; Fagnoni, M. 1908: Giacomo Ciamician and the Concept of Green Chemistry. *ChemSusChem.* **2008**, *1*, 63–66.
8. Zhu, S.; Wang, D. Photocatalysis: Basic Principles, Diverse Forms of Implementations and Emerging Scientific Opportunities. *Adv. Energy Mater.* **2017**, *7*, 1700841.
9. Guo, Q.; Zhou, C.; Ma, Z.; Yang, X. Fundamentals of TiO_2 Photocatalysis: Concepts, Mechanisms, and Challenges. *Adv. Mate.* **2019**, *31*, 1901997.
10. Renz, C. Über Die Einwirkung von Oxyden Auf Silbernitrat Und Goldchlorid Im Licht. *Helvetica Chimica Acta.* **1932**, *15*, 1077–1084.
11. Goodeve, C. F.; Kitchener, J. A. The Mechanism of Photosensitisation by Solids. *Trans. Faraday Soc.* **1938**, *34*, 902.
12. Ravelli, D.; Dondi, D.; Fagnoni, M.; Albini, A. Photocatalysis. A Multi-Faceted Concept for Green Chemistry. *Chem. Soc. Rev.* **2009**, *38*, 1999.
13. Lotfabadi, P. Analyzing Passive Solar Strategies in the Case of High-Rise Building. *Renew. Sust. Energ. Rev.* **2015**, *52*, 1340–1353.
14. Boddy, P. J. Oxygen Evolution on Semiconducting TiO_2. *J. Electrochem. Soc.* **1968**, *115*, 199.
15. FUJISHIMA, A.; HONDA, K. Electrochemical Photolysis of Water at a Semiconductor Electrode. *Nature* **1972**, *238*, 37–38.
16. Schrauzer, G. N.; Guth, T. D. Photolysis of Water and Photoreduction of Nitrogen on Titanium Dioxide. *J. Am. Chem. Soc.* **1977**, *99*, 7189–7193.
17. Kawai, T.; Sakata, T. Photocatalytic Hydrogen Production from Liquid Methanol and Water. *J. Chem. Soc., Chem. Commun.* **1980**, No. 15, 694.
18. Thompson, T. L.; Yates, J. T. Surface Science Studies of the Photoactivation of TiO_2 New Photochemical Processes. *Chem. Rev.* **2006**, *106*, 4428–4453.
19. Ardo, S.; Meyer, G. J. Photodriven Heterogeneous Charge Transfer with Transition-Metal Compounds Anchored to TiO_2 semiconductor Surfaces. *Chem. Soc. Rev.* **2009**, *38*, 115–164.
20. Tong, H.; Ouyang, S.; Bi, Y.; Umezawa, N.; Oshikiri, M.; Ye, J. Nano-Photocatalytic Materials: Possibilities and Challenges. *Adv. Mater.* **2011**, *24*, 229–251.
21. Mishra, A.; Mehta, A.; Basu, S.; Shetti, N. P.; Reddy, K. R.; Aminabhavi, T. M. Graphitic Carbon Nitride (g–C_3N_4)–Based Metal-Free Photocatalysts for Water Splitting: A Review. *Carbon* **2019**, *149*, 693–721.

22. Cheng, L.; Xiang, Q.; Liao, Y.; Zhang, H. CdS-Based Photocatalysts. *Energy Environ. Sci* **2018**, *11*, 1362–1391.
23. Patial, S.; Hasija, V.; Raizada, P.; Singh, P.; Khan Singh, A. A. P.; Asiri, A. M. Tunable Photocatalytic Activity of $SrTiO_3$ for Water Splitting: Strategies and Future Scenario. *J. Environ. Chem. Eng.* **2020**, *8*, 103791.
24. Lin, L.; Hisatomi, T.; Chen, S.; Takata, T.; Domen, K. Visible-Light-Driven Photocatalytic Water Splitting: Recent Progress and Challenges. *Trends Chem.* **2020**, *2*, 813–824.
25. Photocatalysis. *RSC Energy Environ. Ser.* **2016**.
26. Ohtani, B. Revisiting the Fundamental Physical Chemistry in Heterogeneous Photocatalysis: Its Thermodynamics and Kinetics. *Phys. Chem. Chem. Phys.* **2014**, *16*, 1788–1797.
27. Liu, B.; Zhao, X.; Terashima, C.; Fujishima, A.; Nakata, K. Thermodynamic and Kinetic Analysis of Heterogeneous Photocatalysis for Semiconductor Systems. *Phys. Chem. Chem. Phys.* **2014**, *16*, 8751.
28. Abe, R. Recent Progress on Photocatalytic and Photoelectrochemical Water Splitting under Visible Light Irradiation. *J. Photochem. Photobiol. C.* **2010**, *11*, 179–209.
29. Li, S.; Gong, J. Strategies for Improving the Performance and Stability of Ni-Based Catalysts for Reforming Reactions. *Chem. Soc. Rev.* **2014**, *43*, 7245–7256.
30. Hoffman, B. M.; Lukoyanov, D.; Yang, Z.-Y.; Dean, D. R.; Seefeldt, L. C. Mechanism of Nitrogen Fixation by Nitrogenase: The Next Stage. *Chem. Rev.* **2014**, *114*, 4041–4062.
31. Canfield, D. E.; Glazer, A. N.; Falkowski, P. G. The Evolution and Future of Earth's Nitrogen Cycle. *Science* **2010**, *330*, 192–196.
32. Zhang, P.; Wang, T.; Chang, X.; Gong, J. Effective Charge Carrier Utilization in Photocatalytic Conversions. *Acc. Chem. Res.* **2016**, *49*, 911–921.
33. Liu, J.; Kelley, M. S.; Wu, W.; Banerjee, A.; Douvalis, A. P.; Wu, J.; Zhang, Y.; Schatz, G. C.; Kanatzidis, M. G. Nitrogenase-Mimic Iron-Containing Chalcogels for Photochemical Reduction of Dinitrogen to Ammonia. *Proc. Natl. Acad. Sci.* **2016**, *113*, 5530–5535.
34. Banerjee, A.; Yuhas, B. D.; Margulies, E. A.; Zhang, Y.; Shim, Y.; Wasielewski, M. R.; Kanatzidis, M. G. Photochemical Nitrogen Conversion to Ammonia in Ambient Conditions with FeMoS-Chalcogels. *J. Am. Chem. Soc.* **2015**, *137*, 2030–2034.

35. Ni, M.; Leung, M. K. H.; Leung, D. Y. C.; Sumathy, K. A Review and Recent Developments in Photocatalytic Water-Splitting Using TiO_2 for Hydrogen Production. *Renew. Sust. Energ. Rev.* **2007**, *11*, 401–425.
36. Kudo, A.; Miseki, Y. Heterogeneous Photocatalyst Materials for Water Splitting. *Chem. Soc. Rev.* **2009**, *38*, 253–278.
37. Hisatomi, T.; Kubota, J.; Domen, K. Recent Advances in Semiconductors for Photocatalytic and Photoelectrochemical Water Splitting. *Chem. Soc. Rev.* **2014**, *43*, 7520–7535.
38. Shi, N.; Li, X.; Fan, T.; Zhou, H.; Zhang, D.; Zhu, H. Artificial Chloroplast: Au/Chloroplast-Morph-TiO_2 with Fast Electron Transfer and Enhanced Photocatalytic Activity. *Int. J. Hydrog. Energy* **2014**, *39*, 5617–5624.
39. Dincer, I.; Acar, C. Review and Evaluation of Hydrogen Production Methods for Better Sustainability. *Int. J. Hydrog. Energy* **2015**, *40*, 11094–11111.
40. Acar, C.; Dincer, I.; Zamfirescu, C. A Review on Selected Heterogeneous Photocatalysts for Hydrogen Production. *Int. J. Energy Res.* **2014**, *38*, 1903–1920.
41. Xu, Y.; Xu, R. Nickel-Based Cocatalysts for Photocatalytic Hydrogen Production. *Appl. Surf. Sci.* **2015**, *351*, 779–793.
42. Wen, J.; Xie, J.; Chen, X.; Li, X. A Review on G-C_3 N_4 -Based Photocatalysts. *Appl. Surf. Sci.* **2017**, *391*, 72–123.
43. Rajaambal, S.; Sivaranjani, K.; GOPINATH, C. S. Recent Developments in Solar H_2 Generation from Water Splitting. *J. Chem. Sci.* **2015**, *127*, 33–47.
44. Samanta, B.; Morales-García, Á.; Illas, F.; Goga, N.; Anta, J. A.; Calero, S.; Bieberle-Hütter, A.; Libisch, F.; Muñoz-García, A. B.; Pavone, M.; Caspary Toroker, M. Challenges of Modeling Nanostructured Materials for Photocatalytic Water Splitting. *Chem. Soc. Rev.* **2022**, *51*, 3794–3818.
45. Chen, Y.; Feng, X.; Guo, X.; Zheng, W. Toward a Fundamental Understanding of Factors Affecting the Function of Cocatalysts in Photocatalytic Water Splitting. *Curr. Opin. Green Sustain. Chem.* **2019**, *17*, 21–28.
46. Rosman, N. N.; Yunus, R. M.; Shah, N. R. A. M.; Shah, R. M.; Arifin, K.; Minggu, L. J.; Ludin, N. A. An Overview of Co-catalysts on Metal Oxides for Photocatalytic Water Splitting. *Int. J. Energy Res.* **2022**, *46*, 11596–11619.

47. Osterloh, F. E.; Parkinson, B. A. Recent Developments in Solar Water-Splitting Photocatalysis. *MRS Bull.* **2011**, *36*, 17–22.

48. Seo, S. W.; Park, S.; Jeong, H.-Y.; Kim, S. H.; Sim, U.; Lee, C. W.; Nam, K. T.; Hong, K. S. Enhanced Performance of $NaTaO_3$ Using Molecular Co-Catalyst $[Mo_3S_4]^{4+}$ for Water Splitting into H_2 and O_2. *Chem. Comm.* **2012**, *48*, 10452.

49. Husin, H.; Su, W.-N.; Chen, H.-M.; Pan, C.-J.; Chang, S.-H.; Rick, J.; Chuang, W.-T.; Sheu, H.-S.; Hwang, B.-J. Photocatalytic Hydrogen Production on Nickel-Loaded $LaxNa_{1-x}TaO_3$ Prepared by Hydrogen Peroxide-Water Based Process. *Green Chem.* **2011**, *13*, 1745.

50. Kudo, A.; Sayama, K.; Tanaka, A.; Asakura, K.; Domen, K.; Maruya, K.; Onishi, T. Nickel-Loaded $K_4Nb_6O_{17}$ Photocatalyst in the Decomposition of H_2O into H_2 and O_2: Structure and Reaction Mechanism. *J. Catal.* **1989**, *120*, 337–352.

51. Ola, O.; Mercedes Maroto-Valer, M. Role of Catalyst Carriers in CO_2 Photoreduction over Nanocrystalline Nickel Loaded TiO_2-Based Photocatalysts. *J. Catal.* **2014**, *309*, 300–308.

52. Liu, Y.; Wang, Z.; Fan, W.; Geng, Z.; Feng, L. Enhancement of the Photocatalytic Performance of Ni-Loaded TiO_2 Photocatalyst under Sunlight. *Ceram. Int.* **2014**, *40*, 3887–3893.

53. Bi, L.; Xu, D.; Zhang, L.; Lin, Y.; Wang, D.; Xie, T. Metal Ni-Loaded g-C_3N_4 for Enhanced Photocatalytic H_2 Evolution Activity: The Change in Surface Band Bending. *Phys. Chem. Chem. Phys.* **2015**, *17*, 29899–29905.

54. Yoon, K. R.; Ko, J. W.; Youn, D.-Y.; Park, C. B.; Kim, I.-D. Synthesis of Ni-Based Co-Catalyst Functionalized W:$BiVO_4$ Nanofibers for Solar Water Oxidation. *Green Chem.* **2016**, *18*, 944–950.

55. Li, J.; Wang, D.; Guan, R.; Zhang, Y.; Zhao, Z.; Zhai, H.; Sun, Z. Vacancy-Enabled Mesoporous TiO_2 Modulated by Nickel Doping with Enhanced Photocatalytic Nitrogen Fixation Performance. *ACS Sustain. Chem. Eng.* **2020**, *8*, 18258–18265.

56. Maeda, K.; Teramura, K.; Lu, D.; Saito, N.; Inoue, Y.; Domen, K. Roles of Rh/Cr_2O_3 (Core/Shell) Nanoparticles Photodeposited on Visible-Light-Responsive $(Ga_{1-x}Zn_x)(N_{1-x}O_x)$ Solid Solutions in Photocatalytic Overall Water Splitting. *J. Phys. Chem. C.* **2007**, *111*, 7554–7560.

57. X. The Bakerian Lecture. —Experimental Relations of Gold (and Other Metals) to Light. *Philos. Trans. R. Soc.* **1857**, *147*, 145–181.
58. Kabashin, A. V.; Evans, P.; Pastkovsky, S.; Hendren, W.; Wurtz, G. A.; Atkinson, R.; Pollard, R.; Podolskiy, V. A.; Zayats, A. V. Plasmonic Nanorod Metamaterials for Biosensing. *Nat. Mater.* **2009**, *8*, 867–871.
59. Camden, J. P.; Dieringer, J. A.; Zhao, J.; Van Duyne, R. P. Controlled Plasmonic Nanostructures for Surface-Enhanced Spectroscopy and Sensing. *Acc. Chem. Res.* **2008**, *41*, 1653–1661.
60. Barnes, W. L.; Dereux, A.; Ebbesen, T. W. Surface Plasmon Subwavelength Optics. *Nature* **2003**, *424*, 824–830.
61. Wark, A. W.; Lee, H. J.; Corn, R. M. Long-Range Surface Plasmon Resonance Imaging for Bioaffinity Sensors. *Anal. Chem.* **2005**, *77*, 3904–3907.
62. Kelly, K. L.; Coronado, E.; Zhao, L. L.; Schatz, G. C. The Optical Properties of Metal Nanoparticles: The Influence of Size, Shape, and Dielectric Environment. *J. Phys. Chem. B.* **2002**, *107*, 668–677.
63. Liu, Z.; Hou, W.; Pavaskar, P.; Aykol, M.; Cronin, S. B. Plasmon Resonant Enhancement of Photocatalytic Water Splitting Under Visible Illumination. *Nano Lett.* **2011**, *11*, 1111–1116.
64. Patra, K. K.; Gopinath, C. S. Bimetallic and Plasmonic Ag-Au on $TiO_2$for Solar Water Splitting: An Active Nanocomposite for Entire Visible-Light-Region Absorption. ChemCatChem **2016**, 8 , 3294–3311.
65. Patra, K. K.; Ghosalya, M. K.; Bajpai, H.; Raj, S.; Gopinath, C. S. Oxidative Disproportionation of MoS_2/GO to MoS_2/MoO_{3-x}/RGO: Integrated and Plasmonic 2D-Multifunctional Nanocomposites for Solar Hydrogen Generation from Near-Infrared and Visible Regions. *J. Phys. Chem. C* .**2019**, 123 21685–21693.
66. San Martín, S.; Rivero, M. J.; Ortiz, I. Unravelling the Mechanisms That Drive the Performance of Photocatalytic Hydrogen Production. *Catalysts* **2020**, *10*, 901.
67. Wang, Z.; Liu, Y.; Martin, D. J.; Wang, W.; Tang, J.; Huang, W. CuO_x–TiO_2 Junction: What Is the Active Component for Photocatalytic H2 Production? *Phys. Chem. Chem. Phys.* **2013**, *15*, 14956.
68. Wu, Y.; Lu, G.; Li, S. The Role of Cu(I) Species for Photocatalytic Hydrogen Generation Over CuO_x /TiO_2. *Catal. Lett.* **2009**, *133*, 97–105.

69. Sheng, P.; Li, W.; Cai, J.; Wang, X.; Tong, X.; Cai, Q.; Grimes, C. A. A Novel Method for the Preparation of a Photocorrosion Stable Core/Shell CdTe/CdS Quantum Dot TiO_2 Nanotube Array Photoelectrode Demonstrating an AM 1.5G Photoconversion Efficiency of 6.12%. *J. Mater. Chem. A.* **2013**, *1*, 7806.
70. Kongkanand, A.; Tvrdy, K.; Takechi, K.; Kuno, M.; Kamat, P. V. Quantum Dot Solar Cells. Tuning Photoresponse through Size and Shape Control of CdSe−TiO_2 Architecture. *J. Am. Chem. Soc.* **2008**, *130*, 4007–4015.
71. Puga, A. V. Photocatalytic Production of Hydrogen from Biomass-Derived Feedstocks. *Coord. Chem. Rev.* **2016**, *315*, 1–66.
72. Chiarello, G. L.; Aguirre, M. H.; Selli, E. Hydrogen Production by Photocatalytic Steam Reforming of Methanol on Noble Metal-Modified TiO_2. *J. Catal.* **2010**, *273*, 182–190.
73. Naldoni, A.; D'Arienzo, M.; Altomare, M.; Marelli, M.; Scotti, R.; Morazzoni, F.; Selli, E.; Dal Santo, V. Pt and Au/TiO_2 Photocatalysts for Methanol Reforming: Role of Metal Nanoparticles in Tuning Charge Trapping Properties and Photoefficiency. *Appl. Catal. B.* **2013**, *130–131*, 239–248.
74. Nalajala, N.; Salgaonkar, K. N.; Chauhan, I.; Mekala, S. P.; Gopinath, C. S. Aqueous Methanol to Formaldehyde and Hydrogen on Pd/TiO_2 by Photocatalysis in Direct Sunlight: Structure Dependent Activity of Nano-Pd and Atomic Pt-Coated Counterparts. ACS Appl. Energy Mater. **2021**, 4, 13347–13360.
75. Zinoviev, S.; Müller-Langer, F.; Das, P.; Bertero, N.; Fornasiero, P.; Kaltschmitt, M.; Centi, G.; Miertus, S. Next-Generation Biofuels: Survey of Emerging Technologies and Sustainability Issues. *ChemSusChem* **2010**, *3* 1106–1133.
76. Sakata, T.; Kawai, T. Heterogeneous Photocatalytic Production of Hydrogen and Methane from Ethanol and Water. *Chem. Phys. Lett.* **1981**, *80*, 341–344.
77. Yang, S.; Wang, H.; Yu, H.; Zhang, S.; Fang, Y.; Zhang, S.; Peng, F. A Facile Fabrication of Hierarchical Ag Nanoparticles-Decorated N-TiO_2 with Enhanced Photocatalytic Hydrogen Production under Solar Light. *Int. J. Hydrog. Energy* **2016**, *41*, 3446–3455.
78. YANG, Y.; CHANG, C.; IDRISS, H. Photo-Catalytic Production of Hydrogen Form Ethanol over M/TiO_2 Catalysts (M=Pd, Pt or Rh). *Appl. Catal. B* **2006**, *67*, 217–222. https://doi.org/10.1016/j.apcatb.2006.05.007.

79. Kondarides, D. I.; Daskalaki, V. M.; Patsoura, A.; Verykios, X. E. Hydrogen Production by Photo-Induced Reforming of Biomass Components and Derivatives at Ambient Conditions. *Catal. Letters* **2007**, *122*, 26–32.
80. Cargnello, M.; Montini, T.; Smolin, S. Y.; Priebe, J. B.; Delgado Jaén, J. J.; Doan-Nguyen, V. V. T.; McKay, I. S.; Schwalbe, J. A.; Pohl, M.-M.; Gordon, T. R.; Lu, Y.; Baxter, J. B.; Brückner, A.; Fornasiero, P.; Murray, C. B. Engineering Titania Nanostructure to Tune and Improve Its Photocatalytic Activity. *Proc. Natl. Acad. Sci.* **2016**, *113*, 3966–3971.
81. Christoforidis, K. C.; Fornasiero, P. Photocatalytic Hydrogen Production: A Rift into the Future Energy Supply. *ChemCatChem* **2017**, *9*, 1523–1544.
82. St. John, M. R.; Furgala, A. J.; Sammells, A. F. Hydrogen Generation by Photocatalytic Oxidation of Glucose by Platinized N-Titania Powder. *J. Phys. Chem.* **1983**, *87*, 801–805.
83. Shimura, K.; Yoshida, H. Heterogeneous Photocatalytic Hydrogen Production from Water and Biomass Derivatives. *Energy Environ. Sci* **2011**, *4* (7), 2467.
84. Martínez, F. M.; Albiter, E.; Alfaro, S.; Luna, A. L.; Colbeau-Justin, C.; Barrera-Andrade, J. M.; Remita, H.; Valenzuela, M. A. Hydrogen Production from Glycerol Photoreforming on TiO_2/HKUST-1 Composites: Effect of Preparation Method. *Catalysts* **2019**, *9*, 338.
85. Maldonado, M. I.; López-Martín, A.; Colón, G.; Peral, J.; Martínez-Costa, J. I.; Malato, S. Solar Pilot Plant Scale Hydrogen Generation by Irradiation of Cu/TiO_2 Composites in Presence of Sacrificial Electron Donors. *Appl. Catal. B* **2018**, *229*, 15–23.
86. Jedsukontorn, T.; Saito, N.; Hunsom, M. Photoinduced Glycerol Oxidation over Plasmonic Au and AuM (M = Pt, Pd and Bi) Nanoparticle-Decorated TiO_2 Photocatalysts. *Nanomaterials* **2018**, *8*, 269.
87. Praveen Kumar, D.; Shankar, M. V.; Mamatha Kumari, M.; Sadanandam, G.; Srinivas, B.; Durgakumari, V. Nano-Size Effects on CuO/TiO_2 Catalysts for Highly Efficient H2 Production under Solar Light Irradiation. *Chem. Comm.* **2013**, 49, 9443.
88. Kong, M.; Li, Y.; Chen, X.; Tian, T.; Fang, P.; Zheng, F.; Zhao, X. Tuning the Relative Concentration Ratio of Bulk Defects to Surface Defects in TiO_2 Nanocrystals Leads to High Photocatalytic Efficiency. *J. Am. Chem. Soc.* **2011**, *133*, 16414–16417.

89. Li, L.; Yan, J.; Wang, T.; Zhao, Z.-J.; Zhang, J.; Gong, J.; Guan, N. Sub-10 Nm Rutile Titanium Dioxide Nanoparticles for Efficient Visible-Light-Driven Photocatalytic Hydrogen Production. *Nat. Commun.* **2015**, *6*.
90. Hirakawa, H.; Hashimoto, M.; Shiraishi, Y.; Hirai, T. Photocatalytic Conversion of Nitrogen to Ammonia with Water on Surface Oxygen Vacancies of Titanium Dioxide. *J. Am. Chem. Soc.* **2017**, *139*, 10929–10936.
91. Hoshino, K. New Avenues in Dinitrogen Fixation Research. *Chem. Eur. J.* **2001**, *7*, 2727–2731.
92. Huang, G.; Xiao, Z.; Chen, R.; Wang, S. Defect Engineering of Cobalt-Based Materials for Electrocatalytic Water Splitting. *ACS Sustain. Chem. Eng.* **2018**, *6*, 15954–15969.
93. Zhang, Y.; Afzal, N.; Pan, L.; Zhang, X.; Zou, J. Structure-Activity Relationship of Defective Metal-Based Photocatalysts for Water Splitting: Experimental and Theoretical Perspectives. *Adv. Sci.* **2019**, *6*, 1900053.
94. Bai, S.; Zhang, N.; Gao, C.; Xiong, Y. Defect Engineering in Photocatalytic Materials. *Nano Energy* **2018**, *53*, 296–336.
95. Guo, X.; Du, H.; Qu, F.; Li, J. Recent Progress in Electrocatalytic Nitrogen Reduction. *J. Mater. Chem. A* **2019**, *7*, 3531–3543.

.



Chapter 2

Synthesis and Experimental Methods

2.1 Synthesis and Experimental Methods:

The preparation of photocatalytic materials with unique properties heavily relies on the synthetic methods used in their development. In heterogeneous catalysis, the catalytic properties of catalysts are greatly influenced by each step of the preparation process, which collectively contribute to the overall catalytic activity. A large emphasis is given on integrating the photocatalyst components by electronic and/or structural means. As listed out in the introduction, having (or physically mixing of) all the components of photocatalysis is not sufficient, but their integration plays a predominant role in utilizing/converting the solar energy and store it in the chemical bonds of the products. Throughout this thesis, we have utilized various methods for synthesizing solar light active photocatalysts, including the SILAR method for the synthesis of QDs sensitized QuAL. Additionally, we have employed facile photo-deposition and hydride-driven metal deposition over TiO_2. A detailed description of these procedures is provided. Furthermore, the importance and theory behind commonly used physical, structural, and spectroscopic characterization techniques for TiO_2-based materials have been briefly outlined.

2.2 Synthesis of catalyst:

2.2.1 Ni-Cu Alloy nanoparticles:

NiCu alloy was prepared by following the procedure reported by Patra et al.[1] 25 ml oleyl amine was taken in 100 ml three-neck RBF (round bottom flask) and kept at 120^0 C for 10 min. to remove any water from the oleyl amine. Then $Ni(NO_3)_2.6H_2O$ (291 mg) and $Cu(CH_3COO)_2$ (130 mg) was added. The temperature was increased to 220^o C, and the reaction mixture was kept under the above conditions for 1 h under stirring to form nanoparticles. After this, the reaction mixture was allowed to cool down to room temperature (RT). $Ni_5Cu_{2.5}$ (NiCu) alloy nanoparticle was washed repeatedly and finally centrifuged with ethanol to remove the catalyst.

2.2.2 Half-Monolayer Pt Integrated Ni-Cu ($0.5\theta_{Pt}$-NC) Bimetallic Nanoparticle:

Synthesis of $0.5\theta_{Pt}$-NC was carried out in two stages and they are described in the following. NiCu alloy nanoparticles were dispersed in 30 ml ethanol in a RBF and $NaBH_4$ was added in 1:4 (NiCu:$NaBH_4$) weight ratio and stirred for 30 minutes; the solution was further

sonicated for 30 min. followed by refluxing at 80 ^{0}C for 1 h. Then it was cooled down to RT, washed and centrifuged with ethanol. This is referred to as NiCu@H^- as the NiCu alloy surface is fully covered with hydride ions.

To prepare half mono-layer (0.5θ) Pt-covered on NiCu alloy nanoparticles, NiCu@H^- (100 mg) is dispersed in 30 ml ethanol in RBF and then K_2PtCl_4 (25 mg) was added. It was sonicated for 30 min, then refluxed at 74 ^{0}C for 12 h. After cooling down to room temperature, it was washed and centrifuged with ethanol. It is referred to as 0.5θ_{Pt}-NC. The main idea behind this procedure is to populate the NiCu alloy surface with hydride ions in the first step and then treating the same with Pt^{2+} ions. Two hydride ions are required to reduce one Pt^{2+} ion and a perfect reduction is expected to provide 0.5 ML Pt covered NiCu alloy surface. As hydride ions are available only on the surface, no bulk reduction of platinum is possible with this current procedure. Pt is expected to be present in the atomic state. In spite of our best efforts, we are unable to observe atomic Pt on single particles of 0.5θ_{Pt}-NC by structural/microscopy methods such as XRD, HRTEM. However, TEM-EDS (TEM-energy dispersive x-ray spectroscopy) measurements made on bigger clusters were helpful to observe the elemental mapping and its content. Electrochemical measurements also fully support the presence of atomic Pt. More details are given in chapter 3 section 3.8.

2.2.3 Synthesis of Au/TiO_2 composite:

Electronically integrated and highly-dispersed Au@TiO_2 was prepared by modified procedure of controlled photochemical deposition. 200 mg P25-TiO_2 was dispersed in 100 ml of water: methanol (60:40) solution in 250 ml quartz round bottom (RB) flask; after stirring for 10 min. 3.08 mg of Au-precursor ($HAuCl_4.3H_2O$) was added to prepare 0.5 wt % Au-containing TiO_2. Other compositions were also prepared in a similar manner with required amount of Au-precursor. The solution was subjected to N_2 purging in the dark for 30 min. with stirring for uniform interaction of $[AuCl_4]^{-1}$ with TiO_2. It is very likely that gold-centre is attracted towards oxygen vacancy sites. This solution was subjected to UV lamp irradiation for 1 h. After irradiation, the solution was centrifuged and washed with hot water (65^o C) several times, and then dried in the oven at 70^o C. Different wt % of Au was also synthesized with 0.1 (0.76 mg of $HAuCl_4.3H_2O$ with similar conditions mentioned above), 0.5, 1 (7.6 mg of $HAuCl_4.3H_2O$ with similar conditions mentioned above) with respect to TiO_2 and they are denoted as 0.1Au@TiO_2, 0.5Au@TiO_2 and 1Au@TiO_2, respectively.

2.2.4 Synthesis of Cu/TiO_2:

Three different methods were used to prepare a Cu/TiO_2 composite. In the first method, 200 mg TiO_2 was dispersed in a 60:40 water-methanol solution in a 250 ml quartz round bottom flask. Copper acetate was added to the solution (at a concentration of 1 wt% of copper with respect to TiO_2) and the solution was purged with nitrogen for 30 minutes with stirring to remove dissolved oxygen. The solution was then irradiated with UV light for 1 hour, followed by centrifugation and washing with deionized water, and drying in an oven at 60°C. This sample was named as TC-PD.

In the second method, 200 mg of TiO_2 P25 was dispersed in 100 ml of deionized water and purged with nitrogen for 30 minutes. 200 mg of $NaBH_4$ was added to the solution, and the mixture was sonicated for 1 hour. The colour of the catalyst changed from white to light blue. After centrifugation and washing, to remove any unreacted $NaBH_4$, it to be noted that DI water which is used for washing is already purged with nitrogen so that no dissolve oxygen should be present in the water, which could react with Ti^{+3}. the sample was dried in an oven at 60°C. This sample was named T-200. For copper deposition, 50 mg of T-200 was dispersed in 50 ml of nitrogen-purged deionized water and sonicated for 15 minutes. Copper acetate was then added to the solution (at a concentration of 1 wt% of copper with respect to T-200) and the solution was stirred in the dark for 1 hour. The sample was then centrifuged, washed with deionized water, and dried in an oven at 60°C. This sample was named as TC-200.

In the third method, light-induced oxygen vacancies mediated copper deposition was employed to prepare TC-PDO. 200 mg of TiO_2 was dispersed in a 100 ml of 60:40 water-methanol solution in a 250 ml quartz round bottom flask and purged with nitrogen for 30 minutes with stirring to remove dissolved oxygen. The solution was then irradiated with UV light for 2 hours, which resulted in the creation of oxygen vacancies and a light blue colour. Copper acetate was dissolved in 1 ml of deionized water, which was earlier purged with nitrogen. This solution was injected into the TiO_2 solution without exposing it to air and stirred overnight in the dark. The sample was then centrifuged, washed with deionized water, and dried in an oven at 60° C. This sample was named as TC-PDO.[2]

2.2.5 Synthesis of NiCu-bimetal Particles:

NiCu nanoparticles was prepared by modified method reported by Li et. al.[3] In this process a mixture of nickel acetylacetonate and copper acetylacetonate in a 1:1 ratio was dissolved in 25 ml of oleyl amine. To this solution, 30 mg of $FeCl_3$ and 264 mg of ascorbic acid were added, and the mixture was sonicated for 1 hour. The resulting solution was subjected to heat treatment at 180°C for 12 hours. After cooling the solution to room temperature, it was centrifuged and washed with a solution of hexane and ethanol. The sample was then dried in an oven at 60° C

2.2.5 NiCu@TiO_2 Composite:

NiCu on TiO_2 catalysts containing 1% NiCu were produced through impregnation with ethanol as the solvent. Initially, 2 mg of the synthesised material was added to 5 mL of ethanol (EtOH) in a 50 mL beaker. Next, 200 mg of TiO_2-P25 was added to 20 mL of EtOH in a separate beaker containing 200 mg of TiO_2-P25. The solutions were sonicated separately for 15 minutes, then combined and sonicated for an additional 1 hour. The mixture was then dried in an air oven at 65° C. The catalysts for all compositions were prepared using the same procedure. The substance was then thoroughly pulverised using a mortar and pestle.

2.2.7 Synthesis of Defective TiO_2:

To synthesise the defective TiO_2, TiO_2-P25 was initially calcined at different temperatures (350° C, 550° C 750° C). Samples obtained was donated as T-X, where X is the calcination temperature. After that 400 mg T-X was mixed with 200 mg of $NaBH_4$ and ground well for 30 min; then it was subjected to annealing under argon atmosphere for 1 hr at 300° C. Before giving the heat, treatment sample was purged with argon for 15 min to create inert atmosphere. When sample temperature was decreased to room temperature, it was subjected to sonication for 1 h in DI water to remove any unreacted $NaBH_4$. The final dried material is designated as BT-X (say BT-350), where X is the calcination temperature, it is to be noted for BT sample, 400 mg of TiO_2 P25 was mixed with 200 mg of $NaBH_4$ and ground well for 30 min; then it was subjected to annealing under argon atmosphere for 1 hr at 300° C. After that procedure is same as BT-X samples.

2.3 Fabrication of Photochemical Device:

QDs sensitized QuAL device was prepared by doctor blade method followed by SILAR method, which is reported by Trevisan et al[4] and Patra et al.[1,5] Briefly, FTO (fluorine doped tin oxide) was cleaned and washed with soap solution, deionized water and ethanol, in the above sequential order. After $TiCl_3$ treatment (to increase the adhesion and homogeneity of TiO_2 film on FTO), P25-TiO_2 paste was applied on cleaned FTO by doctor blade method on 1x1 cm^2 area followed by calcination at 450^0 C for 30 min. CdS and ZnS QDs are assembled in the pores of titania film by the SILAR method and it is described below: Pre-coated TiO_2 film on FTO was immersed (a) in an aqueous solution of 0.1 M $Zn(CH_3COO)_2$ for 1 min., (b) then washed with deionized (DI) water, followed by (c) immersion in 0.1 M solution (1:1 water: methanol) of Na_2S for 1 min., and (d) finally washed with DI water. This is for one full SILAR cycle of assembly of ZnS QD in the titania pores. Intermediate washing with DI water removes any ions that are not chemisorbed or bonded to the surface, and hence one full SILAR cycle leads to the maximum of a monolayer of a chalcogenide. In a similar process 5 CdS SILAR cycles was carried out with aqueous solution of Cd $(NO_2)_3$ and Na_2S sequentially. Finally, two SILAR cycle of ZnS coating was carried out to make TiO_2/ZnS/CdS photoanode with top ZnS layers as passivating layers. For the solar to hydrogen measurement, the co-catalyst (or cathode) was drop-casted alongside the photoanode on FTO. Pt, NiCu and $0.5\theta_{Pt}$-NiCu were employed as cathode materials. Catalyst materials and devices made were thoroughly characterized by various analytical methods.

2.4 Solar Hydrogen Production Measurement for TiO_2/ZnS/CdS/ZnS System:

Hydrogen production was measured at zero potential in the wireless configuration using one sun condition. For the hydrogen production measurements, 30 ml of 0.25 M Na_2S and 0.35 M Na_2SO_3 as hole scavenger in 70 ml quartz RBF was taken and purged with N_2 for 10 min, then photo-electrode was immersed into the solution and irradiated with light (100 mW cm^{-2} with 450 W Newport Solar Simulator with AM1.5 filter). Hydrogen was the only product in the gas phase and it was confirmed by using GC (Gas Chromatograph, Agilent 7890A) measurements. For hydrogen quantification, inverted burette method[29] was employed and the volume displaced was noted periodically.

2.5 Photochemical Hydrogen Production Measurement:

For photocatalytic hydrogen production, 3 mg of any Au@TiO_2 catalyst was taken in 50 ml borosilicate RB flask, with 20 ml of different concentration of aqueous glycerol (0.14, 0.6 and 1.4 M glycerol), and subjected to 10 min. of N_2 purging. In case of cellulose, as a sacrificial reagent, cellulose weight was optimized; it was found that, 10 mg cellulose in 20 ml water is giving the better activity; same amount was also followed by tissue paper. Then the photocatalyst was irradiated with light under one sun condition (100 mW/cm^2 with a 450 W Newport solar simulator fitted with 1.5 AM filter) or direct sunlight (average light intensity was 60 mW/cm^2). Hydrogen was the only gas-phase product, and it was confirmed and quantified by GC (Agilent 7890A) analysis.

2.6 Photochemical Glycerol Oxidation Measurement:

To measure the glycerol oxidation products, 5 mg catalyst was initially dispersed in 5 ml of 0.05 M glycerol aqueous solution, and then kept under nitrogen or oxygen purging for 30 min., depending on the type of reaction carried out subsequently. After that, the catalyst-glycerol suspension was irradiated under one sun condition or direct sunlight. All oxidized products of glycerol are quantified by Agilent GC (7890A) and ^1H NMR. Liquid products identification and quantification were carried out by NMR (Bruker AV 500), with 1 mmol KHP (potassium hydrogen phthalate) as the internal standard.

$$C_x = \frac{I_x}{I_{CAL}} \mathbf{X} \frac{N_{CAl}}{N_x} \mathbf{X} C_{CAL}$$

where C_x, I_x, $I_{cal,}$ N_{cal}, N_x, C_{cal} are the concentration of the product, integral area of the product, integral area of the standard, number of protons of standard and product, and concentration of standard, respectively. Various liquid products by NMR and hydrogen measured through GC are reproducible within 5% error margin. For copper-based system 3 mg of catalyst in 5% aqueous glycerol was used.

2.7 Photo-electrochemical measurement:

Photo-electrochemical performance of TiO_2/ZnS/CdS photoanode was evaluated in the three-electrode system with Pt as a counter electrode and Ag/AgCl as a reference electrode using aqueous solution of Na_2S/Na_2SO_3. From the chronoamperometry

measurement, photo-response and maximum current density and stability measurements were carried out with 1*1 cm^2 film.

2.8 Electrochemical measurement:

A three-electrode setup was used for the electrochemical experiment, with platinum and Ag/AgCl serving as the counter and reference electrodes in 0.5 M H_2SO_4, respectively. A glassy carbon electrode was covered with a catalyst paste layer containing a total of 5 micrograms of catalyst. A cyclic voltammogram (CV) collected at various scan rates in the non-Faradaic region to measure the double-layer capacitance, which was used to estimate the electrochemical active surface area (ECSA) of the catalysts.[38–39]

2.9 Photocatalytic Ammonia Production Measurement:

For photocatalytic Nitrogen to ammonia measurement was carried out by spectroscopic method. For the nitrogen fixation reaction 5 mg catalyst was dispersed in 25 ml DI water. Then it was purged with nitrogen for 1 hr under ice bath under stirring to achieve the maximum soluble nitrogen. After that solution was kept under solar simulator equipped 1.5 AM filter with 300 mW/cm^2. After two hours of continuous reaction, 1 ml of the solution was added into 1 ml sodium potassium tartrate (500 mg/ml) then 100 µl. of Nessler's reagent (Merck). After 10 min., light absorption analysis at 420 nm was carried out. With respect absorption, quantification of ammonia was carried out. Before and after reaction sample was also analysed to remove the probability of contamination. Initially a calibration of light absorption was made with known concentrations of ammonia in water.

2.10 Structural Characterization Methods:

Catalyst materials and devices made were thoroughly characterized by various analytical methods.

UV-Visible absorption spectroscopy is a scientific methodology employed to investigate the interaction between matter and ultraviolet (UV) and visible (Vis) light. UV-Vis spectroscopy operates on the fundamental principle of molecular light absorption, whereby the excitation of electrons from lower to higher energy levels within the molecule occurs as a consequence of light absorption. A UV-Vis spectrophotometer is utilised to measure the absorption of light by a sample as a function of wavelength. This is achieved by passing a beam

of light through the sample and recording the amount of light that is absorbed. The absorption of light by the sample occurs at distinct wavelengths that are indicative of the energy disparity between the molecule's ground state and its excited state. The phenomenon of electronic transitions within a molecule is initiated by the absorption of light, resulting in the excitation of electrons from lower energy states to higher energy states. The Beer-Lambert law states that the concentration of the absorbing species in a sample is directly proportional to the amount of absorption observed. The UV-Visible spectrum acquired through the utilisation of a spectrophotometer depicts the quantity of light that has been absorbed with respect to the wavelength, thereby furnishing insights into the electronic configuration of the specimen. The spectral absorption peaks' position and intensity are correlated with the sample's chemical composition and structure. Diffuse reflectance refers to the scattering of light in various directions upon striking a surface, without any specific directionality. The UV-Vis measurement was conducted using a Shimadzu spectrophotometer (model-UV2550) with spectral grade $BaSO_4$ as a reference material. The absorption was recorded within the wavelength range of 200 to 800 nm.

A potentiostat is an electronic device used in electrochemistry to control the potential difference (voltage) between a working electrode and a reference electrode, while measuring the resulting current flowing through the working electrode. The working principle of a potentiostat can be described as follows: (1) Voltage Control: A potentiostat applies a constant voltage between the working electrode and the reference electrode, called the set potential. This voltage is controlled by a feedback loop that adjusts the voltage to maintain a constant potential difference between the two electrodes. (2) Current Measurement: The potentiostat measures the current flowing through the working electrode. This current is proportional to the rate of electrochemical reactions occurring at the surface of the electrode. (3) Feedback Control: The potentiostat adjusts the voltage to maintain a constant current flowing through the working electrode. This is achieved by applying a small voltage to the working electrode and measuring the resulting current. The potentiostat then adjusts the voltage until the desired current is obtained. (4) Data Collection: The potentiostat records the potential and current values over time, which can be used to analyse the electrochemical behaviour of the system under study. Photo electrochemical and electrochemical measurements were carried out using Gamry potentiostat (model 3000) in a three-electrode

system with Ag/AgCl as the reference electrode and Pt foil as counter electrode under one sun condition (Newport instruments - 300 W xenon arc lamp fitted with AM 1.5 filter). All the measurement was carried out at room temperature.

XRD (X-ray diffraction) is a widely used technique for characterizing catalyst materials by determining their crystal structure, crystalline phase(s), percent crystallinity, and crystallite size. X-rays, which are invisible and electrically neutral electromagnetic radiation, are used to probe the structural arrangement of atoms and molecules in a range of materials. X-ray diffraction is based on the coherent scattering of rays that can interfere with each other, resulting in bright and dark fringes. Bragg's law relates the possibility of constructive interference to the interplanar separations of crystal planes. The output of XRD measurements is obtained as a plot of diffracted X-rays versus incident angle, with the angle where constructive interference occurs giving a sharp intensity peak. The width of the diffraction peaks signifies the dimension of the reflecting planes, and the crystallite size can be estimated using the Scherrer formula. Powder X-ray diffraction (XRD) data was collected by Pan analytic X'pert pro dual goniometer diffractometer using Cu-Kα (1.5418 Å) radiation with Ni-filter with a scan rate of 0.50 min-1 and a step size of 0.02°.

FESEM stands for Field Emission Scanning Electron Microscope, which is a type of electron microscope that uses a focused beam of high-energy electrons to produce a high-resolution image of a sample. The working principle of FESEM is based on the interaction of the electron beam with the sample. FESEM uses a tungsten filament or a field emission source to produce a beam of electrons. The beam is focused using a series of electromagnetic lenses and directed towards the sample. When the electron beam interacts with the sample, some of the electrons are scattered, while others are absorbed or transmitted through the sample. The scattered electrons are collected by detectors and used to produce an image of the sample. The image is formed by varying the intensity of the electron beam and detecting the electrons that are scattered in different directions. The resulting image shows the topography and morphology of the sample at high resolution. Fiesld emission scanning electron microscope (FESEM) and energy dispersive X-ray (EDX) were performed on FESEM system (FEI NOVA NANOSEM 450) equipped with EDX.

HRTEM (High-Resolution Transmission Electron Microscopy) is a powerful imaging technique used in materials science to study the atomic structure of materials. The working

principle of HRTEM involves the transmission of a beam of electrons through a thin sample. The electrons are accelerated by an electron gun and focused onto the sample using a series of electromagnetic lenses. The sample is typically prepared by cutting it into a thin slice (less than 100 nm thick) using a focused ion beam or a diamond saw. The thin sample allows electrons to pass through it, creating an image on a detector located on the other side of the sample. As the electrons pass through the sample, they interact with the atoms in the material, causing scattering and diffraction of the electron beam. The scattered electrons interfere with each other, creating a complex pattern of bright and dark spots on the detector. This pattern is called an electron diffraction pattern and contains information about the atomic structure of the material. By analysing the electron diffraction pattern, HRTEM can produce a high-resolution image of the atomic structure of the material. The image shows the arrangement of atoms in the material at the atomic scale, allowing to study defects, interfaces, and other structural features. HRTEM and EDS analysis of the materials was conducted on JEOL JEM F-200 HRTEM operating at 200 kV.

The Raman spectroscopy method is employed to investigate the rotational and vibrational modes of molecules through the measurement of the inelastic scattering of monochromatic light. The present methodology involves exposing a specimen to a monochromatic light source, commonly a laser, inducing molecular excitation within the sample. A portion of the photons emanating from the laser undergo scattering upon interaction with the sample, with the majority of the scattered light exhibiting equivalent energy levels to the initial light source, commonly referred to as elastic or Rayleigh scattering. A minute fraction of the dispersed light exhibits distinct energy levels as a result of its interaction with the vibrational and rotational modes of the molecules present in the specimen; the phenomenon under discussion is commonly referred to as inelastic or Raman scattering. The spectrometer is utilised to gather and analyse the dispersed light, effectively segregating it into its constituent wavelengths. The Raman spectrum is produced through the graphical representation of the intensity of the light that has undergone inelastic scattering, with respect to the shift in wavelength relative to the incident light. The Raman spectrum provides information on the rotational and vibrational modes of the molecules present in the sample. The Raman spectrum of a molecule is distinct and can serve as a means of identifying both the molecule and its chemical composition. The Raman spectra were acquired utilising

the Horiba JY LabRAM HR 800 Raman spectrometer, which employed a 633 nm excitation source.

X-ray photoelectron spectroscopy (XPS) is a highly surface-sensitive analytical technique employed for the purpose of acquiring chemical information from the surfaces of various materials. X-ray photoelectron spectroscopy (XPS) instruments are designed to operate under high vacuum conditions in order to minimise collision events and facilitate the detection of photoelectrons emitted from the sample surface. The resulting emission intensity versus electron binding energy spectrum is then analysed to provide valuable information about the sample's chemical composition and electronic structure. The photoelectrons' binding energies exhibit element-specific characteristics, thereby furnishing insights into surface elemental analysis and chemical state. The phenomenon of X-ray fluorescence or Auger electron ejection takes place subsequent to ionisation, and through the utilisation of high-resolution X-ray photoelectron spectroscopy, it is possible to obtain valuable chemical state information pertaining to the surface. The analysis of X-ray photoelectron spectroscopy was conducted at Thermo Fisher Scientific Instruments UK, utilising a monochromatic Al K Alfa source with a beam current of 6 mA and 12KV.

When the nuclei of specific atoms are subjected to a second, oscillating magnetic field while being in a strong magnetic field, this physical phenomenon known as nuclear magnetic resonance (NMR) takes place. NMR is used in various scientific fields, including chemistry, biochemistry, and medicine, to determine the properties of molecules and materials. The working principle of NMR can be explained as follows: (1) The sample is placed in a strong magnetic field: The sample, which contains atoms with a nuclear spin, is placed in a strong external magnetic field. This field causes the magnetic moments of the nuclei to align with the direction of the field. (2) Radiofrequency (RF) energy is applied: A second magnetic field, perpendicular to the main magnetic field, is applied to the sample at a specific frequency. This field causes the magnetic moments of the nuclei to process, or rotate, around the direction of the applied field. (3) Absorption of RF energy: When the frequency of the oscillating magnetic field is exactly equal to the resonance frequency of the nucleus, it is absorbed by the nucleus and the energy of the magnetic moment increases. (4) Relaxation and emission of RF energy: The excited nucleus will then relax back to its original state and emit RF energy at the same frequency as the absorbed energy. The emitted energy is detected by the NMR

instrument, and the signal is processed to produce an NMR spectrum. The NMR spectrum provides information about the chemical environment of the nucleus and its interactions with neighbouring nuclei. Glycerol product quantification was carried out with Bruker AV 500, with NS-32, DS-4, SW- 24.9934 ppm with water suppression sequence using Bruker Top Spin. Many characterizations were repeated using at least three sets of samples/materials prepared in different batches.

Photoluminescence (PL) spectra are generated by shining light onto a material, causing electrons to transition from their ground state to an excited state. When these electrons return to their ground state, they release energy in the form of light, which is measured as a spectrum. The working principle of PL spectra is based on the interaction between light and matter. When light of a specific wavelength is absorbed by a material, it excites the electrons in the material to higher energy levels. These excited electrons then relax back to their ground state, releasing the excess energy as photons of light. The PL spectrum is obtained by measuring the intensity of this emitted light at different wavelengths. The spectrum provides information about the energy levels of the electrons in the material, which can be used to study the electronic properties of the material. In addition to providing information about the electronic properties of the material, PL spectra can also be used to study the structural properties of the material. For example, defects or impurities in the material can give rise to specific features in the PL spectrum, which can be used to identify and study these defects. Pl measurement was carried out on Horiba FluoroMax plus spectrophotometer, by keeping the excitation and emission slit width 3 with 1220 grating density.

For gas analysis Agilent GC (7890A) was used with molecular sieve coated packed column using TCD (Thermal conductive detector) as detector.

Zeta potential is the electrokinetic potential that exists at the interface of a solid and a liquid or a liquid and a liquid. It is a measure of the magnitude of the electrical charge that is present at the surface of a particle or colloid in a liquid medium. The zeta potential is an important parameter that determines the stability of colloidal dispersions. The zeta potential arises from the movement of ions in the liquid surrounding the particle or colloid. When a particle is placed in a liquid medium, a layer of ions forms around the particle. This layer is called the electrical double layer (EDL) and consists of a diffuse layer of counterions that

balance the surface charge of the particle and a compact layer of co-ions. The EDL has a thickness that depends on the ionic strength of the medium, the surface charge density of the particle, and the dielectric constant of the medium. When an electric field is applied to the system, the charged particles in the liquid will move in response to the field, and the ions in the EDL will be dragged along with the particle. The magnitude and direction of the zeta potential is determined by the rate of movement of the particles in the electric field. A high zeta potential indicates that the particles are well dispersed and repel each other, resulting in a stable colloidal suspension. A low zeta potential, on the other hand, indicates that the particles are more likely to aggregate and settle out of the liquid. Zeta potential measurement was carried out by Brookhaven Instruments Nano-Brook series zeta potential analyser.

2.11 References:

1. Patra, K. K.; Bharad, P. A.; Jain, V.; Gopinath, C. S. Direct Solar-to-Hydrogen Generation by Quasi-Artificial Leaf Approach: Possibly Scalable and Economical Device. *J. Mater. Chem. A.* **2019,** *7*, 3179-3189.
2. Wu, H.; Jiang, W.; Shi, L.; Li, R.; Huang, L.; Li, C. Photo-Assisted Sequential Assembling of Uniform Metal Nanoclusters on Semiconductor Support. iScience **2022**, 25, 103572.
3. Li, Z.; Yu, C.; Wen, Y.; Gao, Y.; Xing, X.; Wei, Z.; Sun, H.; Zhang, Y.-W.; Song, W. Mesoporous Hollow Cu–Ni Alloy Nanocage from Core–Shell Cu@Ni Nanocube for Efficient Hydrogen Evolution Reaction. ACS Catal. **2019**, 9, 5084–5095.
4. Trevisan, R.; Rodenas, P.; Gonzalez-Pedro, V.; Sima, C.; Sanchez, R. S.; Barea, E. M.; Mora-Sero, I.; Fabregat-Santiago, F.; Gimenez, S. Harnessing Infrared Photons for Photoelectrochemical Hydrogen Generation. A PbS Quantum Dot Based "Quasi-Artificial Leaf". *J. Phys. Chem. Lett.* **2013,** *4*, 141-146.
5. Patra, K. K.; Bhuskute, B. D.; Gopinath, C. S. Possibly Scalable Solar Hydrogen Generation with Quasi-Artificial Leaf Approach. Sci. Rep. **2017**, 7, 6515.



Chapter 3

Can Half-a-Monolayer of Pt Simulate Activity Like That of Bulk Pt? Solar Hydrogen Activity Demonstration with Quasi-artificial Leaf Device

Chapter 3 has been Published and details are[1]

Bajpai, H.; Patra, K. K.; Ranjan, R.; Nalajala, N.; Reddy, K. P.; Gopinath, C. S. Can Half-a-Monolayer of Pt Simulate Activity Like That of Bulk Pt? Solar Hydrogen Activity Demonstration with Quasi-Artificial Leaf Device. ACS Appl. Mater. Interfaces. **2020**, 12, 30420–30430.

Can Half-a-Monolayer of Pt Simulate Activity Like That of Bulk Pt? Solar Hydrogen Activity Demonstration with Quasi-Artificial Leaf Device

3.1 Introduction:

Global energy demand is increasing rapidly, and a huge amount of energy comes from limited non-renewable fossil fuels at present. With the consumption of more carbon-based fuels, we are also changing the equilibrium of our environment due to the daily addition of CO_2 and other greenhouse gases.[1] To fullfil the world's energy demands while decreasing the carbon footprint, solar energy is one of the best possible alternatives to fossil fuels. Nonetheless, the conversion of solar energy into chemical energy is challenging, and much more concerted research is required in this area.[2–5] The conversion of solar energy into chemical energy is one of the keys to a sustainable energy future. It is well-known that hydrogen from water splitting is a clean fuel source compared to carbon-based fuel.[6] However, it is impossible that any single photocatalyst material (such as TiO_2, CdS) can help to achieve solar water splitting.[7,8] Conversely, a combination of more than one semiconductor with appropriate bandgaps and band edges and their integration into a photoanode device for photocatalytic solar water splitting is a promising strategy.[9–11] A photocatalyst device should fulfill the following requirements: (i) the photoanode device should absorb light from UV, visible, and possibly near IR (NIR) ranges (that are available in sunlight) to generate the maximum number of electron−hole pairs; (ii) efficient separation of electron and hole, and diffusion of them toward the redox sites; (iii) effective utilization of electron and hole for reduction and oxidation, respectively, of water at relevant cocatalyst sites.[12–16] It is desirable to employ quantum dots (QDs), especially of surface plasmon material, to increase the light absorption.[17] High-quality heterojunction between quantum dots and semiconductor can separate the electron and hole efficiently and minimize recombination.[18] Utilization of charge carriers can be fulfilled by cocatalysts, which will work as an active site for hydrogen and oxygen evolution.[19,20] While hydrogen evolution is a two-electron process, its counterpart, oxygen evolution, is a four-electron process; the latter part is the rate-determining step due to sluggish kinetics and lowers the overall rate of the reaction. However, by using holes for the oxidation of a sacrificial reagent, H_2 evolution can be made kinetically fast.[18]

Nature does the water splitting in photosynthesis in a very efficient way with limited light absorption. The porous network of the chloroplast in the leaf absorbs the light, and the water molecules are oxidized and reduced in photosystems II and I, respectively. While oxygen escapes into the atmosphere, hydrogen is stored in NADPH. Many efforts have been carried out to mimic natural leaf functions. Herein the porous network of TiO_2 is sensitized by ZnS and CdS quantum dots. Light absorption by different components leads to charge carrier generation, and their utilization occurs to reduce water to produce H_2 and oxidize the sacrificial reagent; this is why it is termed as quasi-artificial leaf (QuAL).[9] To utilize the electron at the active site for hydrogen evolution, Pt is by far the best cocatalyst; but for large scale production, we need to find an alternative to Pt, due to its high cost and low abundance. For a less expensive substitute for Pt, many studies have been made with earth-abundant metal catalysts; however, in terms of activity and stability, they are significantly inferior to Pt. In the present study, we explored the possibility of simulating the activity of bulk Pt with just half-a-monoloayer of Pt ($0.5\theta_{Pt}$) integrated on another earth-abundant cocatalyst and demonstrating the same through the QuAL device. QDs are promising materials, and due to their morphology, size, and cross-section, the optical properties are also proven to be different from their bulk counterparts and favourable for light harvesting.[14,17,21,22] By sensitizing such QDs with porous TiO_2, light absorption can be increased; heterojunction between QD and TiO_2 significantly increases the charge separation and diffusion. TiO_2 also absorbs 4−5% of UV light available from sunlight.[23,24] In view of the above facts, we prepared a QD sensitized photoanode (TiO_2/ZnS/CdS) by successive ionic layer adsorption and reaction (SILAR).[25] We used an additional ZnS layer as a passivation layer after the CdS deposition. Several control photoanodes were also made to clarify the mechanism of the photoanode function. Our best photoanode (TiO_2/ZnS/ CdS) shows hydrogen generation activity of 4 mL/h from a 1 cm^2 size device. The $0.5\theta_{Pt}$ corresponding to about 1014 atoms/cm^2 is integrated with reasonably active, economically viable, and earth-abundant NiCu bimetal cocatalyst, which has the potential to work as a better cocatalyst for large scale solar hydrogen production.[26−28] Hydrogen evolution takes place on the surface of the cocatalyst; hence, by limiting the platinum on the surface, we could achieve the activity like that of platinum.[29] Here we report on QuAL of TiO_2/ZnS/CdS as a photoanode and platinum half-monolayer-integrated NiCu alloy nanoparticle for photocatalytic hydrogen production.

3.2 UV–Visible Absorption Spectroscopy:

For any visiblelight-driven photocatalyst material to be successful, it should show good absorption of light in a wide range of UV–visible regions. Indeed, this is the first critical requirement for a material to be considered for evaluation. Optical properties of TiO_2, TiO_2/CdS, and TiO_2/ZnS/CdS were evaluated by UV–visible spectroscopy, and the optical band gap was calculated by TAUC plot which is shown in Figure 3.1, parts a and b, respectively. The pristine TiO_2 film shows an absorption onset at 385 nm, which corresponds to a bandgap of 3.2 eV. Upon sensitizing titania with CdS quantum dots, a strong redshift is observed without a break in absorption and exhibits an absorption up to about 510 nm with an optical band gap of 2.4 eV (Figure 3.1a).

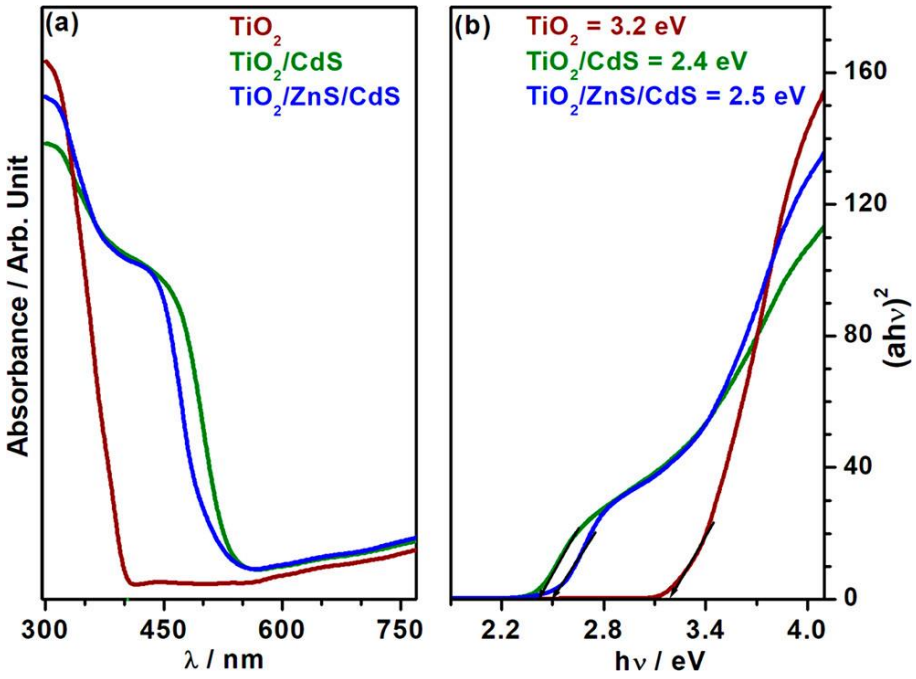


Figure 3.1. (a) UV–visible absorption spectra of TiO_2, TiO_2/CdS, TiO_2/ZnS/CdS; the latter two photoanodes are deposited with two ZnS protective layers. (b) Tauc plot of TiO_2, TiO_2/CdS, and TiO_2/ZnS/CdS for their respective band gap indicated by arrows.

It is to be noted that the SILAR method allows the in-situ assembly of CdS QDs into the mesopores of titania,[25] through the diffusion of Cd^{2+} and S^{2-} ions. This is the specialty of the SILAR method which provides a route for in situ assembly of QDs, which no other method offers. QD formation in the pores ensures the heterostructure formation and hence electronic integration between titania and CdS. When the ZnS seed layer was introduced before CdS

integration with titania, a small but finite blue-shift was observed, and the optical band gap also increased to 2.5 eV (Figure 3.1b). In fact, this observation is in contrast to that of a red shift observed by Lee et al.[30] Nonetheless, high current density and solar cell efficiency observed by Lee et al.[30] and more hydrogen generation observed in the present work with seed ZnS layers are in agreement with each other. Similar to our earlier work on the TiO_2/CdS/PbS system,[25] high absorption of light in the present system (Figure 3.1) is expected to lead to 20% IPCE up to 520 nm. It is to be underscored that ZnS and CdS possesses Wurtzite crystal structure with a hexagonal crystal system. A solid solution is highly possible between CdS and ZnS; according to Vegard's law, the bandgap of such a solid solution is expected to vary between them (CdS (2.4 eV) to ZnS (3.6 eV)), depending on the composition;[31–33] however, due to the limited amount of ZnS, a marginal, but definite, blue shift of 0.1 eV was observed in the present photoanode.

3.3 Photocatalytic Hydrogen Production:

Solar to hydrogen production was measured under one sun conditions. Hydrogen evolution was evaluated in a systematic way, using TiO_2, TiO_2/ CdS, and TiO_2/ZnS/CdS with a different cocatalyst (Pt, NiCu alloy, and $0.5\theta_{Pt}$-NC). The final layer of ZnS is the protective layer, which is also transparent to sunlight and prevents corrosion; however, it will not be mentioned hereafter, as it is part of all QuAL devices.[9] A photoanode with 1 × 1 cm^2 area was used for all measurements. TiO_2-only coated photoelectrode did not show any measurable hydrogen evolution with any of the cocatalysts. Expectedly, TiO_2 absorbs only UV light, which is only 4% of the whole solar spectrum; further charge carrier recombination is high, and hence no hydrogen generation was observed with pure titania. Solar to hydrogen conversion was carried out with TiO_2/ZnS/CdS and TiO_2/CdS photoanodes using Pt, NiCu alloy, and $0.5\theta_{Pt}$-NC as cocatalysts, and the results are shown in Figure 3.2. Hydrogen generation as a function of irradiation time is shown in Figure 3.2a for TiO_2/ZnS/CdS and TiO_2/CdS photoanodes measured with $0.5\theta_{Pt}$-NC as a cocatalyst. Hydrogen production was observed to be 4−4.5 and 2.2−2.5 mL/h with TiO_2/ZnS/CdS and TiO_2/CdS photoanodes, respectively. A careful look at the near-linear increase in hydrogen generation with time indicates constant activity with time, and no decrease in activity was observed. This indicates the robustness of the photoanode device. Indeed, the activity measurements shown in Figure 3.2a, b have been repeated with the same photoanode for at least five cycles, and it remained the same.

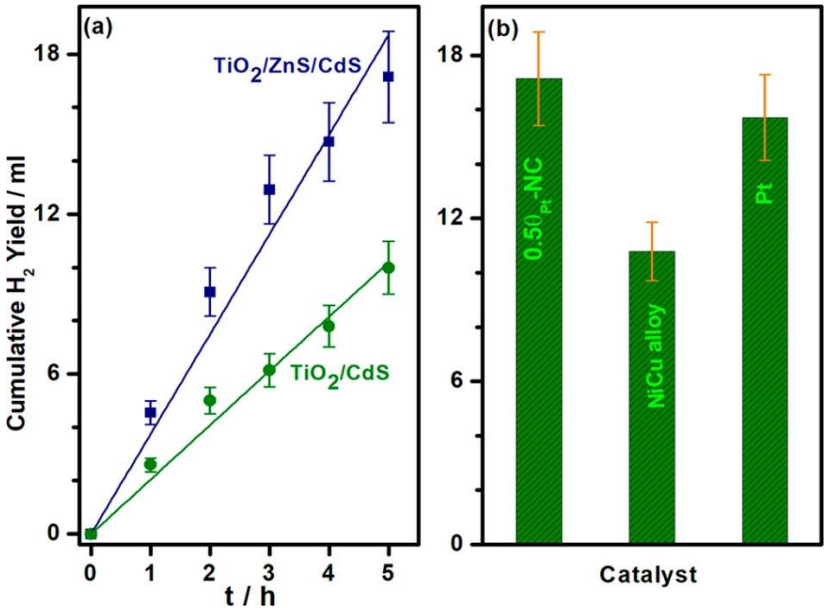


Figure 3.2. (a) Photocatalytic hydrogen production from TiO_2/ZnS/CdS and TiO_2/CdS photoanodes with 0.5θ_{Pt}-NC as a cocatalyst. (b) Photocatalytic hydrogen production from TiO_2/ZnS/CdS with 0.5θ_{Pt}-NC, NiCu alloy, or Pt as a cocatalyst for 5 h under one sun conditions.

Solar to hydrogen production was also evaluated with different cocatalysts. Amounts of [16, 11], and 17 mL of hydrogen were produced in 5 h by using Pt, NiCu alloy, and 0.5θ_{Pt}-NC as cocatalyst, respectively, with the TiO_2/ZnS/CdS photoanode (Figure 3.2b). Within an error margin of 10%, both Pt and 0.5θ_{Pt}-NC cocatalysts show the same activity, which is very intriguing. It is also confirmed from several characterization experiments that there is no bulk Pt with the latter cocatalyst. Hydrogen production observed with the TiO_2/ZnS/CdS (4− 4.5 mL/h) device is about 2-fold that of TiO_2/CdS (2.2−2.5 mL/h) with the same 0.5θ_{Pt}-NC cocatalyst. In the case of both photoelectrodes, they absorb light in the visible region to a similar extent, and charge carrier recombination is also expected to be similar, due to similar heterostructures (except for the seed ZnS layer in the latter device), which prevents electron−hole recombination. In the case of TiO_2/ZnS/CdS, by introducing a single layer of ZnS, a higher solar to hydrogen yield was observed, indicating that it could be because of significantly lower electron−hole recombination,[30] which is further supported by PEC. As indicated in the previous section, an interface made of a solid solution of CdS+ZnS between titania and CdS enhances the charge separation. This aspect will be discussed later. The photoanode with 0.5θ_{Pt}-NC cocatalyst generates 17 mL of hydrogen in 5 h, which is similar to that for Pt itself or marginally higher; at best, the hydrogen generation capacity is equal for

Pt and 0.5θ_{Pt}-NC, within the error limit. Here the underlying important concept is that by decreasing the Pt amount to the bare minimum in the monolayer (or less) and keeping it on the surface of another earth abundant cocatalyst, hydrogen generation activity should be retained like that of Pt or close to that. The 0.5θ_{Pt}-NC nanoparticles fit the above concept very well and were evaluated for hydrogen evolution with the TiO_2/ZnS/CdS photoanode. With the same photoanode, NiCu alloy and Pt were used as the cocatalyst, and the activity evaluation shows 11 ± 1 mL and 16 ± 1.6 mL, respectively, in 5 h. At least five batches of 0.5θ_{Pt}-NC and NiCu alloy cocatalysts were prepared and evaluated for activity; results are reproducible within an error limit of 10%. It should be noted that the absolute amount of Pt employed in Pt is much higher than Pt in 0.5θ_{Pt}NC. Due to the synergistic effect of Ni and Pt and their spatial close proximity on the surface of the 0.5θ_{Pt}-NC cocatalyst, solar hydrogen production is similar to that of bulk Pt but by using a tiny fraction of Pt. More detailed studies would be required to distinguish the activity difference in a quantitative manner. It should be underscored that Ni and Pt belong to the same group (group VIIIB) in the periodic table with unfilled d-orbitals. Both elements would be activated simultaneously and in a similar way, especially for hydrogen generation, which produces a multiplication effect (rather than a simple additive effect), and enhances the activity of the cocatalyst. This is supported by the similar onset potential for Pt and 0.5θ_{Pt}-NC, which will be discussed later. For the stability, initially, hydrogen evolution activity was evaluated for 5 h with the TiO_2/ZnS/CdS photoanode and 0.5θ_{Pt}-NC cocatalyst. However, after 5 h of activity evaluation, a decrease in activity was found and the simultaneous observation of cocatalyst dislodging from the device was observed. When hydrogen bubbles are evolving over the cocatalyst surface, after about 5 h, slow dislodging of cocatalyst particles was observed along with hydrogen bubbles. This indicates the unsatisfactory adherence of cocatalyst on the FTO plates, and we devised a method to make the cocatalyst stay on the FTO plate for a longer period, as described below. Among the few commercial binders evaluated, nafion and cocatalyst were found to mix and bind well. This mixture also adheres to the FTO plate well, and longer times for experiments were carried out. As the volume of nafion (Nph) increases from 1 to 10 µL for a fixed amount of 1 mg of cocatalyst, the activity decreases, mainly due to the lower amount of cocatalyst in it. In view of this, part of the nafion was replaced with graphite. By keeping stability and activity in mind, we used graphite and nafion with different percentages of 0.5θ_{Pt}NC. We prepared 1, 10, and 15 wt % of 0.5θ_{Pt}-NC cocatalyst mixed with graphite for the remaining

amount. This is denoted as X% 0.5θ_{Pt}-NC@C. For the deposition on FTO, we took 1 mg of X% 0.5θ_{Pt}-NC@C dispersed in 500 µL of ethanol and 1 µL of nafion by 30 min sonication, in which 10% 0.5θ_{Pt}-NC@C/Nph shows the best activity (Figure 3.3a) and stability up to an evaluation time of 25 h (Figure 3.3b). Even though the cocatalyst amount is low, better dispersion leads to high activity and similar activity to that of bare 0.5θ_{Pt}-NC.

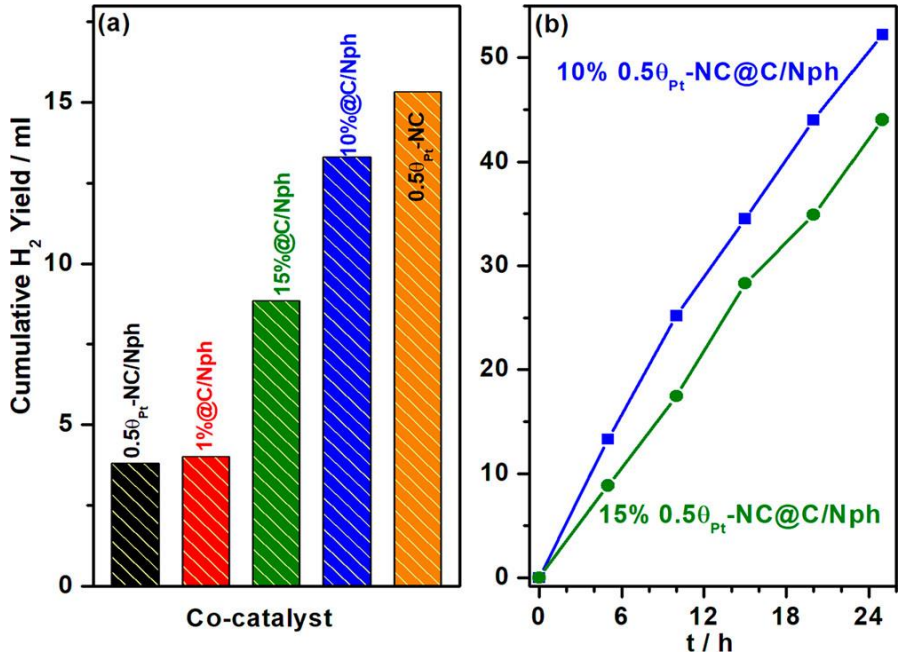


Figure 3.3. (a) Photocatalytic hydrogen production of the TiO_2/ZnS/CdS photoanode with pure 0.5θ_{Pt}-NC cocatalyst, 0.5θ_{Pt}-NC/Nph (cocatalyst with 1 µL of naphion), 1%, 10%, and 15% of 0.5θPt-NC cocatalyst mixed with 99%, 90%, and 85% of graphite and mixed with 1 µL of naphion (namely 1%@C/Nph, 10%@C/Nph, and 15%@C/Nph). (b) Stability of the TiO_2/ZnS/CdS photoanode with 10% and 15% 0.5θ_{Pt}-NC@C/Nph under one sun conditions. It is to be underscored that just 10% of 0.5θ_{Pt}-NC cocatalyst mixed with 90% graphite in 1 µL of naphion produced activity comparable to that of virgin 0.5θ_{Pt}-NC. This reiterates that the inherent activity of 0.5θ_{Pt}-NC cocatalyst is likely to be much higher than the value reported in this manuscript.

This result suggests the inherent activity of 0.5θ_{Pt}-NC should be much higher than the values reported in the current manuscript. It is also to be noted that Patra et al.[27] has reported 10.5 mL/h hydrogen production with a TiO_2/Mn-doped CdS photoanode and NiCu alloy cocatalyst. Hence, it is very important to investigate the highly efficient photoanode along

with cocatalyst optimization. We also plan to improve stability so that it can replace Pt as a cocatalyst for large scale H_2 production.

3.4 Elemental Mapping and Textural Properties of the Photoanode:

Figure 4 shows the representative SEM and elemental mapping from the vertical cross-section of the fractured TiO_2/ZnS/CdS device for Ti, Cd, Zn, and S elements. Thickness of the film is found to be around 11 µm (Figure 3.4a). The average thickness of the photoanode was measured by SEM and the surface profilometer at different spots on the photoanode, and a representative result is shown in Figure 3.5. The average thickness was found to be 9 µm, which is shown in Figure 3.5a.

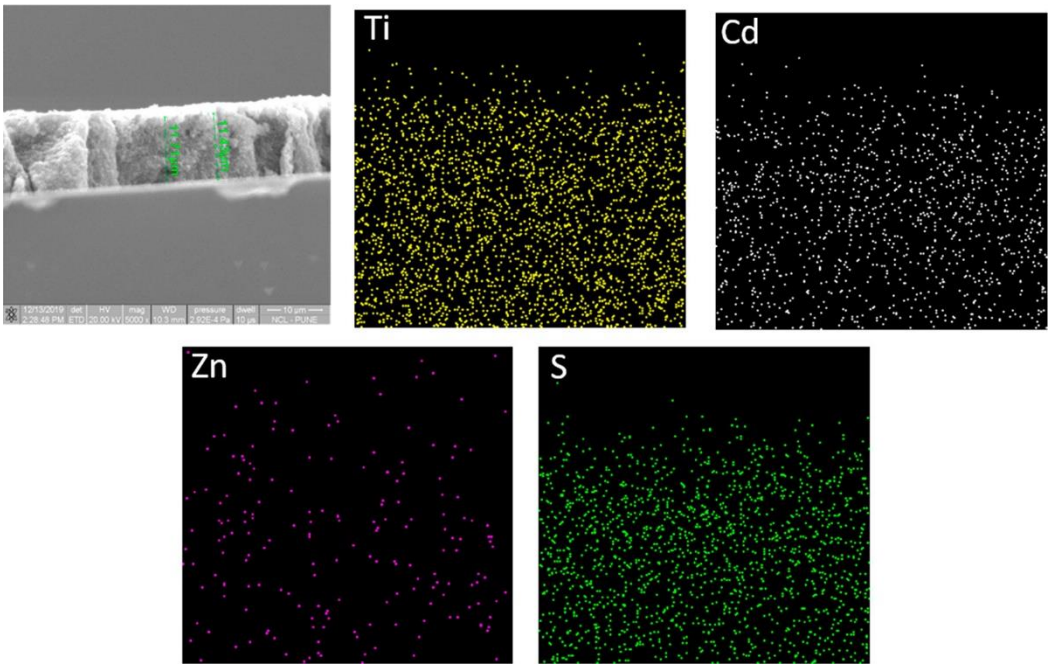


Figure 3.4. FESEM (top-left) and EDX elemental mapping of the TiO_2/ZnS/CdS photoanode for Ti, Cd, Zn, and S. Elemental mapping was measured only on the photoanode area; the FTO and glass areas were carefully avoided, to show the low concentration of Zn distribution.

At the edge of the photoanode, the thickness was found to be 12 µm for all films; this is likely due to the application of the doctor blade method to make titania film. From the following EDX elemental mapping, it is evident that Cd and S are uniformly distributed in the TiO_2 porous thin film from the top to the bottom layers. The TiO_2 film made by the doctor blade method gives a porous network of TiO_2 channels, which is suitable for Cd, S, and Zn ions to diffuse into the mesopores of TiO_2 and make abundant heterostructure between TiO_2, CdS,

and ZnS. Heterostructure between TiO_2 and CdS is necessary for efficient electron transfer. It is also to be noted that Zn ions are found to be minimal throughout the film uniformly.

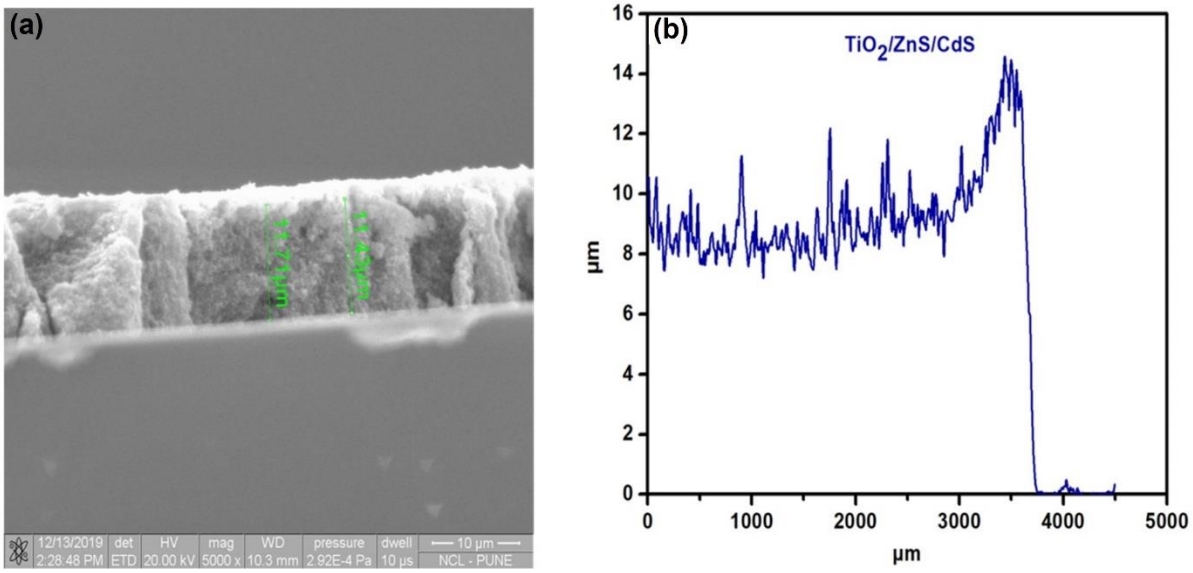


Figure 3.5. (a) FESEM image for the cross-section of the TiO_2/ZnS/CdS photoanode. (b) Representative surface profile measured for TiO_2/ZnS/CdS photoanode.

The heterostructure between TiO_2 and a solid solution of ZnS +CdS is to prevent the electron−hole recombination. From elemental mapping, it is evident that the heterojunctions between TiO_2 and CdS/ZnS are helping to improve the overall electron transfer and hence photocatalytic performance. The most important observation is the dispersion of CdS components throughout the film from top to bottom layers, underscoring that there are no layers of CdS observed, rather the uniformly distributed QDs. X-ray diffraction was recorded for P25-TiO_2, TiO_2/ZnS/CdS, and TiO_2/CdS photoanodes, and the results are shown in Figure 3.6.

Predominant anatase (75%) with 25% rutile titania for all three photoanodes were observed; no new diffraction features due to CdS or ZnS was observed for either of the photoanodes. Chemical analysis carried out by ICP shows 2.10 wt % CdS and 0.42 wt % ZnS, and the rest is titania for the photoanodes; an intermediate ZnS layer in the TiO_2/ ZnS/CdS photoanode did not change the value significantly.

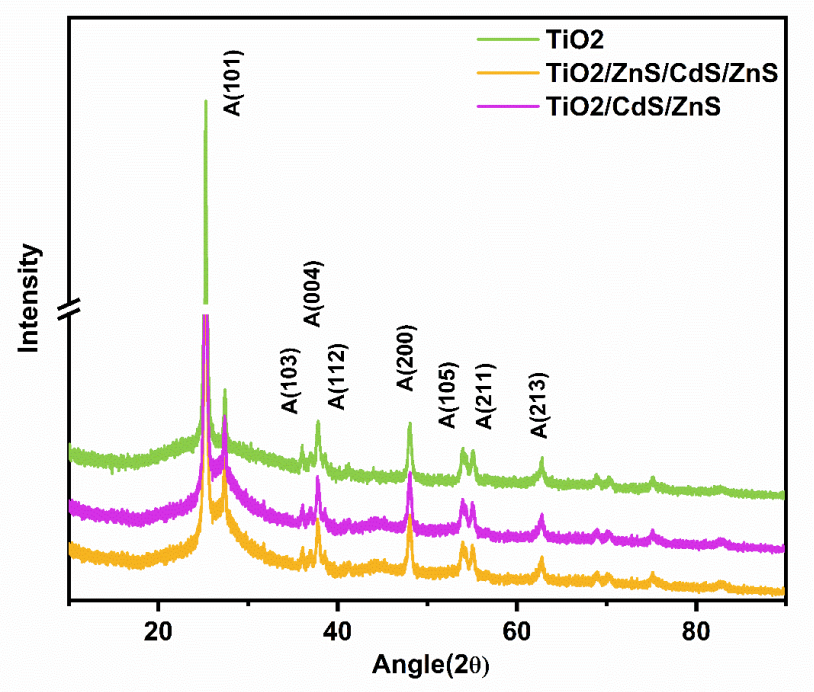


Figure 3.6 X-ray diffraction pattern recorded for P25-TiO_2, and TiO_2/CdS and TiO_2/ZnS/CdS photoanodes. Due to uniform distribution of small amount (2.5 wt %) of quantum dots of chalcogenides, no diffraction features of them were observed.

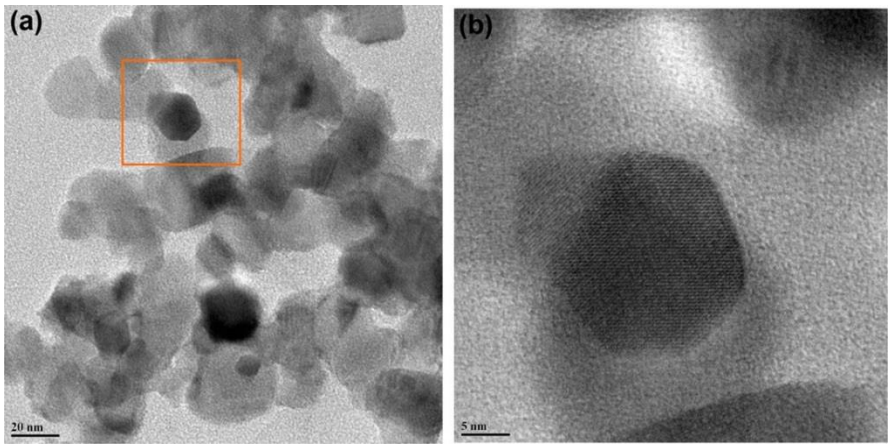


Figure 3.7. TEM images recorded for the TiO_2/ZnS/CdS photoanode. The square area shown in panel a is recorded at high resolution and shown in panel b. hexagonal particles observed are due to CdS and confirmed from a (110) interplanar d-spacing of 0.210 nm. Heterojunctions between CdS and TiO_2 particles are directly observed in TEM images.

Indeed, the weight measurements made for the FTO plate, before and after SILAR cycles, also indicate that a 2.5 wt % of chalcogenides was incorporated in the titania layers. ICP analysis and weight difference measurements are observed to be in good agreement with

each other. The heterojunction between CdS and TiO_2 was further explored by TEM studies, and the results are shown in Figure 3.7. Photoanode material was carefully removed from the FTO plate, and a small amount was sonicated and coated on the TEM grid to study the microstructure. The uniform distribution of CdS and TiO_2 nanoparticles can be clearly seen in Figure 5a. CdS particles could be easily identified with hexagonal Wurtzite structure and characteristic d-values. One such CdS particle imaged at high resolution is shown in Figure 5b, which shows the (110) plane with a d-value of 0.210 nm. A careful analysis of TEM images indicates that the CdS particles are surrounded by TiO_2 nanoparticles and suggests the formation of CdS in the pores of TiO_2, due to the SILAR preparation method. The particle size for TiO_2 was found to be 20 ± 2 nm. The lattice spacing for TiO_2 was measured to be 0.35 nm for the (101) plane.

3.5 Photoelectrochemical Measurement:

Photoelectrochemical performance of the TiO_2/ZnS/CdS photoanode was evaluated in the three-electrode system with Pt as a counter electrode and Ag/AgCl as a reference electrode using an aqueous solution of Na_2S/Na_2SO_3. From the chronoamperometry measurement, photoresponse and maximum current density and stability measurements were carried out with a 1 × 1 cm^2 film, and the results are shown in Figure 3.8. TiO_2/ZnS/CdS shows a current density of 3.8 mA/cm^2 compared to TiO_2/CdS, which exhibits a 3.4 mA/cm^2 current density at zero applied potential. Photoresponse at 0 V was measured to clarify the stability and photoresponse, and the result is shown in Figure 3.8a. Better current density and photoresponse (than TiO_2/CdS) suggests that TiO_2/ZnS/CdS has improved heterostructure, which gives better electron transfer to TiO_2 compared to TiO_2/CdS; indeed, similar differences in photocatalytic activity of photoanodes were observed (Figure 3.2). Chronoamperometry measurement was also made for 3 h under one sun conditions (1.5 AM), which is shown in Figure 5b, to evaluate the stability of the TiO_2/ZnS/CdS photoanode. Current density decreases from initial 4.5 mA/cm^2 to stable 4 ± 0.1 mA/cm^2 in 1 h, and thereafter it remains constant within the error bar. Photocurrent density values observed in the continuous light-on mode (Figure 3.8b) is comparable to the value observed in light on/off measurements (Figure 3.8a). Stable

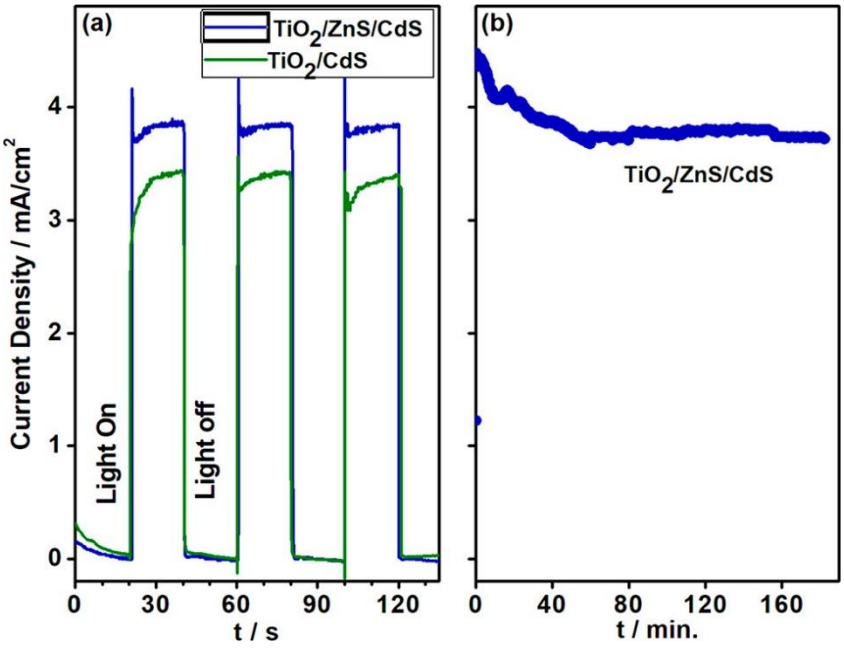


Figure 3.8. (a) Chronoamperometry measurement at 0 V under one sun conditions. (b) Photoelectrochemical stability of the photoanode for 3 h under one sun conditions by chronoamperometry.

photocatalytic activity observed for several hours suggests that there is no degradation of the photoanode. Indeed, the stable photocurrent density values and the constant hydrogen generation values observed in Figures 3.2 and 3.3 are in good correspondence.

3.6 Structural and Microscopy Analysis of Cocatalysts:

To understand the structural aspects of NiCu alloy in different forms, XRD, TEM, and HRTEM measurements were made and compared. Figure 3.9a shows the X-ray diffraction pattern recorded for NiCu@bimetal, NC@H^-, NiCu alloy, and 0.5θ_{Pt}-NC. Figure 3.9b, c and d, e shows TEM images of NiCu alloy and 0.5θ_{Pt}-NC, respectively; the inset shows the HRTEM image of 0.5θ_{Pt}-NC. We have synthesized two forms of the Ni−Cu nanoparticle, one is an alloy and the other is a bimetal[27] for the reference. NiCu alloy shows the typical alloy features corresponding to JCPDS no. 47-1406. NiCu@bimetal shows the diffraction pattern of Cu and Ni corresponding to JCPDS no. 04-0836 and JCPDS no. 04-0850, respectively; indeed, it is easy to distinguish the bimetal by observing individual metal peaks, while in the alloy it merges into one. In a previous report by Patra et. al,[27] it was shown that NiCu in alloy form shows better activity for hydrogen evolution. Hence, NiCu alloy was chosen for the present studies. The XRD pattern of NiCu@H^- shows a diffraction pattern identical to that of the bimetal form

of NiCu. When NiCu@H⁻ is treated with Pt(II), the intensity of the diffraction pattern drastically changes because of the reduction in particle size, which is also reflected in HRTEM of $0.5\theta_{Pt}$-NC (Figure 3.9e).

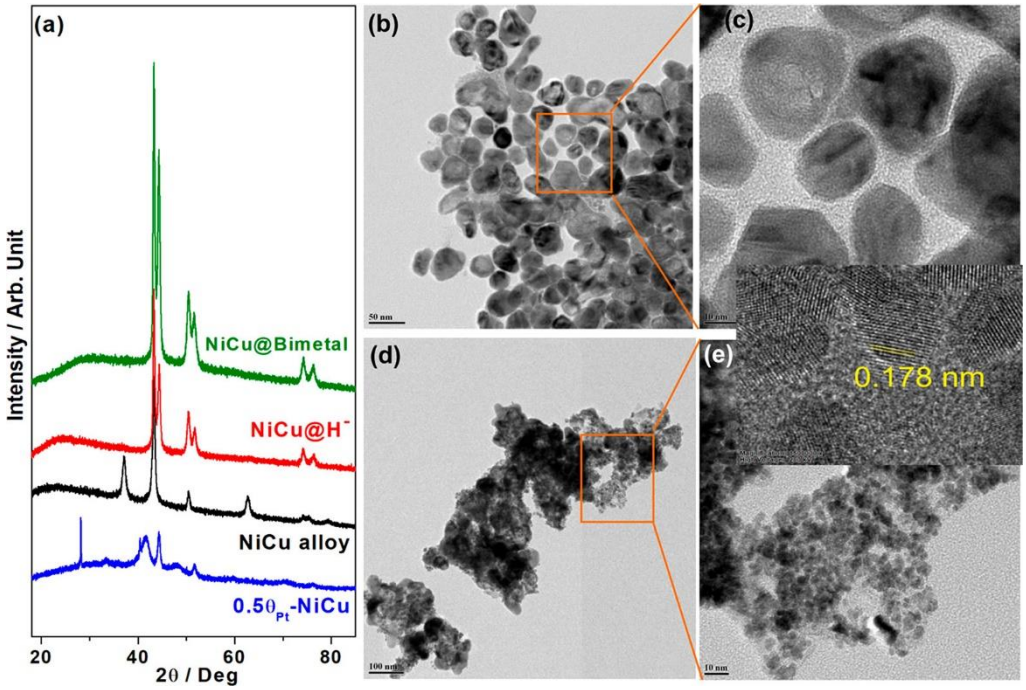
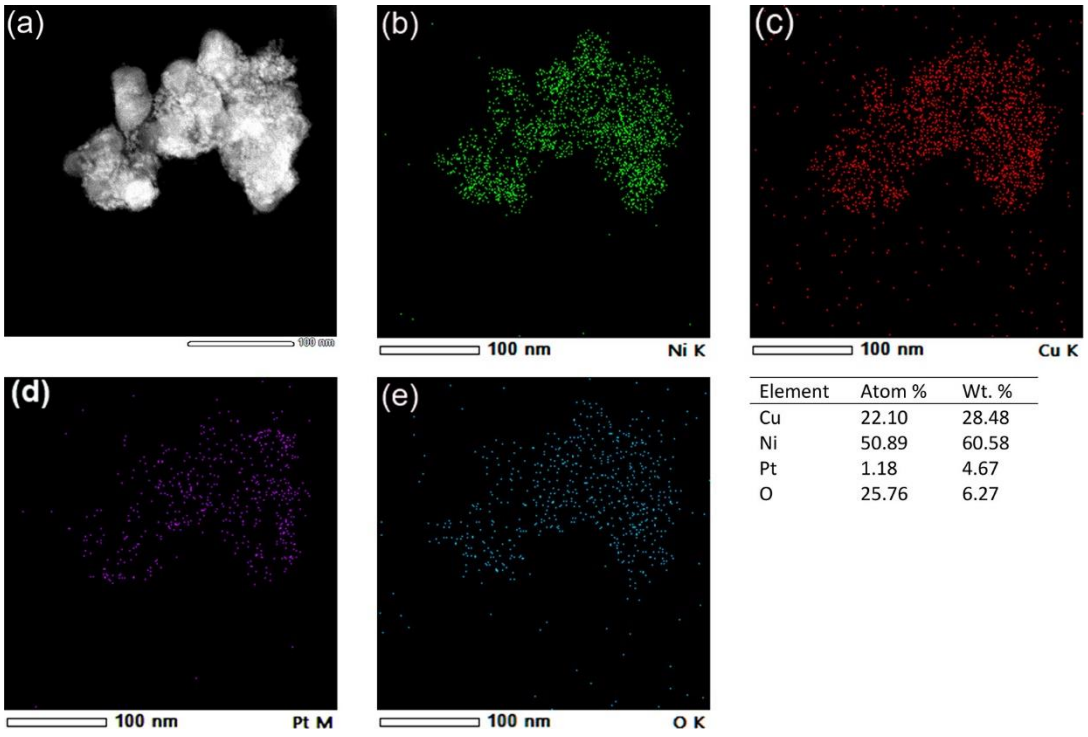


Figure 3.9. (a) X-ray diffraction pattern NC@bimetal, NiCu alloy, NiCu@H⁻, and $0.5\theta_{Pt}$-NC. HRTEM images observed for (b and c) NiCu alloy, and (d and e) $0.5\theta_{Pt}$-NC. A decrease in particle size from NiCu alloy (25–40 nm) to $0.5\theta_{Pt}$-NC (4–5 nm) in panels c and e, respectively, is noted. The inset shown for HRTEM of $0.5\theta_{Pt}$-NC displays the abundant (200) facet of NiCu alloy.

The diffraction pattern shifted to lower 2θ and was broadened. TEM images shown in Figure 3.9b, c for NiCu alloy display a particle size in the range of 25 and 40 nm with an average size of 34 nm. However, a severe reduction in particle size to about 4–5 nm was observed after Pt deposition. An approximate spherical shape particle is observed before and after Pt deposition on NiCu alloy. The HRTEM image shown for $0.5\theta_{Pt}$-NC displays well resolved lattice fringes for the (200) facet of NiCu alloy.[34] Similar images were observed for NiCu alloy also. The principle adopted for Pt deposition in our synthesis method was expected to lead to half-a-monolayer of Pt on NiCu alloy. A careful analysis by TEM-EDX was attempted to evaluate the spatial distribution of all elements, particularly Pt, on $0.5\theta_{Pt}$NC particles, and the results observed are shown in Figure 3.10. Figure 3.10a shows the TEM image of a cluster of $0.5\theta_{Pt}$-

NC particles, and it was evaluated for all elements present on it (Figure 3.10b−e). Ni and Cu were observed uniformly all over the cocatalyst surface, supporting the alloy (bimetal) nature of the cocatalyst.



Element	Atom %	Wt. %
Cu	22.10	28.48
Ni	50.89	60.58
Pt	1.18	4.67
O	25.76	6.27

Figure 3.10. (a) TEM and EDS images recorded $0.5\theta_{Pt}$-NC for distribution of (b) Ni, (c) Cu, (d) Pt, and (e) O elements. Atom and weight percent of elements are also given for quantitative information. It is to be noted that oxygen arises due to surface oxidation.

The atom % ratio of Ni:Cu is observed to be 2.3:1, indicating a marginal Ni enrichment. Apart from Ni and Cu, a significant amount of oxygen and a small amount of Pt were also observed. The presence of oxygen is attributed to the surface oxidation of Ni and Cu, and it is supported by XPS measurements and discussed later (Figure 3.11). It is to be noted that the distribution of Pt is uniform on the surface of $0.5\theta_{Pt}$-NC, and it is as expected from the preparation method employed. Unlike Ni and Cu, no clustering of Pt is observed, which supports the above conclusion. A 1.18 atom % (4.67 wt %) Pt was measured from the EDX analysis. In fact, more detailed and high-resolution studies would be required to understand the distribution of Pt, possibly by controlling the Pt content to less than 0.5 ML. Interestingly, oxygen was also observed to be distributed uniformly and without any clustering, despite 25.76 atom % (6.27 wt %).

3.7 XPS:

XPS analysis was performed as well to explore the effect of surface composition of materials on the possible oxidation aspects of Ni and Cu. It is well-known that both Ni and Cu are pyrophoric in nature, and even with careful storage and handling, surface oxidation of them cannot be avoided due to some exposure to air while preparing the sample for XPS analysis and their introduction into the XPS chamber.

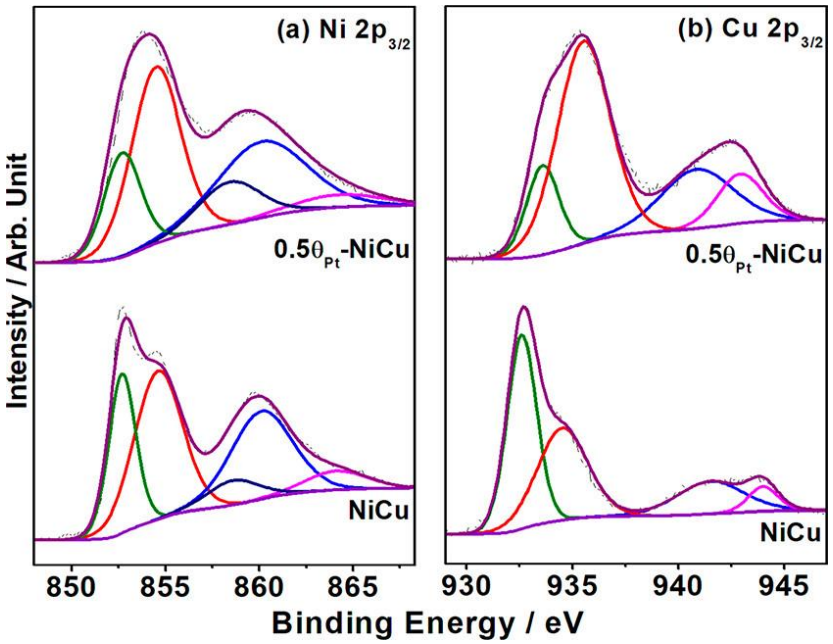


Figure 3.11. XPS of (a) Ni 2p3/2 and (b) Cu 2p3/2 core levels of NiCu alloy and $0.5\theta_{Pt}$-NC. Green colored peaks correspond to metallic Ni or Cu while red colored peaks are attributed to a mixture of oxidized Ni (NiO and $Ni(OH)_2$) and Cu (CuO) species. The satellite feature is fitted with blue- and pink-colored peaks.

Figure 3.11a shows Ni 2p3/2 spectra of NiCu alloy and $0.5\theta_{Pt}$-NC cocatalysts. NiCu alloy exhibits the characteristic peaks for Ni metal (852.7 eV) and oxidized Ni species (NiO and $Ni(OH)_2$) at 855.5 eV. Although XPS explores about 10 nm depth, a mixture of metallic Ni and oxidized Ni species are possible within the probing depth.[35] However, we attribute the oxidized Ni species (observed before and after Pt deposition) due to atmospheric degradation and not due to preparation method. After hydride treatment and half-a-monolayer platinum deposition, the amount of metallic Ni is marginally decreased on the surface, which is clearly visible from the Ni-metal peak intensity. With the metallic Ni feature, the NiO feature also decreases and the $Ni(OH)_2$ feature increases on the surface. This is fully supported by the shift

in the satellite feature to higher BE, compared to that of NiCu alloy. It is also to be reiterated that XRD does not show any oxide or hydroxide features in Figure 3.9a. In addition, excess borohydride added in the preparation of NiCu@H^- is expected to reduce any oxidized Ni and Cu species on NiCu alloy. In view of these facts, cocatalysts prepared and employed for the activity studies are metallic in nature, and the surface contaminations observed with Ni and Cu 2p levels are due to atmospheric degradation. The Cu 2p3/2 feature (Figure 3.11b) in NiCu alloy shows Cu (932.5 eV) and Cu(II) features at 934.5 eV along with a satellite feature between 939 and 945 eV.36,37 The narrow line width of 932.5 eV supports the oxidation state to be zero. In the case of NiCu alloy, the Cu feature is supported by the deconvolution of Cu 2p3/2 spectra. Metallic Cu intensity decreases upon Pt deposition on $0.5\theta_{Pt}$-NC, as in the Ni case while Cu(II) content increases which is also confirmed by an increase in the intensity of satellite features. Indeed, Ni and Cu are equally vulnerable to surface oxidation and hence show significant amounts of oxidized species on the surface. We would like to indicate the possibility of galvanic displacement during Pt deposition, which may change the surface composition. As mentioneded previously, the initial average particle size of NiCu alloy is 34 nm, and upon Pt deposition, the particle size decreased drastically to about 4−5 nm. Although the particle size reduction would be helpful to improve the activity due to significantly increased surface area, the reasons behind size reduction are yet to be determined and this will be addressed in future publications.

3.8 Electrochemical Measurement:

Electrochemical measurement was carried out using a three-electrode system using platinum and Ag/AgCl as a counter and reference electrode, respectively, in 0.5 M H_2SO_4. The catalyst paste was coated on a glassy carbon electrode with a total catalyst amount of 5 µg. The electrochemically active surface area (ECSA) of the catalysts was estimated from the double-layer capacitance,[38,39] which was determined using the cyclic voltammogram recorded at different scan rates in the non-Faradaic region in 0.5 M H_2SO_4 solution, and the result is shown in Figure 3.12. The ratio of the double layer capacitance to the specific capacitance provides ECSA values.[40] Details of the ECSA calculation and specific capacitance values are available in refs [38−40]. From the fitted capacitances shown in Figure 3.12, the active surface area of NiCu (62.5 cm^2) was found to be larger than that of $0.5\theta_{Pt}$-NC (35.4 cm^2). Contrary to the expectations, larger ECSA

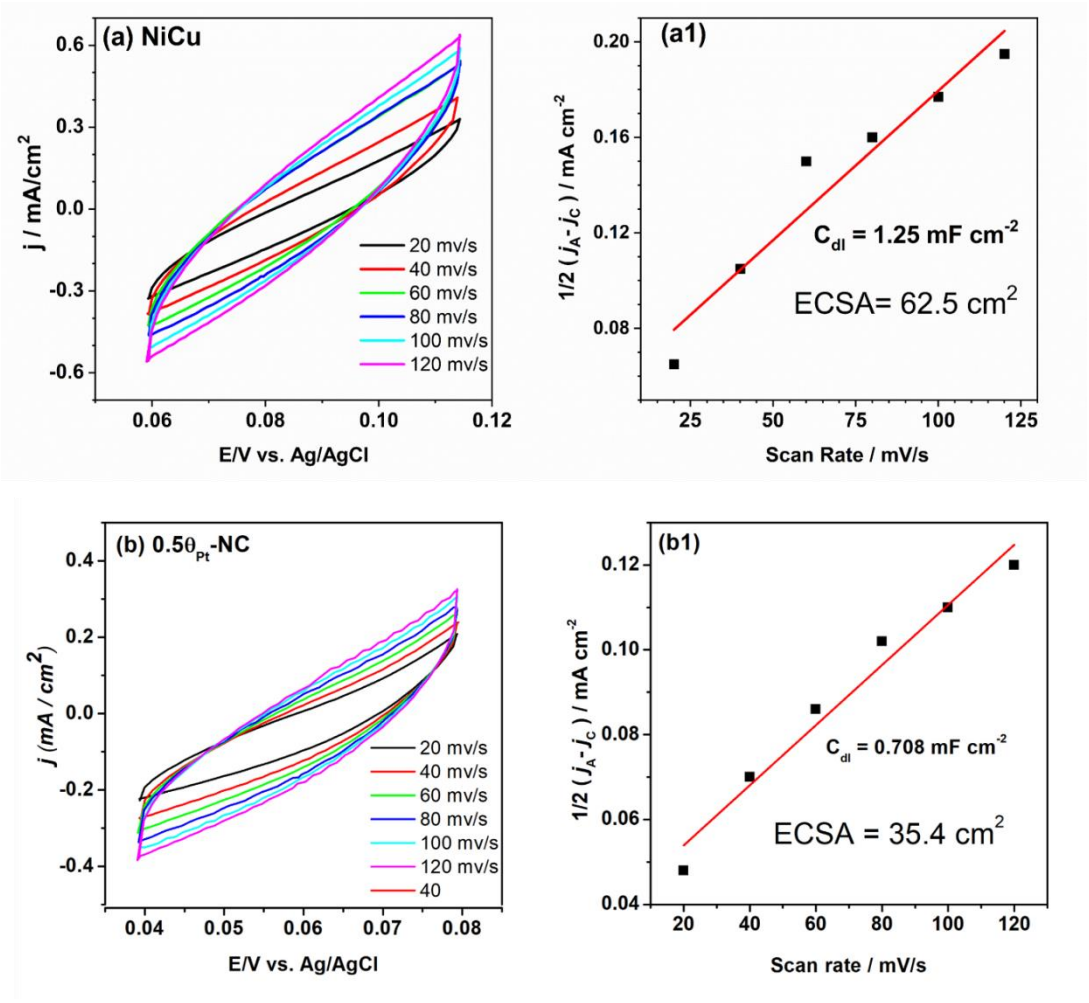


Figure 3.12. Cyclic voltammetry results recorded in 0.5 M sulfuric acid solution at different scan rates for (a) NiCu, and (b) 0.5θ_{Pt}-NC catalysts. Double layer capacitance (Cdl) was calculated from the plots shown in a1 and b1 panels for NiCu and 0.5θPt-NC, respectively, and ECSA is defined to be equal to Cdl/Cs; Specific capacitance (Cs) of Ni is reported to be 20 μF/cm^2.

was observed with NiCu than with 0.5θ_{Pt}-NC, despite the smaller particle size of the latter. The corresponding ECSA-corrected LSV and Tafel plots of NiCu and 0.5θ_{Pt}-NC are shown in Figure 3.13a, b. The polarization curve of NiCu (Figure 3.13a) alloy shows the onset potential at 0.2 V vs RHE; however, when NiCu alloy is integrated with half-amonolayer of Pt, the onset potential dramatically decreased to 0.05 V. This observation highlights that the facile electron transfer is dramatically enhanced due to synergistic effect of 0.5 ML of Pt with NC. It is evident from the present measurements that a fraction of ML of platinum on the surface of NiCu alloy can enhance the HER activity drastically, despite the low ECSA.

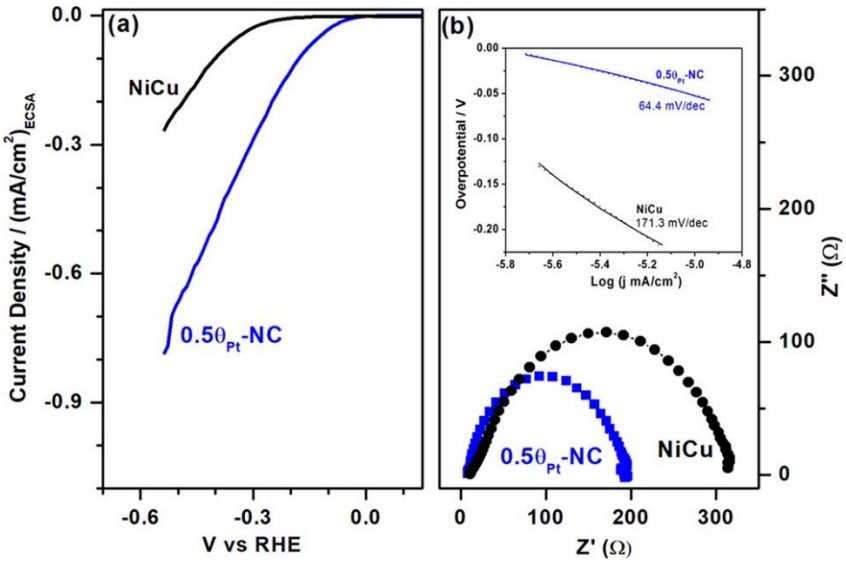


Figure 3.13. (a) ECSA-corrected LSV and (b) Nyquist plots obtained from electrochemical impedance measurement which provides charge transfer resistance of NiCu alloy and $0.5\theta_{Pt}$-NC catalysts. Inset in panel b shows Tafel slopes with linear fitting for both catalysts.

Results shown in Figure 3.13a also indicate that there is no bulk Pt deposited on the cocatalyst. To understand the charge transfer resistance at the catalyst electrolyte interface, we performed the electrochemical impedance measurement, and the result is shown in Figure 3.13b. The radius of the semicircle represents the charge transfer resistance at the interface, suggesting facile electron transfer in $0.5\theta_{Pt}$-NC as compared to NiCu alloy (Figure 3.13b). This observation demonstrates that $0.5\theta_{Pt}$-NC has a less resistive pathway; further, due to the synergistic effect of Ni and Pt, it enhances the HER activity. Tafel slopes are measured to be 171.32 and 64.4 $mV \cdot dec^{-1}$ for NiCu and $0.5\theta_{Pt}$-NC, respectively (Figure 3.13b inset). The smaller Tafel slope also suggests a higher HER activity with $0.5\theta_{Pt}$-NC catalyst.

3.9 Mechanism:

A combination of two or more semiconductors with desired bandgaps and band-edge potentials with an efficient cocatalyst can lead to an efficient photocatalytic water splitting system, which might be scalable. The system reported in this manuscript has this type of potential. Herein with the detailed characterization studies and the activity evaluation carried out, a possible mechanism of solar to chemical conversion is given in Figure 3.14. CdS with a bandgap 2.4 eV can absorb light up to 522 nm, which covers about 44% of the visible light part of the solar spectrum. TiO_2 can absorb 4–5% of UV light present in the solar spectrum

and can add efficiency to the device. Upon light absorption, electrons are excited to the conduction band (CB) of CdS QDs; thereafter these electrons are transferred to the CB of TiO_2. The heterojunction observed between titania and CdS helps for this electron transfer. This facilitates the electrons to reach the $0.5\theta_{Pt}$-NC cocatalyst, which is coated adjacent to the photoanode on the FTO plate. These electrons are utilized to reduce water. Sensitization of TiO_2 first with a monolayer of wide band gap ZnS reduces the electron−hole recombination and enhances the charge separation and utilization at the cocatalyst sites. UV−vis absorption by the TiO_2/ZnS/CdS photoanode shows a marginal increase in the bandgap to 2.5 eV (compared to 2.4 eV with the TiO_2/CdS photoanode), indicating a formation of a solid solution of ZnS and CdS to CdZnS.[32,33] This leads to a different interface between titania and CdS with the TiO_2/ZnS/CdS photoanode, compared to no such interface in the TiO_2/CdS photoanode. Indeed, a pure ZnS layer, without forming a solid solution, would actually hinder the electron transfer from CdS to titania,[12,31−33] due to the high energy of the CB edge of ZnS. Larger amounts of photocatalytic hydrogen production observed with TiO_2/ZnS/CdS (Figure 3.2) compared to TiO_2/CdS demonstrates this. Increase in the photoelectron current density (Figure 3.8) and the TEM results (Figure 3.7) also support a better quality heterostructure with TiO_2/ZnS/CdS. The SILAR method employed for assembling CdS and ZnS QDs inside the pores of titania should be underscored. Due to layer-by-layer construction of the chalcogenides because of diffusion of ionic precursors (Cd^{2+}, Zn^{2+}, and S^{2-}), the QDs are assembled inside the pores in situ. This method allows the formation of heterostructure between the semiconductors in the best possible way and helps to enhance the charge separation and utilization. It is also to be noted that electron transfer occurs from CdS to TiO_2, and the hole-transfer happens in the exact reverse direction. It is an added advantage for effective electron transfer toward the cocatalyst sites, and it mimics the electron-transfer from photosystem II to photosystem I in the natural leaf. In the case of the cocatalyst part, $0.5\theta_{Pt}$-NC shows an onset potential similar to that of Pt/C. This fact further demonstrates that hydrogen evolution is enhanced due to the atomic Pt layer available on the surface.

3.10 Conclusion:

In summary, we developed a QuAL device with a TiO_2 film sensitized with ZnS and CdS quantum dots (QDs) and integrated it with half-a-monolayer of Pt covered on Ni−Cu ($0.5\theta_{Pt}$-NC) alloy nanoparticles. The critical novelty of the present work is to successfully demonstrate

the activity of bulk Pt from a mere half-a-monolayer of Pt coated on the surface of NiCu alloy. However, it is to be demonstrated on other metal and metallic

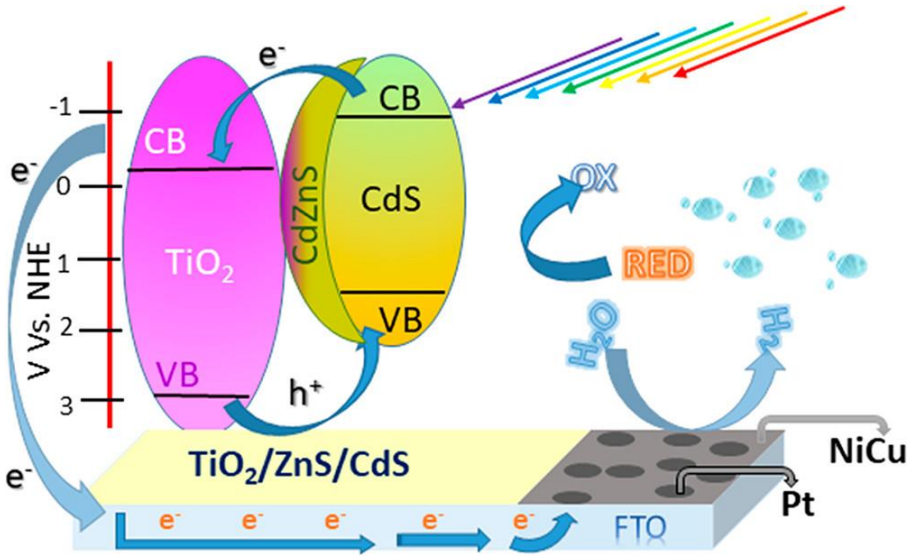


Figure 3.14. A possible mechanism for the solar to hydrogen production over the TiO_2/ZnS/CdS photoanode; blue lines show the transfer of the electron and holes. Gray and black dots represent NiCu alloy and 0.5 ML Pt integrated, respectively (only for the representation). The first layer of ZnS interacts with CdS to form a CdZnS solid-solution interface between titania and CdS, which helps for effective charge separation and conduction.

surfaces. The preparation method described can also be extended to other noble metals. The QuAL device with $0.5\theta_{Pt}$-NC cocatalyst was demonstrated to show solar hydrogen production at a rate of 4 mL/h, and the photoanode shows a current density of 4 ± 0.1 mA cm^{-2} at zero applied potential. An innovative ZnS seed layer integration with CdS QDs leads to a solid solution of the CdS+ZnS interface, and this increased the charge carrier separation, resulting in high current density and solar hydrogen generation under one sun conditions. Hence, a proper band alignment among the semiconductor components could lead to better solar to H_2 conversion with low charge carrier recombination. On the other hand, for the cocatalyst part, $0.5\theta_{Pt}$-NC shows low overpotential compared to NiCu alloy due to the synergistic effect between Ni and Pt on the surface, which enhances the H_2 evolution on the surface of the cocatalyst. As we indicated in the manuscript, inherent activity of $0.5\theta_{Pt}$-NC is likely to be higher, and a correct combination of binders is likely to bring out the best possible activity. Over the last two decades, a large amount of work has been reported in the field of

photocatalytic water splitting; however, there is no great breakthrough yet in this area of research. We believe there is a lot of potential associated with QuAL and artificial leaf devices, and more work in this direction is desired. Simulation of bulk Pt activity with half-a-monolayer of Pt would lower the cost of the device, so more effort is required in this direction. Economically viable and different metallic cocatalysts should also be evaluated with an atomic platinum layer.

3.11 References:

1. Armaroli, N.; Balzani, V. The Future of Energy Supply: Challenges and Opportunities. *Angew. Chem. Int. Ed.* **2007**, 46, 52−66.
2. She, H.; Zhou, H.; Li, L.; Zhao, Z.; Jiang, M.; Huang, J.; Wang, L.; Wang, Q. Construction of a Two-Dimensional Composite Derived from TiO_2 and SnS_2 for Enhanced Photocatalytic Reduction of CO_2 into CH_4. *ACS Sus. Chem. Eng.* **2019**, 7, 650−659.
3. Lewis, N. S.; Nocera, D. G. Powering the planet: Chemical Challenges in Solar Energy Utilization. *Proc. Natl. Acad. Sci. U. S. A.* **2006**, 103, 15729−15735.
4. Wang, Z.; Li, C.; Domen, K. Recent Developments in Heterogeneous Photocatalysts for Solar-Driven Overall Water Splitting. *Chem. Soc. Rev.* **2019**, 48, 2109−2125.
5. Turner, J. A. Sustainable Hydrogen Production. *Science* **2004**, 305, 972−974.
6. Nocera, D. G. The Artificial Leaf. *Acc. Chem. Res.* **2012**, 45, 767− 776.
7. Bharad, P. A.; Sivaranjani, K.; Gopinath, C. S. A Rational Approach Towards Enhancing Solar Water Splitting: A Case Study of Au−RGO/N-RGO−TiO_2. *Nanoscale* **2015**, 7, 11206−11215.
8. Tudu, B.; Nalajala, N.; Reddy, K. P.; Saikia, P.; Gopinath, C. S. Electronic Integration and Thin Film Aspects of Au−Pd/rGO/TiO_2 for Improved Solar Hydrogen Generation. *ACS Appl. Mater. Interfaces* **2019**, 11, 32869−32878.
9. Trevisan, R.; Rodenas, P.; Gonzalez-Pedro, V.; Sima, C.; Sanchez, R. S.; Barea, E. M.; Mora-Sero, I.; Fabregat-Santiago, F.; Gimenez, S. Harnessing Infrared Photons for Photoelectrochemical Hydrogen Generation. A PbS Quantum Dot Based "Quasi-Artificial Leaf. *J. Phys. Chem. Lett.* **2013,** 4, 141−146.
10. Maeda, K.; Mallouk, T. E. Two-Dimensional Metal Oxide Nanosheets as Building Blocks for Artificial Photosynthetic Assemblies. *Bull. Chem. Soc. Jpn.* **2019**, 92, 38−54.

11. Roy, N.; Suzuki, N.; Terashima, C.; Fujishima, A. Recent Improvements in the Production of Solar Fuels: From CO_2 Reduction to Water Splitting and Artificial Photosynthesis. *Bull. Chem. Soc. Jpn.* **2019**, 92, 178−192.
12. Rajaambal, S.; Sivaranjani, K.; Gopinath, C. S. Recent Developments in Solar H_2 Generation from Water Splitting. *J. Chem. Sci.* **2015**, 127, 33−47.
13. Zou, Z.; Ye, J.; Sayama, K.; Arakawa, H. Direct Splitting of Water under Visible Light Irradiation with an Oxide Semiconductor Photocatalyst. *Nature* **2001**, 414, 625−627.
14. Sivaranjani, K.; Agarkar, S.; Ogale, S. B.; Gopinath, C. S. Toward a Quantitative Correlation between Microstructure and DSSC Efficiency: A Case Study of $TiO_{2-x}N_x$ Nanoparticles in a Mesoporous Framework. *J. Phys. Chem. C* **2012**, 116, 2581−2587.
15. Patra, K. K.; Gopinath, C. S. Bimetallic and Plasmonic Ag−Au on TiO_2 for Solar Water Splitting: An Active Nanocomposite for Entire Visible-Light-Region Absorption. *ChemCatChem* **2016**, 8, 3294−3311.
16. Melvin, A. A.; Illath, K.; Das, T.; Raja, T.; Bhattacharyya, S.; Gopinath, C. S. M−Au/TiO_2 (M = Ag, Pd, and Pt) Nanophotocatalyst for Overall Solar Water Splitting: Role of Interfaces. *Nanoscale* **2015**, 7, 13477−13488.
17. Patra, K. K.; Ghosalya, M. K.; Bajpai, H.; Raj, S.; Gopinath, C. S. Oxidative Disproportionation of MoS_2/GO to MoS_2/MoO_{3-x}/RGO: Integrated and Plasmonic 2D-Multifunctional Nanocomposite for Solar Hydrogen Generation from NIR and Visible Regions. *J. Phys. Chem. C* **2019**, 123, 21685−21693.
18. Rajaambal, S.; Mapa, M.; Gopinath, C. S. $In_{1-x}Ga_xN$@ZnO: A Rationally Designed and Quantum Dot Integrated Material for Water Splitting and Solar Harvesting Applications. *Dalton Trans.* **2014**, 43, 12546−12554.
19. Yang, J.; Wang, D.; Han, H.; Li, C. Roles of Cocatalysts in Photocatalysis and Photoelectrocatalysis. *Acc. Chem. Res.* **2013**, 46, 1900−1909.
20. Zhang, S.; Liu, Z.; Chen, D.; Guo, Z.; Ruan, M. Oxygen Vacancies Engineering in TiO_2 Homojunction/ZnFe-LDH for Enhanced Photoelectrochemical Water Oxidation. *Chem. Eng. J.* **2020**, 395, 125101.
21. Alivisatos, A. P. Semiconductor Clusters, Nanocrystals, and Quantum Dots. *Science* **1996**, 271, 933−937.
22. Brus, L. Quantum Crystallites and Nonlinear Optics. *Appl. Phys. A: Solids Surf.* **1991**, 53, 465−474.

23. Preethi, L. K.; Mathews, T.; Nand, M.; Jha, S. N.; Gopinath, C. S.; Dash, S. Band Alignment and Charge Transfer Pathway in Three Phase Anatase-Rutile-Brookite TiO_2 Nanotubes: An Efficient Photocatalyst for Water Splitting. *Appl. Catal. B* **2017**, 218, 9−19.
24. Nalajala, N.; Patra, K. K.; Bharad, P. A.; Gopinath, C. S. Why the Thin Film form of a Photocatalyst is Better than the Particulate form for Direct Solar-to-Hydrogen Conversion: A Poor Man's Approach. *RSC Adv.* **2019**, 9, 6094−6100.
25. Patra, K. K.; Bhuskute, B. D.; Gopinath, C. S. Possibly Scalable Solar Hydrogen Generation with Quasi-Artificial Leaf Approach. *Sci. Rep.* **2017**, 7, 6515.
26. Du, P.; Eisenberg, R. Catalysts made of Earth-Abundant Elements (Co, Ni, Fe) for Water Splitting: Recent Progress and Future Challenges. *Energy Environ. Sci.* **2012**, 5, 6012−6021.
27. Patra, K. K.; Bharad, P. A.; Jain, V.; Gopinath, C. S. Direct Solarto-Hydrogen Generation by Quasi-Artificial Leaf Approach: Possibly Scalable and Economical Device. *J. Mater. Chem. A* **2019**, 7, 3179− 3189.
28. Ran, J.; Zhang, J.; Yu, J.; Jaroniec, M.; Qiao, S. Z. Earth-Abundant Cocatalysts for Semiconductor-Based Photocatalytic Water Splitting. *Chem. Soc. Rev.* **2014**, 43, 7787−7812.
29. Nalajala, N.; Gooty Saleha, W. F.; Ladewig, B. P.; Neergat, M. Sodium Borohydride Treatment: A Simple and Effective Process for The Removal of Stabilizer and Capping Agents from Shape-Controlled Palladium Nanoparticles. *Chem. Commun.* **2014**, 50, 9365−9368.
30. Lee, Y.-S.; Gopi, C. V. V. M.; Venkata-Haritha, M.; Kim, H.-J. Recombination Control in High-Performance Quantum Dot-Sensitized Solar Cells with a Novel TiO_2/ZnS/CdS/ZnS Heterostructure. *Dalton Trans.* **2016**, 45, 12914−12923.
31. Maitri, M.; Sivaranjani, K.; Bhange, D. S.; Saha, B.; Chakraborty, P.; Viswanath, A. K.; Gopinath, C. S. Structure, Electronic Structure, Optical and Dehydrogenation Catalytic study of $(Zn_{1-z}In_z)(O_{1-x}N_x)$ Solid Solution. *Chem. Mater.* **2010**, 22, 565−578.
32. Maitri, M.; Thushara, K. S.; Saha, B.; Chakraborty, P.; Janet, C. M.; Viswanath, R. P.; Madhavan Nair, C.; Murti, K. V. G. K.; Gopinath, C. S. Electronic Structure and Catalytic Studies of Solid Solution of GaN in ZnO. *Chem. Mater.* **2009**, 21, 2973−2979.

33. Yu, J.; Zhang, J.; Jaroniec, M. Preparation and Enhanced Visiblelight Photocatalytic H2-Production Activity of CdS quantum dotssensitized $Zn_{1-x}Cd_xS$ solid Solution. *Green Chem.* **2010**, 12, 1611−1614.
34. Argueta-Figueroa, L.; Morales-Luckie, R. A.; Scougall-Vilchis, R. J.; Olea-Mejía, O. F. Synthesis, Characterization and Antibacterial Activity of Copper, Nickel and Bimetallic Cu−Ni Nanoparticles for Potential use in Dental Materials. *Prog. Nat. Sci.* **2014**, 24, 321−328.
35. Velu, S.; Suzuki, K.; Vijayaraj, M.; Barman, S.; Gopinath, C. S. In Situ XPS Investigations of Cu1-xNixZnAl-Mixed Metal Oxide Catalysts used in the Oxidative Steam Reforming of Bio-Ethanol. *Appl. Catal. B* **2005**, 55, 287−299.
36. Gnanakumar, E. S.; Naik, J. M.; Manikandan, M.; Raja, T.; Gopinath, C. S. Role of Nanointerfaces in Cu- and Cu + Au-Based Near-Ambient-Temperature CO Oxidation Catalysts. *ChemCatChem* **2014**, 6, 3116−3124.
37. Roy, K.; Gopinath, C. S. UV Photoelectron Spectroscopy at Near Ambient Pressures: Mapping Valence Band Electronic Structure Changes from Cu to CuO. *Anal. Chem.* **2014**, 86, 3683−3687.
38. Gao, M. Y.; Yang, C.; Zhang, Q. B.; Yu, Y. W.; Hua, Y. X.; Li, Y.; Dong, P. Electrochemical fabrication of porous Ni-Cu alloy nanosheets with high catalytic activity for hydrogen evolution. *Electrochim. Acta* **2016**, 215, 609−616.
39. Deng, H.; Zhang, C.; Xie, Y.; Tumlin, T.; Giri, L.; Karna, S. P.; Lin, J. Laser Induced MoS2/Carbon Hybrids for Hydrogen Evolution Reaction Catalysts. *J. Mater. Chem. A* **2016**, 4, 6824−6830.
40. McCrory, C. C. L.; Jung, S.; Peters, J. C.; Jaramillo, T. F. Benchmarking heterogeneous electrocatalysts for the oxygen evolution reaction. *J. Am. Chem. Soc.* **2013**, 135, 16977−16987.



Chapter 4

Biomass Components to H_2 and Value-Added Products by Sunlight Driven Photocatalysis with Integrated Photocatalysts: Concurrent Utilisation of Electrons and Holes

Part of chapter 4 has been Published and details are[1]

Bajpai, H.; Chauhan, I.; Salgaonkar, K. N.; Mhamane, N. B.; Gopinath, C. S. Biomass Components toward H_2 and Value-Added Products by Sunlight-Driven Photocatalysis with Electronically Integrated $Au^{\delta-}$–TiO_2: Concurrent Utilization of Electrons and Holes. RSC Sustainability 2023

Chapter 4a: Biomass Components toward H_2 and Value-Added Products by Sunlight-Driven Photocatalysis with Electronically Integrated Auδ^-–TiO_2: Concurrent Utilization of Electrons and Holes

4.1 Introduction:

Fossil fuels for global energy are like glucose to the human body, which move the entire world but are also the main cause of CO_2 emission and hence contribute to climate change; however, unlike fossil fuels, the global energy demand can be at least partially fulfilled by renewable energy sources, e.g., solar and wind energy.[1] Hydrogen as a fuel is ideal with high gravimetric energy density (120 MJ kg^{-1}) compared to any other fossil fuel and produces no harmful by-products, except water, when subjected to combustion. However, in the present scenario, >95% of hydrogen is produced by fossil fuels, such as steam reforming of methane/naphtha, resulting in greenhouse gases as by-products and causing global warming. To deal with global warming and the future energy crisis while considering limited fossil fuel availability, combining solar energy and biomass/ biowaste can lead to sustainable and green energy by solar water splitting (SWS).[2–4] Can we also concurrently convert biomass to value-added products (VAPs), so that the whole process could be considered green? We are partially successful in our efforts to convert biomass to H_2 and VAPs. SWS at zero potential can fulfil the future energy demand; however, the main drawback is its low efficiency. It has been 51 years since the first report of SWS appeared in 1972, and we are still far away from finding an efficient photocatalytic system of hydrogen generation from SWS.[5] Certain factors hamper efficiency, such as (1) sluggish oxygen evolution kinetics, (2) high rate of electron–hole recombination, and (3) 3–5 orders of difference in time scales of photophysical and photochemical processes.[6–8] Since biomass components, such as cellulose and glucose, have very low economic value and glycerol is a by-product of biodiesel industries; it is worth employing them as feedstock and/or sacrificial agent. It is also known that the production of biodiesel and hence glycerol generation is also increasing every year by 10%. The conversion of glycerol into VAPs is a point of attraction in the present era, as its under-utilization is posing a threat to the biodiesel industry; glycerol availability at a very low price should be exploited commercially.[9–11] Glycerol could be used in photocatalytic water splitting not only to increase H_2 production but also as a sacrificial reagent to consume holes for partial oxidation to VAPs.[12–15] The same concept can be extended to other biomass components for their

conversion to VAPs. Plasmonic metals (Au, Ag, Cu) integrated with semiconductors are known to enhance charge separation and work as a photosensitizer due to the surface plasmon resonance (SPR) effect, via either the direct electron transfer or resonant energy transfer.[16–18]. Since TiO_2 is a well-known stable semiconductor, the large bandgap and high electron–hole recombination result in low efficiency. Plasmonic metals, especially gold shows significantly different absorption spectra with different particle sizes and morphologies and can be integrated with TiO_2 to utilize visible light in direct sunlight.[19–22] However, in SWS, the overall kinetics is mainly hindered due to the four electron O_2 evolution process, therefore, to enhance the overall kinetics, a sacrificial reagent,[23] such as methanol, triethanolamine, sulphide–sulphite is normally employed, which consumes holes rapidly and minimizes electron–hole recombination. From the term sacrificial, it is clear that these chemicals increase hydrogen production; however, can we prudently utilize holes, so that hole consumption leads to the conversion of sacrificial agents to VAPs too? Hence, a versatile catalyst is required to meet the dual purpose of photocatalytic H_2 production as well as oxidation of low-value sacrificial agent (biomass component) specifically into VAPs.[24–27] Zang et al.[28] employed Au/TiO_2 system for photo-reforming of ethanol; they obtained 7 mmol h^{-1} g^{-1}. of H_2 generation with formaldehyde and carbon dioxide as by-products but did not quantify the by-products. Wang et al.[29] attempted photocatalytic H_2 generation using Ag_2O/TiO_2 system, however, the reported H_2 yield was 0.3 mmol h^{-1} g^{-1}, and there was no VAP reported. For the Cu/TiO_2 system, several researchers have attempted photo-reforming of glycerol as a model sacrificial reagent. Trang et al.[30] reported 16 mmol h^{-1} g^{-1} H_2 yield under direct sunlight; however, there are no VAPs reported. With 1.6 mmol h^{-1} g^{-1} of H_2, Montini et al. produced CO_2, CH_4, glycolaldehyde, and di-hydroxy acetone by converting glycerol into VAPs.[31] In the majority of the literature, authors mostly paid attention to H_2 production and not much on the selectivity of the oxidation products; however, in the present study, we exploited the large-scale and concurrent utilization of electrons and holes toward hydrogen and VAPs, respectively. Herein we report the Au@TiO_2 integrated composite, prepared via the facile photo deposition method, by taking advantage of the positive zeta potential of TiO_2. Elemental mapping and XPS was employed to understand the distribution and electronic environment of the Au@TiO_2, respectively. The photocatalytic HER was carried out with Au@TiO_2 in aqueous glycerol, which also showed high glycerol conversion and selectively to

three major VAPs. HER studies were also carried out with glucose and cellulose. ^{1}H NMR was employed to identify and quantify the oxidation products.

4.2 UV-visible absorption:

By Au@TiO_2 UV-visible reflectance spectrum was measured and converted to absorption. UV-Vis spectra were recorded on all Au@TiO_2 photocatalysts and the results are shown in Fig. 4.1, along with parent TiO_2. SPR absorption features were observed on all Au@TiO_2 materials at 545 nm, irrespective of Au content.[32] While 0.1Au@TiO_2 showed low absorption intensity, the other two compositions show comparable absorption behaviour with an increase of SPR intensity, associated with higher absorption ability in the visible region compared to 0.1Au@TiO_2. It is also to be noted that the colour associated with the photocatalyst appeared to be increasingly becoming deep purple (inset image of Fig. 4.1). It is likely that the deep purple colour associated with 1Au@TiO_2 could be preventing more light absorption, compared to 0.5Au@TiO_2, which resulted in low photocatalytic hydrogen evolution, and the same is discussed in the later section.

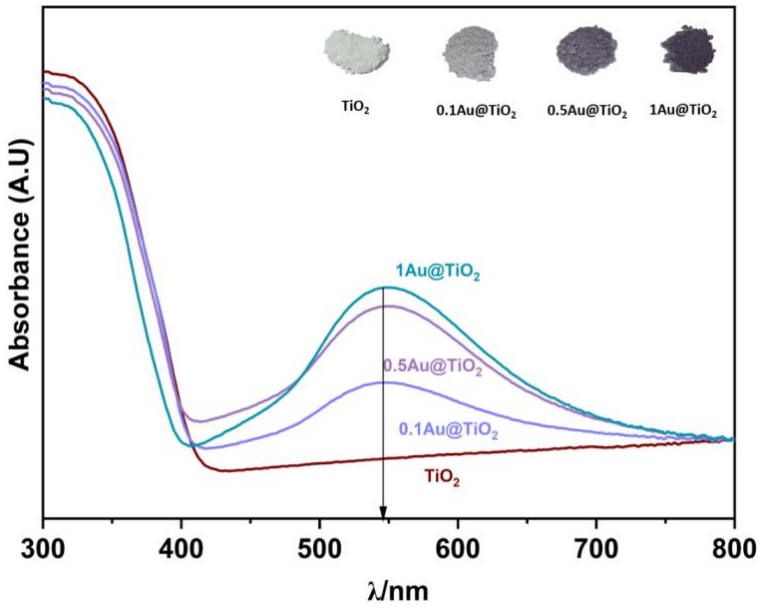


Figure 4.1. (a) UV-visible absorption spectra of TiO_2, 0.1Au@TiO_2, 0.5Au@TiO_2 and 1Au@TiO_2; inset shows the image of all photocatalysts. SPR feature was observed at 545 nm for all xAu@TiO_2.

4.3 Solar hydrogen production:

Solar hydrogen production was measured under one sun (100 mW cm^{-2}) and direct sunlight in Pune, Maharashtra, India, from February to May with an average light intensity of 60 mW cm^{-2}. It is to be noted that sunlight power fluctuates between 52 and 70 mW cm^{-2} depending on the time of the day, cloud cover, etc. However, for practical purposes, we considered 60 mW cm^{-2} as the average solar power. 60–65 mW cm^{-2} power was observed for at least 50% of the total reaction time. Solar hydrogen evolution measurement was carried out systematically under different reaction conditions. During hydrogen evolution measurement, 3 mg of the catalyst was used with 20 ml solution and kept under irradiation without stirring. It is to be noted that a uniform suspension, without settling of any particles, was observed with the catalyst in an aqueous glycerol solution, and hence the experiments were carried out without stirring (see photos shown in Fig. 4.2)



Figure 4.2. Digital photographs to show a uniform dispersion of the catalyst during reaction under direct sunlight.

In Fig. 4.3, different weight percent loadings of Au on TiO_2 were subjected to hydrogen evolution under direct sunlight with 0.6 M glycerol as a sacrificial reagent. TiO_2 gave 0.86 mmol h^{-1} g^{-1} of hydrogen, after loading with Au (x$Au@TiO_2$), and absorption of composite shifted to the visible light range due to the SPR effect of Au, as shown in UV-Vis absorption spectra (Fig. 4.1), indicating the strong absorption at 545 nm resulting in higher H_2 production. With 0.1 wt% of Au loading, hydrogen evolution was observed to be 7.4 mmol h^{-1} g^{-1}, which is 8-fold higher than that of bare TiO_2. While increasing the weight% of Au from 0.1 to 1, 0.5% exhibited the highest hydrogen production (18 mmol h^{-1} g^{-1}) than the 1% Au-containing (16.5 mmol h^{-1} g^{-1}) composite under direct sunlight. It is to be noted that comparable SPR feature

intensity was observed for 0.5 and 1 wt% of Au@TiO_2, reflecting a similar observation as in solar hydrogen production. These observations hint that the Au-dispersion remains the same for 0.5 and 1 wt% of Au. In fact, a marginally lower H_2 yield was observed with 1 wt% Au, indicating that there could be other changes. This is supported by a significant change observed with Au 4f binding energy and the same is explained later in the XPS section.

Some of the top results reported for H_2 production with Au and Cu-based systems from literature are compiled in Table 4.1. Results obtained from the current studies are superior to the results reported earlier with hydrogen and VAPs production, as shown in Table 4.1; also, direct sunlight irradiation shows significantly better results than with one sun

Table4.1. Top H_2 production results reported in the literature for Au@TiO_2 along with reaction conditions.

Catalyst	Light source and power	H_2 (mmol/h.g)	Reaction conditions	VAPs	Ref.
1.5 % Au/ TiO_2 P25	UV light	28.3	10% glycerol in water (6.5 mg in 20 ml solution)	NA	11
1% Au/TiO_2 P25	One sun (UV -Vis)	0.307	Water: methanol= 3:1 (20 mg catalyst in 40 ml solution)	NA	16
5%Au/TiO_2 hierarchical spheres	UV-Vis (100 mW/cm^2)	8.06	30 vol% methanol in water (50 mg catalyst in 100 ml solution)	NA	36
0.5% Au/TiO_2 nanorods	UV light	29	10 % glycerol in water (6.5 mg catalyst in 20 ml solution)	NA	37
2%Au/TiO_2	UV light	30.3	10 % glycerol in water (6.5 mg catalyst in 20 ml solution)	NA	38
0.3% AuTiO_2	Simulated light (21.1 mW/cm^2)	0.2	1% TEOA with water (250 mg with continuous flow of Nitrogen)	NA	39
1%Au/TiO_2 anatase	Solar Lamp (10.7 mW/cm^2)	2.55	5% glycerol in water (50 mg in 50 ml solution	NA	40
$Cu_2O/Bi_2O_3/TiO_2$	UV-Vis	6.2	5% Glycerol	NA	41
Cu_2O/TiO_2	400 W metal Halide Lamp	4.7	5 v/v% glycerol/water (100 mg catalyst in 200 ml) with pH 10	NA	42
Cu_2O/TiO_2	SB-110P/F lamp (100 W), 365 nm	15.3	5 v/v% glycerol/water (2.5 mg catalyst in 25 ml)	NA	43
CuOx–PtO_2/TiO_2	300 W Xenon lamp	1.3	10% glycerol (50 mg catalyst in 100 ml)	NA	44
3% Cu/TiO_2	100 mW/ cm^2	0.05	1 % acetic acid (25 mg in 25 ml)	CH_4, CO_2	45
0.5%Au@TiO_2	One Sun condition (100 mW/cm^2)	15	5% (0.6 M) glycerol in water (3 mg in 20 ml)	Dihydroxyacetone, Glycolaldehyde, Formic acid	Current work
0.5%Au@TiO_2	Direct Sunlight (60 mW/cm^2)	18	5% (0.6 M) glycerol in water (3 mg in 20 ml)	Dihydroxyacetone, Glycolaldehyde, Formic acid	Current work

condition. Reported higher hydrogen production, than that from this study, is invariably observed under UV irradiation; needless to say, that significant UV light absorption by titania too contributes to the total activity. While glycerol was used as a sacrificial agent by a few groups for hydrogen generation, no other VAPs of glycerol were observed or reported in the literature. This factor makes the current work far superior in terms of the concurrent utilization of holes and electron charge carriers for versatile light energy to chemical energy conversion to H_2 as well as VAPs.

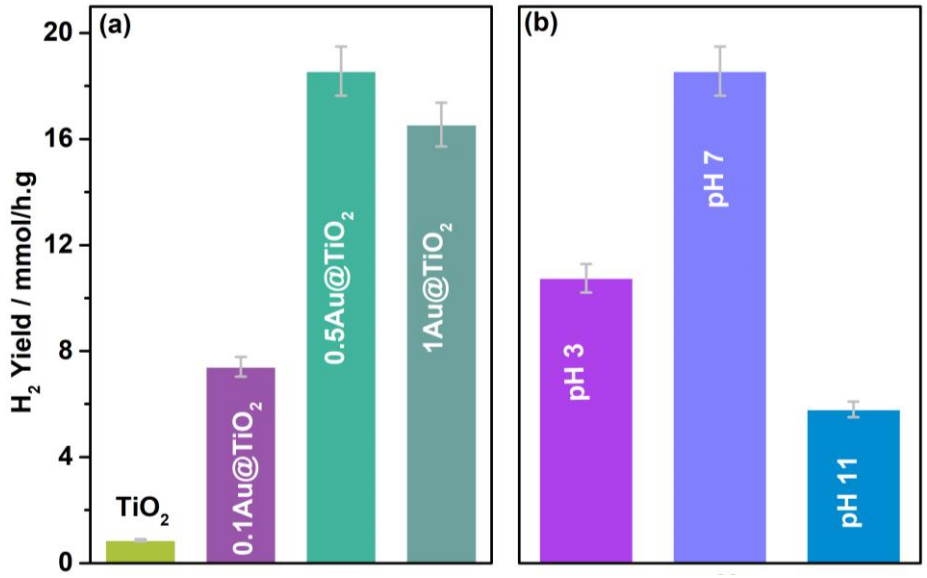


Figure 4.3 (a) Photocatalytic hydrogen yield observed for (a) different wt. % of Au on TiO_2 and (b) 0.5Au@TiO_2 at different pH conditions; to maintain the pH, 0.01 M HCl and NaOH were used as acid and base, respectively. 5% glycerol was used as sacrificial reagent under direct sunlight with an average light intensity of 60 mW/cm^2.

As shown in the structural characterization studies in the following sections, the highest hydrogen generation activity observed with 0.5Au@TiO_2 is attributed to atom-like sub-nanometre Au cluster dispersion over TiO_2, as discussed in the later sections. Furthermore, photocatalytic hydrogen evolution measurements at different pH values were carried out with 0.5Au@TiO_2 catalyst with 5% glycerol under direct sunlight, and the results are shown in Fig. 4.3. The pH change was achieved with the required amount of dilute (0.01 M) HCl and NaOH under acidic and alkaline conditions, respectively, and pH change was ensured using a pH meter (Mettler Toledo seven compact). Interestingly and critically, the highest amount of hydrogen was observed at neutral pH; hydrogen production was found to

decrease on either increasing or decreasing the pH to basic or acidic conditions. In the acidic pH, zeta potential is close to the zero-point charge, which results in significant agglomeration of TiO_2 particles and hence a decrease in photocatalytic activity was observed, however, under basic pH conditions, due to the abundantly-available hydroxyl groups, the dissociation of Ti–OH is decreased drastically. The zeta potentials measured for all three pH conditions are shown in Fig. 4.4, fully supporting this result. These factors are known to hinder the photocatalytic activity, and it was suggested from the kinetic model by Estahbanati et al.[46]

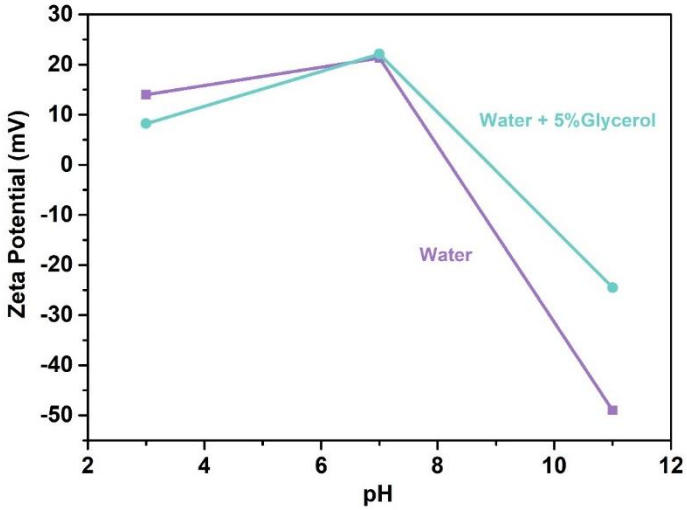


Figure 4.4. Zeta potential of 0.5Au@TiO_2 in water and water+glycerol solution at different pH. Zeta potential at acidic pH is closer to zero compared to neutral, which is more positive and also in agreement with the high photocatalytic activity reported in the main manuscript at neutral pH, than acidic or basic pH. Highly hydroxylated surface under basic conditions makes the zeta potential to be highly negative

At neutral pH (pH = 7) good dispersion of the catalyst in the water/glycerol was observed. Even after a few days, we did not observe any settling of the catalyst (Fig. 4.2) but a highly-dispersed uniform suspension was maintained, which is also an interesting observation in the present work. In general, with powdered catalyst, due to the stirring, significant scattering of the light occurs and the same reduces the light absorption by the catalyst; if there is no stirring, the catalyst would settle at the bottom of the reactor and also reduces the photoactivity of the composite; this problem could be overcome by making the catalyst in a thin film form (as in Si PV) or should be dispersed in the solution throughout the reaction.[6,47] Three different glycerol concentrations (1, 5, and 10%) were employed to

understand the effect of sacrificial reagent concentration; activity was measured periodically with 0.5Au@TiO_2 in 20 ml aqueous glycerol solution under one sun condition and the results are shown in Fig. 4.5. An interesting trend in results was observed, and the following points deserved to be highlighted. (1) 5% (0.6 M) glycerol containing aqueous solution showed a constant H_2 yield of 15 mmol h^{-1} g^{-1} as a function of irradiation time; among the three different glycerol concentrations (1, 5, and 10%), indeed, 5% showed the best performance. (2) While 10% (1.4 M) glycerol concentration also showed a constant H_2 yield of 11 mmol h^{-1} g^{-1}, it is lower than that at 5% glycerol concentration. (3) In contrast to the above two points, 1% (0.14 M) glycerol-containing solution showed the lowest H_2 yield, although initially, it showed 7 mmol h^{-1} g^{-1} yield, H_2 yield reaches a plateau at later hours. The influence of the sacrificial agent concentration on hydrogen generation has been addressed significantly in the literature.[33–35] Dependence of the hydrogen generation has been demonstrated with different concentrations of the reactant. Beyond a threshold concentration of the sacrificial agent, active sites are saturated with those molecules and the same decreases the

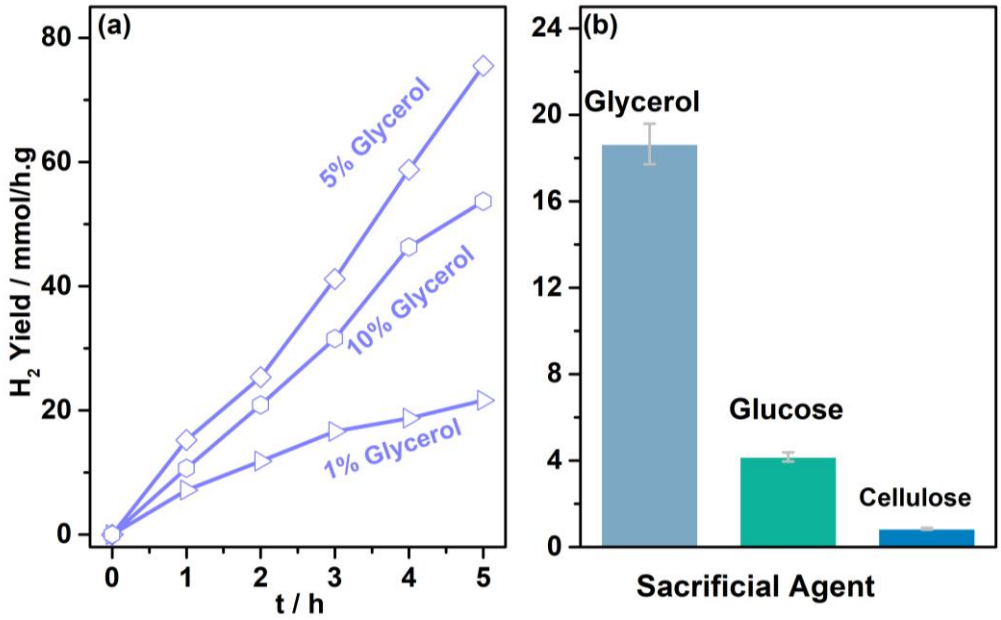


Figure 4.5. (a) photocatalytic hydrogen yield observed with 0.5 wt % of Au over TiO_2 with different concentrations of glycerol under one sun condition (100 mW/cm^2, AM 1.5 filter). (b) Photocatalytic hydrogen yield observed with different biomass components as sacrificial reagents using 0.5 wt% Au on TiO_2 under direct sunlight with an average intensity of 60 mW/cm_2.

photoactivity. In the present case, the viscosity factor of glycerol also adds to the diffusion issues, which decreases the rate at 10% glycerol concentrations. Generally, the observed results indicated that an optimum glycerol concentration was required to achieve the best performance in the present experiments; except hydrogen, no other gaseous product was observed.

For the oxidation product of the glycerol, due to the high concentration of glycerol employed for the results shown in Fig. 4.3 and 4.5, it was challenging to identify and quantify the product by NMR. Another set of study was carried out to explore the products of glycerol oxidation at low glycerol concentrations, which will be discussed later. In addition to glycerol, glucose, and cellulose were also evaluated as sacrificial agents; it is known that they all have similar building blocks, except for chain lengths. The average H_2 yield obtained is shown in Fig. 4.5b. 20 ml of 0.35 M glucose solution was employed with 3 mg of the catalyst (0.5Au@TiO_2); this is mainly to maintain the similar number of carbon atoms as that of 5% glycerol solution. 4.1 mmol h^{-1} g^{-1} H_2 yield was observed under direct sunlight with glucose, while glycerol solution exhibited 18 mmol h^{-1} g^{-1}. A four-fold decrease in H_2 yield with glucose is attributed primarily to the 6-carbon unit; more difficult C–C cleavage is the leading/silent reaction also occurs, which consumes a significant number of electrons and protons and slows down the overall kinetics. However, the result was still significant, and, in fact, it opens a new window to the utilization of biomass components for photocatalytic hydrogen production. One more reason for the lower activity with glucose, compared to that with glycerol as a sacrificial reagent, is due to the settling of the catalyst in the bottom of the RB flask; due to this, the light absorption capacity decreases and results in lower photoactivity. In the case of cellulose, 200 mg of cellulose was taken in 20 ml water with 3 mg catalyst and subjected to direct sunlight irradiation for 5 h. Since cellulose is not soluble in water, activity decreased drastically to 0.8 mmol h^{-1} g^{-1}. To improve and produce an efficient sacrificial reagent for photocatalytic hydrogen production, the solubility of cellulose needs to be increased but without employing harsh basic or acidic conditions. Dispersed cellulose particles in the solution would tend to scatter the light, rather than light absorption, which also results in lower photoactivity.[6,48–50] Ideally a systematic approach from waste biomass components to hydrogen and any VAP would be more appealing.[51,52] Our efforts to identify any oxidation products of glycerol from the results shown in Fig. 4.3 and 4.5 was not successful, due to high

glycerol and low catalyst content. Hence the conditions were modified to enhance the oxidized product concentration and the observed results are shown and discussed in the following sections.

4.4 Glycerol oxidation by direct solar photocatalysis:

Glycerol oxidation products were measured from systematic photocatalytic experiments. 5 mg of 0.5Au@TiO_2 with 5 ml of 0.05 M glycerol was used for photocatalytic glycerol oxidation. These experiments were carried out in aerobic (purged with O_2), anaerobic (purged with N_2), and dry air conditions. Fig. 4.6 shows the data on photocatalytic glycerol oxidation carried out under the three conditions mentioned above, and the products observed along with hydrogen under (a) direct sunlight, and (b) under one sun condition. Three major liquid products, namely, glycolaldehyde, dihydroxyacetone, and formic acid, were observed under both reaction conditions. In anaerobic conditions under direct sunlight, 0.32, 0.12, and 0.17 M g^{-1} of glycolaldehyde, dihydroxyacetone, and formic acid were observed, respectively, in 5 h; along with the liquid products, 32 mmol g^{-1} of hydrogen was observed in 5 h reaction time.

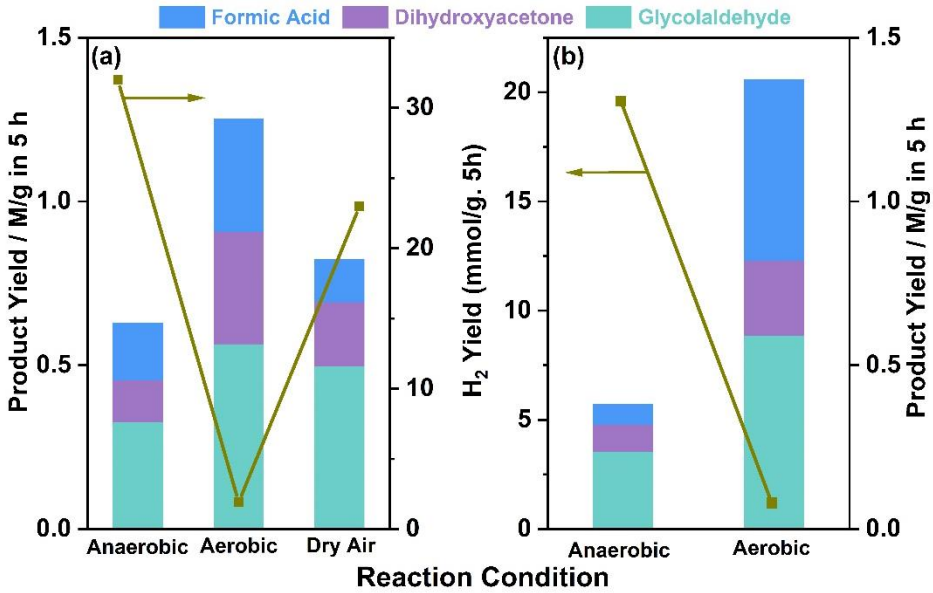


Figure 4.6 Photocatalytic glycerol oxidation with 0.5%Au@TiO_2 under, (a) direct sunlight with an average intensity of 60 mW/cm^2, and (b) one sun condition (100 mW/cm^2). All products concentration is for five hours of reaction time in both panels.

When purging was carried out using dry air, the amount of oxidation product was also found to be increased; 0.49, 0.19, 0.13 M g^{-1} of glycolaldehyde, dihydroxyacetone, and formic acid, respectively, were observed along with 23 mmol g^{-1} hydrogen in 5 h; 2.8 mmol g^{-1} of CO_2 was also observed in the gaseous products. In the case of the aerobic condition, the overall product formation rate increased twice that of anaerobic conditions, along with glycerol conversion. Significant overoxidation to CO_2 (7.5 mmol g^{-1}) was also observed, and hydrogen generation decreased to 1.9 mmol g^{-1}. This indicates that in the presence of oxygen, oxidation of glycerol also occurs instead of water reduction. Expectedly, oxygen helps in the oxidation of the glycerol, through superoxo/peroxo radicals by electron consumption or the oxygen reduction reaction, this in turn decreases the hydrogen production. Under one sun condition, similar liquid, and gaseous products were observed with the same trend. However, overoxidation was comparatively lower with a smaller amount of CO_2 production (5.3 mmol g^{-1}) under one sun condition than under direct sunlight.

An interesting observation to be noted is the significantly large amount of formic acid and smaller CO_2 under one sun irradiation and aerobic conditions, compared to direct sunlight irradiation. A careful comparison of both results revealed that while glycolaldehyde was observed at the same level, formic acid was observed to increase at the cost of dihydroxyacetone under one sun condition. It is also to be noted that the temperature of the solution and the catalyst increases to around 60 ^oC under direct sunlight, while the same was observed to be 47 ^oC under one sun condition, carried out under laboratory ambient conditions. Hence, the overall increase in the reaction rate in direct sunlight may be partly attributed to an enhancement in temperature. Controlled experiments were also carried out at 60 ^oC under one sun condition to ensure the temperature effect in direct sunlight. The results observed at 60 ^oC are equivalent to those of sunlight conditions within the experimental accuracy. This further confirmed the influence of temperature under both natural and simulated light conditions. More power (100 mW cm^{-2}) under one sun condition leads to the decomposition of dihydroxyacetone to formic acid. More experiments under a controlled atmosphere are required to ascertain the extent of the influence of the temperature and illumination power.

In addition, the advantage of higher temperature and lower light power with direct sunlight may be utilized in a prudent manner. These experiments suggest that with regulated

oxygen content, aqueous glycerol can be a very efficient reactant to generate VAPs along with hydrogen. A simple back calculation by accounting for all the carbon-containing products, including CO_2, originating from the oxidation of glycerol, leads to glycerol conversion levels between 6 and 13% in 5 h with 52% selectivity for glycolaldehyde under anaerobic conditions. High TON values of 1280 and 920 were observed with 0.5Au@TiO_2 for hydrogen under anaerobic and dry air conditions, respectively, while high TON values (68–113) were observed for VAPs under aerobic conditions (Tables 4a.2 to 4a.4).

Table 4.2. Product analysis of glycerol oxidation in **anaerobic condition**.

Product	Concentration (M/g. 5h)	Yield (mmol/g.5h)	Selectivity (%)[#]	Selectivity with respect to no of Carbon (%)	TON (Au loading)	TOF (Au loading)/h
Glycolaldehyde	0.32	1.6	52	54	64	12.8
Dihydroxyacetone	0.12	0.6	20	31	24	4.8
Formic Acid	0.17	0.85	28	15	34	6.8
CO_2	ND	ND	ND	ND	ND	ND
H_2	NA	32 mmol/g.	NA	NA	1280	256

Note: Glycerol Conversion is 6% , [#]: Selectivity among the organic products

Table 4.3. Product analysis of glycerol oxidation in **aerobic condition**.

Product	Concentration (M/g. 5h)	Yield (mmol/g. 5h)	Selectivity (%)[#]	Selectivity with respect to no of Carbon (%)	TON (Au loading)	TOF (Au loading)/h
Glycolaldehyde	0.56	2.82	20	29	112.8	22.56
Dihydroxyacetone	0.34	1.7	13	26	68	13.6
Formic Acid	0.34	1.7	13	8	68	13.6
CO_2	NA	7.5	54	37	300	60
H_2	NA	1.9	NA	NA	76	15.2

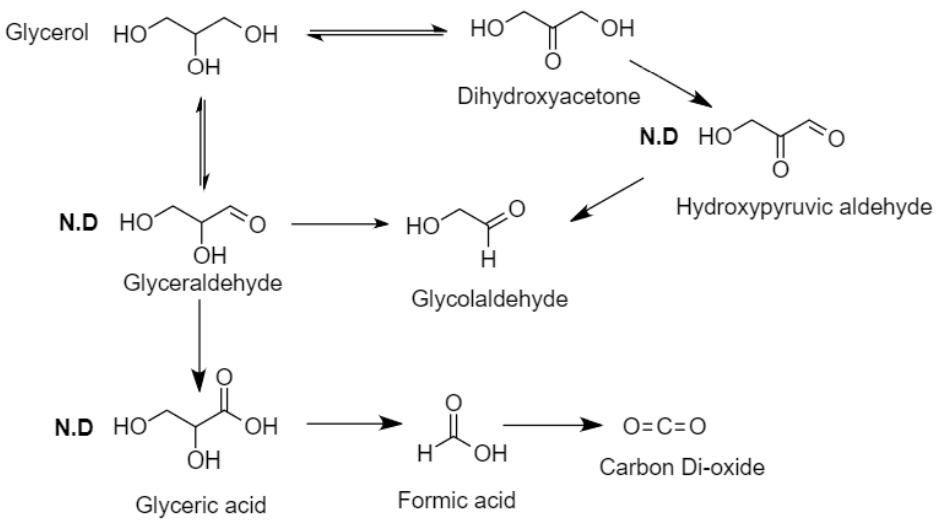
Note: Glycerol Conversion is 6% , [#]: Selectivity among the organic products

Table 4.4 Product analysis of glycerol oxidation by using **dry air**

Product	Concentration (M/g. 5h)	Yield (mmol/g. 5h)	Selectivity (%)[#]	Selectivity with respect to no of Carbon (%)	TON (Au loading)	TOF (Au loading)/h
Glycolaldehyde	0.49	2.4	35	43	96	19.2
Dihydroxyacetone	0.19	0.95	14	26	38	7.6
Formic Acid	0.13	0.65	10	6	5.2	1
CO_2	NA	2.8	41	25	112	22.4
H_2	NA	23	NA	NA	920	184

Note: Glycerol Conversion is 6%, [#]: Selectivity among the organic products

A marginal decrease in hydrogen production by 1Au@TiO_2 than that by 0.5Au@TiO_2 suggested the higher activity associated with Au-clusters with the latter. We attribute this to the high dispersion of gold and electronic integration with TiO_2 with the latter. By changing the batch to a continuous flow type with controlled oxygen or dry air, the higher activity would be possible by minimizing CO_2. More experiments in this direction are desired. The present results also demonstrate the cleavage of C–C bonds occurring from glycerol all the way to formic acid and then to CO_2, and Fig. 4.7 shows a plausible pathway for glycerol oxidation to VAPs. Hence, there are possibilities existing to one-tune the reaction conditions to maximize the value-added liquid oxidation products with hydrogen production.



N.D: Not Detected

Figure 4.7. Plausible reaction pathway for glycerol oxidation to VAPs over Au@TiO_2 composites

As formic acid is expected to undergo fast oxidation to CO_2, a product separation stage and recirculation of unreacted glycerol would be a good idea for achieving higher glycerol conversion to the same VAPs.

4.5 Structural analysis and elemental mapping:

XRD, HRTEM, and elemental mapping methods were employed to understand the structure and morphology of the photocatalysts. XRD results of TiO_2 and xAu@TiO_2 are shown in Fig. 4.8. As expected, anatase and rutile features were observed in both photocatalysts.

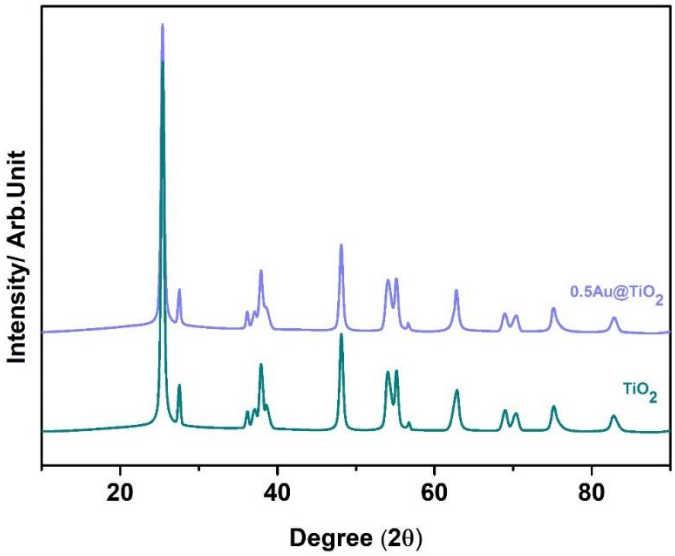


Figure 4.8. X-ray diffraction pattern of TiO_2 and x$Au@TiO_2$ (x = 0.1, 0.5 and 1). Same features are observed indicates with all of the catalysts underscore a possible fine-distribution of atom-like or very small size gold clusters. STEM results shown in Figure 4.10 fully support this conclusion.

However, after gold integration with TiO_2, no difference is discernible in the XRD pattern up to 1 wt% of Au integrated TiO_2 compared to virgin TiO_2; indeed, 0.5 and 1 wt% of Au loading is too small and this could be one reason for the absence of any gold features in the XRD results. However, it rules out the clustering of gold atoms to big particle size(s). This naturally leads to the question of the status of gold in x$Au@TiO_2$ the photocatalysts.

To understand the structural and/or integration aspects of Au and its distribution over TiO_2, HRTEM analysis was carried out and the representative results are shown in Fig. 4.9. TiO_2 particles with an average size of 20 ± 1 nm were observed, which is typical for P25 TiO_2. However, after careful investigations of multiple batches of 0.5$Au@TiO_2$, we did not observe any Au particle over TiO_2. Nonetheless, it is essential to understand the role of gold to understand the SPR features at 545 nm, as shown in Fig. 4.1, and very high photocatalytic activity was observed for hydrogen generation and glycerol oxidation under solar irradiation conditions. To investigate this phenomenon, we carried out elemental mapping, and the results are shown in Fig. 4.10. Elemental mapping gives an idea about the small Au-cluster formation on TiO_2, and demonstrates the homogeneous distribution of Au on TiO_2 particles. Ti and O mapping shown in Fig. 4.10 panels follow the expected trend In their distribution. However, in the case of Au (yellow), a very one and homogeneous dispersion of Au on TiO_2

particles was observed. It is to be noted that the atomic weight of gold is more than four times that of titanium, and gold content in terms of the atomic percent is about 0.12–0.14% in 0.5Au@TiO_2. Although many earlier studies have reported Au@TiO_2 such a □ne distribution has not been shown; uniform distribution is shown, probably, for the first time, with a photo deposition method. It is to be noted that the zeta potential of TiO_2 P25 is positive, and hence negatively charged metal-ion precursor could be loaded over TiO_2. During nitrogen purging in the dark, the negative charge $[AuCl4]^{-1}$ is expected to be uniformly deposited over TiO_2 upon UV irradiation, and $[AuCl4]^{-1}$ gets reduced to Au with uniform dispersion.[53] We also speculate the oxygen vacancies on the titania surface could be a possible driving force for a very high distribution. Under irradiation conditions, pre-deposited gold precursor ions get homogenously reduced over TiO_2. Indeed, this leads to a

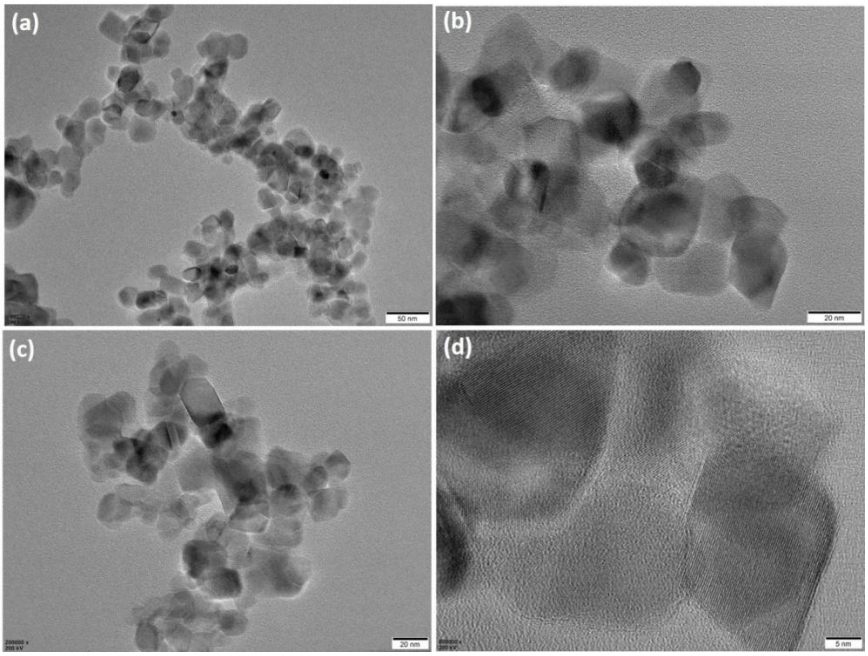


Figure 4.9. HRTEM images of 0.5Au@TiO_2. No gold feature was observed in HRTEM indicates the size of gold to be atom or atom-like clusters, scale of panel a (50 nm), Panel b, c (20 nm) and panel c (5 nm).

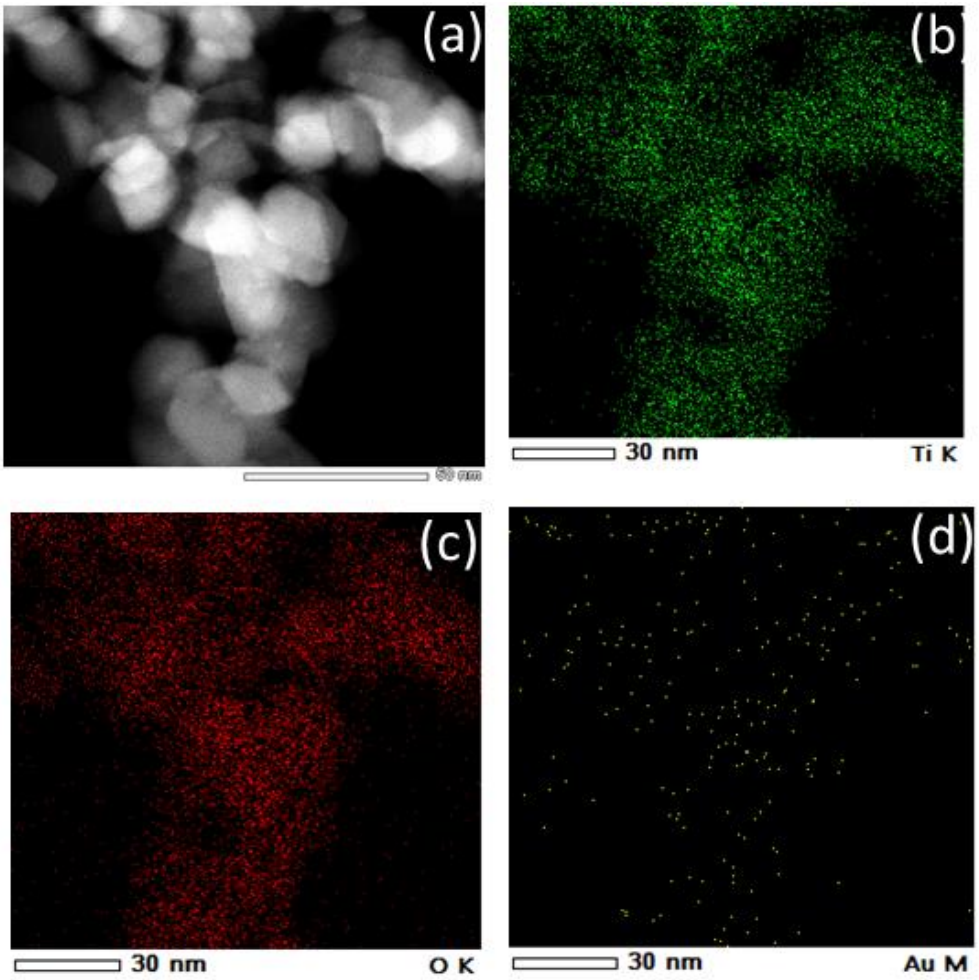


Figure 4.10: STEM image of 0.5%Au@TiO_2 and corresponding elemental distribution for Ti (green), Au (yellow), and oxygen (red) at scale bar of (a-d) 30 nm. Very uniform distribution of Au over TiO_2 nanoparticle could be observed at high resolution.

highly integrated xAu@TiO_2. The lower the amount of gold deposited, the better the distribution observed. The low atom percent of Au and its high dispersion on titania are the reasons that its features could not be detected in XRD, while UV-Vis absorption shows the characteristic SPR feature. The specific surface area of Au on TiO_2 is likely to be higher, which results in high hydrogen production as well as glycerol conversion to VAPs. A number of earlier studies indicated the electronic and structural integration of the catalyst components leading to a facile charge transfer between semiconductors and the metal towards efficient photocatalytic activity, which was also analyzed by XPS and discussed in the next section.

4.6 X-ray photoelectron spectroscopy:

XPS provides information on the electronic interaction between various components as well as the surface composition of composite materials. To understand the electronic interaction between TiO_2 and Au, XPS studies were carried out and the results are shown in Fig. 4.11. The deconvolution of Ti 2p core level shows that Ti was present in two different states for Ti^{3+} (457.45 ± 0.05 eV) and Ti4+(458.6 ± 0.05 eV); however, Ti^{4+} was predominantly available (92%), while only 8% of Ti3+ was available on the virgin TiO_2 surface.54 However, with 0.5Au@TiO_2, there was a decrease in the Ti^{3+} content by 50% (to 4%) as that of pristine TiO_2, and this is attributed to the deposition/integration of gold with those sites. As metal atoms are known to be electrophilic, there is a driving force to deposit gold in Ti^{3+} or oxygen vacancy sites. This integration also leads to charge transfer from TiO_2 to Au and makes the composite electronically integrated. In Fig. 4.11b, O 1s spectra of TiO_2 and 0.5Au@TiO_2 are shown. Three different oxygen species observed at 529.75 ± 0.05 eV (red trace), 530.45 ± 0.05 eV (blue trace), ~531.8 eV (green trace) are attributed to lattice oxygen of TiO_2, oxygen associated with $Ti^{3+,}$ and the hydroxyl group, respectively. While there was no change in the hydroxyl group intensity was observed before and after Au-integration, the percentage of oxygen associated with Ti^{3+} decreased marginally in the O 1s spectra. This reiterates that gold cluster deposition occurs selectively at the defect sites.

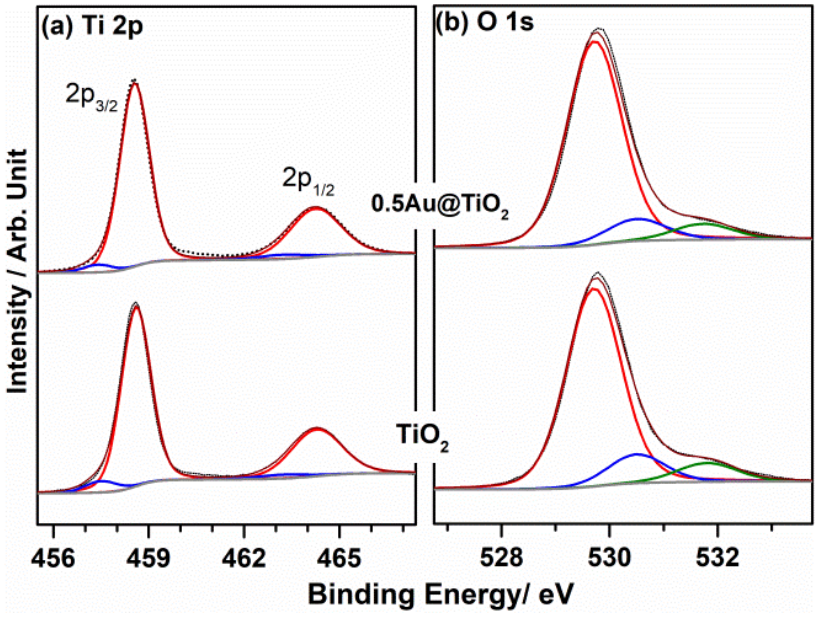


Figure 4.11. (a) Ti 2p, and (b) O 1s core level spectra of TiO_2P25 and 0.5Au@TiO_2. Ti^{3+} and Ti^{4+} are given in blue and red traces, respectively. Red, blue and green traces in O 1s corresponds to TiO_2 lattice oxygen, O-associated with Ti^{3+} and OH group, respectively.

Fig. 4.12 shows the Au 4f spectrum of 0.5Au@TiO_2. Generally, bulk and metallic gold species appear at 84 ± 0.1 eV for the Au 4f7/2 core level in the XPS spectrum.[54–56] However, interestingly, there was a large negative shift of 0.9 eV was observed with the Au 4f core levels of 0.5Au@TiO_2. Almost 1 eV shift to low BE suggests a large charge transfer from titania to gold. This observation could be possibly due to a combination of the following reasons. (a) As mentioned in the discussion of Ti 2p and O 1s, Au species gets integrated into the defect site of TiO_2, which is fully supported by the observation of a 50% decrease in Ti^{3+} content in 0.5Au@TiO_2, compared to that in virgin TiO_2. These XPS results also point toward an electronic integration between Au and TiO_2, and helping to create metal-semiconductor nano-Schottky

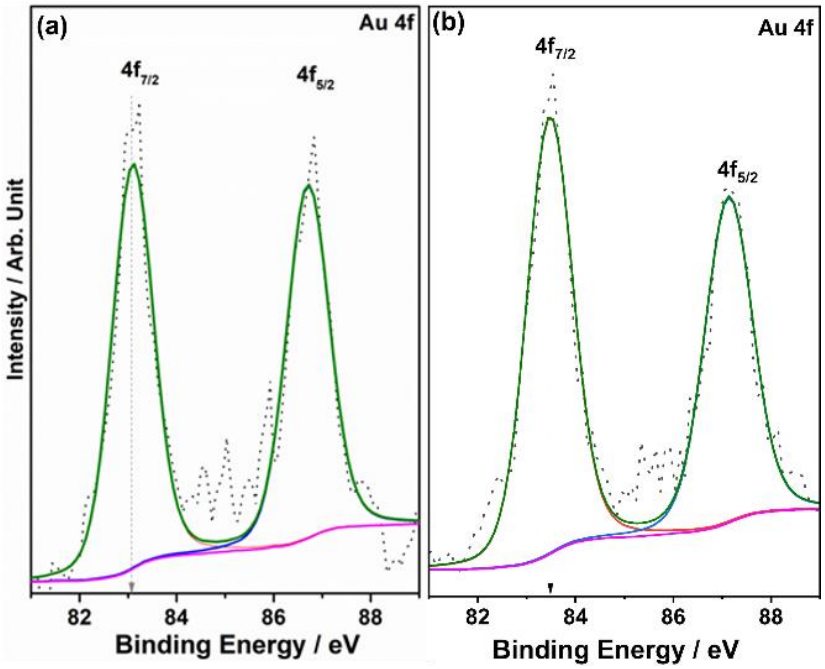


Figure 4.12. XPS spectra for Au 4f core levels for (a) 0.5Au@TiO_2 and (b) 1Au@TiO_2. Compared to the standard metallic gold 4f7/2 feature at 84.0 eV, appearance of the same at 83.1 and 83.4 eV for 0.5Au@TiO_2 and 1Au@TiO_2, respectively, underscores the difference in electronic integration between Au and TiO_2, and the extent of anionic character of gold.

or heterojunctions. Such junctions are essential for electron–hole pair separation, which in turn increase the utilization of the charge carriers through redox reactions. (b) Small clusters of gold are expected to behave differently than nanoclusters or bulk gold. Elemental mapping indicates the extensive distribution of small gold clusters. Due to the small size of such clusters, gold is likely deposited uniformly on the interior and exterior surfaces of the pores of titania. (c) Small clusters are expected to be electrophilic and prefer to bind at sites richer

in electrons. This leads to a preferential interaction between defect sites of titania and small gold clusters. Combining the above factors makes the gold cluster behave more like anionic gold. However, a significant reduction in BE shift was observed with 1Au@TiO_2 (0.6 eV at 83.4 eV compared to that with metallic gold at 84 eV) and shows a reduction in anionic character compared to that with 0.5Au@TiO_2 (Fig. 4.12b). Although the gold content was doubled, hydrogen generation was observed to be marginally lower, suggesting that the state of gold does matter for the best performance. This synergy between the metal and semiconductor helps toward the charge separation, which in turn helps high photocatalytic glycerol oxidation to VAPS and hydrogen evolution.

4.7 Mechanism:

The integration of the plasmonic metal with semiconductors can lead to efficient photocatalytic activity. Based on the experimental data obtained from various studies and discussed in the earlier sections for Au@TiO_2, a possible reaction mechanism is proposed in Fig. 13. TiO_2 exhibits a bandgap of 3.2 eV which absorb only 4–5% of the UV light present in

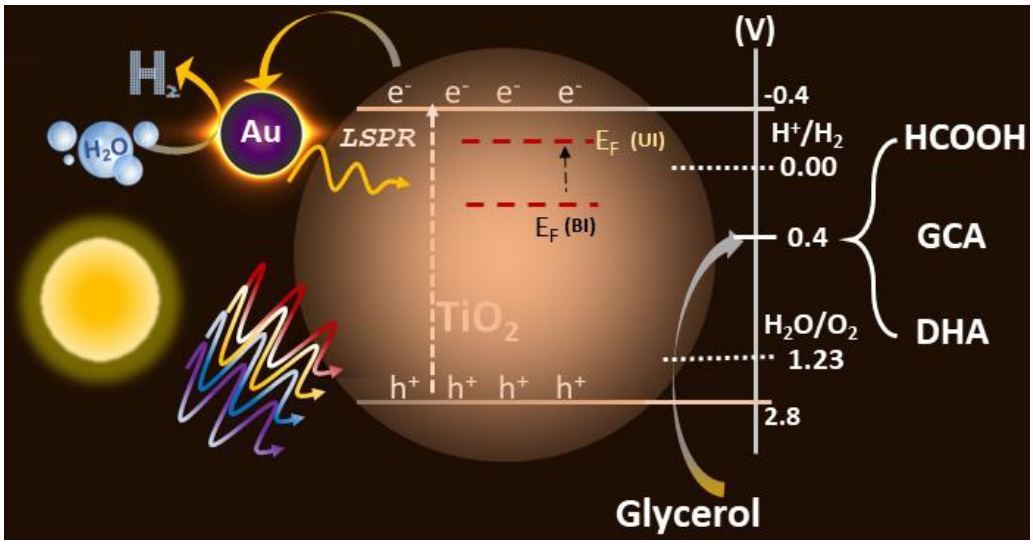


Figure 4.13. Possible mechanism for plasmon-induced Au@TiO_2 toward photocatalytic hydrogen generation and glycerol oxidation towards the value-added products. EF levels shown are indicative and not to the scale; however, an upward shift under illumination occurs due to electron storage in gold clusters. Abbreviations: EF(UI) Fermi level under illumination, EF(BI) Fermi level before illumination or fresh catalyst, GCA (glycolaldehyde), DHA (Dihydroxyacetone).

the solar spectrum, the electron and hole separation is, indeed, one of the main issues for the low efficiency of photocatalytic activity with virgin TiO_2. Small and highly-dispersed gold cluster integration enhanced its light absorption capacity to the visible region, amplifying its electron–hole generation via the LSPR effect of gold particles, which is evident from the UV-Vis spectra. Also, the electronically integrated anionic Au-clusters with TiO_2 suggest a negative shift of the Fermi level of the composite, which is more facile for charge separation and enhances hydrogen generation 20 times, compared to that in virgin TiO_2. [57,58]

Photocatalysis involves both photophysical and photochemical processes. It is well-known that the time scale of photophysical (# ns) and photochemical ($ ms) processes are very different and it is necessary to address this issue.6 By selectively storing electrons in gold, utilization of holes, which are also known as the minority charge carriers, for oxidation increases to a large extent. Basically, the charge separation enhances both the reduction and oxidation aspects of the photocatalysis and hence an overall increase in the activity is observed. Further, the integration of Au helps in the photophysical process via the LSPR effect and as an electron sink for efficient charge separation, this leads to an enhanced redox process and underscores the dual functional character of the gold clusters with light absorption as well as catalysis. XPS results show that gold is present as anionic gold, which also proves the electron transfer is occurring from TiO_2 to gold, where water reduction is taking place. However, the oxidation process occurs via holes present in the valence band of TiO_2, from glycerol to VAPs (Fig. 4.7). Glycerol and glucose require low oxidation potential (0.4 V vs. RHE with Pt/C and 0.4 vs. RHE with Au, respectively) than water,[59,60] while VB of TiO_2 is around 2.7 V with high oxidation potential. The potential required for both reduction and oxidation is met with the above arrangement, which helps in the large utilization of holes, resulting in low charge recombination and high photocatalytic activity. The large dispersion of atom-like gold clusters observed in STEM results (Fig. 4.10) supports the effective charge carrier separation as well as its utilization. Further, by depositing gold at the oxygen vacancy sites, not only electronic integration was achieved, but charge recombination was also minimized. These factors increased the charge utilization and improved the redox activity towards H_2 and VAP formation. A significantly high formic acid formation underscores the high potential associated with holes and helps achieve C–C cleavage of glycerol components. This particular aspect should be utilized to tackle other biomass components too.

4.8 Conclusions:

We synthesized xAu@TiO_2 (x = 0.1, 0.5, and 1 wt%) composite via facile photo-deposition, with small Au clusters uniformly deposited and electronically integrated on TiO_2. 0.5Au@TiO_2 exhibits maximum hydrogen yield in direct sunlight with glycerol as a sacrificial agent compared to other biomass components. This study focused on two aspects; (1) novel integration of gold with TiO_2 and its large distribution due to small clusters, which increases the effective charge transfer between semiconductor to metal and reduces the electron–hole recombination. (2) Glycerol is not only a promising sacrificial reagent but could be oxidized to value-added products under aerobic conditions. This aspect helps in the utilization of photogenerated electrons and holes to hydrogen and value-added products of glycerol, respectively. Glucose and cellulose were also shown to exhibit hydrogen generation activity, and it is suggested to explore them more with different catalyst systems to find a potential solution for hydrogen and value-added products. We believe the low activity with glucose/ cellulose, compared to glycerol, is due to the consumption of charge carriers in breaking C–C bonds in the initial hours. Hence, prolonging the reaction for a longer time in sunlight is expected to produce VAPs and more hydrogen. Alternately, 1.5 and 2 sun conditions could be employed to perform the glycerol and glucose oxidation reactions, which is expected to increase the temperature further, in addition to light power. More work in this direction is likely to improve the activity in the desired direction of the biomass components to VAPS and hydrogen.

The preparation method can be utilized to prepare different noble metal integrated TiO_2 composites, a combination of SPR active metal and another transition metal in the form of alloy or bimetal co-catalysts is likely to provide more options for tuning the redox potential and hence the possibility of selectively producing one value-added product at a time and hence product separation step could be avoided. A combination of such co-catalysts with different semiconductors could also be evaluated for partial oxidation of biomass components by photocatalysis.[61] With an ideal catalyst, one may be able to achieve maximum C–C cleavage towards making 100% of C1- oxygenates, such as formic acid and formaldehyde. For maximum light absorption, thin-film and powder form with proper dispersion have the potential for large-scale application.[6,47,62] Recent work by Domen et al. on a 100 m^2 photocatalyst panel for water splitting in sunlight indicates the possibility to circulate a thin

layer of suspension over large area devices for the maximum absorption of sunlight to maximize the reactivity.[63] Less expensive system should be more practical and sustainable for large-scale synthesis, but earlier literature reports did not address the identification and quantification of the oxidized VAPs produced during hydrogen evolution. In fact, we suggest the practitioners of photocatalysis move from employing a mere sacrificial agent to generating VAPs, as this makes an attractive proposition. It has been 50 years since the announcement of the first proof of concept of water splitting by Fujishima and Honda;[5] however, photocatalytic hydrogen evolution research and technology is still at the infantry level. We believe that a small step suggested in the present manuscript could significantly impact these strategies and can potentially make the photocatalytic hydrogen evolution and glycerol oxidation process by photocatalysis attractive.

4.9 Reference:

1. Gong, J.; Li, C.; Wasielewski, M. R. Advances in Solar Energy Conversion. *Chem. Soc. Rev.* **2019**, *48*, 1862–1864.
2. Rajaambal, S.; Sivaranjani, K.; Gopinath, C. S. Recent Developments in Solar H2 Generation from Water Splitting. *J. Chem. Sci.* **2015**, *127*, 33–47.
3. Shaner, M. R.; Atwater, H. A.; Lewis, N. S.; McFarland, E. W. A Comparative Technoeconomic Analysis of Renewable Hydrogen Production Using Solar Energy. *Energy Environ. Sci.* **2016**, *9*, 2354–2371.
4. Walter, M. G.; Warren, E. L.; McKone, J. R.; Boettcher, S. W.; Mi, Q.; Santori, E. A.; Lewis, N. S. Solar Water Splitting Cells. *Chem. Rev.* **2010**, *110*, 6446–6473.
5. FUJISHIMA, A.; HONDA, K. Electrochemical Photolysis of Water at a Semiconductor Electrode. *Nature* **1972**, *238*, 37–38.
6. Gopinath, C. S.; Nalajala, N. A Scalable and Thin Film Approach for Solar Hydrogen Generation: A Review on Enhanced Photocatalytic Water Splitting. *J. Mater. Chem. A* **2021**, *9*, 1353–1371. (b) Rajaambal, S.; Mapa, M.; Gopinath, C. S. In1−xGa$_x$N@ZnO: A Rationally Designed and Quantum Dot Integrated Material for Water Splitting and Solar Harvesting Applications. *Dalton Trans.* **2014**, *43*, 12546.
7. Patra, K. K.; Bharad, P. A.; Jain, V.; Gopinath, C. S. Direct Solar-to-Hydrogen Generation by Quasi-Artificial Leaf Approach: Possibly Scalable and Economical Device. *J. Mater. Chem. A* **2019**, *7*, 3179–3189.

8. Fajrina, N.; Tahir, M. A Critical Review in Strategies to Improve Photocatalytic Water Splitting towards Hydrogen Production. *Int. J. Hydrog. Energy* **2019**, *44*, 540–577.
9. Karimi Estahbanati, M. R.; Feilizadeh, M.; Attar, F.; Iliuta, M. C. Current Developments and Future Trends in Photocatalytic Glycerol Valorization: Process Analysis. *React. Chem. Eng.* **2021**, *6*, 197–219.
10. Lv, D.; Lei, Y.; Zhang, D.; Song, X.; Li, Y.-W.; Niemantsverdriet, J. W. H.; Hao, W.; Deng, Y.; Su, R. Effect of Pd and Au on Hydrogen Abstraction and C–C Cleavage in Photoconversion of Glycerol: Beyond Charge Separation. *J. Phys. Chem. C.* **2020**, *124*, 20320–20327.
11. Deas, R.; Pearce, S.; Goss, K.; Wang, Q.; Chen, W.-T.; Waterhouse, G. I. N. Hierarchical Au/TiO_2 Nanoflower Photocatalysts with Outstanding Performance for Alcohol Photoreforming under UV Irradiation. *Appl. Catal. A-Gen.* **2020**, *602*, 117706.
12. Dodekatos, G.; Tüysüz, H. Plasmonic Au/TiO_2 nanostructures for Glycerol Oxidation. *Catal. Sci. Technol.* **2016**, *6*, 7307–7315.
13. Sakurai, H.; Kiuchi, M.; Heck, C.; Jin, T. Hydrogen Evolution from Glycerol Aqueous Solution under Aerobic Conditions over Pt/$TiO_2$and Au/TiO_2 granular Photocatalysts. *Chem. Comm.* **2016**, *52*, 13612–13615.
14. Dodekatos, G.; Schünemann, S.; Tüysüz, H. Recent Advances in Thermo-, Photo-, and Electrocatalytic Glycerol Oxidation. *ACS Catal.* **2018**, *8*, 6301–6333.
15. Wu, B.-H.; Liu, W.-T.; Chen, T.-Y.; Perng, T.-P.; Huang, J.-H.; Chen, L.-J. Plasmon-Enhanced Photocatalytic Hydrogen Production on Au/TiO_2 Hybrid Nanocrystal Arrays. *Nano Energy* **2016**, *27*, 412–419.
16. Melvin, A. A.; Illath, K.; Das, T.; Raja, T.; Bhattacharyya, S.; Gopinath, C. S. M–Au/TiO_2(M = Ag, Pd, and Pt) Nanophotocatalyst for Overall Solar Water Splitting: Role of Interfaces. *Nanoscale* **2015**, *7*, 13477–13488.
17. (a) Devaraji, P.; Gopinath, C. S. Pt – g-C3N4 – (Au/TiO_2): Electronically Integrated Nanocomposite for Solar Hydrogen Generation. *Int. J. Hydrog. Energy* **2018**, *43*, 601–613. (b) Devaraji, P.; Sathu, N. K.; Gopinath, C. S. Ambient Oxidation of Benzene to Phenol by Photocatalysis on Au/$Ti0._{98}V_{0.02}O_2$: Role of Holes. *ACS Catal.* **2014**, *4*, 2844–2853.
18. (a) Patra, K. K.; Gopinath, C. S. Harnessing Visible-Light and Limited Near-IR Photons through Plasmon Effect of Gold Nanorod with $AgTiO_2$. *J. Phys. Chem. C* **2018**, *122*,

1206–1214. (b) Patra, K. K.; Bhuskute, B. D.; Gopinath, C. S. Possibly Scalable Solar Hydrogen Generation with Quasi-Artificial Leaf Approach. *Sci. Rep.* **2017**, *7*. (c) Patra, K. K.; Gopinath, C. S. Bimetallic and Plasmonic Ag-Au on TiO_2 for Solar Water Splitting: An Active Nanocomposite for Entire Visible-Light-Region Absorption. *ChemCatChem* **2016**, *8* , 3294–3311.

19. Méndez, F. J.; González-Millán, A.; García-Macedo, J. A. A New Insight into Au/TiO_2-Catalyzed Hydrogen Production from Water-Methanol Mixture Using Lamps Containing Simultaneous Ultraviolet and Visible Radiation. *Int. J. Hydrog. Energy* **2019**, *44*, 14945–14954.
20. Shi, X.; Lou, Z.; Zhang, P.; Fujitsuka, M.; Majima, T. 3D-Array of Au–TiO_2 Yolk–Shell as Plasmonic Photocatalyst Boosting Multi-Scattering with Enhanced Hydrogen Evolution. *ACS Appl. Mater. Interfaces* **2016**, *8*, 31738–31745.
21. Fiorenza, R.; Bellardita, M.; D'Urso, L.; Compagnini, G.; Palmisano, L.; Scirè, S. Au/TiO_2-CeO_2 Catalysts for Photocatalytic Water Splitting and VOCs Oxidation Reactions. *Catalysts* **2016**, *6*, 121
22. (a) Priebe, J. B.; Radnik, J.; Lennox, A. J. J.; Pohl, M.-M.; Karnahl, M.; Hollmann, D.; Grabow, K.; Bentrup, U.; Junge, H.; Beller, M.; Brückner, A. Solar Hydrogen Production by Plasmonic Au–TiO_2 Catalysts: Impact of Synthesis Protocol and TiO_2 Phase on Charge Transfer Efficiency and H2 Evolution Rates. *ACS Catal.* **2015**, *5*, 2137–2148. (b) Bharad, P. A.; Sivaranjani, K.; Gopinath, C. S. A Rational Approach towards Enhancing Solar Water Splitting: A Case Study of Au–RGO/N-RGO–TiO_2. *Nanoscale* **2015**, *7*, 11206–11215.
23. Bajpai, H.; Patra, K. K.; Ranjan, R.; Nalajala, N.; Reddy, K. P.; Gopinath, C. S. Can Half-a-Monolayer of Pt Simulate Activity Like That of Bulk Pt? Solar Hydrogen Activity Demonstration with Quasi-Artificial Leaf Device. *ACS Appl. Mater. Interfaces* **2020**, *12*, 30420–30430.
24. Villa, A.; Veith, G. M.; Prati, L. Selective Oxidation of Glycerol under Acidic Conditions Using Gold Catalysts. *Angew. Chem. Int. Ed.* **2010**, *49*, 4499–4502.
25. Puga, A. V.; Forneli, A.; García, H.; Corma, A. Production of H2by Ethanol Photoreforming on Au/TiO_2. *Adv. Funct. Mater.* **2013**, *24*, 241–248.
26. (a) Taboada, E.; Angurell, I.; Llorca, J. Hydrogen Photoproduction from Bio-Derived Alcohols in an Optical Fiber Honeycomb Reactor Loaded with Au/TiO_2. *J. Photochem.*

Photobiol. A. **2014**, *281*, 35–39. (b) Sathu, N. K.; Devaraji, P.; Gopinath, C. S. Green Leaf to Inorganic Leaf: A Case Study of ZnO. *J. Nanosci. Nanotechnol.* **2016**, *16*, 9203–9208.

27. Zhou, B.; Song, J.; Zhang, Z.; Jiang, Z.; Zhang, P.; Han, B. Highly Selective Photocatalytic Oxidation of Biomass-Derived Chemicals to Carboxyl Compounds over Au/TiO_2. *Green Chem.* **2017**, *19*, 1075–1081.
28. Zhang, X.; Luo, L.; Yun, R.; Pu, M.; Zhang, B.; Xiang, X. Increasing the Activity and Selectivity of TiO_2-Supported Au Catalysts for Renewable Hydrogen Generation from Ethanol Photoreforming by Engineering Ti^{3+} Defects. *ACS Sustain. Chem. Eng.* **2019**, *7*, 13856–13864.
29. Wang, C.; Cai, X.; Chen, Y.; Cheng, Z.; Luo, X.; Mo, S.; Jia, L.; Shu, R.; Lin, P.; Yang, Z.; Sun, S.; Pu, E.; Shen, Y. Efficient Hydrogen Production from Glycerol Photoreforming over Ag_2O TiO_2 Synthesized by a Sol–Gel Method. *Int. J. Hydrog. Energy* **2017**, *42*, 17063–17074.
30. Trang, T. N. Q.; Tu, L. T. N.; Man, T. V.; Mathesh, M.; Nam, N. D.; Thu, V. T. H. A High-Efficiency Photoelectrochemistry of Cu_2O/TiO_2 Nanotubes Based Composite for Hydrogen Evolution under Sunlight. *Compos. B. Eng.* **2019**, *174*, 106969.
31. Montini, T.; Gombac, V.; Sordelli, L.; Delgado, J. J.; Chen, X.; Adami, G.; Fornasiero, P. Nanostructured Cu/TiO_2 Photocatalysts for H_2 Production from Ethanol and Glycerol Aqueous Solutions. *ChemCatChem* **2010**, *3*, 574–577.
32. Yang, Y.; Li, F.; Chen, J.; Fan, J.; Xiang, Q. Single Au Atoms Anchored on Amino-Group-Enriched Graphitic Carbon Nitride for Photocatalytic CO_2 Reduction. *ChemSusChem* **2020**, *13*, 1979–1985.
33. Al-Mazroai, L. S.; Bowker, M.; Davies, P.; Dickinson, A.; Greaves, J.; James, D.; Millard, L. The Photocatalytic Reforming of Methanol. *Catal. Today* **2007**, *122*, 46–50.
34. Strataki, N.; Bekiari, V.; Kondarides, D. I.; Lianos, P. Hydrogen Production by Photocatalytic Alcohol Reforming Employing Highly Efficient Nanocrystalline Titania Films. *Appl. Catal. B* **2007**, *77* , 184–189.
35. Li, Y.; Lu, G.; Li, S. Photocatalytic Hydrogen Generation and Decomposition of Oxalic Acid over Platinized TiO_2. *Appl. Catal. A-Gen.* **2001**, *214*, 179–185.
36. Hu, H.; Qian, D.; Lin, P.; Ding, Z.; Cui, C. Oxygen Vacancies Mediated In-Situ Growth of Noble-Metal (Ag, Au, Pt) Nanoparticles on 3D TiO_2 Hierarchical Spheres for Efficient

Photocatalytic Hydrogen Evolution from Water Splitting. *Int. J. Hydrog. Energy* **2020**, *45*, 629–639.

37. Dosado, A. G.; Chen, W.-T.; Chan, A.; Sun-Waterhouse, D.; Waterhouse, G. I. N. Novel Au/TiO_2 Photocatalysts for Hydrogen Production in Alcohol–Water Mixtures Based on Hydrogen Titanate Nanotube Precursors. *J. Catal.* **2015**, *330*, 238–254.
38. Chen, W.-T.; Chan, A.; Sun-Waterhouse, D.; Llorca, J.; Idriss, H.; Waterhouse, G. I. N. Performance Comparison of Ni/TiO_2 and Au/TiO_2 Photocatalysts for H_2 Production in Different Alcohol-Water Mixtures. *J. Catal.* **2018**, *367*, 27–42.
39. Jiménez-Calvo, P.; Caps, V.; Ghazzal, M. N.; Colbeau-Justin, C.; Keller, V. Au/TiO_2(P25)-gC_3N_4 Composites with Low gC3N4 Content Enhance TiO_2 Sensitization for Remarkable H_2 Production from Water under Visible-Light Irradiation. *Nano Energy* **2020**, *75*, 104888.
40. Balsamo, S. A.; Sciré, S.; Condorelli, M.; Fiorenza, R. Photocatalytic H_2 Production on Au/TiO_2: Effect of Au Photodeposition on Different TiO_2 Crystalline Phases. *J* **2022**, *5*, 92–104.
41. Police, A. K. R.; Vattikuti, S. V. P.; Mandari, K. K.; Chennaiahgari, M.; M.V., P. S.; Valluri, D. K.; Byon, C. Bismuth Oxide Cocatalyst and Copper Oxide Sensitizer in $Cu_2O/TiO_2/Bi_2O_3$ Ternary Photocatalyst for Efficient Hydrogen Production under Solar Light Irradiation. *Ceram. Int.* **2018**, *44*, 11783–11791.
42. Segovia-Guzmán, M. O.; Román-Aguirre, M.; Verde-Gomez, J. Y.; Collins-Martínez, V. H.; Zaragoza-Galán, G.; Ramos-Sánchez, V. H. Green Cu_2O/TiO_2 Heterojunction for Glycerol Photoreforming. *Catal. Today* **2020**, *349*, 88–97.
43. Majeed, I.; Nadeem, M. A.; Badshah, A.; Kanodarwala, F. K.; Ali, H.; Khan, M. A.; Stride, J. A.; Nadeem, M. A. Titania Supported MOF-199 Derived Cu–Cu_2O Nanoparticles: Highly Efficient Non-Noble Metal Photocatalysts for Hydrogen Production from Alcohol–Water Mixtures. *Catal. Sci. Technol.* **2017**, *7*, 677–686.
44. Jung, M.; Hart, J. N.; Boensch, D.; Scott, J.; Ng, Y. H.; Amal, R. Hydrogen Evolution via Glycerol Photoreforming over Cu–Pt Nanoalloys on TiO_2. *Appl. Catal. A-Gen.* **2016**, *518*, 221–230.
45. Imizcoz, M.; Puga, A. V. Optimising Hydrogen Production via Solar Acetic Acid Photoreforming on Cu/TiO_2. *Catal. Sci. Technol.* **2019**, *9*, 1098–1102.

46. Karimi Estahbanati, M. R.; Mahinpey, N.; Feilizadeh, M.; Attar, F.; Iliuta, M. C. Kinetic Study of the Effects of pH on the Photocatalytic Hydrogen Production from Alcohols. *Int. J. Hydrog. Energy* **2019**, *44*, 32030–32041.
47. Nalajala, N.; Patra, K. K.; Bharad, P. A.; Gopinath, C. S. Why the Thin Film Form of a Photocatalyst Is Better than the Particulate Form for Direct Solar-to-Hydrogen Conversion: A Poor Man's Approach. *RSC Adv.* **2019**, *9*, 6094–6100.
48. Tudu, B.; Nalajala, N.; Prabhakar Reddy, K.; Saikia, P.; Gopinath, C. S. Rationally Designed, Efficient, and Earth-Abundant Ni–Fe Cocatalysts for Solar Hydrogen Generation. *ACS Sustain. Chem. Eng.* **2021**, *9*, 13915–13925.
49. Tudu, B.; Nalajala, N.; Saikia, P.; Gopinath, C. S. Cu–Ni Bimetal Integrated TiO_2 Thin Film for Enhanced Solar Hydrogen Generation. *Sol. RRL* **2020**, *4*, 1900557.
50. Tudu, B.; Nalajala, N.; P. Reddy, K.; Saikia, P.; Gopinath, C. S. Electronic Integration and Thin Film Aspects of Au–Pd/rGO/TiO_2 for Improved Solar Hydrogen Generation. *ACS Appl. Mater. Interfaces* **2019**, *11*, 32869–32878.
51. Kasap, H.; Achilleos, D. S.; Huang, A.; Reisner, E. Photoreforming of Lignocellulose into H_2 Using Nanoengineered Carbon Nitride under Benign Conditions. *J. Am. Chem. Soc.* **2018**, *140*, 11604–11607.
52. Wakerley, D. W.; Kuehnel, M. F.; Orchard, K. L.; Ly, K. H.; Rosser, T. E.; Reisner, E. Solar-Driven Reforming of Lignocellulose to H_2 with a CdS/CdO_x Photocatalyst. *Nat. Energy* **2017**, *2*.
53. Wu, H.; Jiang, W.; Shi, L.; Li, R.; Huang, L.; Li, C. Photo-Assisted Sequential Assembling of Uniform Metal Nanoclusters on Semiconductor Support. *iScience* **2022**,*25*, 103572.
54. Sivaranjani, K.; Gopinath, C. S. Porosity Driven Photocatalytic Activity of Wormhole Mesoporous TiO_2-xN_x in Direct Sunlight. *J. Mater. Chem.* **2011**, *21*, 2639.
55. Roy, K.; Vinod, C. P.; Gopinath, C. S. Design and Performance Aspects of a Custom-Built Ambient Pressure Photoelectron Spectrometer toward Bridging the Pressure Gap: Oxidation of Cu, Ag, and Au Surfaces at 1 Mbar O2 Pressure. *J. Phys. Chem. C.* **2013**, *117*, 4717–4726.
56. Melvin, A. A.; Bharad, P. A.; Illath, K.; Lawrence, M. P.; Gopinath, C. S. Is There Any Real Effect of Low Dimensional Morphologies towards Light Harvesting? A Case Study of Au-rGO-TiO_2 Nanocomposites. *ChemistrySelect* **2016**, *1*, 917–923.

57. Cheng, L.; Zhang, D.; Liao, Y.; Li, F.; Zhang, H.; Xiang, Q. Constructing Functionalized Plasmonic Gold/Titanium Dioxide Nanosheets with Small Gold Nanoparticles for Efficient Photocatalytic Hydrogen Evolution. *J. Colloid Interface Sci.* **2019**, *555*, 94–103.
58. Subramanian, V.; Wolf, E. E.; Kamat, P. V. Catalysis with TiO_2/Gold Nanocomposites. Effect of Metal Particle Size on the Fermi Level Equilibration. *J. Am. Chem. Soc.* **2004**, *126*, 4943–4950.
59. Simões, M.; Baranton, S.; Coutanceau, C. Electro-Oxidation of Glycerol at Pd Based Nano-Catalysts for an Application in Alkaline Fuel Cells for Chemicals and Energy Cogeneration. *Appl. Catal. B* **2010**, *93*, 354–362.
60. Schlegel, N.; Wiberg, G. K. H.; Arenz, M. On the Electrooxidation of Glucose on Gold: Towards an Electrochemical Glucaric Acid Production as Value-Added Chemical. *Electrochim. Acta* **2022**, *410*, 140023.
61. Ran, J.; Zhang, J.; Yu, J.; Jaroniec, M.; Qiao, S. Z. Earth-Abundant Cocatalysts for Semiconductor-Based Photocatalytic Water Splitting. *Chem. Soc. Rev.* **2014**, *43*, 7787–7812.
62. Nalajala, N.; Salgaonkar, K. N.; Chauhan, I.; Mekala, S. P.; Gopinath, C. S. Aqueous Methanol to Formaldehyde and Hydrogen on Pd/TiO_2 by Photocatalysis in Direct Sunlight: Structure Dependent Activity of Nano-Pd and Atomic Pt-Coated Counterparts. *ACS Appl. Energy Mater.* **2021**, *4*, 13347–13360.
63. Nishiyama, H.; Yamada, T.; Nakabayashi, M.; Maehara, Y.; Yamaguchi, M.; Kuromiya, Y.; Nagatsuma, Y.; Tokudome, H.; Akiyama, S.; Watanabe, T.; Narushima, R.; Okunaka, S.; Shibata, N.; Takata, T.; Hisatomi, T.; Domen, K. Photocatalytic Solar Hydrogen Production from Water on a 100-M^2 Scale. *Nature* **2021**, *598*, 304–307.

Chapter 4b: Uniformly Integrated Sub-Nano Cu Particles over TiO_2: Concurrent Utilization of Electrons and Holes towards Efficient Photocatalytic Hydrogen Evolution and selective oxidation of Biomass.

4.10 Introduction:

Due to the industrial revolution in the last one century, there has been a huge amount of carbon dioxide emitted into the atmosphere, which has caused ecological concerns.[1] As the world's population continues to increase, there will be an increased demand for natural resources such as fossil fuel. The demand for energy has been steadily increasing for the past few decades, which led to a rise in the consumption of more fossil fuels. Even if the percentage of total energy demand met by renewable sources has increased from 8 to 11 %, carbon footprints are still growing at an exponential rate. In fact an increase in volume of consumption adds to the carbon footprint enormously from across the globe. This underscores the need for alternative fuels that do not produce carbon emissions, such as hydrogen, which should be easily available.[2, 3]

Hydrogen has the potential to solve future energy crises, and it may also be used in hydrogenation processes to make value added compounds, like, ammonia, methanol. In the future, hydrogen may be the key to prevent and resolve energy crises.[4] Yet, the most significant obstacle to overcome is the manufacturing of hydrogen in a sustainable manner. At present, 92% hydrogen consumed by industries is produced through a process known as steam reforming of methane/naphtha, which results in the production of CO_2. As a result, environmentally friendly techniques of producing hydrogen are required.[5] When paired with biomass and biomass components, such as cellulose, glucose, and glycerol, photocatalysis presents an attractive option for the generation of hydrogen.[2, 6-9] This combination demonstrates a great potential for the generation of hydrogen as well as carbon-containing products with enhanced value.

The process of splitting water is an endothermic one that requires an energy input of 237 kJ/mol. Nevertheless, the process that results in oxygen evolution is kinetically sluggish and rate-determining; as a consequence, the efficiency of the entire reaction is reduced mainly due to increased oxidation potential.[5, 10] Carbohydrates and alcohols, on the other hand, have a lower oxidation potential and are readily accessible; in addition, the oxygenates

of these compounds have a great value addition.[8, 11-14] It is necessary to make use of sacrificial reagents like methanol, Na_2S-Na_2SO_3, and tri-ethanolamine in order to increase the kinetics of the hydrogen evolution process.[15, 16] Because of their low cost, components of biomass, such as, cellulose, glucose, can also be employed as sacrificial reagents. Moreover, glycerol, a by-product of the bio-diesel sector, can also be used. The amount of glycerol that is produced is correlated with the amount of demand for bio-diesel. Glycerol price is very low (US 0.11 $), due to large production (of biodiesel) compares to its demand; that is why it is considered as a biowaste; however, from US department of energy, glycerol is listed as one of the top ten molecules which can be used as platform raw-material to produce value-added chemicals.[17, 18] With suitable catalyst and conditions, glycerol can be selectively converted in to value added chemical; however, it is still a challenge to convert glycerol with high selectivity towards oxygenates. A sustainable method of photocatalytic water splitting can be accomplished by employing glycerol as a sacrificial reagent or by producing selective VAPs instead.[19] This can be better dealt by transforming glycerol into VAP. This approach can also be implemented for use with several different components of biomass.[9, 20-22]

TiO_2 is a well-known semiconductor that is characterised by a wide band gap with absorption in the UV region, and a high degree of chemical stability. Because of the significant charge recombination, its efficiency is limited; however, this limitation may be tackled by forming a Schottky junction with other metal as a co-catalyst and possibly as light absorber. When coupled with metal nanoparticles, more importantly which has high activity towards respective photocatalytic activity, it has the potential to improve charge carrier utilization for redox reactions.[23] Copper oxide can be reduced to copper metal, and can function as a plasmonic metal or serving as both a metal cocatalyst and semiconductor at the interface between copper metal and Cu_2O.[24] This makes the surface chemistry of Cu/TiO_2 fascinating in photocatalysis.[12, 25-27] In spite of these advancements, the total efficiency of water splitting is still somewhat low due to the slow kinetics of four-electron oxygen evolution process. The utilisation of sacrificial reagents that have a lower oxidation potential has enabled an increase in the rate of hydrogen evolution by better utilization of holes as well as electrons, respectively.[12, 15, 16] Unfortunately, there are only limited number of studies carried out which employed sacrificial reagents as reactants in order to make VAPs and hydrogen simultaneously. Producing hydrogen and VAPs at the same time by using electrons and holes

is a prudent approach that is both sustainable and cost-effective for an effective photocatalytic system.[19, 28-30]

Zhen et. al have studied $Cu/Cu_2O.Cu/TiO_2$ interface towards hydrogen evolution using TEOA (Triethanolamine) as a sacrificial reagent, and they have observed 7.8 mmol/g_{cat} of hydrogen production in two hr; however oxidation process of TEOA was not discussed;[16] Reddy et. al.[31] has prepared Cu/Ag integrated over TiO_2 nanotube via photo-deposition method, and photocatalytic hydrogen evolution was carried out using 5% glycerol as a sacrificial reagent; although maximum hydrogen evolution was observed (56.6 mmol of hydrogen), but there is no mention about oxidation products, which is very essential towards a sustainable system. Recently Guzman et Al. have also prepared Cu/TiO_2 system with glycerol and observed 4.7 mmol/g_{cat} of hydrogen.[29]. Pecoraro et al. has studied photo reforming of glycerol and calculated hydrogen evolution as well as oxidation product, where they observed 0.12 mmol/h. g. of hydrogen with dihydroxy acetone and glyceraldehyde as value-added products.[30] There are very few reports where authors have focused on utilization electrons as well as holes. In the present study, we report on a Cu/TiO_2 composite that was made by three distinct methods and used to assess the products of hydrogen evolution and glycerol oxidation. To comprehend the dispersion of Cu across titania, we employed HRTEM and elemental mapping, and other relevant characterization techniques to investigate the nature of the interaction between titania and Cu. Oxidation products of glycerol was identified as well as quantified by ^1H NMR.

4.11 Structural Analysis:

In order to determine the integration and structural aspects of copper over TiO_2, HRTEM and elemental mapping were carried out for all three composites. Figure 4.14 corresponds to TC-200, where HRTEM images (a and b) depict the particle distribution of TiO_2 with an average size of 20±1 nm. Upon careful investigation at 5 nm scale (panel b), no copper particles were observed, despite evidence from XPS and photocatalytic activity that copper is deposited over TiO_2. In fact, many more images were also analysed and only a representative HRTEM image is shown in panel b. Elemental mapping (Fig.4.14.c-f) was performed to understand the system's distribution and integration. STEM images and respective elemental mapping (panels e and f) show the expected distribution of Ti (green) and oxygen (yellow), while panel d reveals the uniform distribution of copper over TiO_2. It is to be noted that during

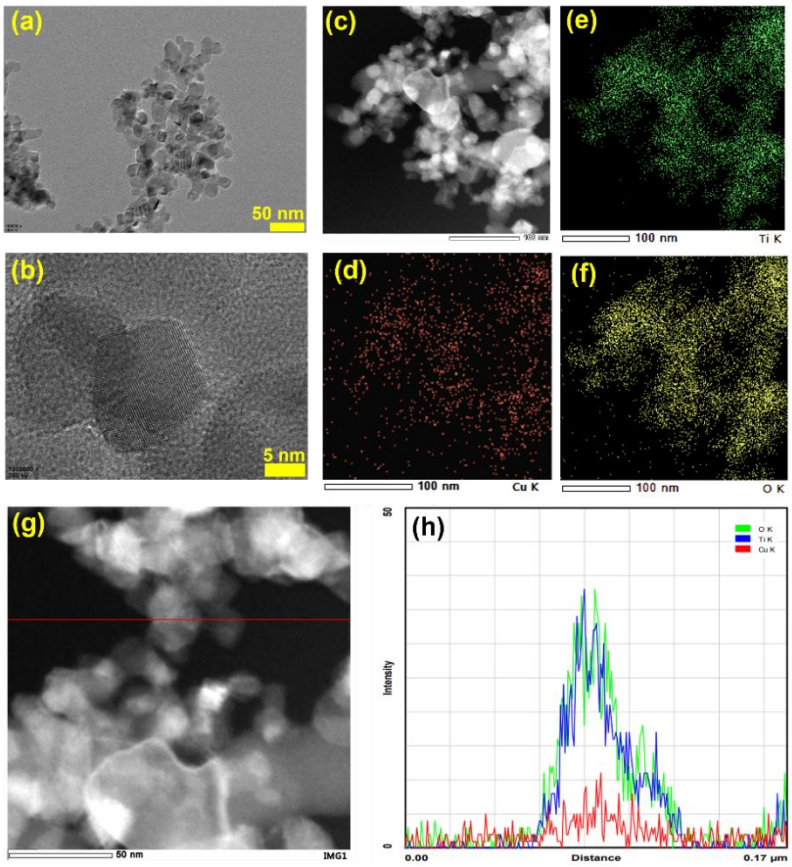


Figure 4.14. TC-200, a-b HRTEM images, c-f STEM image and corresponding distribution of Cu (red), Ti (green) and oxygen (yellow), g-h shows the line profile and distribution of Ti (blue), oxygen (green) and Cu (red).

synthesis, TiO_2 was treated with $NaBH_4$ which resulted in the formation of oxygen vacancies over the surface of TiO_2; it is well known that each oxygen vacancy is associated with two electrons, which is the source of reduction of metal ion reduction to metal. It is very likely that the copper reduction happened predominantly at these vacancy sites, inhibiting the formation of large copper cluster/particles. As expected, these electron-rich sites served as anchor sites for Cu^{2+} and resulted in uniform distribution, as confirmed by the line profile analysis (Fig.4.14g and h), which clearly shows homogeneous integration of Cu all over the surface of TiO_2. This integration led to a higher hydrogen evolution than virgin TiO_2 due to enhanced charge transfer. However, photo-deposited TiO_2 demonstrates even higher efficiency towards hydrogen evolution, which will be discussed in a later section.

Fig.4.15 displays the HRTEM examination of TC-PD, representing photo-deposited copper over TiO_2. HRTEM images of TC-PD in panels a and b show TiO_2 particles, which are

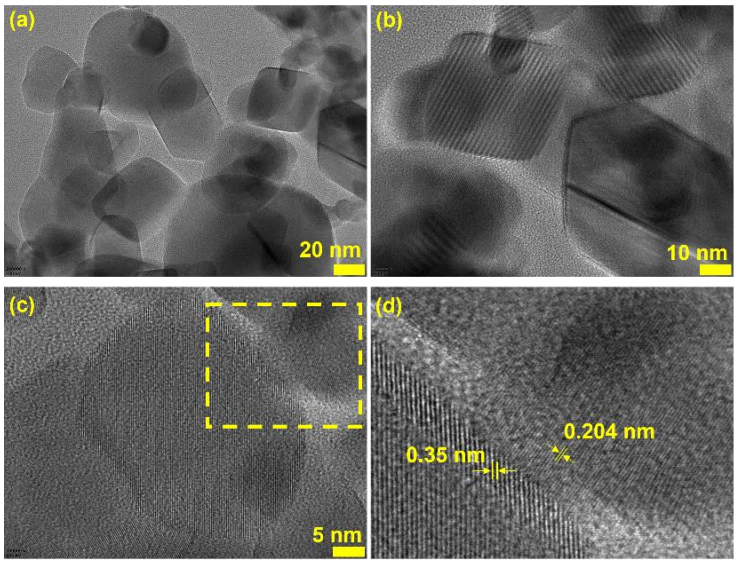


Figure 4.15. TC-PD, HRTEM images on different scale, image d is the enlarge image of highlighted section in image c, Schottky junction was observed in d between TiO_2 and Cu.

expected for P25-TiO_2 particles. HRTEM image shown in panels c and d highlights d spacing (d_{110}) and the interface between TiO_2 and copper; indeed, this is clearly shown in the image in panel d (enlarge image of highlighted area in panel c). The d spacing with 0.35 nm corresponds to TiO_2 (101) facet, and 0.204 nm is attributed to metallic copper (111) faceted nanoparticle.[32] It is evident from Fig.4.15d that a Schottky junction has formed, resulting in higher photoactivity. Although copper is not uniformly distributed in TC-PD, as there is less control over the photo-deposition process (unlike the hydride reduction process in the earlier method TC-200), the copper particles grow in size to around 10 to 15 nm. It is to be underscored that photocatalytic activity with respect to hydrogen evolution is higher compared to TC-200, where a higher active surface area is available for photocatalysis. The enhanced electronic interaction in photo-deposition methods seems to reduce the charge recombination and increases the charge utilization for further redox reactions, in spite of bigger particle size than TC-200.

The analysis of the structure and integration of TC-PDO is presented in Figure 4.16. Panel a and b display the HRTEM images of the TC-PDO composite, which is similar to TC-200, and no copper particles is observed. To investigate more on this, elemental mapping and line profile analysis were carried out. Figure 4.16.c-f shows STEM images and elemental mapping for Cu (red), Ti (green), and O (yellow). The elemental mapping indicates the uniform distribution of small copper clusters over TiO_2, leading to a high surface area with respect to

copper. It is important to note that light-induced oxygen vacancies were created on TiO_2, before Cu-integration in synthesis, and the same appeared pale blue in colour. It is well known that pale-blue color appears due to formation of oxygen vacancies. Ionic-copper in methanol was injected into the TiO_2 solution without exposing it to air, and stirred overnight in the dark, allowing only electron-rich oxygen vacancies sites to reduce the copper (II) to copper metal, resulting in formation of very fine copper particles. This process resulted in the highest homogeneity of small copper clusters over TiO_2, which is clearly evident from elemental mapping. Line profile analysis was also conducted to investigate the distribution of copper over a single TiO_2 particle (Fig.4.16. g and h), which confirmed the

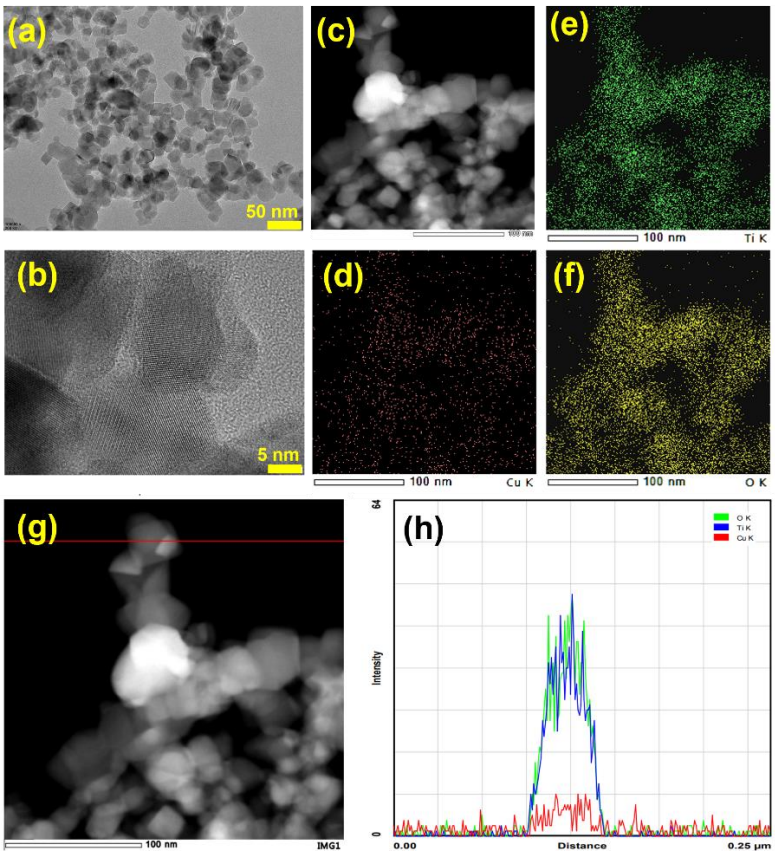


Figure 4.16. TC-PDO, a-b HRTEM images, c-f STEM image and corresponding distribution of Cu (red), Ti (green) and oxygen (yellow), g-h shows the line profile and distribution of Ti (blue), oxygen (green) and Cu (red).

presence of small copper clusters. TC-PDO, which incorporates the desired aspects of the other two composites, namely high surface area and high electronic integration, exhibits the highest activity due to photo-induced followed by copper deposition in dark. These aspects will be further discussed in later characterizations.

4.12 Photo-catalytic Water Splitting:

The experiment aimed to investigate the photocatalytic hydrogen evolution under the following reaction conditions. Although few other conditions were evaluated, the conditions mentioned below gave the best activity and we restrict our discussion with respect to that. We employed 3 mg of catalyst in 20 ml of 5% aqueous solution of glycerol, and the measurements were conducted under one sun condition (100 mW/cm^2) to ensure accuracy. To minimize light scattering and its negative influence on the photocatalytic activity, the measurements were carried out without stirring under static conditions. All Cu/TiO_2 composites were subjected for the photocatalytic study, and solar irradiation (one sun or direct sunlight) was applied for hydrogen evolution, with 5% glycerol serving as a sacrificial reagent at pH 7, and the results are shown in Fig. 4.17. The integration of Cu-cluster as co-catalyst was found to enhance the hydrogen evolution rate, and presence of Cu was also confirmed by Raman and UV-Vis spectra. In particular, the TC-200 composite showed a 3-fold higher activity compared to virgin TiO_2. This result was due to the uniform distribution of Cu over the surface, as observed by elemental mapping and line profile analysis. The uniform distribution of Cu facilitated electronic integration through Schottky junctions, leading to an enhancement in the photocatalytic activity.

Two other samples, TC-PD and TC-PDO, were also evaluated in the similar manner and the results are shown in Fig. 4.17a. TC-PD showed the formation of Cu particles and Schottky junction with TiO_2, resulting in a 2-fold increase in hydrogen evolution compared to TC-200. Although TC-200 exhibits a more uniform distribution of Cu over TiO_2, yet the photoactivity showed the lower activity is attributed to lower active surface area. This observation suggested that the role of electronic integration and surface species over the catalyst system played an important role in determining the photocatalytic activity. TC-PDO exhibited the highest activity due to its homogeneous distribution and lower surface hydroxy group, resulting in higher photoactivity. The stability of all composites was

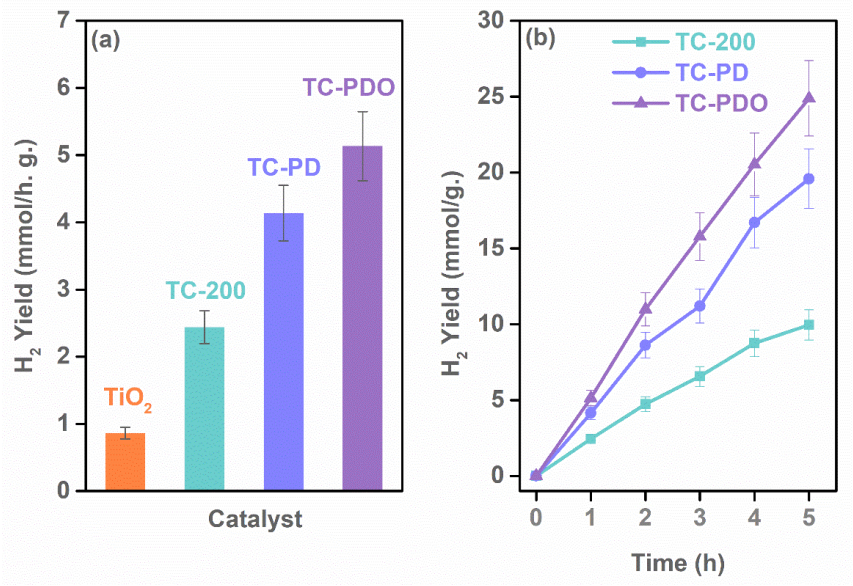


Figure 4.17. (a) Photocatalytic hydrogen yield observed for different composites of 1% of Cu on TiO_2, and (b) Photocatalytic activity displayed for 5 hr for all the composite. 5% glycerol was used as sacrificial reagent under one sun conditions with a solar simulator at pH=7.

monitored for continuous five hours and showed a linear trend, and the results are shown in Fig. 4.17.b. All three TC catalysts show a linear increase in H_2-generation activity. However, the slope demonstrates the highest activity is observed with TC-PDO, among the three TC catalysts.

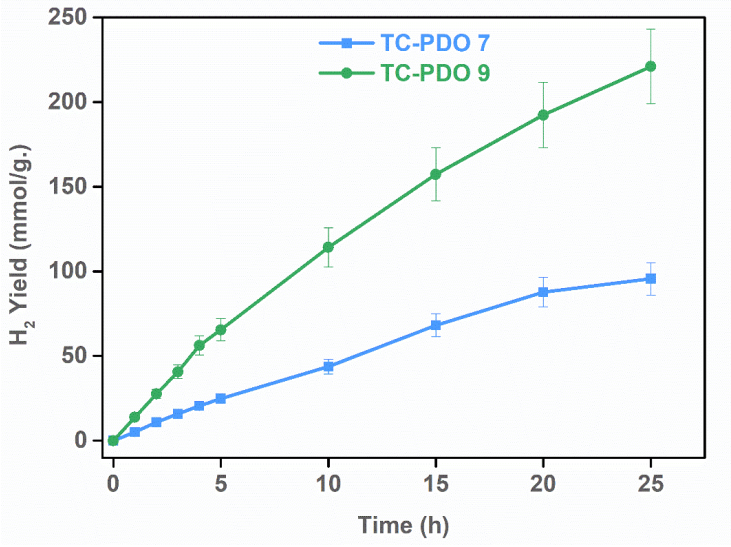


Figure 4.18. Sustainability of the TC-PDO catalyst evaluated for 25 hr at two different pH conditions. NaOH was used to adjust the pH to 9. 5% glycerol was used as sacrificial reagent under one sun conditions.

To further investigate the impact of pH on the photocatalytic activity and stability, we have carried out pH-dependent studies and the results are shown in Figure 4.18. The results showed that at pH 9, almost 2-fold increase in photocatalytic activity was observed compared to pH 7; especially this is evident after first 5 h reaction. Beyond 5 h, a decline in rate is evident under both pH conditions and the same reflects in the slope of the time dependent yield plot. pH dependent activity in photocatalysis is well-known, as it shifts the VB and CB edges systematically.[33] It is known that the Cu/TiO_2 system's photocatalytic activity is not stable at acidic pH, while it is stable at basic/high pH.[34] Specifically, during the glycerol oxidation process, the formation of formic acid could destabilize the copper integrated over TiO_2, causing copper species to leach out into the solution and lowering hydrogen evolution in the longer term. However, at pH 9, the basic medium neutralizes the effect of formic acid, leading to stable activity for 25 hours within the experimental error limit of 10%. Indeed, for every unit change in pH, the VB and CB potentials shifted by 59 mV; acid (pH = 1) to basic (pH-11) medium would shift the VB and CB by 590 mV or 0.6 V towards vacuum level or less negative value. The glycerol oxidation process also plays an essential role in the photocatalytic activity at different pH levels, which is discussed in the next section.

4.13 Photocatalytic Glycerol Oxidation:

The conversion of glycerol to value-added products can contribute to the sustainability of the process. In the current study, 3 mg of TC-PDO catalyst was employed with 20 ml of 5% aqueous glycerol at pH 7 and pH 9 for 25 hours to examine the glycerol oxidation products. By employing ^1H NMR, we have identified and quantified all the four products, namely, glycolaldehyde, formic acid, dihydroxyacetone, and glyceraldehyde. To avoid overoxidation of glycerol, all reactions were conducted in a nitrogen environment by purging the solution with nitrogen for 15 minutes. Under one sun condition at pH 7, we observed the formation of 40.4, 11.0, 8.0, and 0.8 mmol/h.g. of glycolaldehyde, formic acid, dihydroxyacetone, and glyceraldehyde, respectively, along with 5.1 mmol/h.g. of hydrogen evolution. At pH 9, the hydrogen evolution was twice as that of observed at pH 7, but there was only a small increase in the formation of liquid products. Further investigation revealed an increase in the formation of glycolaldehyde (47.55 mmol/h.g.) and formic acid (11.14 mmol/h.g.), along with a reduction in dihydroxyacetone, indicating an enhancement of C-C cleavage. The reactions were conducted at ambient temperature, and no gaseous products,

other than hydrogen, was observed, indicating that there was no over-oxidation. The selectivity towards glycerol to oxygenates is shown in Fig. 4.19b. At pH 7, we observed 67% selectivity towards glycolaldehyde, confirming the preferential C-C cleavage towards C_2 products. Formic acid (18.3%), dihydroxyacetone (13.3%), and glyceraldehyde (1.3%) showed selectivity towards more C_1 and C_2. At pH 9, the selectivity for glycolaldehyde increased to 73.8%, but there was a slight decrease in the selectivity for other products. The high pH condition is favourable for C-C cleavage and C_2 oxygenates, resulting in higher selectivity and hydrogen evolution. The overall conversion was almost the same at both pH conditions, indicating that hydrogen generation is coming from both water splitting and glycerol oxidation. The absence of CO_2 production demonstrates the viability of this sustainable strategy towards green hydrogen and value-added products.

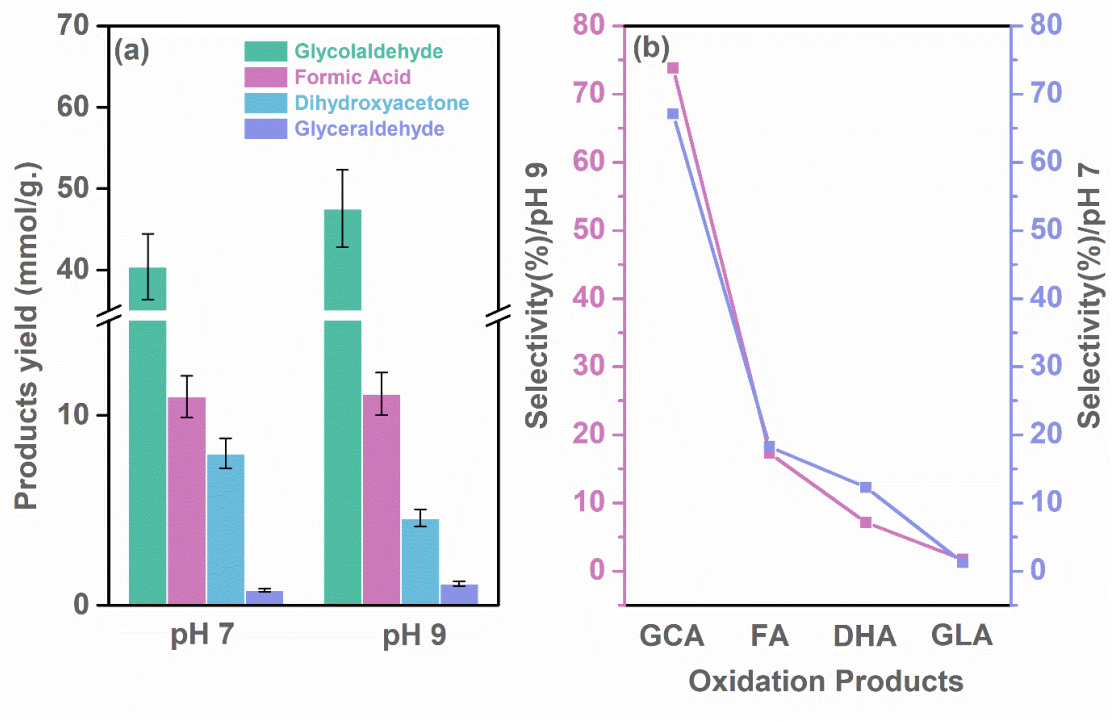


Figure 4.19. Photocatalytic glycerol oxidation with TC-PDO under 7 pH and 9. (a) Product yields observed at different pH, and (b) selectivity of the products at different pH. 5% glycerol was used as sacrificial reagent under one sun conditions at 100 mW/cm^2 and all products yield and selectivity is for twenty-five hours of reaction time in both panels, GCA (glycolaldehyde), FA (formic acid), DHA (dihydroxyacetone), GCA (glyceraldehyde).

4.14 UV-Visible Spectra:

Light absorption is the first and critical step in photocatalysis and good light absorption is the key for generating sufficient number of charge carriers. Figure.4.20a shows the optical absorption studies carried out for TiO_2 and Cu/TiO_2 composite, which were prepared by various methods. The TAUC plot was utilized to investigate changes in the band gap of the parent material and the analysis is provided in Fig. 4.20.b. The absorption spectra of TiO_2 showed an onset of light absorption at 380 nm, corresponding to a band gap of 3.2 eV. After the integration of copper, a marginal red shift in onset of light absorption was observed; nonetheless, there is no significant change in the band gap of the composite in TC-200 and TC-PD. In TC-PDO, a change of 0.05 eV in the band gap was observed, which did not affect absorption significantly, but could potentially influence the photocatalytic activity. Copper is present in the metallic state, as evidenced by XPS analysis; due to its small amount of 1 wt % and well-dispersed and deposited over TiO_2, the absorption spectra did not exhibit any distinct plasmonic behaviour related to copper. However, an enlargement of plasmon region above 550 nm reveals a weak plasmonic absorption. Nonetheless an increase in background for all TC materials makes it difficult for further analysis. However, the absorption coefficient of Cu/TiO_2 composites enhanced between 1.5-2 times that of TiO_2 and indicated the plasmon effect in overall absorption of light due to its integrated nature of copper with TiO_2.

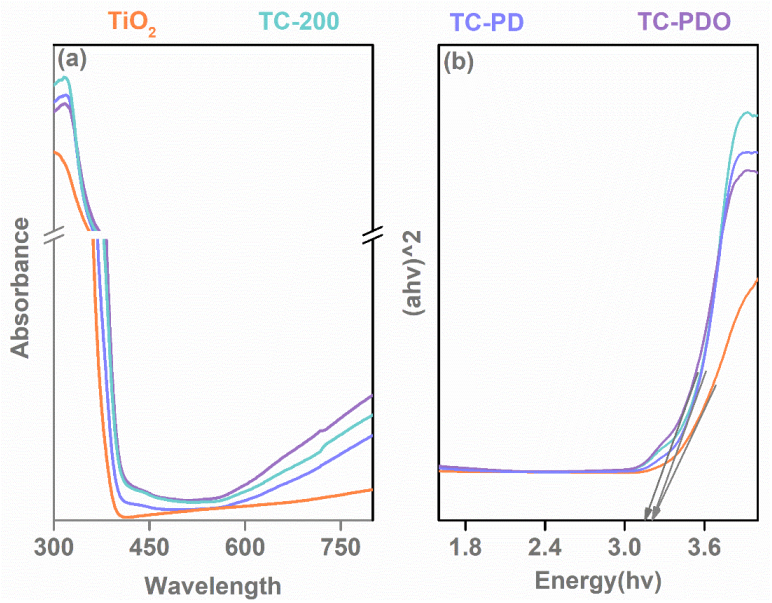


Figure 4.20. (a) UV-Visible absorption spectra of TiO_2, TC-200, TC-PD, TC-PDO. (b) Tauc plot of TiO_2, TC-200, TC-PD, TC-PDO for their respective band gap indicated by arrows

4.15 Raman Analysis:

Figure 4.21 shows the Raman spectra and relative intensity of different bands of TiO_2, TC-200, TC-PD, TC-PDO, and after reaction with TC-PDO at pH 7 and pH 9. In fig.4.21a and b, all the composites show similar Raman features at 143 (E_g), 194 (E_g), 397 ($B1_g$), 518(A_{1g}+B_{1g}), and 639 (E_g) cm^{-1} for the anatase phase of P25. There is no shift in the Raman bands observed

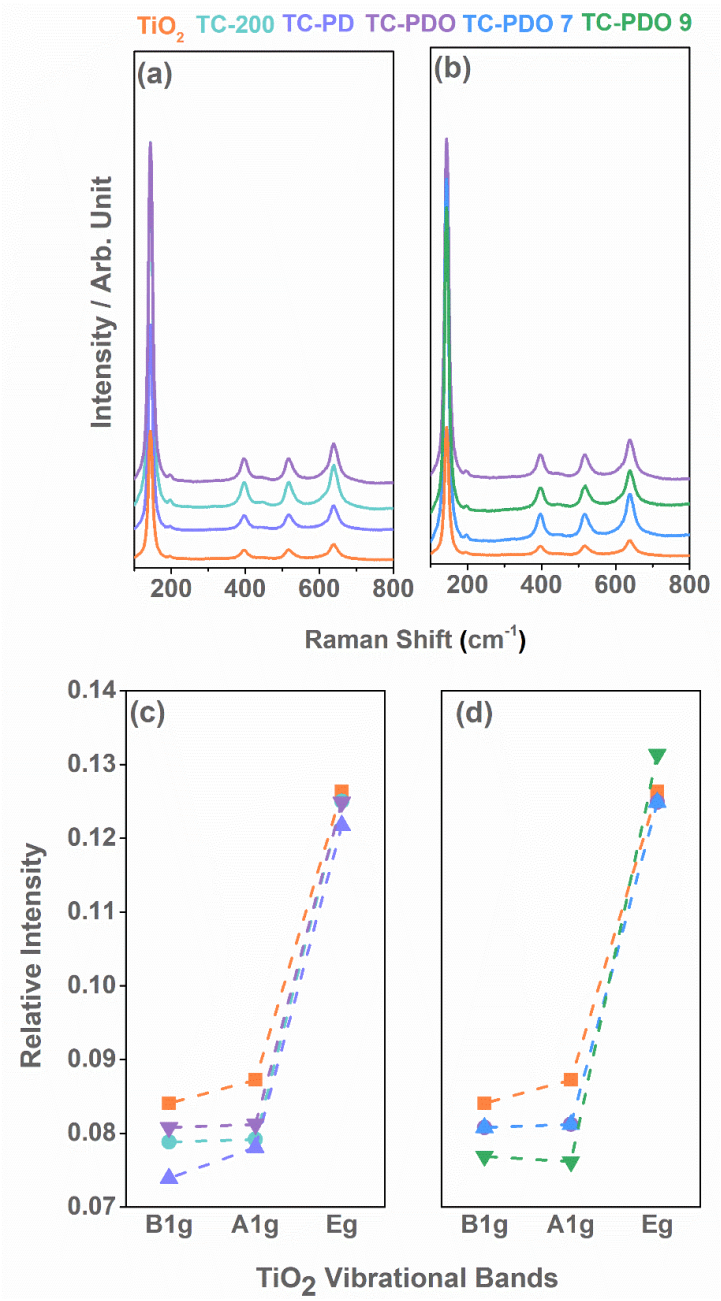


Figure 4.21. (a) Raman spectra of TiO_2, TC-200, TC-PD, TC-PDO. (b) Raman spectra of TiO_2, TC-PDO, TC-PDO 7, TC-PDO 9. (c) Relative intensity of different band for TiO_2, TC-200, TC-PD, TC-PDO. (d) Relative intensity of different band for TiO_2, TC-PDO, TC-PDO 7, TC-PDO 9. Where TC-PDO 7 and TCO PD 9 are after reaction samples.

in Cu/TiO_2 composites, and no additional peak is observed with respect to copper species, likely due to the low copper content. After reaction, TC-PDO samples at pH 7 and pH 9 were also analysed to understand the difference in activity, but no observable shift is present in TC-PDO 7 and 9 with respect to TiO_2 and TC-PDO. Although no shift in Raman peaks is observed, a marginal change in the FWHM as well as changes in relative intensity was observed. A careful analysis also reveals the intensity of TC spectra increase by a factor between 1.5-2.5, compared to TiO_2; even though similar amount of material was employed for Raman analysis, an enhancement in intensity suggests the influence of plasmon effect in increasing the intensity. Figure 4.21c and d show the relative intensity of E_g, B_{1g}, and A_{1g} for TiO_2, TC-200, TC-PD, TC-PDO, and after reaction TC-PDO at pH 7 and pH 9. It is known that the E_g, B_{1g}, and A_{1g} bands are related to symmetrical stretching vibration, symmetrical bending vibration, and asymmetrical stretching vibration of O-Ti-O, respectively.[35] It is clear from Figure 4.21.c and d that after copper integration, the relative intensity corresponding to symmetrical bending vibration and asymmetrical stretching vibration decreased, indicating the electronic interaction between Cu and TiO_2. However, a detailed and controlled investigation is needed to understand how these bands behave in different environments, which is beyond the scope of this work.

4.16 X-ray Photo-electron Spectroscopy:

XPS is a surface analytical technique that examines the electronic interaction and surface composition of a system. As photocatalysis is a surface physico-chemical process, the XPS analysis can be directly linked to the photocatalytic activity. Fig. 4.22 shows the observed XPS data for investigating the electronic interaction between Cu and TiO_2 in all three composites. In Fig. 4.22.a, Ti exhibits two different oxidation states for all samples at 457.5 ± 0.05 eV and 458 ± 0.05eV for Ti^{3+} and Ti^{4+}, respectively. Ti^{4+} is predominantly present in all cases, while the Ti^{3+} content varies with different composites. TC-200 has the highest Ti^{3+} content at 10.5% compared to other samples (TC-PD, 8.4%; TC-PDO, 9%). It is note-worthy that during photo-deposition, most of the electron-rich site attaches to Cu species, resulting in a lower defect site for TC-PDO and TC-PD compared to TC-200. This change is also attributed to charge transfer from TiO_2 to copper, resulting in electronic integration and high photocatalytic activity. In Fig. 4.22, the O 1s spectra show three different oxygen species that correspond to lattice oxygen of TiO_2 (529.75 ± 0.05 eV, red trace), oxygen near to defect site

(531 ± 0.05 eV, blue trace), and oxygen related to hydroxyl group (532 ± 0.05 eV, green trace). The oxygen related to Ti^{3+} shows the same trend as the Ti 2p spectra of Ti^{3+}. However, in the case of the hydroxy group, a significant change is observed. TC-200 exhibits higher content pf hydroxyl group (21.56%) than TC-PD (15.08%) and TC-PDO (9.65%).[14] The decrease in the hydroxyl group content increases the photocatalytic activity. In TC-PDO, 55% less hydroxy group is available, where the hydroxyl group can hinder the reaction between TiO_2 and glycerol or occupy the active site for glycerol oxidation, which agrees with the photoactivity part. It is interesting to note that during the synthesis for TC-200, TiO_2 was initially treated with $NaBH_4$, then washed and dried in the oven, resulting in higher hydroxyl group content. If the exposure to air is prevented, this composite can have the same activity as TC-PDO. Since photo-deposition is limited to a few metals, the $NaBH_4$ treated method can be applied to almost all metals.

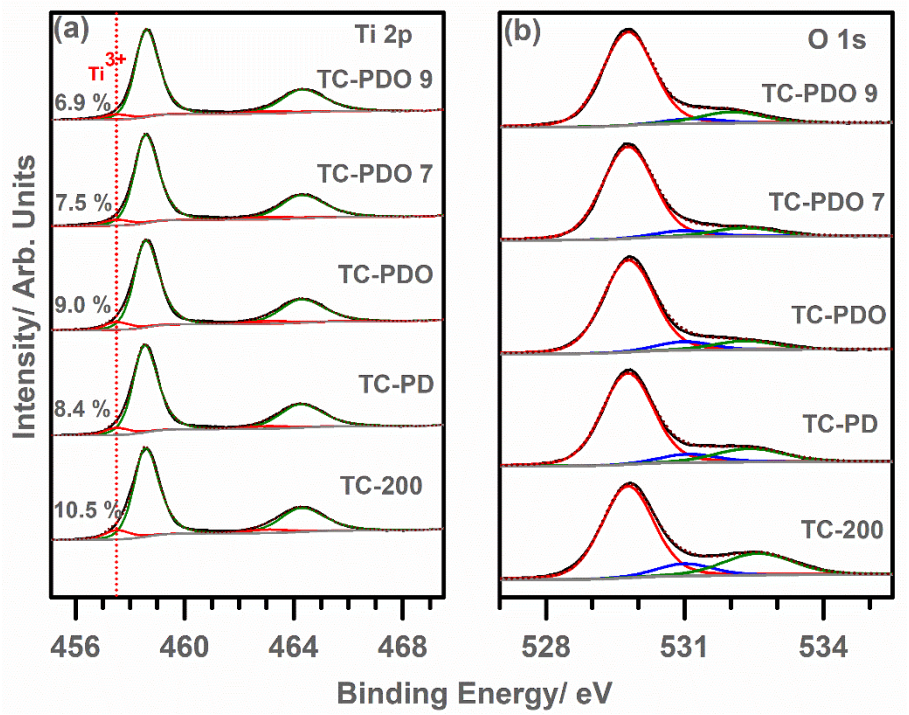


Figure 4.22. (a) Ti 2p, and (b) O 1s core level spectra of TiO_2, TC-200, TC-PD, TC-PDO, TC-PDO 7, TC-PDO. Ti^{3+} is given in red traces, respectively. Red, blue and green traces in O 1s corresponds to TiO_2 lattice oxygen, O-associated with Ti^{3+} and OH group, respectively.

Figure 4.23 displays the Cu 2p XPS and Auger spectra of the Cu/TiO_2 composites. The XPS spectra can distinguish between Cu^{2+}, and Cu^{+} and Cu^{0} species, with Cu^{2+} exhibiting a distinct satellite feature. From Figure 4.23.a, it can be seen that Cu^{2+} is not present on the

surface of the samples, but it is challenging to differentiate between Cu^{+} and Cu^{0} using XPS spectral data alone. Hence, Auger spectra (Figure 4.23b) were used for identifying copper oxidation states. The Cu LMM feature shows Cu^{0} at 918.8 eV and Cu^{+} feature at 916.8 eV.[36-38] Spectral analysis reveals that copper is present in the metallic form in all the samples, indicating its integration over TiO_2 as a co-catalyst. There is also evidence of electron transfer from TiO_2 to copper. After the reaction, the samples were analysed for TC-PDO at pH 7 and pH 9. Figure 4.33 a show lower Ti^{3+} content in both cases compared to TC-PDO. However, at pH 9, only 6.5% of defects were observed, possibly due to higher charge transfer at pH 9. However, it is not conclusive evidence for higher photoactivity, since at high pH, copper is more stable, and glycerol adsorption/desorption are more favourable.

The integration of a co-catalyst with a semiconductor is an effective approach for photo-catalytic applications, and a proposed mechanism is illustrated in Figure 4.24, based on various characterization techniques. While TiO_2 has a wide band gap (3.2 eV) that only

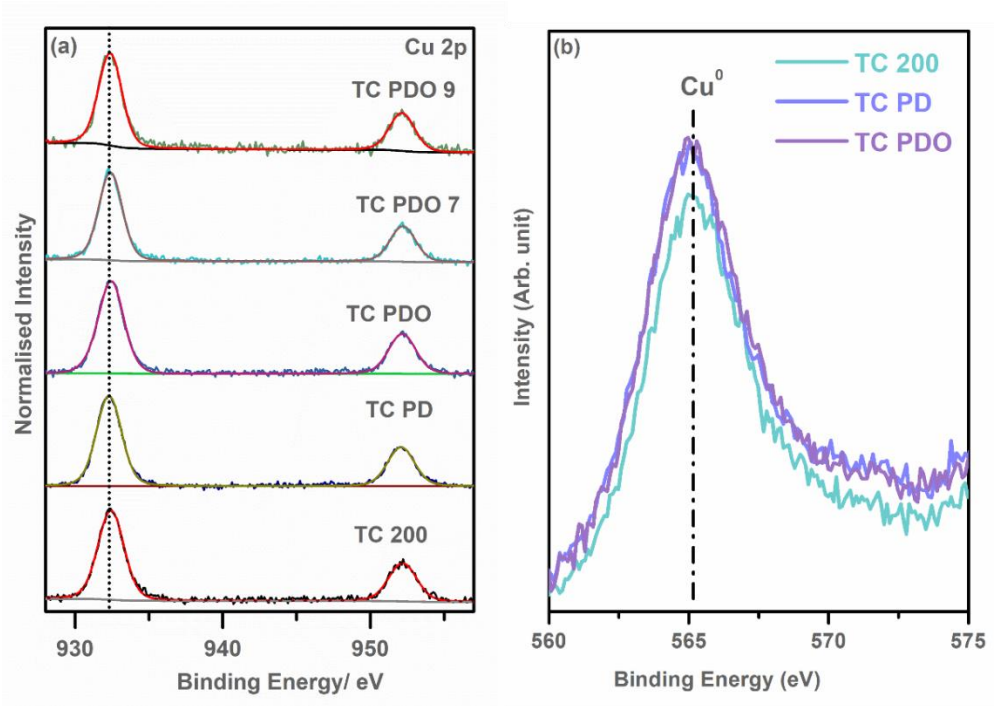


Figure 4.23. (a) Cu 2p, and (b) Cu Auger spectra of TiO_2, TC-200, TC-PD, TC-PDO, TC-PDO 7, TC-PDO 9.

absorbs a small portion (4%) of the solar spectrum in the UV range, its efficiency is hindered by high charge recombination. However, the incorporation of an earth-abundant co-catalyst with TiO_2 can offer a sustainable method for producing hydrogen. In TC-PDO, the homogeneous dispersion of Cu over TiO_2 is discussed in the structural section, which enhances charge separation, as evidenced by its photocatalytic activity. All three methods (photo-deposition, Photo-induced dark deposition, and $NaBH_4$ reduction) involve charge transfer from TiO_2 to copper, as confirmed by XPS studies.

4.17 Mechanism:

Photocatalytic water splitting involves both photophysical (ns) and photochemical (µs) processes. Photophysical processes include charge carrier generation and transfer from bulk to surface, which take place on a time scale ranging from pico/femtoseconds to nanoseconds, whereas photochemical reactions occur on a nano/micro/millisecond time scale. Due to few orders of magnitude difference in lifetimes of light induced physical and chemical processes, it becomes even more difficult to utilize the charge carriers quickly. One of the strategies is to separate the charge carriers and store the electrons suitably, preferably in a co-catalyst. As the reduction reaction occurs on co-catalyst surface, storing electrons in them is advantageous. However, it requires a large dispersion of metallic co-catalyst integrated with the light absorbing semiconductors. This strategy not only helps for reduction reaction, but also enhances the oxidation reaction. It is to be mentioned that holes are the minority carriers and demanding reactions, such as OER, requires more holes to be available in a small volume. Indeed, in overall water splitting, oxygen evolution requires a potential of 1.23 eV and involves a four-electron process that hinders the overall kinetics of water splitting. To enhance hydrogen evolution, glycerol is used as a sacrificial reagent due to its lower oxidation potential (0.4 V) compared to oxygen evolution (1.23 V).[8] TiO_2 exhibits a large band gap, with a CB position at -0.4 V and a valence band position at around 2.8 V, which is suitable for water splitting. However, a uniform distribution of copper metal acts as both an electron sinks and an active site for hydrogen evolution, thereby enhancing charge separation. The holes in the valence band can oxidize glycerol molecules, since the TiO_2 valence band is much lower than the glycerol oxidation potential, making it easier to oxidize glycerol into a value-added product. A large, uniform dispersion of copper provides more active sites for hydrogen evolution, resulting in the availability of holes for C-C cleavage of glycerol and leading to

higher selectivity for C_2 and C_1 Oxygenates. Cu-metal particles being surface plasmon active material, more electrons would be available on light absorption, which can enhance the reduction reactions.

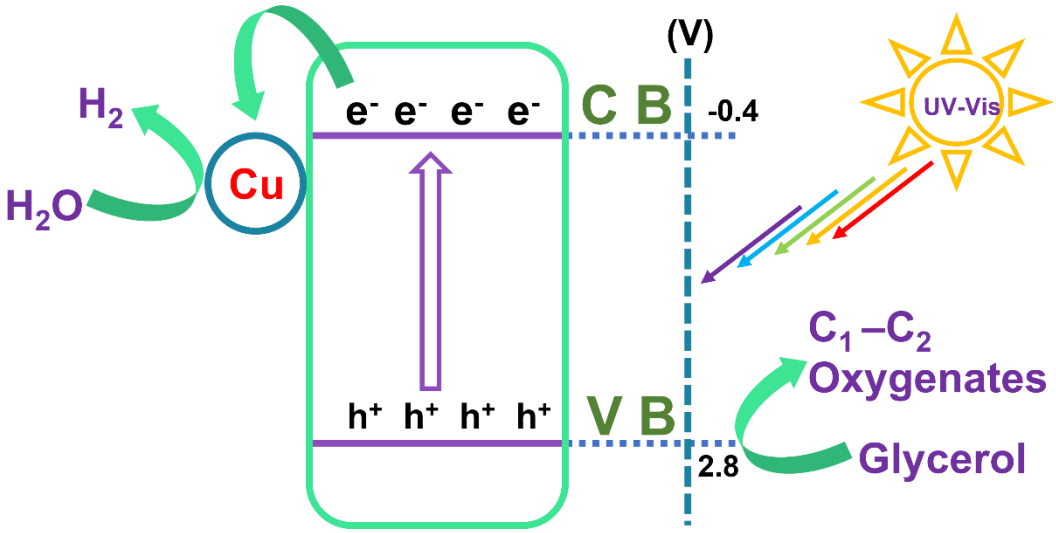


Figure 4.24. Possible mechanism for Cu/TiO_2 toward photocatalytic hydrogen generation and glycerol oxidation towards the value-added products.

4.18 Conclusion:

Throughout this study, we utilised three distinct approaches in order to produce Cu/TiO_2 composites. We demonstrated that TC-PDO exhibits greater activity towards hydrogen evolution and higher selectivity towards glycolaldehyde. Our efforts were concentrated on three primary facets: 1) achieving a higher dispersion of copper as small clusters in order to increase the active surface area of the co-catalyst; 2) utilising a biomass-based feedstock as a sacrificial reagent in order to increase the utilisation of electrons and holes; and 3) selectively oxidising glycerol into products that have additional value. A significant amount of C-C cleavage was also observed, which led to a greater proportion of C_2 and C_1 products in comparison to C_3 products. This suggests that the availability of holes also controls the selectivity of the products.

We utilised three distinct approaches, and although TC-200 may be utilised for the reduction of any metal over TiO_2, its disadvantage is that it is exposed to air, which results in increased hydroxyl species and decreased photoactivity. On the other hand, TC-PDO is a photo-induced method for depositing metal, which varies from typical photo deposition in

that it delivers uniform deposition as well as high electronic integration. Methodology proposed in this chapter can be utilised for a variety of different applications. Employing electrons and holes concurrently for the production of value-added molecules is certainly better than utilizing electrons predominantly to produce hydrogen. This also paves the road for effective and sustainable method for the development of renewable energy sources. A significant difference in the utilization of reduced and oxidized products formation indicates the consumption of electrons are far higher than oxidized products. This indicates the need for further improvements in enhancing the oxidation and more scope is present to bring better strategies.

4.19 References:

1. Patnaik, R., Impact of Industrialization on Environment and Sustainable Solutions – Reflections from a South Indian Region. *IOP Conference Series: Earth and Environmental Science* **2018,** *120*, 012016.
2. Toe, C. Y.; Tsounis, C.; Zhang, J.; Masood, H.; Gunawan, D.; Scott, J.; Amal, R., Advancing photoreforming of organics: highlights on photocatalyst and system designs for selective oxidation reactions. *Energy Environ. Sci* **2021,** *14*, 1140-1175.
3. Ran, J.; Zhang, J.; Yu, J.; Jaroniec, M.; Qiao, S. Z., Earth-abundant cocatalysts for semiconductor-based photocatalytic water splitting. *J. Chem. Sci.* **2014,** *43*, 7787-7812.
4. Maeda, K.; Domen, K., Photocatalytic Water Splitting: Recent Progress and Future Challenges. *J. Phys. Chem. Lett.* **2010,** *1*, 2655-2661.
5. Chen, S.; Takata, T.; Domen, K., Particulate photocatalysts for overall water splitting. *Nat. Rev. Mater.* **2017,** *2*, 17050.
6. Uekert, T.; Pichler, C. M.; Schubert, T.; Reisner, E., Solar-driven reforming of solid waste for a sustainable future. *Nat. Sustain.* **2021,** *4*, 383-391.
7. Wu, Y.-H.; Kuznetsov, D. A.; Pflug, N. C.; Fedorov, A.; Müller, C. R., Solar-driven valorisation of glycerol on BiVO4 photoanodes: effect of co-catalyst and reaction media on reaction selectivity. *J. Mater. Chem. A* **2021,** *9*, 6252-6260.
8. Bajpai, H.; Chauhan, I.; Salgaonkar, K. N.; Mhamane, N. B.; Gopinath, C. S., Biomass components toward H_2 and value-added products by sunlight-driven photocatalysis

with electronically integrated Auδ^-–TiO_2: concurrent utilization of electrons and holes. *RSC Sustainability* **2023**.

9. Uekert, T.; Dorchies, F.; Pichler, C. M.; Reisner, E., Photoreforming of food waste into value-added products over visible-light-absorbing catalysts. *Green Chem.* **2020,** *22*, 3262-3271.
10. Christoforidis, K. C.; Fornasiero, P., Photocatalytic Hydrogen Production: A Rift into the Future Energy Supply. *ChemCatChem.* **2017,** *9*, 1523-1544.
11. Salgaonkar, K. N.; Kale, S. R.; Nalajala, N.; Mansuri, S.; Gopinath, C. S., Selective and Generic Photocatalytic Oxidation of Alcohol with Pd−TiO_2 Thin Films: Butanols to Butanal/Butanone with Different Morphologies of Pd and $0.5\theta_{Pt}$-Pd Counterparts. Chem. Asian J. **2023,** *18*, e202201239.
12. Chen, W.-T.; Dong, Y.; Yadav, P.; Aughterson, R. D.; Sun-Waterhouse, D.; Waterhouse, G. I. N., Effect of alcohol sacrificial agent on the performance of Cu/TiO_2 photocatalysts for UV-driven hydrogen production. *Appl. Catal. A-Gen.* **2020,** *602*, 117703.
13. Montini, T.; Gombac, V.; Sordelli, L.; Delgado, J. J.; Chen, X.; Adami, G.; Fornasiero, P., Nanostructured Cu/TiO_2 Photocatalysts for H2 Production from Ethanol and Glycerol Aqueous Solutions. ChemCatChem. **2011,** *3*, 574-577.
14. Bharad, P. A.; Nikam, A. V.; Thomas, F.; Gopinath, C. S., CuO_x-TiO_2 Composites: Electronically Integrated Nanocomposites for Solar Hydrogen Generation. ChemistrySelect. **2018,** *3*, 12022-12030.
15. Bajpai, H.; Patra, K. K.; Ranjan, R.; Nalajala, N.; Reddy, K. P.; Gopinath, C. S., Can Half-a-Monolayer of Pt Simulate Activity Like That of Bulk Pt? Solar Hydrogen Activity Demonstration with Quasi-artificial Leaf Device. *ACS Appl. Mater. Interfaces* **2020,** *12*, 30420-30430.
16. Zhen, W.; Jiao, W.; Wu, Y.; Jing, H.; Lu, G., The role of a metallic copper interlayer during visible photocatalytic hydrogen generation over a Cu/Cu_2O/Cu/TiO_2 catalyst. *Catal. Sci. Technol.* **2017,** *7*, 5028-5037.
17. Quispe, C. A. G.; Coronado, C. J. R.; Carvalho Jr, J. A., Glycerol: Production, consumption, prices, characterization and new trends in combustion. *Renew. Sust. Energ. Rev* **2013,** *27*, 475-493.

18. Bozell, J. J.; Petersen, G. R., Technology development for the production of biobased products from biorefinery carbohydrates—the US Department of Energy's "Top 10" revisited. *Green Chem.* **2010,** *12*, 539-554.
19. Xiong, L.; Qi, H.; Zhang, S.; Zhang, L.; Liu, X.; Wang, A.; Tang, J., Highly Selective Transformation of Biomass Derivatives to Valuable Chemicals by Single-Atom Photocatalyst Ni/TiO_2. *Adv. Mater.* **2023**, 2209646.
20. Kozlova, E. A.; Kurenkova, A. Y.; Gerasimov, E. Y.; Gromov, N. V.; Medvedeva, T. B.; Saraev, A. A.; Kaichev, V. V., Comparative study of photoreforming of glycerol on Pt/TiO_2 and CuOx/TiO2 photocatalysts under UV light. *Mater. Lett.* **2021,** *283*, 128901.
21. Jang, W.-S.; Pham, V. N.; Yang, S.-H.; Baik, J.; Lee, H.; Kim, Y.-M., Enhanced selective photocatalytic oxidation of a bio-derived platform chemical with vacancy-induced core-shell anatase TiO_2 nanoparticles. *Appl. Catal. B* **2023,** *322*, 122140.
22. Uekert, T.; Kasap, H.; Reisner, E., Photoreforming of Nonrecyclable Plastic Waste over a Carbon Nitride/Nickel Phosphide Catalyst. *J. Am. Chem. Soc.* **2019,** *141*, 15201-15210.
23. Tudu, B.; Nalajala, N.; Prabhakar Reddy, K.; Saikia, P.; Gopinath, C. S., Rationally Designed, Efficient, and Earth-Abundant Ni–Fe Cocatalysts for Solar Hydrogen Generation. *ACS Sustain. Chem. Eng.* **2021,** *9*, 13915-13925.
24. Clarizia, L.; Vitiello, G.; Luciani, G.; Somma, I. D.; Andreozzi, R.; Marotta, R., In situ photodeposited nanoCu on TiO_2 as a catalyst for hydrogen production under UV/visible radiation. *Appl. Catal. A-Gen.* **2016,** *518*, 142-149.
25. Heciak, A.; Morawski, A. W.; Grzmil, B.; Mozia, S., Cu-modified TiO_2 photocatalysts for decomposition of acetic acid with simultaneous formation of C1–C3 hydrocarbons and hydrogen. *Appl. Catal. B* **2013,** *140-141*, 108-114.
26. Lakhera, S. K.; T.P, R.; B.S, R. K.; Rabiee, N.; Bernaurdshaw, N., Pivotal role of oxygen during the synthesis of Cu$(OH)_2$/TiO_2 and its effect on photocatalytic hydrogen production activity. *Catal. Today* **2023**.
27. Martín-Gómez, J.; Escamilla, J. C.; Hidalgo-Carrillo, J.; López-Tenllado, F. J.; Estévez-Toledano, R. C.; Herrera-Beurnio, M. C.; Castillo-Rodríguez, M.; Urbano, F. J.; Marinas, A., Influence of sacrificial agent on Cu photodeposition over TiO_2/MCH composites for photocatalytic hydrogen production. *Catal. Today* **2023,** *413-415*, 113928.

28. Shimura, K.; Yoshida, H., Heterogeneous photocatalytic hydrogen production from water and biomass derivatives. *Energy Environ. Sci.* **2011,** *4*, 2467-2481.
29. Segovia-Guzmán, M. O.; Román-Aguirre, M.; Verde-Gomez, J. Y.; Collins-Martínez, V. H.; Zaragoza-Galán, G.; Ramos-Sánchez, V. H., Green Cu_2O/TiO_2 heterojunction for glycerol photoreforming. *Catal. Today* **2020,** *349*, 88-97.
30. Pecoraro, C. M.; Bellardita, M.; Loddo, V.; Di Franco, F.; Palmisano, L.; Santamaria, M., A facile way to synthesize noble metal free TiO_2 based catalysts for glycerol photoreforming. *J. Ind. Eng. Chem.* **2023,** *118*, 247-258.
31. Reddy, N. L.; Kumar, S.; Krishnan, V.; Sathish, M.; Shankar, M. V., Multifunctional Cu/Ag quantum dots on TiO_2 nanotubes as highly efficient photocatalysts for enhanced solar hydrogen evolution. *J. Catal.* **2017,** *350*, 226-239.
32. Cheng, G.; Hight Walker, A. R., Transmission electron microscopy characterization of colloidal copper nanoparticles and their chemical reactivity. *Anal. Bioanal. Chem.* **2010,** *396*, 1057-1069.
33. Bak, T.; Nowotny, J.; Rekas, M.; Sorrell, C. C., Photo-electrochemical hydrogen generation from water using solar energy. Materials-related aspects. *Int. J. Hydrogen Energy* **2002,** *27*, 991-1022.
34. Bashiri, R.; Mohamed, N. M.; Kait, C. F.; Sufian, S., Hydrogen production from water photosplitting using Cu/TiO_2 nanoparticles: Effect of hydrolysis rate and reaction medium. *Int. J. Hydrogen Energy* **2015,** *40*, 6021-6037.
35. Tian, F.; Zhang, Y.; Zhang, J.; Pan, C., Raman Spectroscopy: A New Approach to Measure the Percentage of Anatase TiO2 Exposed (001) Facets. *J. Phys. Chem. C* **2012,** *116*, 7515-7519.
36. Li, D.; Wang, G.; Cheng, L.; Wang, C.; Mei, X., Engineering the Self-Assembly Induced Emission of Copper Nanoclusters as 3D Nanomaterials with Mesoporous Sphere Structures by the Crosslinking of Ce^{3+}. *ACS Omega* **2018,** *3*, 14755-14765.
37. Menkin, S.; O'Keefe, C. A.; Gunnarsdóttir, A. B.; Dey, S.; Pesci, F. M.; Shen, Z.; Aguadero, A.; Grey, C. P., Toward an Understanding of SEI Formation and Lithium Plating on Copper in Anode-Free Batteries. *J. Phys. Chem. C* **2021,** *125*, 16719-16732.
38. Roy, K.; Gopinath, C. S., UV Photoelectron Spectroscopy at Near Ambient Pressures: Mapping Valence Band Electronic Structure Changes from Cu to CuO. *Anal. Chem.* **2014,** *86*, 3683-3687.

Chapter 4c: Optimizing Ni-Cu Bimetallic Nanoparticles Integrated with Titania for Efficient Hydrogen Production from Biomass: A Photocatalytic Study

4.20 Introduction:

The growing need for energy worldwide, along with the depletion of fossil fuels and their impact on the environment, has led to the quest for alternative energy sources that are sustainable, clean, and don't pollute the environment.[1] Since hydrogen is both clean and green, it has the potential to become a competitive alternative energy source to traditional fossil fuels.[2] Moving away from technologies that produce greenhouse gases and contribute to climate damage, such as those based on fossil fuels, is also necessary because of the rising need for energy worldwide and concerns about the environment.[3] The existing ways of producing hydrogen through the use of fossil fuels, however, result in the emission of greenhouse gases and contribute to climate change. Electrolysis of water, photocatalytic water splitting, and photoelectrochemical (PEC) water splitting are all examples of acceptable methods that may be used to generate sustainable energy and are necessary for addressing this problem. Because solar energy or renewable energy derived from sunlight and water are used as feedstock in these processes, it is possible to produce hydrogen in an environmentally friendly manner using these techniques.[4-7] However, the cost of production of hydrogen by the above methods are to be decreased to acceptable level to the majority of population; this requires further technology developments and large scale operations that can bring down the cost of hydrogen.

One of the potential approaches for creating clean and sustainable hydrogen (H_2) energy using solar light and water is called photocatalytic water splitting. Because of its superior energy density (120 MJ/kg) compared to other hydrocarbon fuels (40-45 MJ/kg), H_2 energy is sometimes referred to as a "future fuel".[8, 9] In order to produce sustainable H_2 energy through the process of water splitting assisted by sunlight, there are three major obstacles to overcome: (a) harvesting the maximum wavelength range of sunlight and converting it into usable chemical energy (H_2), (b) effective utilisation of charge carriers at the redox sites by dispersing them instantly and minimizing their recombination, and (c) overcoming the thermodynamically uphill nature of water splitting (ΔG = 237 kJ/mol; equivalent to 1.23 eV) and supplying the overpotential that is required to initiate the water

splitting reaction.[4] An effective photocatalyst that can use the maximum amount of solar energy, from the ultraviolet area all the way up to the near-infrared, is essential for overcoming the above listed obstacles. The process of water splitting that is facilitated by semiconductor photocatalysts is comparable to photosynthesis, in which water is split in the presence of sunlight in nature; however, the effectiveness of photosynthesis is only ~1%.

Since the announcement of PEC water splitting into hydrogen and oxygen by using Pt and TiO_2 photoelectrode by Fujishima and Honda on 1972, it has attracted a lot of interest.[10] Bard and Fox[11] have expanded the notion of using photoelectrodes to photocatalysis, which is how they came up with the term, because of its stability, proper band-edge position, low cost, and abundant supply. TiO_2 is the most employed semiconductor photocatalyst for the process of water splitting.[11] Yet, due to its broad bandgap (3.2 eV), it is unable to utilise visible light within the solar spectrum. Moreover, the fast recombination of photogenerated electron–hole pair reduces the photocatalytic efficiency of the material. In order to enhance the performance of TiO_2 photocatalysis, many methods have been investigated, including metal deposition, the incorporation of sacrificial reagents, dye sensitization, and the doping of metal and nonmetal cations in TiO_2 lattice.[3,5,12,13] It has been discovered that the production of solar hydrogen has significantly improved by the deposition of noble metals on TiO_2 and other photocatalysts as well as the inclusion of sacrificial oxidation reagents. In order to effectively separate the photogenerated electron–hole pairs, minimize recombination and in turn increase the charge utilisation in photocatalysis events, it is possible for metal nanoparticles (NPs) to establish the Schottky junction at the interface between metal and semiconductors. In spite of the fact that naturally plentiful and low-cost non-noble metal-based cocatalysts are available, their usage is not high for several reasons, including the relatively easy oxidation of transition metals. However, by adopting suitable synthesis and integration with photocatalytic semiconductors, it can be utilised for solar hydrogen production, which is also economically viable. In order to investigate the earth-abundant first-row transition metals as cocatalysts for the solar H_2 evolution process, some research has been done, and much more needs to be carried out.[14-17]

In photocatalytic water splitting, utilization of biomass as a sacrificial agent has a number of advantages and possibly it can improve the value addition. To begin with, it

includes processes that require less energy than the conventional OER. While OER requires high potential and overpotential, is a four-electron process and hence kinetically sluggish; however, oxidation of biomass components requires far low potential and add value with formation of products. These reactions replace the role of the slow oxygen evolution reaction, which enhances the efficiency of hydrogen evolution in a synergetic manner. The second advantage of biomass is that it makes use of organic waste, which have the potential to be transformed into valuable organic products. Finally, it suppresses the return reaction between H_2 and O_2 that occurs during the photocatalytic splitting of water. The presence of biomass organic molecules during photocatalytic hydrogen production provides an alternative catalytic pathway. This pathway allows the highly endergonic nature and large energy requirement of water oxidation to be replaced with the oxidation of organic molecules, which in turn allows the production of hydrogen and value-added products. This often contains a lower Gibb's free energy of reaction, which lessens the thermodynamic energy barrier and lowers the total energy input necessary to drive hydrogen synthesis at realistic rates.[13, 18-22] This is beneficial since it allows for more efficient generation of hydrogen.

It is possible to employ a considerable amount of trash, especially biomass/biowaste related, with high enthalpy to promote chemical reactions. For example, waste from businesses such as food and beverage manufacturing, agricultural production, and biofuel production may be used as chemical feedstocks.[20, 22] Throughout the course of the last decade, selective oxidation for photocatalytic organic synthesis and/or biomass degradation has also been the subject of substantial research and investigation. Overall, utilizing the biomass as a sacrificial reagent for photocatalytic water splitting as well as production of value-added chemical is an attractive strategy towards sustainable future.[13]

In the present study, we employed impregnation method to integrate TiO_2 with various compositions of NiCu bimetallic system. We synthesized various compositions of NiCu bimetallic nanoparticles and utilized glycerol as a sacrificial reagent. Additionally, we expanded our investigation to include real-time biomass, specifically cellulose and tissue paper. This study shows the potential of cellulose as a feedstock for hydrogen evolution reaction.

4.21 Solar Hydrogen Evolution:

With the addition of Ni-Cu as a cocatalyst, the hydrogen generation activity of various composites was thoroughly investigated, as detailed in chapter 2, section 2.1.5. All catalysts were synthesized using solvothermal followed by impregnation methods. Catalyst code is denoted as TNC-xy; T-TiO_2, NC-for NiCu, and xy for composition of Ni and Cu employed. The results of the photocatalytic H_2 generation measured with different compositions of NiCu nanoparticles loaded on TiO_2 are presented in Fig. 4.25. Solar hydrogen production was measured under one sun (100 mW/cm^2) conditions and carried out systematically with different biomass components. The hydrogen evolution measurement was performed using 3 mg of catalyst in a 20 ml solution, kept under irradiation without stirring, and the photocatalytic reaction was conducted at neutral pH (pH = 7$\pm$0.2). When glycerol was used as a sacrificial reagent, TiO_2 produced only 0.8 mmol $h^{-1}g^{-1}$ hydrogen. Incorporating Ni nanoparticles onto TiO_2 (TNC-10) increased the H_2 production rate doubled to 1.5 mmol $h^{-1}g^{-1}$ However, when only copper was integrated with TiO_2 (TNC-01), the photocatalytic hydrogen evolution was enhanced 10-fold compared to TiO_2, and 5-fold compared to TNC-10. To further enhance the photoactivity, different ratios of NiCu bimetal nanoparticles were incorporated onto TiO_2. It is to be reiterated again that the total amount of co-catalyst is maintained to be 1 wt %, irrespective of NiCu composition.

By varying the ratio between Ni and Cu, it was found that TNC-23 (Ni:Cu 2:3) exhibited the highest hydrogen production rate of 22 mmol $h^{-1}g^{-1}$ of photocatalyst, surpassing TNC-32 (16.5 mmol/h.g) and TNC-11 (14 mmol $h^{-1}g^{-1}$). The wet impregnation method employed was effective in creating Schottky junctions between TiO_2 and the bimetallic nanoparticles, as revealed in HRTEM images (shown later in Fig.4.29). Interestingly, when only Ni or Cu were incorporated onto TiO_2, the activity was lower compared to any composition of the NiCu bimetallic nanoparticles, indicating a synergy between Ni and Cu in enhancing charge transfer from bulk to surface. It is also likely that the extent of charge separation to be the highest with NiCu(2:3) composition.

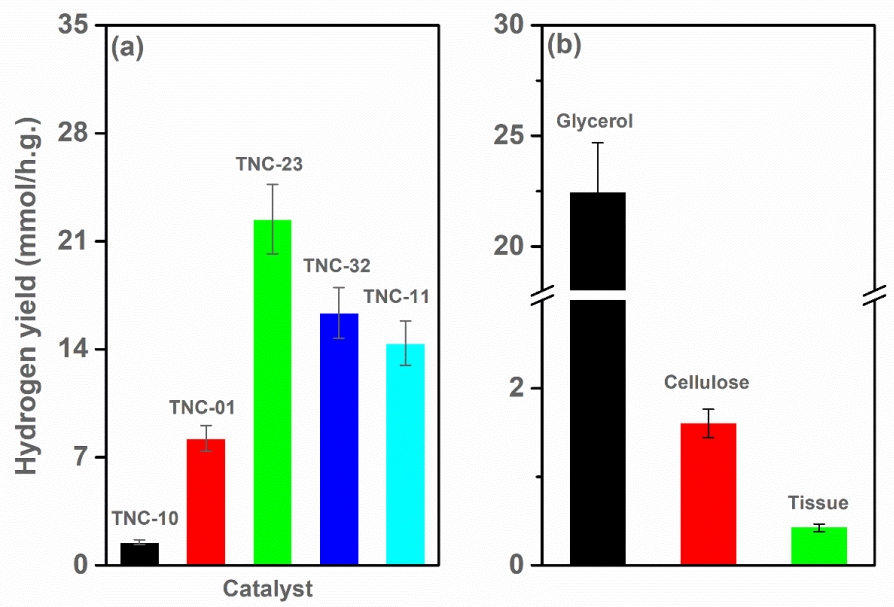


Figure 4. 25. (a) Photocatalytic hydrogen yield observed for (a) different compositions of 1% of NiCu bimetal nanoparticles on TiO_2, and (b) Photocatalytic activity displayed for different sacrificial reagents measured with TNC-23; 5% glycerol was used as sacrificial reagent under one sun conditions with a solar simulator at pH=7; 20 mg cellulose or tissue paper was employed as sacrificial reagent for photocatalytic reaction.

In addition to glycerol, cellulose and tissue paper were also evaluated as sacrificial agents. Cellulose and tissue paper represent real-world biomass, unlike glycerol which is a by-product of biodiesel production. Cellulose and tissue paper have similar building blocks as that of glycerol, except for chain length. Hydrogen evolution from cellulose was found to be sustainable and energy-efficient, as it directly utilizes biomass for green hydrogen production, reducing the need for energy-intensive steps. Fig. 4.25b shows the average H_2 yield obtained from cellulose, where a 20 ml solution containing 10 mg of cellulose and 3 mg of catalyst (TNC-23) resulted in the H_2 yield of 1.6 mmol $h^{-1}g^{-1}$ under one sun condition, compared to 22 mmol $h^{-1}g^{-1}$ from glycerol. Twelve-fold decrease in H_2 yield from cellulose is attributed to the long-chain structure of cellulose, which results in more difficult C-C cleavage and slows down the overall kinetics by consuming a significant number of electrons and protons. Nevertheless, this result is still significant and opens up possibilities for utilizing biomass components for photocatalytic hydrogen production. The solubility of cellulose needs to be increased without employing harsh acidic or basic conditions, which could be a potential avenue for future research. In the experiment with tissue paper, 10 mg of tissue paper (Cleen from Paper Kraft

MFG. Pvt. Ltd.) was mixed with 20 ml of water and 3 mg of catalyst, and then subjected to one sun irradiation. However, due to the non-uniform dispersion of tissue paper in water, the activity decreased to 0.4 mmol $h^{-1}g^{-1}$ A more systematic approach from waste biomass components to hydrogen and any value-added products (VAP) would be more appealing in this case. We speculate the following, in view of the long-chain of C-C bonds in cellulose. Unless a significantly large extent of C-C cleavage occurs, it may be difficult to start observing the low molecular weight oxygenate products, such as methanol, ethanol. We believe that large number of holes are utilized in the C-C cleavage and making the cellulose into smaller fragments. However, this process needs to continue sufficiently long time under one sun illumination, till the simple or reasonable size oxygenate products formation is observed. In addition, very low concentration of cellulose may be utilized to enhance the products formation, by utilizing the charges effectively. Hence more efforts are required in this direction.

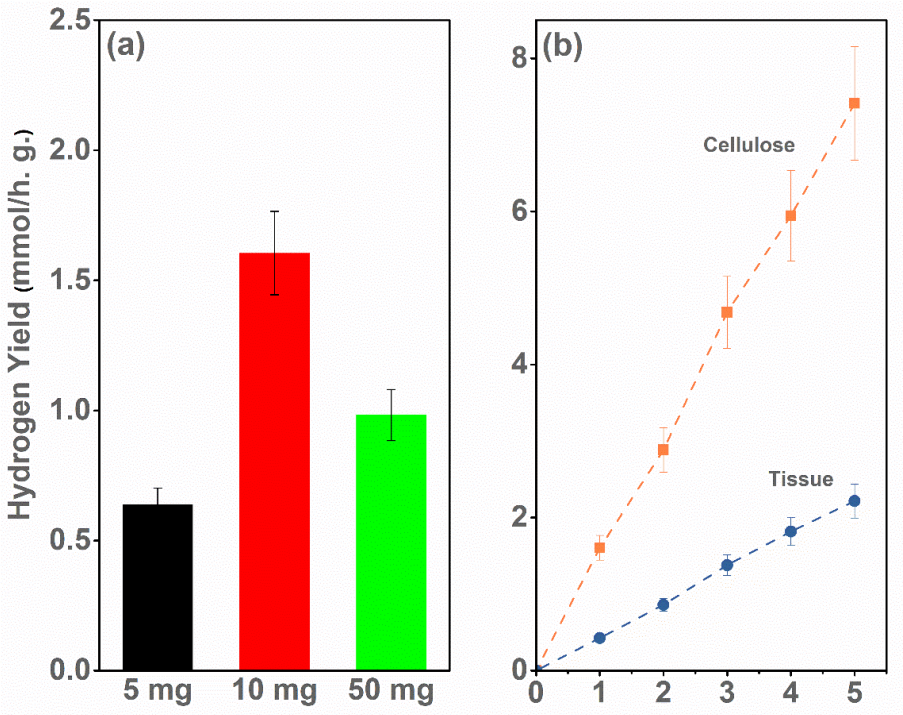


Figure 4.26. (a) Photocatalytic hydrogen yield observed for different concentration of Cellulose with TNC-23. (b) Photocatalytic hydrogen production observed as a function of illumination time, using cellulose and tissue paper as sacrificial reagent with TNC-23; 20 mg of cellulose and tissue paper was used for photocatalytic reaction.

To understand the effect of sacrificial reagent concentration, three different cellulose concentrations (5 mg, 10 mg, and 50 mg) were employed, and the activity was measured with TNC-23 in 20 ml of DI water with cellulose under one sun condition. The results, as shown in Fig. 4.26, revealed the following: First, a solution containing 10 mg of cellulose showed a constant hydrogen yield of 1.6 mmol $h^{-1}g^{-1}$ as a function of irradiation time. Second, among the three different cellulose concentrations (5 mg, 10 mg, and 50 mg) tested, 10 mg exhibited the best performance. Third, while 10 mg of tissue paper also showed a constant hydrogen yield of 0.4 mmol $h^{-1}g^{-1}$, it was far lower than that of cellulose. The dependence of hydrogen generation on the concentration of the reactant was demonstrated, and stability was shown up to 5 hours with both 10 mg of cellulose and tissue paper. It is worth noting that beyond a threshold concentration of the sacrificial agent, the active sites may become saturated with these molecules, leading to a decrease in photoactivity. In the present case, the solubility factor of cellulose also contributes to the scattering of light, which further decreases the photoactivity. These results indicate that an optimal cellulose concentration is required to achieve the best photoactivity in this experiment.

4.22 UV-Vis Absorption Spectra:

An ultraviolet-visible diffuse reflectance spectroscopy (DRS) investigation was carried out in order to evaluate the optical characteristics of TNC photocatalysts. The fact that the bandgap of titania nanoparticles cannot be altered by the presence of the bimetallic alloy was demonstrated by the fact that all TNC composites exhibited an absorption cut-off at a wavelength of around 380 nm (Figure 4.27). A rise in the absorption coefficient at longer wavelengths, on the other hand, revealed that light absorption had moved from the ultraviolet part of the solar spectrum to the visible region of the spectrum. It is important to keep in mind that scattering of light at longer wavelengths (greater than 450 nm) may also be a component that contributes to the linear rise in absorption, and not due to visible light absorption. Indeed, the experiment reported in Fig. 4.26 carried out with 550 nm filter produces no hydrogen, hinting the enhanced absorption seen at higher wavelength is indeed due to scattering.

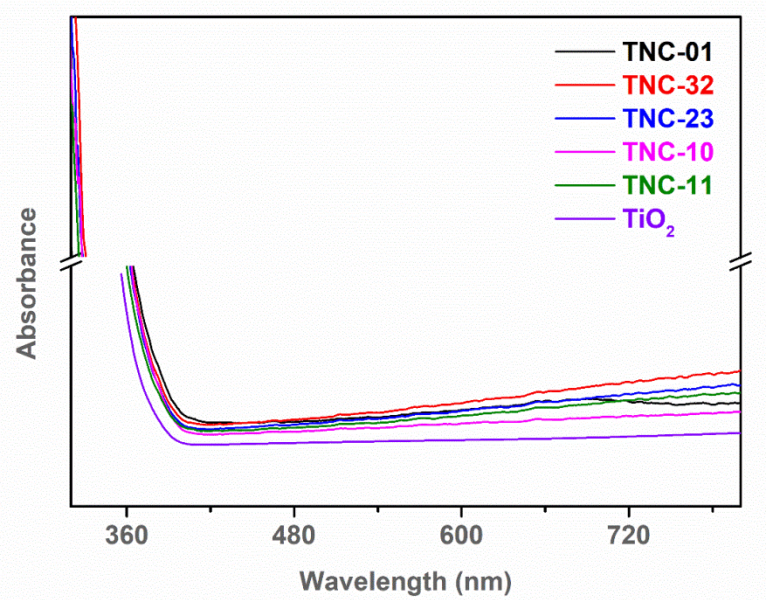


Figure 4.27. UV-Vis spectra of TiO_2, TNC-01, TNC-10, TNC-23, TNC-32, TNC-11.

The plasmonic behaviour of Cu may be responsible for the feeble absorption that was seen in TNC-01 at 650 nm. Nevertheless, the fact that there was no evidence of surface plasmon resonance (SPR) observed with any of the other NiCu bimetallic nanoparticles supports the formation of Cu-Ni alloy, which may lessen the intensity of SPR absorption.

4.23 Structural Characterization:

In order to explore the integration and structural characteristics of the bimetallic junction with TiO_2, we employed XRD, HRTEM, and elemental mapping. The XRD patterns of TNC-32, TNC-23, TNC-11, TNC-10, and TNC-01 are shown in Fig. 4.28. Diffraction features observed are exclusively from anatase and rutile phases of TiO_2. It is also to be noted the 1 wt % of NiCu alloy is too small amount to be observed in XRD. As XRD patterns showed no signs of alteration, it may be deduced that the bimetallic alloy had no impact on the anatase and rutile phases of the titanium dioxide. The fact that water splitting is a surface-dependent process and the co-catalyst should be accessible on the surface, and the earlier results (Figs. 4.25-4.26) have attested the activity due to NiCu cocatalysts, it is expected that the NiCu bimetallic nanoparticles were integrated onto the surface of TiO_2.

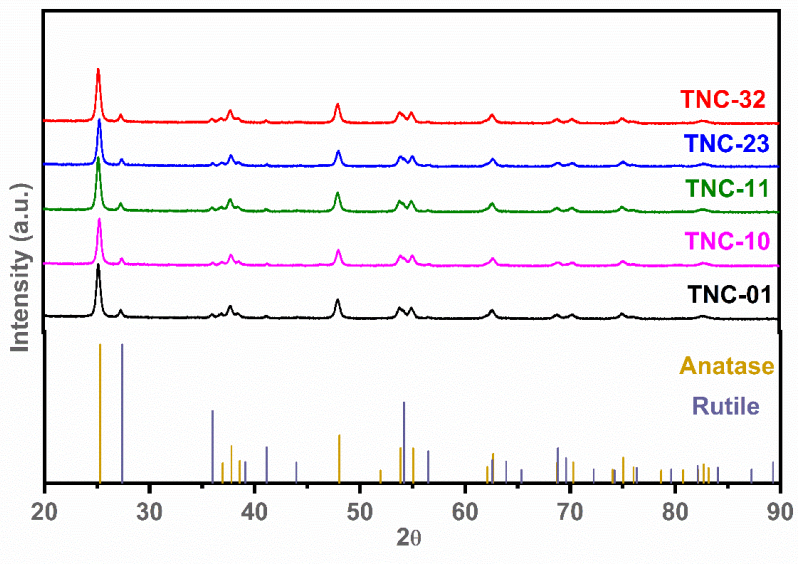


Figure 4.28. XRD patterns of TiO_2, TNC-01, TNC-10, TNC-23, TNC-32, TNC-11. No bimetallic or monometallic feature was observed in the diffraction patterns.

Although photocatalysis results indicate the integration of NiCu with TiO_2, no direct proof for the same could be obtained from XRD or light absorption results. Since the amount of NiCu is too low, a careful investigation was carried out with TEM and HRTEM and the results obtained are shown in Fig. 4.29. Panels a and b shows the TEM images for virgin NiCu(2:3) nanoparticles. A small aggregate of NiCu particle could be seen. In panels c, d, and e, HRTEM images of TNC-23 are displayed at 20 nm and 5 nm scales, respectively. The NiCu ratio was tuned for increased hydrogen generation, the HRTEM analysis showed that the integration of TiO_2 and NiCu bimetallic nanoparticles is extremely important (Fig. 4.29). The distribution of NiCu bimetallic nanoparticles is shown in panel e, coupled with an enlarged view of the yellow square seen in panel e. Panel e indicates that there are dark gradients of the nanoparticles over TiO_2. The Schottky junction between TiO_2 and NiCu bimetallic nanoparticles can be seen in the magnified picture. The d-spacing of the TiO_2 nanoparticles is 0.35 nm (101), while the d-spacing of the NiCu bimetallic nanoparticles is 0.18 nm (200). A nicely integrated TiO_2-NiCu assembly lead to a high quality Schottky junction, which helps for charge separation. Electrons are stored in the metal or bimetal alloy, while TiO_2 executes the oxidation reactions.

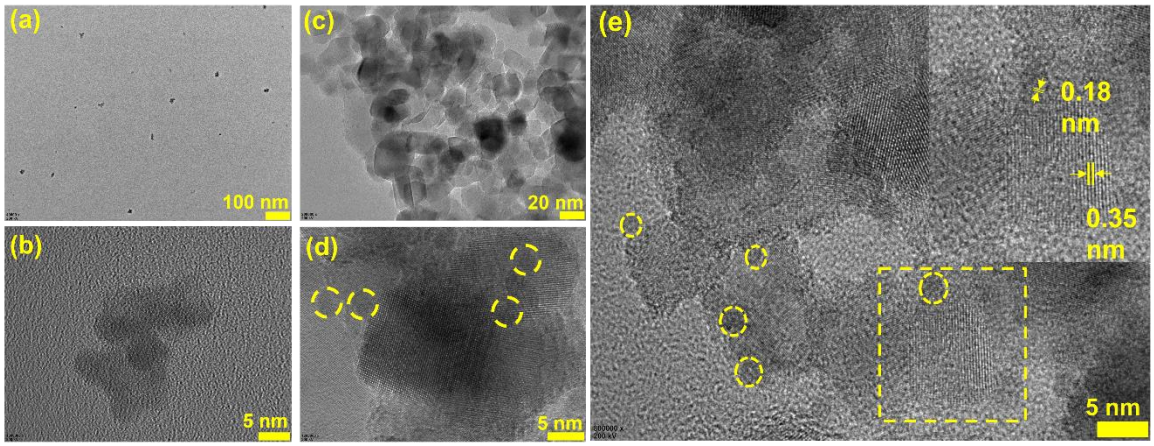


Figure 4.29. TEM and HRTEM images recorded for virgin NiCu(2:3) and TNC-23. a and b show the TEM and HRTEM images of NiCu-23 bimetal nanoparticles. Panel c shows TEM image of TNC-23. HRTEM images are shown for TNC-23 in panel d and e. Inset in image e is the enlarged image of highlighted square in image e. Schottky junction was observed in e between TiO_2 and NiCu bimetal nanoparticle. Broken yellow circles shown in d and e is for the observation of NiCu nanoparticles.

4.24 Conclusion:

In the present study, we have successfully synthesized a series of mono (Ni or Cu) and different compositions of bimetallic (NiCu) nanoparticles integrated with commercial titania (P25) using a solvothermal route, specifically focusing on copper (Cu) and nickel (Ni) based catalysts. Aim of the present work is to optimize the ratio between Ni and Cu in order to maximize hydrogen (H_2) production with biomass as a sacrificial reagent. The synthesized catalysts were then evaluated for solar hydrogen generation using different types of bio-mass, namely glycerol, cellulose, and tissue paper, as sacrificial reagents. Current findings revealed that the photocatalyst TNC-23 (with 1 wt% composition of the bimetallic nanoparticles) exhibited the highest hydrogen yield (HY) with glycerol, cellulose, and tissue paper, producing 22, 1.6, and 0.6 mmol $h^{-1}g^{-1}$, respectively, which outperformed other compositions of photocatalysts. The improved activity of TNC-23 can be attributed to enhanced absorption of light and efficient generation and utilization of charge carriers, resembling the natural process of photosynthesis in green leaves. The optimized composition of Cu and Ni in the bimetallic nanoparticles resulted in synergistic effects that enhanced the photocatalytic activity, leading to higher hydrogen production.

One of the notable aspects of the present research effort is in employing the biomass, particularly glycerol and cellulose, as sacrificial reagents for hydrogen production. Glycerol, being a by-product of biodiesel production, offers a sustainable and renewable source for hydrogen production. Furthermore, using raw biomass directly as a sacrificial reagent eliminates the need for an energy-intensive pre-treatment process, making the overall hydrogen production process more energy-efficient and environment friendly. Nonetheless, there is a long way towards improving and optimizing the activity with long-chain components, like cellulose.

In addition to the role of biomass, present research effort also emphasizes the importance of other factors such as light absorption, charge carrier dispersion, and charge utilization at redox sites. These aspects need to be intricately integrated to achieve optimal photocatalytic activity. Further studies are required to corroborate and validate the proposed mechanisms and findings presented in our article. The results of our research highlight the potential of photocatalysis as a sustainable and green approach for hydrogen production, utilizing biomass as a sacrificial reagent. The use of bimetallic nanoparticles supported on titania, optimized composition of Cu and Ni, and the choice of biomass as a sacrificial reagent open up new avenues for renewable and environment friendly hydrogen production. Our findings contribute to the growing body of knowledge in the field of photocatalysis and pave the way for future research in this area.

4.25 References:

1. Christoforidis, K. C.; Fornasiero, P., Photocatalytic Hydrogen Production: A Rift into the Future Energy Supply. *ChemCatChem* **2017,** *9*, 1523-1544.
2. Maeda, K.; Domen, K., Photocatalytic Water Splitting: Recent Progress and Future Challenges. *J. Phys. Chem. Lett.* **2010,** *1*, 2655-2661.
3. Wang, F.; Li, Q.; Xu, D., Recent Progress in Semiconductor-Based Nanocomposite Photocatalysts for Solar-to-Chemical Energy Conversion. *Adv. Energy Mater.* **2017,** *7*, 1700529.
4. Liao, C.-H.; Huang, C.-W.; Wu, J. C. S., Hydrogen Production from Semiconductor-based Photocatalysis via Water Splitting. *Catalyst* **2012,** *2*, 490-516.

5. Sivaranjani, K.; Agarkar, S.; Ogale, S. B.; Gopinath, C. S., Toward a Quantitative Correlation between Microstructure and DSSC Efficiency: A Case Study of TiO_2–xNx Nanoparticles in a Disordered Mesoporous Framework. *J. Phys. Chem. C* **2012,** *116*, 2581-2587.
6. Ghosh, S.; Basu, R. N., Multifunctional nanostructured electrocatalysts for energy conversion and storage: current status and perspectives. *Nanoscale* **2018,** *10*, 11241-11280.
7. Liu, J.; Ke, J.; Li, Y.; Liu, B.; Wang, L.; Xiao, H.; Wang, S., Co_3O_4 quantum dots/TiO_2 nanobelt hybrids for highly efficient photocatalytic overall water splitting. *Appl. Catal. B: Environ.* **2018,** *236*, 396-403.
8. Staffell, I.; Scamman, D.; Velazquez Abad, A.; Balcombe, P.; Dodds, P. E.; Ekins, P.; Shah, N.; Ward, K. R., The role of hydrogen and fuel cells in the global energy system. *Energy Environ. Sci.* **2019,** *12*, 463-491.
9. Peng, Y.; Jiang, K.; Hill, W.; Lu, Z.; Yao, H.; Wang, H., Large-Scale, Low-Cost, and High-Efficiency Water-Splitting System for Clean H2 Generation. *ACS Appl. Mater. Interfaces* **2019,** *11*, 3971-3977.
10. Fujishima, A.; Honda, K., Electrochemical Photolysis of Water at a Semiconductor Electrode. *Nature* **1972,** *238*, 37-38.
11. Bard, A. J.; Fox, M. A., Artificial Photosynthesis: Solar Splitting of Water to Hydrogen and Oxygen. *Acc. Chem. Res.* **1995,** *28*, 141-145.
12. Ran, J.; Zhang, J.; Yu, J.; Jaroniec, M.; Qiao, S. Z., Earth-abundant cocatalysts for semiconductor-based photocatalytic water splitting. *Chem. Soc. Rev.* **2014,** *43*, 7787-7812.
13. Toe, C. Y.; Tsounis, C.; Zhang, J.; Masood, H.; Gunawan, D.; Scott, J.; Amal, R., Advancing photoreforming of organics: highlights on photocatalyst and system designs for selective oxidation reactions. *Energy Environ. Sci.* **2021,** *14*, 1140-1175.
14. Du, P.; Eisenberg, R., Catalysts made of earth-abundant elements (Co, Ni, Fe) for water splitting: Recent progress and future challenges. *Energy Environ. Sci* **2012,** *5*, 6012-6021.
15. Furukawa, S.; Nishimura, G.; Takayama, T.; Komatsu, T., Highly Active Ni- and Co-Based Bimetallic Catalysts for Hydrogen Production From Ammonia-Borane. *Front. Chem.* **2019,** *7*.

16. Bajpai, H.; Patra, K. K.; Ranjan, R.; Nalajala, N.; Reddy, K. P.; Gopinath, C. S., Can Half-a-Monolayer of Pt Simulate Activity Like That of Bulk Pt? Solar Hydrogen Activity Demonstration with Quasi-artificial Leaf Device. *ACS Appl. Mater. Interfaces* **2020,** *12*, 30420-30430.
17. Tudu, B.; Nalajala, N.; Prabhakar Reddy, K.; Saikia, P.; Gopinath, C. S., Rationally Designed, Efficient, and Earth-Abundant Ni–Fe Cocatalysts for Solar Hydrogen Generation. *ACS Sus. Chem. Eng.* **2021,** *9*, 13915-13925.
18. Xiong, L.; Qi, H.; Zhang, S.; Zhang, L.; Liu, X.; Wang, A.; Tang, J., Highly Selective Transformation of Biomass Derivatives to Valuable Chemicals by Single-Atom Photocatalyst Ni/TiO_2. *Adv. Mater.* **2023**, 2209646.
19. Bozell, J. J.; Petersen, G. R., Technology development for the production of biobased products from biorefinery carbohydrates—the US Department of Energy's "Top 10" revisited. *Green Chem* **2010,** *12*, 539-554.
20. Shimura, K.; Yoshida, H., Heterogeneous photocatalytic hydrogen production from water and biomass derivatives. *Energy Environ. Sci* **2011,** *4*, 2467-2481.
21. Kumaravel, V.; Imam, M. D.; Badreldin, A.; Chava, R. K.; Do, J. Y.; Kang, M.; Abdel-Wahab, A., Photocatalytic Hydrogen Production: Role of Sacrificial Reagents on the Activity of Oxide, Carbon, and Sulfide Catalysts. *Catalyst* **2019,** *9*, 276.
22. Uekert, T.; Dorchies, F.; Pichler, C. M.; Reisner, E., Photoreforming of food waste into value-added products over visible-light-absorbing catalysts. *Green Chem.* **2020,** *22*, 3262-3271.



Chapter 5

Defect Optimization in TiO_2, for Efficient Photocatalytic Nitrogen Fixation

Enhancing Photocatalytic Nitrogen Fixation through Defective TiO_2 Composites: Optimization of Surface Defects

5.1 Introduction:

Nitrogen is a crucial constituent for the survival of all living organisms, owing to its presence in amino acids, proteins, and nucleic acids. Nitrogenous compounds are widely distributed in the natural world, and the transformation of molecular nitrogen to ammonia is a crucial mechanism for the generation of molecules that sustain life on planet Earth. The biological nitrogen cycle is heavily dependent on the natural process of ammonia production facilitated by the nitrogenase enzyme.[1, 2] The demand for fertilisers in order to satisfy the increasing food requirements during the initial years of the 20th century resulted in the development of the Haber-Bosch process. This process pertains to the transformation of molecular nitrogen with hydrogen into ammonia, and constitutes roughly 1-3% of the global energy usage.[3] Nevertheless, the ecological implications of this procedure are a matter of apprehension. The manufacturing procedure necessitates a substantial quantity of energy, predominantly sourced from non-renewable fossil fuels, resulting in a noteworthy detrimental effect on the ecosystem.[4-6] Moreover, the utilisation of fertilisers and other chemical compounds intensifies this effect. In contrast, ammonia has the potential to be a feasible alternative for hydrogen storage, due to its comparatively simplified transportation in comparison to hydrogen.[7-9] With the projected global population to be 9 billion by 2042, there will be a sustained rise in the demand for both food and fertilisers. Hence, it is imperative to substitute the existing procedure with a viable and environmentally conscious substitute.[10] The process of nitrogen conversion to ammonia is exothermic, resulting in the liberation of energy (-92 kJ/mol).[11] However, the process of breaking the nitrogen's triple bond, which has an energy requirement of 941 kJ/mol, necessitates the use of elevated temperatures and pressure. Three pathways for nitrogen to ammonia synthesis have been proposed by researchers, namely the dissociative pathway, the associative pathway, and the associative distal pathway.[10]

The present method of ammonia synthesis is not environmentally sustainable, as it heavily depends on hydrogen generated from methane reforming and coal gasification, resulting in the emission of 1.87 tonne of CO_2 per tonne of NH_3.[12] Although water shows potential as a hydrogen source, the process of splitting it into hydrogen necessitates

temperatures of higher than 1000° C, which poses challenges in terms of energy efficiency and economic feasibility.[13] In order to advance the promotion of sustainable and environmentally conscious ammonia production, it is imperative to investigate alternative methodologies that have the potential to diminish the carbon footprint. A plausible resolution entails the utilisation of sustainable energy resources, such as solar or wind power, to produce hydrogen via the process of water electrolysis. An additional option involves the development of novel catalysts that can expedite the conversion of nitrogen to ammonia under near-ambient temperatures and pressures, thereby enhancing the energy efficiency and cost-effectiveness of the procedure.[14-18]

The utilisation of photo-catalytic nitrogen fixation has the potential to serve as a viable substitute for the Haber-Bosch process. The utilisation of solar energy to catalyse the nitrogen fixation reaction obviates the necessity for fossil fuels and mitigates carbon emissions. Furthermore, this particular procedure can be executed under normal atmospheric conditions and temperature, rendering it a more economical and energy-efficient substitute for the Haber-Bosch process.[11,14,15] The implementation of photo-catalytic nitrogen fixation technology holds potential for advancing a sustainable and environmentally conscious approach to ammonia production, a crucial element in sustaining life on planet Earth. The initial documentation of the prospective application of photocatalytic nitrogen fixation in ambient atmosphere under visible light was presented by Schrauzer and Guth.[19] The challenge of achieving efficient nitrogen to ammonia fixation arises due to the low binding energy of nitrogen to the catalyst surface and the high activation energy of the intermediate species.[10] The activation of the triple bond in nitrogen is a significant hindrance in the attainment of effective nitrogen fixation, which is contingent exclusively upon electrons induced by light in the conduction band of semiconductors. In order to address this issue, it is necessary to incorporate active electron donor sites that exhibit both effective electron donation capacity and robust adsorption properties towards nitrogen molecules.[20] The active centres exhibit the capability to adsorb nitrogen molecules, thereby reducing the strength of the nitrogen triple bond and facilitating the subsequent reduction process, owing to their significant electron-donating capacity. The presence of active oxygen vacancies on the surface can serve as centres for electron trapping and donation towards the conversion of nitrogen to ammonia.[21-23]

Titanium dioxide (TiO_2) is a semiconductor that has been the subject of extensive research due to its potential applications in various fields, including water splitting, degradation of organic impurities, antibacterial activity, and solar cells. The compound exhibits favourable characteristics for utilisation in photocatalytic processes owing to its high stability, abundance, and negligible toxicity.[17] Numerous strategies have been suggested to enhance the efficacy of TiO_2, such as the introduction of defects. The presence of oxygen vacancies within the TiO_2 lattice leads to the emergence of Ti^{3+} sites that exhibit a significant electron density and a low formation energy. The generation of Ti^{3+} sites is a viable strategy to enhance light absorption in the visible and near-infrared regions through the establishment of a confined bandgap.[24-28] It is noteworthy that enhancing light absorption is of paramount significance; however, it is equally imperative to optimise the electronic structure to enable the expeditious transfer of charges to redox sites.[29] The present investigation involved the synthesis of Ti^{3+} enriched TiO_2 via $NaBH_4$ treatment, followed by temperature treatment to optimise the defect and improve the photocatalytic nitrogen fixation process. The composites underwent characterization through the utilisation of HRTEM, XPS, and RAMAN methodologies.

5.2 XRD and UV-Vis Characterization:

Photocatalyst synthesis details are described in Sec. 2.2.7. The materials' crystal structure and optical properties were analysed using XRD and UV-Visible absorption spectroscopy methods. The XRD pattern of P25 TiO_2 and calcined P25 TiO_2 at various temperatures is depicted in Figure 5.1a. As expected, P25-TiO_2 shows typical anatase and rutile features. Interestingly, T-350 and T-550 exhibit comparable and characteristic features as that of P25; whereas T-750 has undergone a transformation predominantly to the rutile phase of TiO_2, which is discernible from its X-ray diffraction pattern. It is also to be noted that, as expected, high temperature treatment leads to an increase in intensity of the rutile features with a significant reduction in line width; this suggests an increase in the crystallite size of rutile particles. The BT-composites were also subjected to XRD analysis, and the results are depicted in Figure 5.1b. A careful look at the XRD reveals the following: Line shape analysis suggests an asymmetric XRD features for BT, BT-350 and BT-550. The XRD pattern also indicates a marginal shift towards elevated angles, implying the formation of defects in BT-350 and BT-550 (fig. 5.1c).[30] The augmentation of full-width at half maximum (FWHM) of XRD

features denotes a reduction in crystallinity in the BT specimens, which is in line with the findings of the HRTEM assessment. However, BT-750 demonstrated analogous characteristics, as that of the rutile phase.

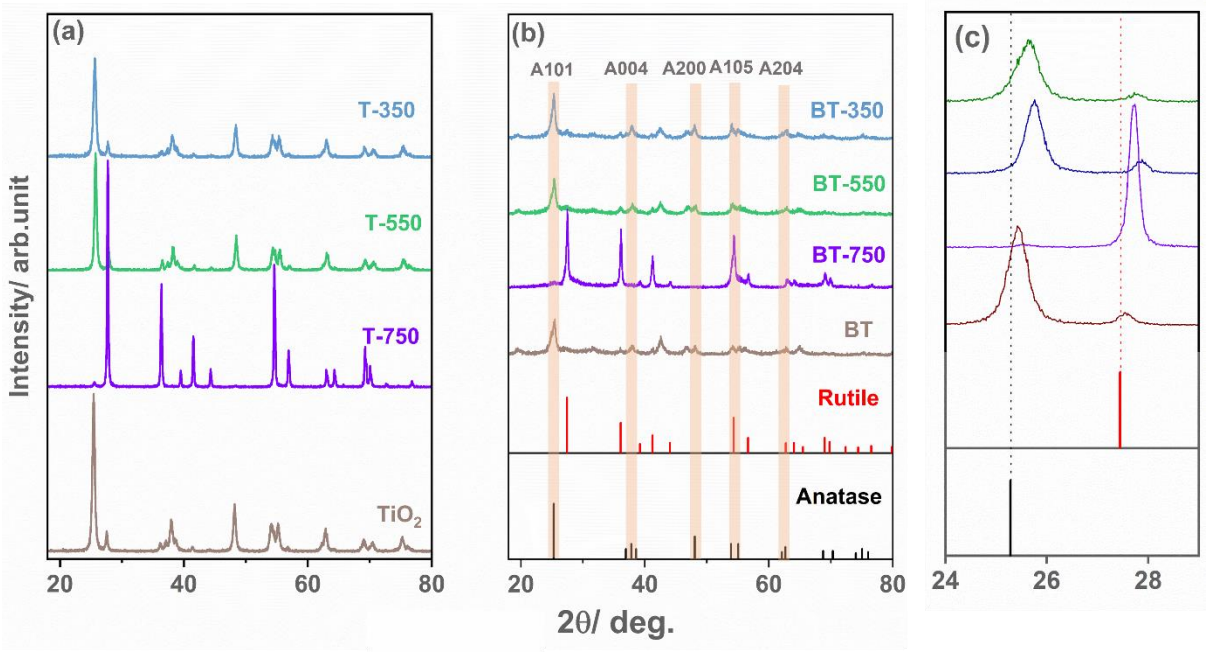


Figure 5.1: (a) XRD pattern of TiO_2, T-350, T-550, T-750 and (b) XRD pattern of BT, BT-350, BT-550, BT-750, (c) Enlarge image of figure 5.1(b) from angle 24 to 29, all colour traces are similar to figure 5.1(b)

Figure 5.2a presents the relative intensity of crystal planes (highlighted planes in fig. 5.1b) in all BT samples, aimed at enhancing comprehension of their characteristics across various composites. Relative intensity is calculated with respect to plane (101). The findings suggest that the comparative magnitude of the composites is consistent across the board, with the exception of BT-350, which displays a distinct characteristic for the (200) plane. The increased relative intensity of the (200) plane observed in BT-350 indicates a higher degree of stability, potentially leading to improved efficacy in facilitating charge transfer during the photocatalytic reaction.

The UV-Visible spectra of TiO_2 and the BT-composites are presented in Figure 5.2b. The spectra of BT-composites display a red shift in comparison to TiO_2. Whilst the absorption

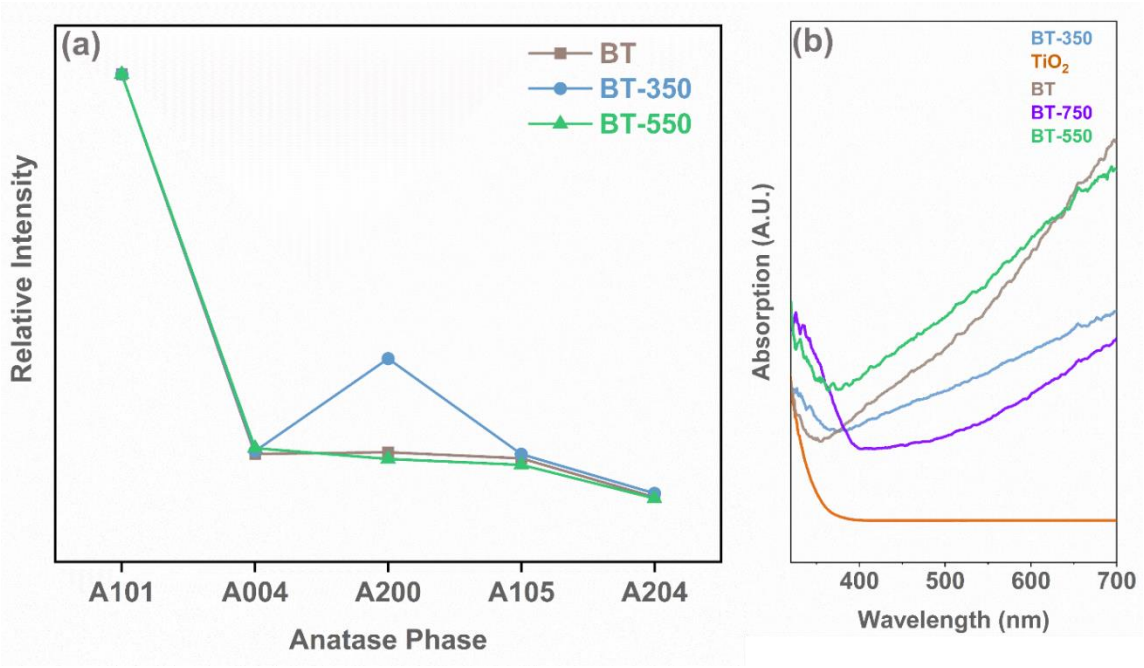


Figure 5.2: (a) Relative Intensity of BT, BT-350, BT-550 for different crystal planes, and (b) UV-Visible absorption spectra of TiO_2, BT, BT-350, BT-550, BT-750.

coefficient is increased in the visible light range with the BT composites, the absorption edge of TiO_2 remains consistent with that of BT, however BT-350 and BT-550 show red-shift in the absorption. The absorption spectra of BT-750 exhibited the most significant red shift. Nonetheless, it is noteworthy that the trend observed in photocatalytic activity did not exhibit congruence with that of UV-Vis's absorption, as elaborated upon in later sections. Importantly, a continuous absorption of visible light photons wavelength above 400 nm indicates a possible broadening of VB and CB states, which depends on the treatment. Intensity variation in the absorption of visible light range photons hints a possibility of different kind of defects created to different levels of population. Indeed, this aspect is worth analysing in a systematic manner with controlled calcination in inert atmosphere.

5.3 HRTEM analysis:

Figure 5.3 displays a comprehensive HRTEM results for BT-350, and offers an intricate perspective of the material on a nanoscale level. The BT-350 sample was subjected to thorough analysis, wherein panel A exhibits a cluster of defective TiO_2 particles having an average particle size of 20±1 nm. The findings presented in panel b demonstrate the presence of deformation in the crystal lattice of the TiO_2 nanoparticles, which is consistent with the observations made in the XRD pattern. In contrast to the many TEM/HRTEM images shown

for parent P25 in the earlier chapters with definite and clear edges of titania particles and a uniform d-spacing observed across the entire particle (provide one or two definite figure numbers here), results shown in Fig. 5.2 is distinctly different. SAED pattern shown in the inset of Fig. 5.2b underscores the large number of defects, which hinders in getting a crystalline pattern. The presence of interrupted lattice planes suggests that the defect has originated within the bulk, while surface defects are discernible in panels c and d, where an amorphous quality is apparent.[25] The aforementioned observations exhibit conformity with other surface methodologies, including X-ray photoelectron spectroscopy (XPS) and Raman spectroscopy.

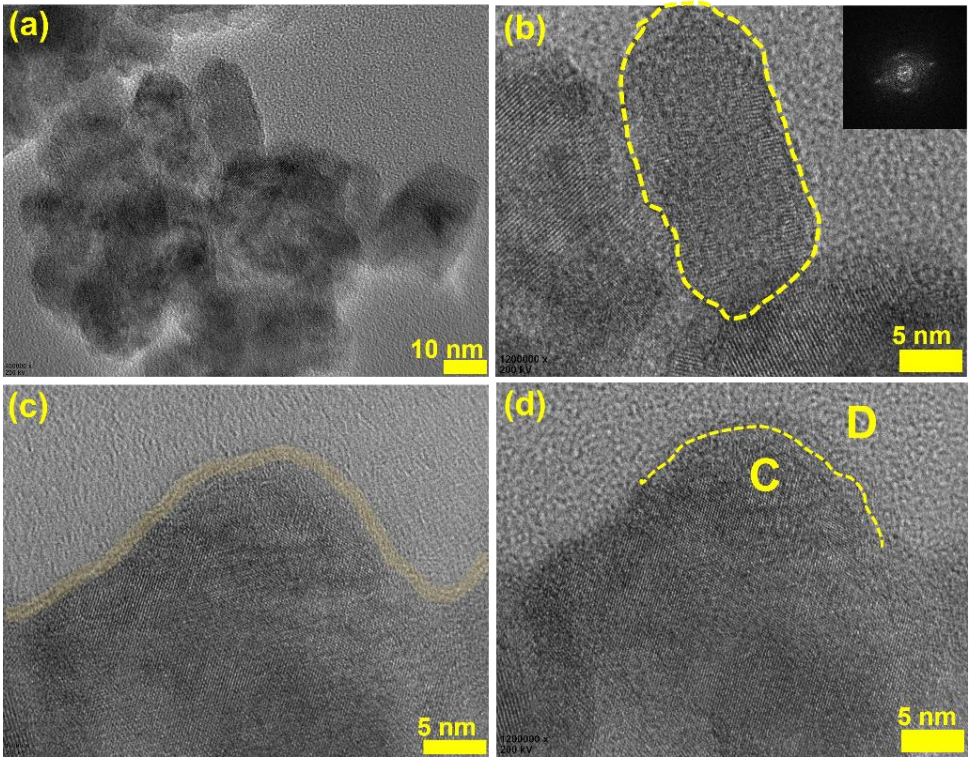


Figure 5.3: HRTEM images of BT-350 at different scales.

5.4 Photocatalytic activity:

Photocatalytic activity for nitrogen fixation was conducted on TiO_2, BT, BT-350, BT-550, and BT-750. A dispersion of 5 mg of any catalyst was prepared in 25 ml of deionized water and employed for all experiments. It should be noted that in order to eliminate contamination, the DI water was subjected to boiling and subsequently transferred it to a sanitised container. It is also to be stated that many control experiments were carried out to rule out the possible nitrogen impurities in the solution or with the catalyst, and some of them are given below. In order to enhance the solubility of nitrogen and attain adsorption-

desorption equilibrium, we subjected the the solution to a one-hour continuous purge of nitrogen in an ice bath before irradiation. After N_2-saturation, the solution was subjected to one sun illumination for continuous 2 hrs. The Nessler's method was employed for ammonia quantification. The pre- and post-samples were analysed to verify the absence of any potential contamination.

No ammonia was detected in the TiO_2 catalyst after the reaction. Conversely, in the case of BT, BT-350, BT-550, and BT-750, the highest quantity of ammonia was produced in BT-350 (88 µmol h^{-1} g^{-1}), followed by BT-550 (81 µmol h^{-1} g^{-1}BT-750 (38 µmol h^{-1} g^{-1}), and BT (28 µmol h^{-1} g^{-1}). In order to establish that the nitrogen present is solely derived from the photocatalytic process and not due to material contamination, a control experiment was conducted using argon purging instead of nitrogen purging. The results indicated the absence of ammonia, thereby confirming the occurrence of photocatalytic nitrogen fixation. It may be noted that nitrogen fixation and water reduction into hydrogen are competitive and electron consuming processes photocatalytic processes. It is expected that molecular hydrogen formation does not occur, and rather protons and electrons are consumed concurrently for nitrogen activation to ammonia. Indeed, electrocatalytic process of ammonia suggests that maximum ammonia production is observed when the hydrogen production is minimum (or no H_2 was produced). No metal co-catalyst employed in the present system also underscores the possibility of hydrogen production is minimum, nevertheless, the absence of hydrogen

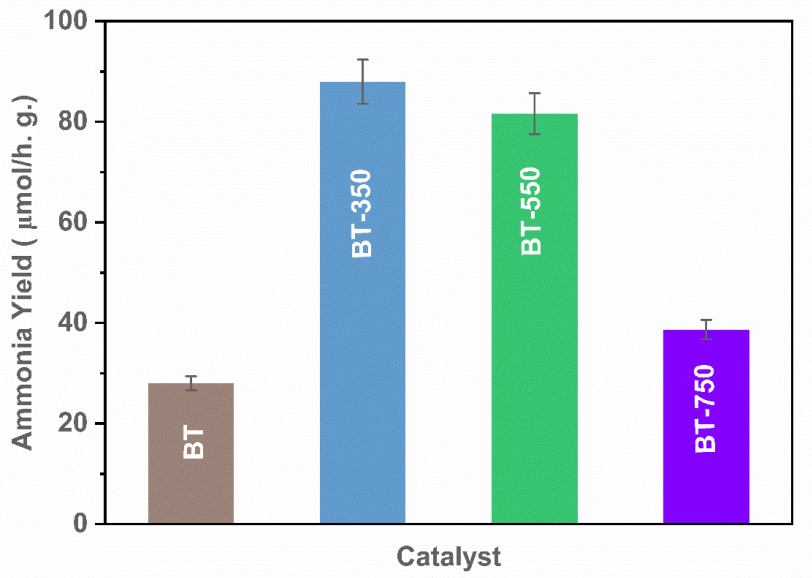


Figure 5.4: Photocatalytic ammonia yield observed for BT, BT-350, BT-550, BT-750.

was confirmed by GC analysis which indicate the defects present on the photocatalyst seem to be more selective towards nitrogen fixation. The XRD analysis revealed that the treatment of TiO_2 with $NaBH_4$ resulted in the formation of defects within the bulk material under various conditions. The observed photocatalytic nitrogen fixation activity indicates that the activity is primarily attributed to defects. It should be noted that in BT-350, the relative intensity of the (200) plane is higher compared to other composites, as shown in Figure 5.2a. This correlation could indicate a higher activity level for BT-350. Nevertheless, the BT-550 exhibits a marginally reduced level of photo-activity in comparison to the BT-350. It was observed that in figure 5.2b, the optical absorption edge for both composites, BT-350 and BT-550, was found to be comparable.

5.5 XPS analysis:

XPS is a tool, employed for the purpose of examining the electronic structure details and electronic interaction and surface composition of a given solid material. The direct correlation between XPS analysis and photocatalytic activity can be attributed to the fact that photocatalysis is a surface chemical process. The electronic structural changes of TiO_2 and other defective TiO_2 samples were investigated through the analysis of XPS data, and the same is presented in Figure 5.5. The results presented in Figure 5.5a indicate the presence of two distinct oxidation states for Ti across all samples, with binding energies of 457.3 ± 0.05 eV and 458.3 ± 0.05eV, which correspond to Ti^{3+} and Ti^{4+}, respectively. The presence of Ti^{4+} is prevalent in all instances, whereas the concentration of Ti^{3+} fluctuates among diverse composites. A careful look at the line width of core level spectra reveals a significant broadening of Ti 2p core levels, when the defects are introduced in BT-X materials. Although the BE of Ti^{4+} largely remains at 458.3 eV, the defective surrounding in the titania leads to a broadening of Ti 2p core levels. The sample denoted as BT-750 exhibits the highest Ti^{3+} concentration at 17.42% in comparison to the other samples, namely BT at 13.1%, BT-350 at 14.9%, and BT-550 at 14.7%. It is noteworthy that in the course of the synthesis procedure, the generation of bulk defects is also observed, as evidenced by X-ray diffraction (XRD) analysis. Given that XPS is a surface-sensitive method, it is limited to the quantification of titanium species present solely on the surface. The BT-750 material exhibits a greater number of surface defects in comparison to BT-350. However, its photocatalytic activity in relation to nitrogen fixation is comparatively lower than that of BT-350. This suggests that the activity

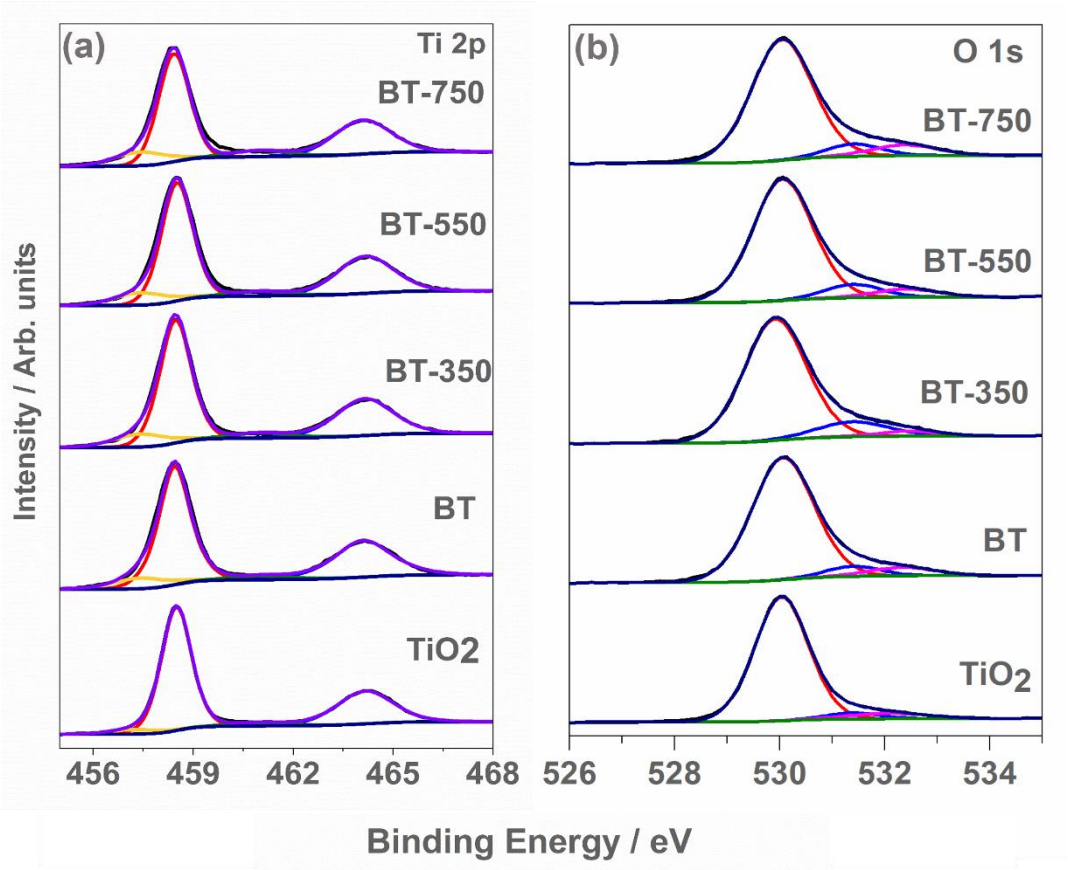


Figure 5.5: (a) Ti 2p, and (b) O 1s core level spectra of TiO_2, BT, BT-350, BT-550, BT-750. Ti^{3+} is given in pink traces. Red, blue and pink traces in O 1s corresponds to TiO_2 lattice oxygen, O-associated with Ti^{3+} and OH group, respectively.

of the material cannot be attributed solely to the presence of surface defects. Furthermore, it can be observed that BT-750 exclusively exists in the rutile crystalline phase, and the same was confirmed earlier by XRD (Fig. 5.1).

The O 1s spectra depicted in Figure 5.5b exhibit three distinct oxygen species, which correspond to the lattice oxygen of TiO_2 (529.75 ± 0.05 eV, red trace), oxygen in proximity to the defect site (531 ± 0.05 eV, blue trace), and oxygen associated with the hydroxyl group (532 ± 0.05 eV, pink trace). The oxygen associated with Ti^{3+} displays a similar pattern to that observed in the Ti 2p spectra of Ti^{3+}. A notable alteration is discernible with regards to the hydroxyl functional group. The BT-750 compound exhibits a greater hydroxyl group concentration (9.16%) in comparison to both BT-350 (3.72%) and BT-550 (6.67%). [31, 32]The photocatalytic activity is enhanced with the reduction in the hydroxyl group concentration; The hydroxyl content in an aqueous solution can impede the efficacy of adsorption and

desorption processes, thereby diminishing the active site for photocatalysis. This observation aligns with the observed photocatalytic activity and highlights the significance of hydroxyl content in this context.

5.6 Photo-Luminiscence (PL) studies:

In order to obtain a deeper understanding of the photo-physics pertaining to excitons in a photocatalyst, an analysis of the PL spectra of TiO_2, BT, BT-350, and BT-550 is required, and a detailed analysis of PL was carried out. PL results obtained are shown in Figure 5.6 with peak deconvolution. It is also to be mentioned that the amount of material utilized for PL spectra are similar and within ±5 wt%. PL spectra of all the four materials recorded shows similar pattern, but with widely different intensity for different materials; indeed, it may be noted that they are all titania materials with different extent of defects and hence this observation is not surprising. P25-TiO_2 displays the highest PL intensity, while BT, BT-550, and BT-350 follow a descending order of intensity. The PL spectra have been deconvoluted owing to the existence of diverse Ti species in the photocatalysts. The prevailing belief is that an increase in intensity is directly correlated to an increase in charge recombination. The PL intensity within the energy range of 1.75 to 2.65 eV is frequently associated with emission related to defects, the emission observed at 2.11 eV is attributed to oxygen vacancies that are associated with under-coordinated Ti, which function as electron trap sites. On the other hand, the emission detected at 2.3 eV is linked to surface defects and Ti^{3+} species.[33-36] Surface defects are indicated by the broad blue traces in the composite materials shown in Fig. 5.6. Red colour trace observed around 3.15 eV for all materials is attributed to the band-gap associated recombination. Green trace observed between the above two features at 2.8 eV may be attributed to the defects associated with free electrons that are present due to oxygen vacancies. The higher photocatalytic activity of BT-350 and BT-550 can be attributed to the reduction in intensity when compared to TiO_2. To clarify, the presence of defect sites serves as catalytic sites for the activation of Nitrogen triple bond. Additionally, a decrease in the intensity of the photoluminescence spectra indicates a greater likelihood of available electrons for Nitrogen activation, which aligns with the photocatalytic activity involved in nitrogen fixation. It is proposed by several research groups that the electrons associated with oxygen vacancies, rather with Ti^{3+}, makes the electrons available in the extended part of

conduction band. It is also well known that the electron energy in the CB is low and closer to vacuum level. On photon absorption by black-TiO_2 the number of electron counts would

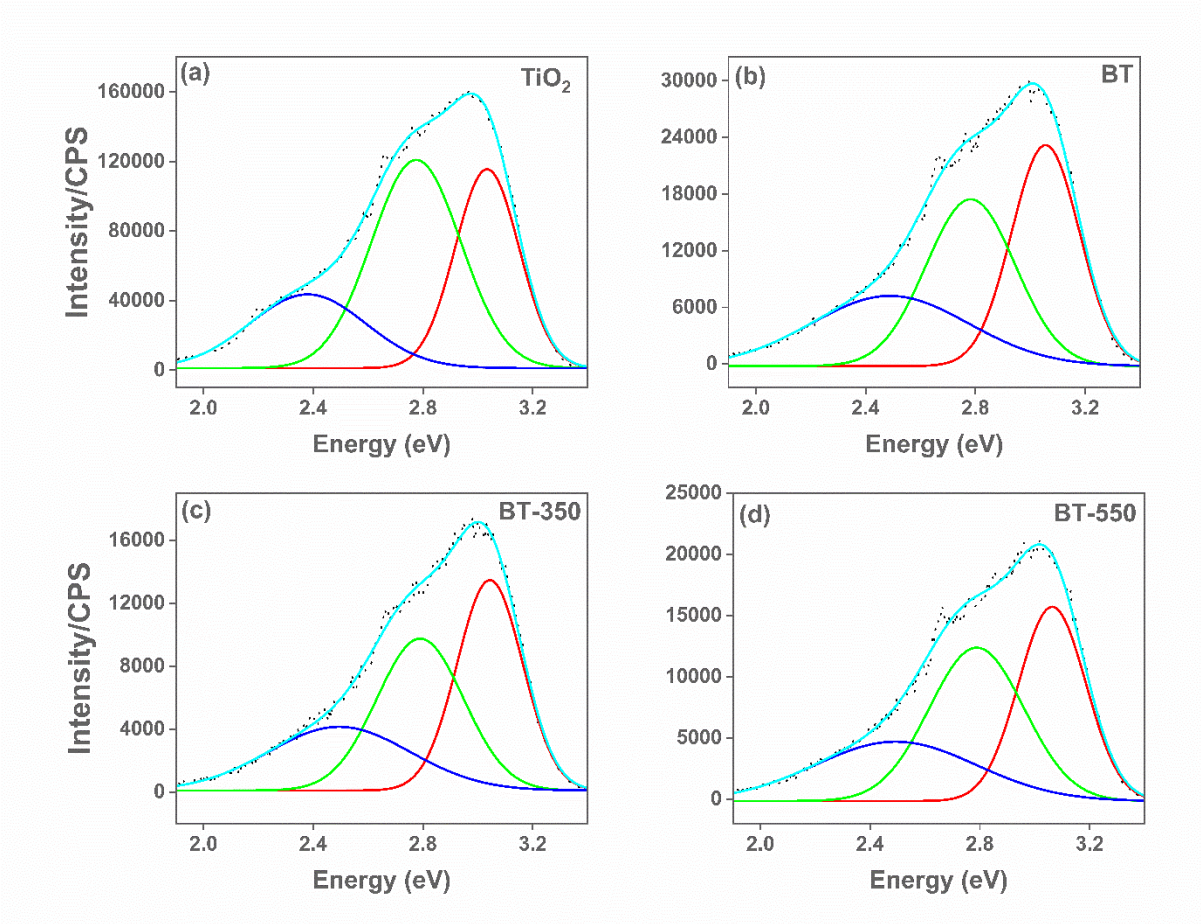


Figure 5.6: Deconvoluted PL spectra of TiO_2, BT, BT-350, BT-550.

Increase and the same could facilitate the charge transfer to nitrogen molecules for weakening the triple bond followed by its dissociation to nitrogen atoms. Protons availability would enhance the dissociation of N_2 molecules and helps for hydrogenation in steps. Furthermore, the process of passivating oxygen vacancies has the potential to enhance the efficacy of charge transfer, thereby leading to improved photocatalytic performance. The emission of high energy (ranging from 2.6 to 3.4 eV) can be explained by two potential causes: band emission in the vicinity of the edge and the confinement of charge carriers within TiO_6 octahedra.[33, 37] The emission intensity of all defective TiO_2 follows a similar decreasing pattern as the low energy emission peak. This observation suggests that BT-350 exhibits lower charge carrier recombination compared to other composites, thereby corroborating the trend observed in photocatalytic nitrogen fixation.

5.7 Raman analysis:

The utilization of RAMAN scattering technique is a highly sensitive and valuable approach in the investigation of microstructural changes that occur within a short range, and hence can be very useful even with amorphous or semi-amorphous materials. The present investigation employed RAMAN spectroscopy to analyse the TiO_2, BT, BT-350, BT-550, and BT-750 composites, with the aim of identifying surface-specific alterations. The Raman spectra of TiO_2 exhibit distinct peaks of the anatase feature at 142, 394, 513, and 636, which correspond to E_g, B_{1g}, A_{1g}+B_{1g}, and E_g bands, respectively, as depicted in Figure 5.7. On the other hand, the composites with defects exhibited significant shifts towards longer wavenumbers. The E_g band is associated with symmetrical vibrational stretching modes; In the instances of BT, BT-350, and BT-550, deviations in the symmetrical vibration modes were detected as a consequence of nonstoichiometric oxygen distribution, which was caused by the presence of oxygen vacancies.[38] The observed shift in the Raman spectra can be attributed to the shortening of the system that is correlated with the 150 cm^{-1} modes with respect TiO_2 (Inset in fig. 5.7a). Nonetheless, critically there is a significant broadening of E_g feature observed for all BT composites, compared to TiO_2, underscoring the presence of defects.

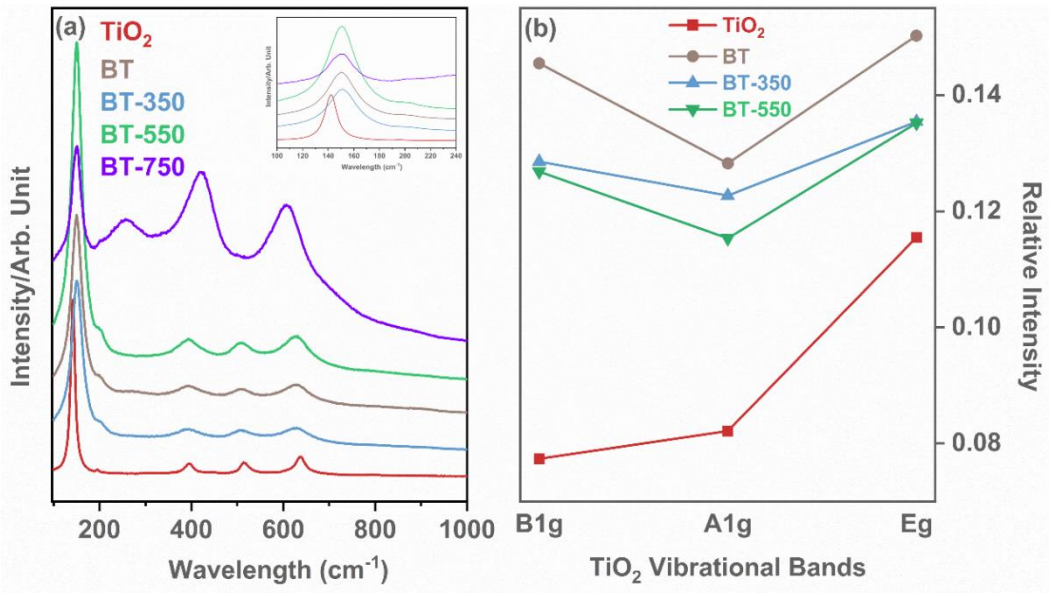


Figure 5.7: (a) Raman spectra of TiO_2, BT, BT-350, BT-550, BT-750. (b) Relative intensity of different band for TiO_2, BT, BT-350, BT-550.

The BT-750 specimen exhibited Raman modes associated with Rutile TiO_2 for B_{1g}, E_g, and A_{1g} modes, as verified by X-ray diffraction (XRD) analysis. Fig. 5.7b was subjected to an

analysis of the relative intensity towards the Vibration band, it is to noted that relative intensity is calculated with respect to vibrational mode at 150 cm^{-1}; here intensity related to E_g band at 150 cm^{-1} is considered, relative to this all-other vibrational intensity is being calculated, which revealed that treatment with NaBH4 resulted in an increase in intensity across all three bands, namely B_{1g}, A_{1g}, and E_g. It is noteworthy that the B_{1g}, A_{1g}, and E_g modes are associated with symmetrical bending vibrations, asymmetrical stretching vibrations, and symmetrical vibration stretching, respectively. The evidence shown in the figure demonstrates that the defective composites exhibit increased intensity in the B_{1g} and A_{1g} modes relative to the E_g mode. This observation suggests an increase in surface bending and asymmetrical stretching vibration, which ultimately enhances the photocatalytic activity in the Defective TiO_2 composites. Based on the comprehensive examination of panel b, it has been found that the proportion of the relative B_{1g}, A_{1g}, and E_g in each of the composites adheres to the sequence: BT>BT-550>BT-350. The aforementioned phenomenon may exhibit a correlation with photocatalytic nitrogen fixation, as the activation of the nitrogen triple bond is a crucial stage in the process, which may be enhanced by an optimized ratio between the vibration band in BT-350.

5.8 Conclusion:

The objective of present investigation was to enhance the process of photocatalytic nitrogen fixation through the production of defective TiO_2 at different calcination temperatures. The study's findings indicate that the BT-350 composite displayed superior photocatalytic activity in relation to nitrogen fixation. This outcome was attributed to the composite's surface defect and optimised vibrational band ratio. The composites were subjected to diverse characterizations to acquire comprehension regarding their crystal nature, surface bonding mode vibration, and optical absorption, which facilitated the identification of the determinants that impact photocatalytic activity. The Raman spectrum indicates the presence of defects on the surface, while the relative intensity of the Raman band vibration modes suggests that an optimised ratio of these modes may be responsible for a higher degree of photocatalytic nitrogen fixation. The highest activity exhibited by BT-350 correlated to the findings from PL spectra and XPS. In the PL study, lower emission intensity is concluded in to lower charge recombination results in higher photocatalytic activity agreeing with the photocatalytic nitrogen fixation for all composites. The XPS analysis

reveals that a decrease in hydroxyl concentration leads to an increase in photocatalytic nitrogen fixation. It can be inferred that the enhancement of ammonia production is associated with optimised surface defects, and not necessarily with more defects. The study revealed that distinct characteristics, namely surface defects and crystal phases, exhibit varying impacts on the process of photocatalytic nitrogen fixation.

The study also revealed that BT-750, despite having a higher surface defects and absorption in the visible region compared to BT-350 and BT-550, demonstrated reduced photocatalytic activity towards nitrogen fixation owing particularly to its rutile phase. The aforementioned results emphasise the significance of taking into account all pertinent variables that may affect photocatalytic performance while enhancing composites for nitrogen fixation.

The study holds significance in terms of augmenting nitrogen fixation in a manner that is both sustainable and efficient; through the acquisition of enhanced comprehension regarding the determinants that impact photocatalytic activity and the refinement of the synthesis parameters of TiO_2 composites, it is plausible to devise more effective and eco-friendly approaches for nitrogen fixation.

5.9 References:

1. Kerru, N.; Gummidi, L.; Maddila, S.; Gangu, K. K.; Jonnalagadda, S. B., A Review on Recent Advances in Nitrogen-Containing Molecules and Their Biological Applications. *Molecules* **2020,** *25*, 1909.
2. Kim, J.; Rees, D. C., Nitrogenase and biological nitrogen fixation. *Biochemistry* **1994,** *33*, 389-397.
3. Li, H.; Mao, C.; Shang, H.; Yang, Z.; Ai, Z.; Zhang, L., New opportunities for efficient N_2 fixation by nanosheet photocatalysts. *Nanoscale* **2018,** *10*, 15429-15435.
4. Wang, M.; Khan, M. A.; Mohsin, I.; Wicks, J.; Ip, A. H.; Sumon, K. Z.; Dinh, C.-T.; Sargent, E. H.; Gates, I. D.; Kibria, M. G., Can sustainable ammonia synthesis pathways compete with fossil-fuel based Haber–Bosch processes? *Energy Environ. Sci* **2021,** *14*, 2535-2548.

5. Humphreys, J.; Lan, R.; Tao, S., Development and Recent Progress on Ammonia Synthesis Catalysts for Haber–Bosch Process. *Adv. energy sustain. res.* **2021,** *2*, 2000043.
6. Erisman, J. W.; Sutton, M. A.; Galloway, J.; Klimont, Z.; Winiwarter, W., How a century of ammonia synthesis changed the world. *Nat. Geosci.* **2008,** *1*, 636-639.
7. Lamb, K. E.; Dolan, M. D.; Kennedy, D. F., Ammonia for hydrogen storage; A review of catalytic ammonia decomposition and hydrogen separation and purification. *Int. J. Hydrogen Energy* **2019,** *44*, 3580-3593.
8. Aziz, M.; Wijayanta, A. T.; Nandiyanto, A. B. D., Ammonia as Effective Hydrogen Storage: A Review on Production, Storage and Utilization. *Energies* **2020,** *13*, 3062.
9. Boggs, B. K.; Botte, G. G., On-board hydrogen storage and production: An application of ammonia electrolysis. *J. Power Sources* **2009,** *192*, 573-581.
10. Zhang, S.; Zhao, Y.; Shi, R.; Waterhouse, G. I. N.; Zhang, T., Photocatalytic ammonia synthesis: Recent progress and future. *EnergyChem* **2019,** *1*, 100013.
11. Chen, X.; Li, N.; Kong, Z.; Ong, W.-J.; Zhao, X., Photocatalytic fixation of nitrogen to ammonia: state-of-the-art advancements and future prospects. *Mater. Horiz.* **2018,** *5*, 9-27.
12. Vu, M.-H.; Sakar, M.; Hassanzadeh-Tabrizi, S. A.; Do, T.-O., Photo(electro)catalytic Nitrogen Fixation: Problems and Possibilities. *Adv. Mater. Interfaces* **2019,** *6*, 1900091.
13. Docao, S.; Koirala, A. R.; Kim, M. G.; Hwang, I. C.; Song, M. K.; Yoon, K. B., Solar photochemical–thermal water splitting at 140 °C with Cu-loaded TiO_2. *Energy Environ. Sci* **2017,** *10*, 628-640.
14. Wang, L.; Wu, W.; Liang, K.; Yu, X., Advanced Strategies for Improving the Photocatalytic Nitrogen Fixation Performance: A Short Review. *Energy & Fuels* **2022,** *36*, 11278-11291.
15. Shi, R.; Zhang, X.; Waterhouse, G. I. N.; Zhao, Y.; Zhang, T., The Journey toward Low Temperature, Low Pressure Catalytic Nitrogen Fixation. *Adv. Energy Mater.* **2020,** *10*, 2000659.
16. Zhang, L.; Hou, S.; Wang, T.; Liu, S.; Gao, X.; Wang, C.; Wang, G., Recent Advances in Application of Graphitic Carbon Nitride-Based Catalysts for Photocatalytic Nitrogen Fixation. *Small* **2022,** *18*, 2202252.

17. Kumar, A.; Choudhary, P.; Kumar, A.; Camargo, P. H. C.; Krishnan, V., Recent Advances in Plasmonic Photocatalysis Based on TiO_2 and Noble Metal Nanoparticles for Energy Conversion, Environmental Remediation, and Organic Synthesis *Small*. **2022,** *18*, 2101638.
18. Do, T.-O.; Mohan, S., Editorial: Special Issue on "Emerging Trends in TiO_2 Photocatalysis and Applications". *Catalyst* **2020,** *10*, 670.
19. Schrauzer, G. N.; Guth, T. D., Photolysis of Water and Photoreduction of Nitrogen on Titanium Dioxide. *J. Am. Chem. Soc.* **1977,** *99*, 7189-7193.
20. Huang, R.; Li, X.; Gao, W.; Zhang, X.; Liang, S.; Luo, M., Recent advances in photocatalytic nitrogen fixation: from active sites to ammonia quantification methods. *RSC Adv.* **2021,** *11*, 14844-14861.
21. Cheng, M.; Xiao, C.; Xie, Y., Photocatalytic nitrogen fixation: the role of defects in photocatalysts. *J. Mater. Chem. A.* **2019,** *7*, 19616-19633.
22. Rajaraman, T. S.; Parikh, S. P.; Gandhi, V. G., Black TiO_2: A review of its properties and conflicting trends. *Chem. Eng. J.* **2020,** *389*, 123918.
23. Wang, S.; Hai, X.; Ding, X.; Chang, K.; Xiang, Y.; Meng, X.; Yang, Z.; Chen, H.; Ye, J., Light-Switchable Oxygen Vacancies in Ultrafine Bi5O7Br Nanotubes for Boosting Solar-Driven Nitrogen Fixation in Pure Water. Adv. Mater. **2017,** *29*, 1701774.
24. Sasikala, R.; Sudarsan, V.; Sudakar, C.; Naik, R.; Panicker, L.; Bharadwaj, S. R., Modification of the photocatalytic properties of self doped TiO_2 nanoparticles for hydrogen generation using sunlight type radiation. *Int. J. Hydrogen Energy* **2009,** *34*, 6105-6113.
25. Kong, M.; Li, Y.; Chen, X.; Tian, T.; Fang, P.; Zheng, F.; Zhao, X., Tuning the Relative Concentration Ratio of Bulk Defects to Surface Defects in TiO_2 Nanocrystals Leads to High Photocatalytic Efficiency. *J. Am. Chem. Soc.* **2011,** *133* , 16414-16417.
26. Cronemeyer, D. C., Infrared Absorption of Reduced Rutile Ti${\mathrm{O}}_{2}$ Single Crystals. *Phys. Rev.* **1959,** *113*, 1222-1226.
27. Li, L.; Yan, J.; Wang, T.; Zhao, Z.-J.; Zhang, J.; Gong, J.; Guan, N., Sub-10 nm rutile titanium dioxide nanoparticles for efficient visible-light-driven photocatalytic hydrogen production. *Nat. Commun.* **2015,** *6*, 5881.

28. Justicia, I.; Ordejón, P.; Canto, G.; Mozos, J. L.; Fraxedas, J.; Battiston, G. A.; Gerbasi, R.; Figueras, A., Designed Self-Doped Titanium Oxide Thin Films for Efficient Visible-Light Photocatalysis. *Adv. Mater.* **2002,** *14*, 1399-1402.
29. Wang, G.; Wang, H.; Ling, Y.; Tang, Y.; Yang, X.; Fitzmorris, R. C.; Wang, C.; Zhang, J. Z.; Li, Y., Hydrogen-Treated TiO_2 Nanowire Arrays for Photoelectrochemical Water Splitting. *Nano Lett.* **2011,** *11*, 3026-3033.
30. Li, J.; Wu, E.-H.; Hou, J.; Huang, P.; Xu, Z.; Jiang, Y.; Liu, Q.-S.; Zhong, Y.-Q., A facile method for the preparation of black TiO_2 by Al reduction of TiO_2 and their visible light photocatalytic activity. *RSC Adv.* **2020,** *10*, 34775-34780.
31. Tudu, B.; Nalajala, N.; Saikia, P.; Gopinath, C. S., Cu–Ni Bimetal Integrated TiO_2 Thin Film for Enhanced Solar Hydrogen Generation. Sol. RRL **2020,** *4*, 1900557.
32. Bajpai, H.; Chauhan, I.; Salgaonkar, K. N.; Mhamane, N. B.; Gopinath, C. S., Biomass components toward H2 and value-added products by sunlight-driven photocatalysis with electronically integrated Auδ−−TiO_2: concurrent utilization of electrons and holes. *RSC Sus.* **2023**.
33. Daude, N.; Gout, C.; Jouanin, C., Electronic band structure of titanium dioxide. *Phys. Rev. B* **1977,** *15* , 3229-3235.
34. Lei, Y.; Zhang, L. D.; Meng, G. W.; Li, G. H.; Zhang, X. Y.; Liang, C. H.; Chen, W.; Wang, S. X., Preparation and photoluminescence of highly ordered TiO_2 nanowire arrays. *Appl. Phys. Lett.* **2001,** *78* , 1125-1127.
35. Jiang, X.; Zhang, Y.; Jiang, J.; Rong, Y.; Wang, Y.; Wu, Y.; Pan, C., Characterization of Oxygen Vacancy Associates within Hydrogenated TiO_2: A Positron Annihilation Study. *J. Phys. Chem. C* **2012,** *116* , 22619-22624.
36. Vásquez, G. C.; Peche-Herrero, M. A.; Maestre, D.; Cremades, A.; Ramírez-Castellanos, J.; González-Calbet, J. M.; Piqueras, J., Effects of Transition Metal Doping on the Growth and Properties of Rutile TiO_2 Nanoparticles. *J. Phys. Chem. C* **2013,** *117* , 1941-1947.
37. Bharad, P. A.; Nikam, A. V.; Thomas, F.; Gopinath, C. S., CuO_x-TiO_2 Composites: Electronically Integrated Nanocomposites for Solar Hydrogen Generation. *Chemistry Select* **2018,** *3* , 12022-12030.

38. Chen, S.; Xiao, Y.; Wang, Y.; Hu, Z.; Zhao, H.; Xie, W., A Facile Approach to Prepare Black TiO_2 with Oxygen Vacancy for Enhancing Photocatalytic Activity. *Nanomaterials* **2018,** *8* , 245.



Chapter 6

Conclusions

6.1 Conclusions and Future scope:

This chapter provides a summary of the current thesis work and discusses the future potential of the created work.

Chapter 1 gives an introduction to the field of photocatalysis, including fundamental principles, how to improve charge separation for efficient redox reactions on co-catalyst surfaces, the role of SPR, the use of sacrificial agents, by reviewing the literature.

Chapter 2 focuses on a comprehensive synthesis of the variety of photocatalysts and co-catalyst materials utilised in the present thesis, and how they are integrated in the final photocatalyst. It also provides principles of various physio-chemical approaches utilised to study the materials.

Chapter 3 focuses on the development of a quasi-artificial leaf (QuAL), which involves sensitizing the porous network of TiO_2 by in-situ assembling and integrating ZnS and CdS quantum dots. The absorption of light by the different components of the QuAL leads to the generation of charge carriers, which can be utilized to reduce water to produce H2 and oxidize sacrificial reagents. To effectively utilize the electron at the active site for hydrogen evolution, Pt is currently the most effective co-catalyst available. However, due to its high cost, finding a less expensive substitute for Pt is essential for large-scale production. Many studies have been conducted using earth-abundant metal catalysts, but they are significantly inferior to Pt in terms of activity and stability. We have prepared a QD-sensitized photo-anode (TiO_2/ZnS/CdS) using the successive ionic layer adsorption and reaction (SILAR) method. An additional ZnS layer was used as a passivation layer after the CdS deposition. Several control photoanodes were also made to better understand the mechanism of photoanode function. The best photoanode (TiO_2/ZnS/CdS) demonstrated a hydrogen generation activity of 4 ml/h from a 1 cm2 sized device. This research highlights the potential for developing cost-effective and efficient substitutes for Pt as a co-catalyst in photocatalytic water splitting, which is crucial for the large-scale production of hydrogen as a clean energy source.

Chapter 4 is divided into three parts**.** The focus of **Chapter 4a** is on the use of biomass components, such as glycerol, glucose, as sacrificial reagents for effective hydrogen generation in photocatalytic water splitting as an alternative to oxygen evolution reaction.

This chapter addresses the prospect of using holes to oxidise the sacrificial agent to value-added products in an efficient manner (VAPs).

In **chapter 4a**, a photo-deposition approach for preparing well-dispersed and atom-like plasmonic Au integrated with P25-TiO_2 is presented. XPS analyses demonstrate that gold exhibits an anionic or electron-rich nature, indicating a significant electronic integration with titania. It is claimed that a charge transfer from oxygen-vacancy sites to gold might help in the simultaneous generation of solar hydrogen and VAPs. In this investigation, glycolaldehyde, dihydroxyacetone, and formic acid were identified as VAPs. These VAPs have vital uses in several disciplines, including the pharmaceutical and chemical industries. This methodology presents a potential method for using the holes produced during photocatalytic water splitting to concurrently create VAPs and hydrogen. In general, chapter 4a investigates a unique strategy for enhancing the effectiveness of photocatalytic water splitting by exploiting biomass components as sacrificial reagents and efficiently utilising holes to form VAPs. This wok can be extended to other biomass component without producing the any harmful by products.

In **chapter 4b**, we investigated the possibility of substituting copper for gold in the photocatalytic water-splitting mechanism. We adopted a new technique of preparation including the intentional reduction of TiO_2. This resulted in the formation of oxygen vacancies on the surface of TiO_2 at room temperature, enabling the deposition of copper atoms over TiO_2. Using glycerol as a sacrificial reagent, our experiments demonstrated that this copper-TiO_2 composite displayed strong photocatalytic hydrogen generation. Also, the influence of pH on the stability and photoactivity of the copper-TiO_2 composite was examined. The results suggested that elevating the solution's pH increased the catalyst's stability and photoactivity. In addition to hydrogen evolution, photo-catalytic glycerol oxidation towards selective glycolaldehyde was also observed. Before and after reaction samples were analysed with X-ray photoelectron spectroscopy (XPS) to determine the involvement of the pH in the photocatalytic process. Our findings indicate that the copper-TiO_2 composite may be a cost-effective alternative to the Au-TiO_2 composite for photocatalytic water splitting. To explore further possibility copper/TiO_2 based composite should be synthesize with different method which can be extent to large scale.

In **chapter 4c,** we investigated the photocatalytic characteristics of a NiCu bimetallic system decorated with TiO_2. This composite was examined for its efficiency in producing hydrogen using biomass as sacrificial reagent like glycerol, cellulose, and standard tissue paper. The co-catalyst was combined with the TiO_2 photocatalyst in order to maximise the use of both charge carriers. The results demonstrated that the NiCu/TiO_2 composite exhibited potent photocatalytic activity for hydrogen generation; we have also explored the stability of the catalyst, and it was shown that the composite retains its photocatalytic activity even after several cycles of usage. Overall, this work confirms the NiCu/TiO_2 composite's potential as a cost-effective and efficient photocatalyst for biomass conversion, this work also demonstrate that different earth abundant bimetal system can be used for higher hydrogen production and selective VAPs.

In **chapter 5**, photocatalytic nitrogen fixation utilising defect engineering on TiO_2 is highlighted. BT was tuned to increase the critical functional defects for enhanced photocatalytic nitrogen fixation via temperature treatment. The activation of nitrogen is an essential stage in nitrogen fixation, and oxygen vacancy defects serve as active sites for nitrogen activation. These defects decrease the bond order of nitrogen, resulting in the creation of ammonia. The photocatalytic activity of TiO_2 with defects at created various temperatures was investigated, and BT-350 was found to exhibit the highest conversion from N_2 to ammonia. The XRD, XPS, RAMAN, PL techniques were employed to acquire a better understanding of the involvement of various variables in this process. Role of surface defects, nitrogen interactions with distinct crystallographic faces, and oxygen vacancies may operate synergistically to activate nitrogen.

Generally, the efforts described in the present thesis is significantly different from the methods adopted routinely by photocatalysis community. Apart from an increasing activity, significant effort has gone into the fundamental understanding of the phenomena through relevant approaches. Nonetheless, there is a long-way to go to reach higher and higher activity with better understanding. We also believe that biomass utilization for hydrogen and VAP formation in sunlight pave the way towards developing sustainable production of chemicals and fuels. More radical thinking and approaches may be required to address tough problems, like N_2 activation.

ABSTRACT

Name of the Student: Himanshu Bajpai **Registration No.:** 10CC17A26026

Faculty of Study: Chemical Science **Year of Submission:** 2023

CSIR Lab: NCL, Pune **Name of the Supervisor:** Dr. C.S. Gopinath

Title of the Thesis: Solar Light Driven Photocatalysis for Hydrogen and Value-added Products Generation

This thesis work focuses on the development of photocatalysis for efficient solar hydrogen and value-added product generation. **Chapter 1** of this thesis provides an overview of the development of photocatalysis, with a focus on the core principles and mechanism behind the process. The chapter also explores several strategies that can increase photocatalytic activity while simultaneously decreasing charge recombination. Some of these strategies include the use of heterojunction and plasmonic effects, as well as the function of sacrificial reagents and defects. **Chapter 2** of the thesis discusses the production of photocatalysts based on TiO_2; chapter explores various methods for preparing these photocatalysts, this chapter also summarizes the various analytical techniques used in the thesis work, including UV-Visible spectroscopy, transmission electron microscopy, RAMAN, XRD. **Chapter 3** focuses on the study of an earth-abundant Ni-Cu co-catalyst coated with half a monolayer of Pt ($0.5\theta_{Pt}$), which is paired with a quasi-artificial leaf (QuAL) device for efficient solar hydrogen production. The QuAL device uses the successive ionic layer absorption and reaction (SILAR) technique to sensitize TiO_2 with ZnS and CdS quantum dots. The photoactivity of the QuAL device using either bulk Pt or a Ni-Cu cocatalyst with $0.5\theta_{Pt}$ coating is found to be identical. **Chapter 4a** demonstrates that the material exhibits well-dispersed plasmonic gold that was electronically integrated with P25-TiO_2. XPS studies have shown that the fundamental nature of gold is electron-rich or anionic, This, in turn, helps the simultaneous production of large amounts of H_2 and value-added products (VAPs) formation from glycerol under one sun condition or in direct sunlight. **Chapter 4b** provides an in-depth analysis of the Cu/TiO_2 composite. The chapter demonstrates that small copper clusters deposited over TiO_2 by creating surface oxygen vacancies at room temperature using different methods resulted in high photocatalytic hydrogen production and selective oxidation of glycerol. **Chapter 4c** of the thesis evaluates photocatalytic hydrogen generation along with VAP formation using biomass components. A NiCu bimetallic system impregnated over TiO_2 is employed as the photocatalyst, demonstrating the exploitation of both charge carriers in a concurrent manner. **Chapter 5** explores photocatalytic nitrogen fixation via defect engineering on TiO_2. The chapter demonstrates that optimizing the functional defects toward higher photocatalytic nitrogen fixation. Creating defects, especially oxygen vacancies, work as an active site for nitrogen activation, by reducing the bond order of nitrogen and resulting in ammonia formation with in-situ generated protons and electrons. **Chapter 6** deliberates on the potential depth and breadth of future research directions in the field of solar water splitting.

List of Publication(s) in SCI Journal(s) Emanating from the Thesis Work

- Bajpai, H.; Chauhan, I.; Salgaonkar, K. N.; Mhamane, N. B.; Gopinath, C. S. Biomass Components toward H_2 and Value-Added Products by Sunlight-Driven Photocatalysis with Electronically Integrated $Au^{\delta-}$–TiO_2: Concurrent Utilization of Electrons and Holes. RSC Sustainability 2023 (DOI: 10.1039/d2su00145d)
- Bajpai, H.; Patra, K. K.; Ranjan, R.; Nalajala, N.; Reddy, K. P.; Gopinath, C. S. Can Half-a-Monolayer of Pt Simulate Activity Like That of Bulk Pt? Solar Hydrogen Activity Demonstration with Quasi-Artificial Leaf Device. ACS Applied Materials & Interfaces 2020, 12, 30420–30430.
- Uniformly Integrated Sub-Nano Cu Particles over TiO_2; Concurrent Utilization of Electrons and Holes towards Efficient Photocatalytic Hydrogen Evolution and selective oxidation of Biomass. (To be Submitted)
- Optimizing Ni-Cu Bimetallic Nanoparticles Integrated with Titania for Efficient Hydrogen Production from Biomass: A Photocatalytic Study. (To be Submitted)
- Enhancing Photocatalytic Nitrogen Fixation through Defective TiO_2 Composites: Optimization of Surface Defects. (To be Submitted)

List of Publication(s) in SCI Journal(s) Out of the Thesis Work

- Chauhan, I.; Patra, K. K.; Bajpai, H.; Mhamane, N. B.; Salgaonkar, K. N.; Gopinath, C. S. Nanostructured Co-Doped $BiVO_4$ for Efficient and Sustainable Photoelectrochemical Chlorine Evolution from Simulated Sea-Water. Dalton Trans. 2023, 52, 2051–2061
- Kumar, P.; Bajpai, H.; Niraj Luwang, M. Cadmium (II) Organo Tetrakis-[1,2]-Oxathiin (CdOTOT): A 3D Sandwiched Frameworks with Efficient Hydrogen Production. J. Catal. 2023, 417, 341–350.
- Kumar, P.; Bajpai, H.; Gopinath, C. S.; Luwang, M. N. Sulfur Functionalization via Epoxide Ring Opening on a Reduced Graphene Oxide Surface to Form Metal (II) Organo-Bis-[1,2]-Oxathiin. Inorg. Chem. 2021, 61, 279–286.
- Patra, K. K.; Ghosalya, M. K.; Bajpai, H.; Raj, S.; Gopinath, C. S. Oxidative Disproportionation of MoS_2/GO to MoS_2/MoO_{3-x}/RGO: Integrated and Plasmonic 2D-Multifunctional Nanocomposites for Solar Hydrogen Generation from Near-Infrared and Visible Regions. J. Phys. Chem. C 2019, 123, 21685–21693.

RSC Sustainability

ROYAL SOCIETY OF CHEMISTRY

PAPER

View Article Online
View Journal

Check for updates

Cite this: DOI: 10.1039/d2su00145d

Biomass components toward H_2 and value-added products by sunlight-driven photocatalysis with electronically integrated $Au^{\delta-}$–TiO_2: concurrent utilization of electrons and holes†

Himanshu Bajpai, [ab] Inderjeet Chauhan, [ab] Kranti N. Salgaonkar, [ab] Nitin B. Mhamane [ab] and Chinnakonda S. Gopinath *[ab]

While the progress of photocatalytic overall water splitting is hindered mainly by sluggish oxygen evolution kinetics, photocatalytic hydrogen generation using biomass components, such as glycerol as a sacrificial reagent, is a prudent way to efficient hydrogen production. Can we also utilize holes effectively to oxidize the sacrificial agent to value-added products (VAPs)? Towards answering this question of concurrent utilization of electrons and holes, a successful attempt has been made. Herein, we report a facile photo-deposition method to prepare well-dispersed plasmonic Au integrated with P25–TiO_2. XPS studies show the nature of gold to be electron-rich or anionic, demonstrating strong electronic integration with titania and possible charge transfer from oxygen-vacancy sites to gold, which in turn helps the simultaneous production of large amounts of H_2 (18 mmol h^{-1} g^{-1}) and VAPs (glycolaldehyde, dihydroxyacetone, and formic acid) formation from glycerol. Elemental mapping and HRTEM images demonstrate a uniform distribution of Au on TiO_2, leading to strong Au–TiO_2 nano-heterojunctions, and hence a high photocatalytic activity. H_2 yield decreases by 4 and 18-fold with glucose and cellulose, respectively, compared to glycerol. A systematic photocatalytic study was carried out under aerobic and anaerobic conditions to understand the glycerol oxidation products. In addition to H_2, 4–10% of glycerol in 5 h was oxidized to VAPs in direct sunlight underscoring the high activity associated with Au@TiO_2. Further, the C–C cleavage of glycerol also occurs to a significant extent. Hence, significantly prolonged irradiation is expected to result in improved results with longer-chain biomass components to VAPs. It is worth exploring the current approach with other metal-integrated semiconductors with different redox potentials and various biomass components towards H_2 and VAP formation.

Received 24th December 2022
Accepted 17th February 2023

DOI: 10.1039/d2su00145d

rsc.li/rscsus

Open Access Article. Published on 17 February 2023. Downloaded on 5/3/2023 8:01:09 AM.
This article is licensed under a Creative Commons Attribution-NonCommercial 3.0 Unported Licence.

Sustainability spotlight

Present research is towards addressing the circular economy by converting biomass component molecules to value added products, namely glycolaldehyde, dihydroxyacetone and formic acid, along with hydrogen by direct sunlight driven photocatalysis. While conventional heterogeneous catalysis of biomass conversion requires high temperature/pressure, present method achieves the same at ambient conditions with solar energy. Further CO_2 is almost completely avoided in the present work by not producing the same in the reaction and by employing solar energy for reaction. Further solar energy is effectively stored in the chemical bonds of value added products. Therefore, this research contributes to the circular economy. Present work aligns with the goals 7 of "Affordable and Clean Energy" 12 of "Responsible Consumption and Production" and 13 of "Climate Action" in the UN's Sustainable Development Goals.

Introduction

Fossil fuels for global energy are like glucose to the human body, which move the entire world but are also the main cause of CO_2 emission and hence contribute to climate change; however, unlike fossil fuels, the global energy demand can be at least partially fulfilled by renewable energy sources, *e.g.*, solar and wind energy.[1] Hydrogen as a fuel is ideal for high gravimetric energy (120 MJ kg^{-1}) compared to any other fossil fuel and produces no harmful by-products, except water, when

[a]*Catalysis and Inorganic Chemistry Division, CSIR – National Chemical Laboratory, Dr Homi Bhabha Road, Pune 411 008, India*

[b]*Academy of Scientific and Innovative Research (AcSIR), Ghaziabad 201 002, India. E-mail: cs.gopinath@ncl.res.in*

† Electronic supplementary information (ESI) available: Contains photographs for the dispersion of the catalyst suspension after 5 h of irradiation (S1), zeta potential (S2), NMR spectra (S3), glycerol oxidation product analysis (S4–S6), plausible reaction pathway of glycerol to VAPs (S7), X-ray diffraction (S8), and HRTEM images (S9). See DOI: https://doi.org/10.1039/d2su00145d

© 2023 The Author(s). Published by the Royal Society of Chemistry

Open Access Article. Published on 17 February 2023. Downloaded on 5/3/2023 8:01:09 AM.
This article is licensed under a Creative Commons Attribution-NonCommercial 3.0 Unported Licence.

subjected to combustion. However, in the present scenario, >95% of hydrogen is produced by fossil fuels, such as steam reforming of methane/naphtha, resulting in greenhouse gases as by-products and causing global warming. To deal with global warming and the future energy crisis while considering limited fossil fuel availability, combining solar energy and biomass/biowaste can lead to sustainable and green energy by solar water splitting (SWS).[2–4] Can we also concurrently convert biomass to value-added products (VAPs), so that the whole process could be considered green? We are partially successful in our efforts to convert biomass to H_2 and VAPs.

SWS at zero potential can fulfill the future energy demand; however, the main drawback is its low efficiency. It has been 50 years since the first report of SWS appeared in 1972, and we are still far away from finding an efficient photocatalytic system of hydrogen generation from SWS.[5] Certain factors hamper efficiency, such as (1) sluggish oxygen evolution kinetics, (2) high rate of electron–hole recombination, and (3) 3–5 orders of difference in time scales of photophysical and photochemical processes.[6–8]

Since biomass components, such as cellulose and glucose, have very low economic value and glycerol is a by-product of biodiesel industries; it is worth employing them as feedstock and/or sacrificial agent. It is also known that the production of biodiesel and hence glycerol generation is also increasing every year by 10%. The conversion of glycerol into VAPs is a point of attraction in the present era, as its under-utilization is posing a threat to the biodiesel industry; glycerol availability at a very low price should be exploited commercially.[9–11] Glycerol could be used in photocatalytic water splitting not only to increase H_2 production but also as a sacrificial reagent to consume holes for partial oxidation to VAPs.[12–15] The same concept can be extended to other biomass components for their conversion to VAPs.

Plasmonic metals (Au, Ag, Cu) integrated with semiconductors are known to enhance charge separation and work as a photosensitizer due to the surface plasmon resonance (SPR) effect, *via* either the direct electron transfer or resonant energy transfer.[16–18] Since TiO_2 is a well-known stable semiconductor, the large bandgap and high electron–hole recombination result in low efficiency. Plasmonic metals, especially gold shows significantly different absorption spectra with different particle sizes and morphologies and can be integrated with TiO_2 to utilize visible light in direct sunlight.[19–22] However, in SWS, the overall kinetics is mainly hindered due to the four-electron O_2 evolution process, therefore, to enhance the overall kinetics, a sacrificial reagent,[23] such as methanol, triethanolamine, sulphide–sulphite is normally employed, which consumes holes rapidly and minimizes electron–hole recombination. From the term sacrificial, it is clear that these chemicals increase hydrogen production; however, can we prudently utilize holes, so that hole consumption leads to the conversion of sacrificial agents to VAPs too? Hence, a versatile catalyst is required to meet the dual purpose of photocatalytic H_2 production as well as oxidation of low-value sacrificial agent (biomass component) specifically into VAPs.[24–27]

Zang *et al.*[28] employed Au/TiO_2 system for photo-reforming of ethanol; they obtained 7 mmol h^{-1} g^{-1} of H_2 generation with formaldehyde and carbon dioxide as by-products but did not quantify the by-products. Wang *et al.*[29] attempted photocatalytic H_2 generation using Ag_2O/TiO_2 system, however, the reported H_2 yield was 0.3 mmol h^{-1} g^{-1}, and there was no VAP reported. For the Cu/TiO_2 system, several researchers have attempted photo-reforming of glycerol as a model sacrificial reagent. Trang *et al.*[30] reported 16 mmol h^{-1} g^{-1} H_2 yield under direct sunlight; however, there are no VAPs reported. With 1.6 mmol h^{-1} g^{-1} of H_2, Montini *et al.* produced CO_2, CH_4, glycolaldehyde, and di-hydroxy acetone by converting glycerol into VAPs.[31] In the majority of the literature, authors mostly paid attention to H_2 production and not much on the selectivity of the oxidation products; however, in the present study, we exploited the large-scale and concurrent utilization of electrons and holes toward hydrogen and VAPs, respectively.

Herein we report the Au@TiO_2 composite, prepared *via* the facile photo deposition method, by taking advantage of the positive zeta potential of TiO_2. Elemental mapping and X-ray photoelectron spectroscopy (XPS) was employed to understand the distribution and electronic environment of the Au@TiO_2, respectively. The photocatalytic hydrogen evolution reaction (HER) was carried out with Au@TiO_2 in aqueous glycerol, which also showed high glycerol conversion and selectively to three major VAPs. HER studies were also carried out with glucose and cellulose. ^{1}H NMR was employed to identify and quantify the oxidation products.

Experimental section

Synthesis of Au/TiO_2 composite

Electronically integrated and highly-dispersed Au@TiO_2 was prepared by a modified procedure of controlled photochemical deposition. 200 mg P25–TiO_2 was dispersed in 100 ml of water : methanol (60 : 40) solution in a 250 ml quartz round bottom (RB) flask; after stirring for 10 min. 3.08 mg of the Au-precursor ($HauCl_4 \cdot 3H_2O$) was added to prepare 0.5 wt% Au-containing TiO_2. Other compositions were also prepared in a similar manner with the required amount of Au-precursor. The solution was subjected to N_2 purging in the dark for 30 min. with stirring for uniform interaction of $[AuCl_4]^{-1}$ with TiO_2. It is very likely that gold-center is attracted to oxygen vacancy sites. This solution was subjected to UV lamp irradiation for 1 h. After irradiation, the solution was centrifuged and washed with hot water (338 K) for several times, and then dried in the oven at 343 K. Different wt% of Au with 0.1, 0.5, and 1% with respect to TiO_2 were also synthesized and they are denoted as 0.1Au@TiO_2, 0.5Au@TiO_2 and 1Au@TiO_2, respectively.

Photochemical hydrogen production measurement

For photocatalytic hydrogen production, 3 mg of any Au@TiO_2 catalyst was taken in a 50 ml borosilicate RB flask, with 20 ml of different percentages of aqueous glycerol (0.14, 0.6, and 1.4 M glycerol), and subjected to 10 min of N_2 purging. Then, the photocatalyst was irradiated with light under one sun condition

© 2023 The Author(s). Published by the Royal Society of Chemistry

Open Access Article. Published on 17 February 2023. Downloaded on 5/3/2023 8:01:09 AM.
This article is licensed under a Creative Commons Attribution-NonCommercial 3.0 Unported Licence.

(100 mW cm^{-2} with a 450 W Newport solar simulator fitted with a 1.5 AM filter) or direct sunlight (average light intensity was 60 mW cm^{-2}). Hydrogen was the only gas-phase product, and it was confirmed and quantified by GC (Agilent 7890A) analysis.

Photochemical glycerol oxidation measurement

To measure the glycerol oxidation products, 5 mg of the catalyst was initially dispersed in 5 ml of 0.05 M glycerol aqueous solution, and then kept under nitrogen or oxygen purging for 30 min, depending on the type of the reaction carried out subsequently. It was realized from the initial measurements with the same glycerol concentration (as that for the above-mentioned H_2 production) for oxidation, the conversion was low and this made the NMR analysis also difficult for the product identification. In view of this difficulty, a few other catalyst : glycerol ratios were also evaluated and optimized to the maximum glycerol conversion along with the ease of product identification. The maximum glycerol conversion to value-added products was observed with a 5 mg catalyst in a 5 ml solution of 50 mM glycerol. The solution was kept under nitrogen or oxygen purging for 30 min, depending on the type of reaction carried out subsequently, after that, the catalyst-glycerol suspension was irradiated under one sun condition or direct sunlight. All oxidized products of glycerol were quantified using Agilent GC (7890A) and ^{1}H NMR. Liquid product identification and quantification were carried out by NMR (Bruker AV 500), with 1 mmol KHP (potassium hydrogen phthalate) as the internal standard.

$$C_x = \frac{I_x}{I_{cal}} \times \frac{N_{cal}}{N_x} \times C_{cal}$$

where C_x, I_x, I_{cal}, N_{cal}, N_x, C_{cal} are the concentration of the product, integral area of the product, integral area of the standard, number of protons from the standard and the product, and concentration of the standard, respectively. Various liquid products were measured by NMR and hydrogen through GC, and the reproducibility was within a 5% error margin.

Materials characterization

Diffuse reflectance UV-Vis measurement was carried out on a Shimadzu spectrophotometer (model-UV2550) with spectral grade $BaSO_4$ as the reference material. Powder X-ray diffraction (XRD) data were collected on a Pan analytic X'pert pro dual goniometer diffractometer using Cu-Kα (1.5418 Å) radiation with a Ni filter. HRTEM analysis of the material was conducted on a JEOL JEM F-200 HTEM instrument operating at 200 kV equipped with EDX (energy dispersive X-ray analysis). XPS analysis was carried out on an instrument from Thermo Fisher Scientific Instruments, UK with monochromatic Al Kα as the X-ray source with 6 mA beam current and operating at 12 kV. All the spectra were calibrated, with respect to adventitious carbon observed at 284.9 eV. Glycerol product quantification was carried out with Bruker AV 500, with NS-32, DS-4, SW-24.9934 ppm with water suppression sequence using Bruker Top Spin. Many characterization tests were repeated using at least three sets of samples/materials prepared in different batches. An Agilent GC (7890A) was used for gas analysis with a molecular sieve-coated packed column using TCD as a detector. Zeta potential measurements were performed on a Brookhaven Instruments NanoBrook series zeta potential analyser.

Results and discussions

UV-visible absorption by Au@TiO_2

UV-visible reflectance spectrum was measured and converted to absorption. UV-Vis spectra were recorded on all Au@TiO_2

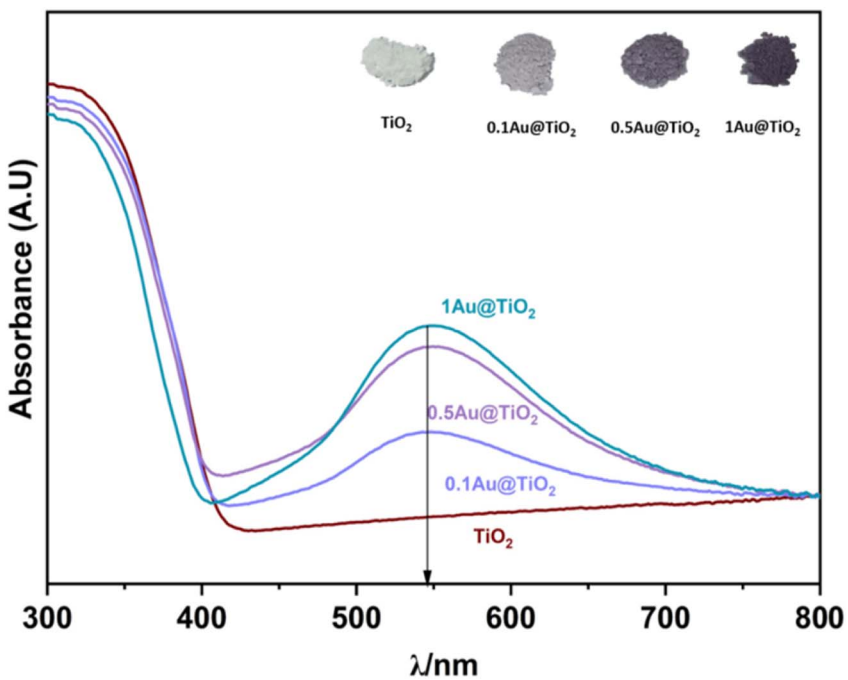


Fig. 1 UV-visible absorption spectra of TiO_2, 0.1Au@TiO_2, 0.5Au@TiO_2, and 1Au@TiO_2, inset shows the image of all photocatalysts. SPR feature was observed at 545 nm for all *x*Au@TiO_2.

© 2023 The Author(s). Published by the Royal Society of Chemistry

Open Access Article. Published on 17 February 2023. Downloaded on 5/3/2023 8:01:09 AM.
This article is licensed under a Creative Commons Attribution-NonCommercial 3.0 Unported Licence.

photocatalysts and the results are shown in Fig. 1, along with parent TiO_2. SPR (surface plasmon resonance) absorption features were observed on all Au@TiO_2 materials at 545 nm, irrespective of Au content.[32] While 0.1Au@TiO_2 showed low-absorption intensity, the other two compositions show comparable absorption behaviour with an increase of SPR intensity, associated with higher absorption ability in the visible region compared to 0.1Au@TiO_2. It is also to be noted that the colour associated with the photocatalyst appeared to be increasingly becoming deep purple (inset image of Fig. 1). It is likely that the deep purple colour associated with 1Au@TiO_2 could be preventing more light absorption, compared to 0.5Au@TiO_2, which resulted in low photocatalytic hydrogen evolution, and the same is discussed in the later section.

Solar hydrogen production

Solar hydrogen production was measured under one sun (100 mW cm^{-2}) and direct sunlight in Pune, Maharashtra, India, from February to May with an average light intensity of 60 mW cm^{-2}. It is to be noted that sunlight power fluctuates between 52 and 70 mW cm^{-2} depending on the time of the day, cloud cover, *etc.* However, for practical purposes, we considered 60 mW cm^{-2} as the average solar power. 60–65 mW cm^{-2} power was observed for at least 50% of the total reaction time. Solar hydrogen evolution measurement was carried out systematically under different reaction conditions. During hydrogen evolution measurement, 3 mg of the catalyst was used with 20 ml solution and kept under irradiation without stirring. It is to be noted that a uniform suspension, without settling of any particles, was observed with the catalyst in an aqueous glycerol solution, and hence the experiments were carried out without stirring (see photos shown in Fig. S1 in ESI†). In Fig. 2a, different weight percent loadings of Au on TiO_2 were subjected to hydrogen evolution under direct sunlight with 0.6 M glycerol as a sacrificial reagent. TiO_2 gave 0.86 mmol h^{-1} g^{-1} of hydrogen, after loading with Au (xAu@TiO_2), and absorption of composite shifted to the visible light range due to the SPR effect of Au, as shown in UV-Vis absorption spectra (Fig. 1), indicating the strong absorption at 545 nm resulting in higher H_2 production. With 0.1 wt% of Au loading, hydrogen evolution was observed to be 7.4 mmol h^{-1} g^{-1}, which is 8-fold higher than that of bare TiO_2.

While increasing the weight% of Au from 0.1 to 1, 0.5% exhibited the highest hydrogen production (18 mmol h^{-1} g^{-1}) than the 1% Au-containing (16.5 mmol h^{-1} g^{-1}) composite under direct sunlight. It is to be noted that comparable SPR feature intensity was observed for 0.5 and 1 wt% of Au@TiO_2, reflecting a similar observation as in solar hydrogen production. These observations hint that the Au-dispersion remains the same for 0.5 and 1 wt% of Au. In fact, a marginally lower H_2 yield was observed with 1 wt% Au, indicating that there could be other changes. This is supported by a significant change observed with Au 4f binding energy and the same is explained later in the XPS section. Some of the top results reported for H_2 production with Au and Cu-based systems from literature are compiled in Table 1. Results obtained from the current studies are superior to the results reported earlier with hydrogen and VAPs production, as shown in Table 1; also, direct sunlight irradiation shows significantly better results than with one sun condition. Reported higher hydrogen production, than that from this study, is invariably observed under UV irradiation; needless to say that significant UV light absorption by titania too contributes to the total activity. While glycerol was used as a sacrificial agent by a few groups for hydrogen generation, no

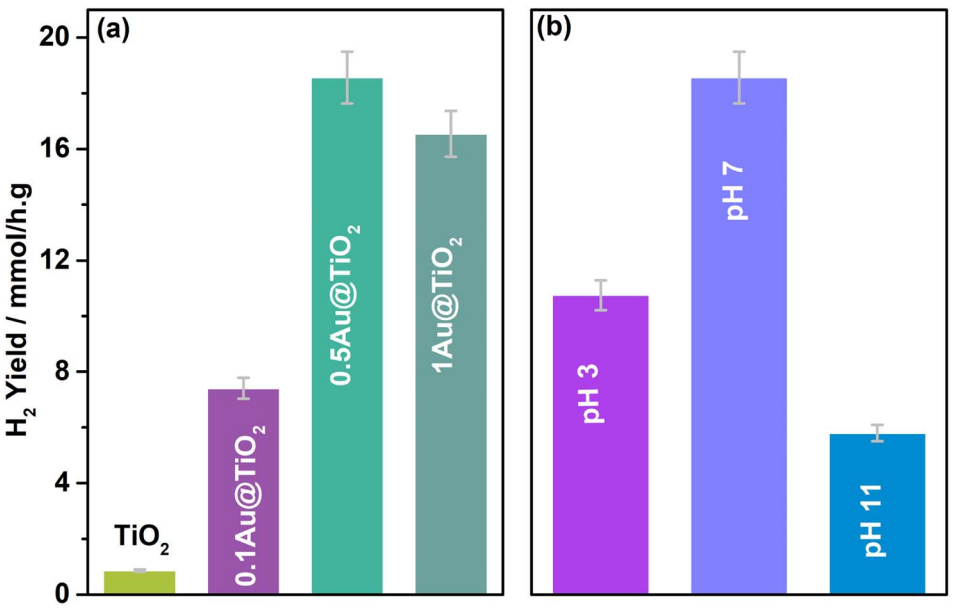


Fig. 2 (a) Photocatalytic hydrogen yield observed for (a) different wt% of Au on TiO_2 and (b) 0.5Au@TiO_2 at different pH conditions; to maintain the pH, 0.01 M HCl and NaOH were used as acid and base, respectively. 5% glycerol was used as a sacrificial reagent under direct sunlight with an average light intensity of 60 mW cm^{-2}.

© 2023 The Author(s). Published by the Royal Society of Chemistry

Open Access Article. Published on 17 February 2023. Downloaded on 5/3/2023 8:01:09 AM.
This article is licensed under a Creative Commons Attribution-NonCommercial 3.0 Unported Licence.

Table 1 Top H_2 production results reported in the literature for Au@TiO_2 along with the reaction conditions

Catalyst	Light source and power	H_2 (mmol h^{-1} g^{-1})	Reaction conditions	VAPs	Ref.
1.5% Au/TiO_2 P25	UV light	28.3	10% glycerol in water (6.5 mg in 20 ml solution)	NA	11
1% Au/TiO_2 P25	One sun (UV-Vis)	0.307	Water : methanol = 3 : 1 (20 mg catalyst in 40 ml solution)	NA	16
5% Au/TiO_2 hierarchical spheres	UV-Vis (100 mW cm^{-2})	8.06	30 vol% methanol in water (50 mg catalyst in 100 ml solution)	NA	36
0.5% Au/TiO_2 nanorods	UV light	29	10% glycerol in water (6.5 mg catalyst in 20 ml solution)	NA	37
2% Au/TiO_2	UV light	30.3	10% glycerol in water (6.5 mg catalyst in 20 ml solution)	NA	38
0.3% AuTiO_2	Simulated light (21.1 mW cm^{-2})	0.2	1% TEOA with water (250 mg with continuous flow of nitrogen)	NA	39
1% Au/TiO_2 anatase	Solar lamp (10.7 mW cm^{-2})	2.55	5% glycerol in water (50 mg in 50 ml solution)	NA	40
$Cu_2O/Bi_2O_3/TiO_2$	UV-Vis	6.2	5% glycerol	NA	41
Cu_2O/TiO_2	400 W metal halide lamp	4.7	5 v/v% glycerol/water (100 mg catalyst in 200 ml) with pH 10	NA	42
Cu_2O/TiO_2	SB-110P/F lamp (100 W), 365 nm	15.3	5 v/v% glycerol/water (2.5 mg catalyst in 25 ml)	NA	43
CuO_x–PtO_2/TiO	300 W xenon lamp	1.3	10% glycerol (50 mg catalyst in 100 ml)	NA	44
3% Cu/TiO_2	100 mW cm^{-2}	0.05	1% acetic acid (25 mg in 25 ml)	CH_4, CO_2	45
0.5% Au@TiO_2	One sun condition (100 mW cm^{-2})	15	5% (0.6 M) glycerol in water (3 mg in 20 ml)	Dihydroxyacetone, glycolaldehyde, formic acid	Current work
0.5% Au@TiO_2	Direct sunlight (60 mW cm^{-2})	18	5% (0.6 M) glycerol in water (3 mg in 20 ml)	Dihydroxyacetone, glycolaldehyde, formic acid	Current work

other VAPs of glycerol were observed or reported in the literature. This factor makes the current work far superior in terms of the concurrent utilization of holes and electron charge carriers for versatile light energy to chemical energy conversion to H_2 as well as VAPs.

As shown in the structural characterization studies in the following sections, the highest hydrogen generation activity observed with 0.5Au@TiO_2 is attributed to an atom-like sub-nanometre Au cluster dispersion over TiO_2, as discussed in the later sections. Furthermore, photocatalytic hydrogen evolution measurements at different pH values were carried out with 0.5Au@TiO_2 catalyst with 5% glycerol under direct sunlight, and the results are shown in Fig. 2b. The pH change was achieved with the required amount of dilute (0.01 M) HCl and NaOH under acidic and alkaline conditions, respectively, and pH change was ensured using a pH meter (Mettler Toledo seven compact S210). Interestingly and critically, the highest amount of hydrogen was observed at neutral pH; hydrogen production was found to decrease on either increasing or decreasing the pH to basic or acidic conditions. In the acidic pH, zeta potential is close to the zero-point charge, which results in significant agglomeration of TiO_2 particles and hence a decrease in photocatalytic activity was observed, however, under basic pH conditions, due to the abundantly-available hydroxyl groups, the dissociation of Ti–OH is decreased drastically. The zeta potentials measured for all three pH conditions are shown in Fig. S2 (in ESI†) fully supporting this result. These factors are known to hinder the photocatalytic activity, and it was suggested from the kinetic model by Estahbanati *et al.*[46] At neutral pH (pH = 7) good dispersion of the catalyst in the water/glycerol was observed. Even after a few days, we did not observe any settling of the catalyst (Fig. S1†) but a highly-dispersed uniform suspension was maintained, which is also an interesting observation in the present work. In general, with powdered catalyst, due to the stirring, significant scattering of the light occurs and the same reduces the light absorption by the catalyst; if there is no stirring, the catalyst would settle at the bottom of the reactor and also reduces the photoactivity of the composite; this problem could be overcome by making the catalyst in a thin film form (as in Si PV) or should be dispersed in the solution throughout the reaction.[6,47]

Three different glycerol concentrations (1, 5, and 10%) were employed to understand the effect of sacrificial reagent concentration; activity was measured periodically with 0.5Au@TiO_2 in 20 ml aqueous glycerol solution under one sun condition and the results are shown in Fig. 3a. An interesting trend in results was observed, and the following points deserved to be highlighted. (1) 5% (0.6 M) glycerol containing aqueous solution showed a constant H_2 yield of 15 mmol h^{-1} g^{-1} as a function of irradiation time; among the three different

Open Access Article. Published on 17 February 2023. Downloaded on 5/3/2023 8:01:09 AM.
This article is licensed under a Creative Commons Attribution-NonCommercial 3.0 Unported Licence.

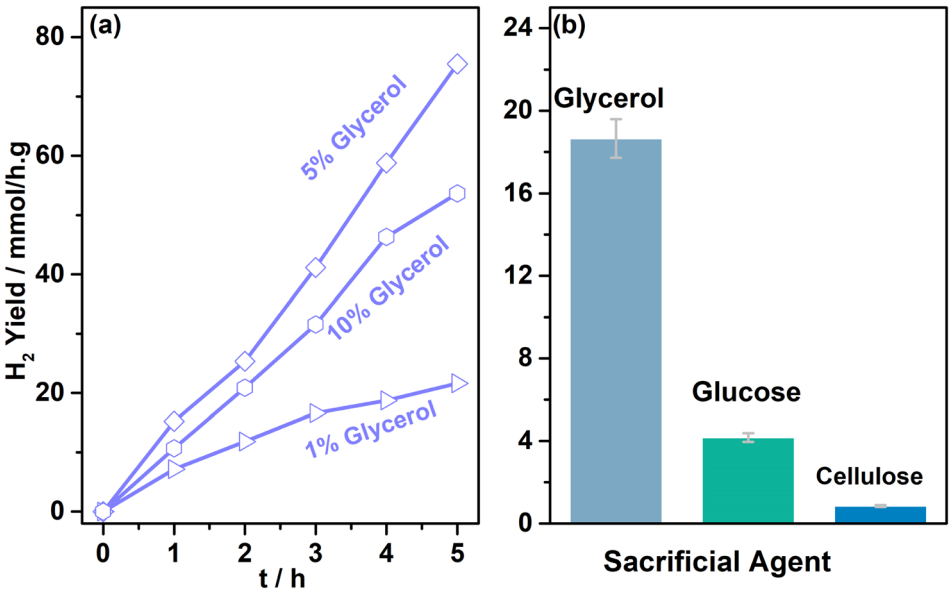


Fig. 3 (a) Photocatalytic hydrogen yield observed with 0.5 wt% of Au over TiO_2 with different concentrations of glycerol under one sun condition (100 mW cm^{-2}, AM 1.5 filter). (b) Photocatalytic hydrogen yield observed with different biomass components as sacrificial reagents using 0.5 wt% Au on TiO_2 under direct sunlight with an average intensity of 60 mW cm^{-2}.

glycerol concentrations (1, 5, and 10%), indeed, 5% showed the best performance. (2) While 10% (1.4 M) glycerol concentration also showed a constant H_2 yield of 11 mmol h^{-1} g^{-1}, it is lower than that at 5% glycerol concentration. (3) In contrast to the above two points, 1% (0.14 M) glycerol-containing solution showed the lowest H_2 yield, although initially, it showed 7 mmol h^{-1} g^{-1} yield, H_2 yield reaches a plateau at later hours. The influence of the sacrificial agent concentration on hydrogen generation has been addressed significantly in the literature.[33–35] Dependence of the hydrogen generation has been demonstrated with different concentrations of the reactant. Beyond a threshold concentration of the sacrificial agent, active sites are saturated with those molecules and the same decreases the photoactivity. In the present case, the viscosity factor of glycerol also adds to the diffusion issues, which decreases the rate at 10% glycerol concentrations. Generally, the observed results indicated that an optimum glycerol concentration was required to achieve the best performance in the present experiments; except hydrogen, no other gaseous product was observed. For the oxidation product of the glycerol, due to the high concentration of glycerol employed for the results shown in Fig. 2 and 3, it was challenging to identify and quantify the product by NMR. Another set of the study was carried out to explore the products of glycerol oxidation at low glycerol concentrations, which will be discussed later.

In addition to glycerol, glucose, and cellulose were also evaluated as sacrificial agents; it is known that they all have similar building blocks, except for chain lengths. The average H_2 yield obtained is shown in Fig. 3b. 20 ml of 0.35 M glucose solution was employed with 3 mg of the catalyst (0.5Au@TiO_2), this is mainly to maintain the similar number of carbon atoms as that of 5% glycerol solution. 4.1 mmol h^{-1} g^{-1} H_2 yield was observed under direct sunlight with glucose, while glycerol solution exhibited 18 mmol h^{-1} g^{-1}. A four-fold decrease in H_2 yield with glucose is attributed primarily to the 6-carbon unit; more difficult C–C cleavage is the leading/silent reaction also occurs, which consumes a significant number of electrons and protons and slows down the overall kinetics. However, the result was still significant, and, in fact, it opens a new window to the utilization of biomass components for photocatalytic hydrogen production. One more reason for the lower activity with glucose, compared to that with glycerol as a sacrificial reagent, is due to the settling of the catalyst in the bottom of the RB flask; due to this, the light absorption capacity decreases and results in lower photoactivity. In the case of cellulose, 200 mg of cellulose was taken in 20 ml water with 3 mg catalyst and subjected to direct sunlight irradiation for 5 h. Because cellulose is not soluble in water, activity decreased drastically to 0.8 mmol h^{-1} g^{-1}. To improve and produce an efficient sacrificial reagent for photocatalytic hydrogen production, the solubility of cellulose needs to be increased but without employing harsh basic or acidic conditions. Dispersed cellulose particles in the solution would tend to scatter the light, rather than light absorption, which also results in lower photoactivity.[6,48–50] Ideally a systematic approach from waste biomass components to hydrogen and any VAP would be more appealing.[51,52] Our efforts to identify any oxidation products of glycerol from the results shown in Fig. 1 and 2 was not successful, due to high glycerol and low catalyst content. Hence the conditions were modified to enhance the oxidized product concentration and the observed results are shown and discussed in the following sections.

Glycerol oxidation by direct solar photocatalysis

Glycerol oxidation products were measured from systematic photocatalytic experiments. 5 mg of 0.5Au@TiO_2 with 5 ml of

© 2023 The Author(s). Published by the Royal Society of Chemistry

Open Access Article. Published on 17 February 2023. Downloaded on 5/3/2023 8:01:09 AM.
This article is licensed under a Creative Commons Attribution-NonCommercial 3.0 Unported Licence.

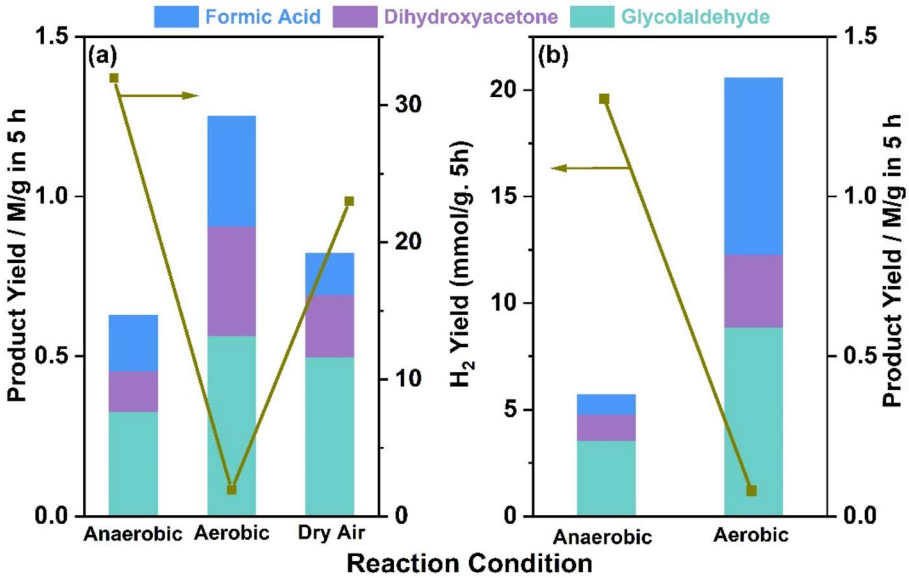


Fig. 4 Photocatalytic glycerol oxidation with 0.5%Au@TiO_2 under (a) direct sunlight with an average intensity of 60 mW cm^{-2}, and (b) one sun condition (100 mW cm^{-2}). All product concentrations were for five hours of the reaction time in both panels.

0.05 M glycerol was used for photocatalytic glycerol oxidation. These experiments were carried out in aerobic (purged with O_2), anaerobic (purged with N_2), and dry air conditions. Representative product analysis data obtained using NMR are shown in Fig. S3 in ESI.† Fig. 4 shows the data on photocatalytic glycerol oxidation carried out under the three conditions mentioned above, and the products observed along with hydrogen under (a) direct sunlight, and (b) under one sun condition. Three major liquid products, namely, glycolaldehyde, dihydroxyacetone, and formic acid, were observed under both reaction conditions. In anaerobic conditions under direct sunlight, 0.32, 0.12, and 0.17 M g^{-1} of glycolaldehyde, dihydroxyacetone, and formic acid were observed, respectively, in 5 h; along with the liquid products, 32 mmol g^{-1} of hydrogen was observed in 5 h reaction time. When purging was carried out using dry air, the amount of oxidation product was also found to be increased; 0.49, 0.19, 0.13 M g^{-1} of glycolaldehyde, dihydroxyacetone, and formic acid, respectively, were observed along with 23 mmol g^{-1} hydrogen in 5 h; 2.8 mmol g^{-1} of CO_2 was also observed in the gaseous products. In the case of the aerobic condition, the overall product formation rate increased twice that of anaerobic conditions, along with glycerol conversion. Significant over-oxidation to CO_2 (7.5 mmol g^{-1}) was also observed, and hydrogen generation decreased to 1.9 mmol g^{-1}. This indicates that in the presence of oxygen, oxidation of glycerol also occurs instead of water reduction. Expectedly, oxygen helps in the oxidation of the glycerol, through superoxo/peroxo radicals by electron consumption or the oxygen reduction reaction, this in turn decreases the hydrogen production.

Under one sun condition, similar liquid, and gaseous products were observed with the same trend. However, over-oxidation was comparatively lower with a smaller amount of CO_2 production (5.3 mmol g^{-1}) under one sun condition than under direct sunlight. An interesting observation to be noted is the significantly large amount of formic acid and smaller CO_2 under one sun irradiation and aerobic conditions, compared to direct sunlight irradiation. A careful comparison of both results revealed that while glycolaldehyde was observed at the same level, formic acid was observed to increase at the cost of dihydroxyacetone under one sun condition. It is also to be noted that the temperature of the solution and the catalyst increases to around 333 K under direct sunlight, while the same was observed to be 320 K under one sun condition, carried out under laboratory ambient conditions. Hence, the overall increase in the reaction rate in direct sunlight may be partly attributed to an enhancement in temperature. Controlled experiments were also carried out at 333 K under one sun condition to ensure the temperature effect in direct sunlight. The results observed at 333 K are equivalent to those of sunlight conditions within the experimental accuracy. This further confirmed the influence of temperature under both natural and simulated light conditions. More power (100 mW cm^{-2}) under one sun condition leads to the decomposition of dihydroxyacetone to formic acid. More experiments under a controlled atmosphere are required to ascertain the extent of the influence of the temperature and illumination power. In addition, the advantage of higher temperature and lower light power with direct sunlight may be utilized in a prudent manner. These experiments suggest that with regulated oxygen content, aqueous glycerol can be a very efficient reactant to generate VAPs along with hydrogen. A simple back calculation by accounting for all the carbon-containing products, including CO_2, originating from the oxidation of glycerol, leads to glycerol conversion levels between 6 and 13% in 5 h with 52% selectivity for glycolaldehyde under anaerobic conditions. High TON values of 1280 and 920 were observed with 0.5Au@TiO_2 for hydrogen under anaerobic and dry air conditions, respectively, while high TON values (68–113) were observed for VAPs under

© 2023 The Author(s). Published by the Royal Society of Chemistry

Open Access Article. Published on 17 February 2023. Downloaded on 5/3/2023 8:01:09 AM.
This article is licensed under a Creative Commons Attribution-NonCommercial 3.0 Unported Licence.

aerobic conditions (Tables S4–S6 in ESI†). A marginal decrease in hydrogen production by 1Au@TiO_2 than that by 0.5Au@TiO_2 suggested the higher activity associated with Au-clusters with the latter. We attribute this to the high dispersion of gold and electronic integration with TiO_2 with the latter. By changing the batch to a continuous flow type with controlled oxygen or dry air, the higher activity would be possible by minimizing CO_2. More experiments in this direction are desired. The present results also demonstrate the cleavage of C–C bonds occurring from glycerol all the way to formic acid and then to CO_2, and Fig. S7† shows a plausible pathway for glycerol oxidation to VAPs. Hence, there are possibilities existing to fine-tune the reaction conditions to maximize the value-added liquid oxidation products with hydrogen production. As formic acid is expected to undergo fast oxidation to CO_2, a product separation stage and recirculation of unreacted glycerol would be a good idea for achieving higher glycerol conversion to the same VAPs.

Structural analysis and elemental mapping

XRD, HRTEM, and elemental mapping methods were employed to understand the structure and morphology of the photocatalysts. XRD results of TiO_2 and *x*Au@TiO_2 are shown in Fig. S8.† As expected, anatase and rutile features were observed in both photocatalysts. However, after gold integration with TiO_2, no difference is discernible in the XRD pattern up to 1 wt% of Au integrated TiO_2 compared to virgin TiO_2; indeed, 0.5 and 1 wt% of Au loading is too small and this could be one reason for the absence of any gold features in the XRD results. However, it rules out the clustering of gold atoms to big particle size(s). This naturally leads to the question of the status of gold in xAu@TiO_2 the photocatalysts.

To understand the structural and/or integration aspects of Au and its distribution over TiO_2, HRTEM analysis was carried out and the representative results are shown in Fig. S9.† TiO_2 particles with an average size of 20 ± 1 nm were observed, which is typical for P25 TiO_2. However, after careful investigations of multiple batches of 0.5Au@TiO_2, we did not observe any Au particle over TiO_2. Nonetheless, it is essential to understand the role of gold to understand the SPR features at 545 nm, as shown in Fig. 1, and very high photocatalytic activity was observed for hydrogen generation and glycerol oxidation under solar irradiation conditions. To investigate this phenomenon, we carried out elemental mapping, and the results are shown in Fig. 5. Elemental mapping gives an idea about the small Au-cluster formation on TiO_2, and demonstrates the homogeneous distribution of Au on TiO_2 particles. Ti and O mapping shown in

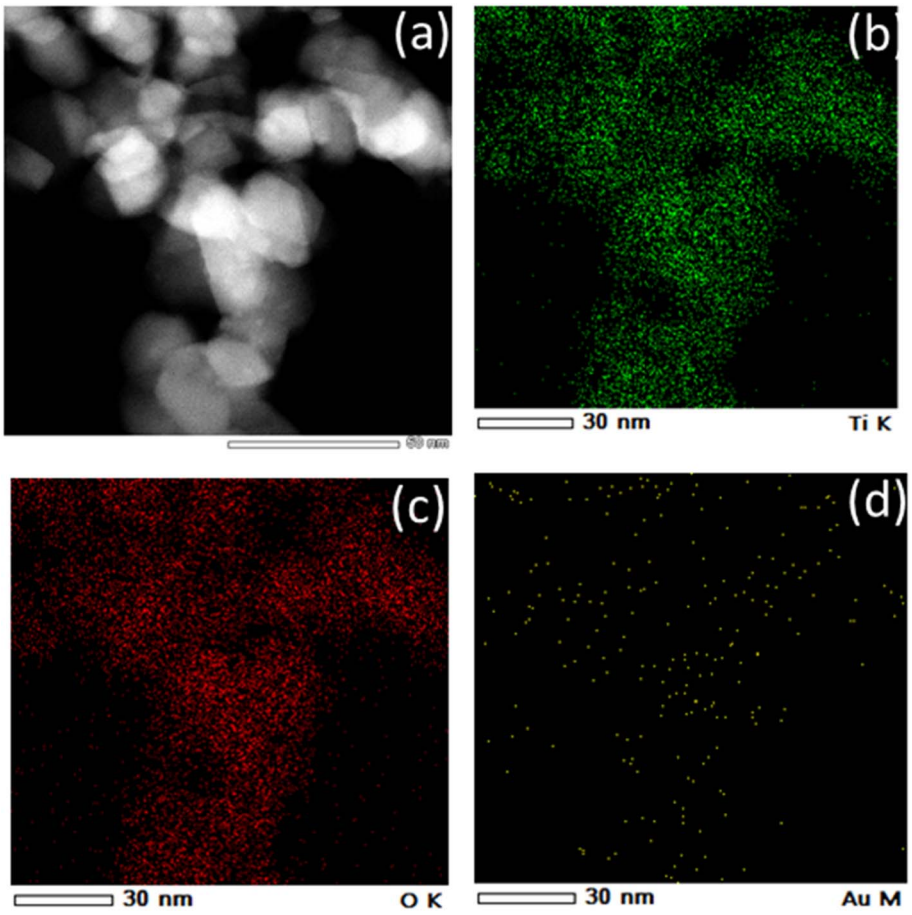


Fig. 5 STEM image of 0.5%Au@TiO_2 and corresponding elemental distribution for Ti (green), Au (yellow), and oxygen (red) at scale bar of (a–d) 30 nm. A very uniform distribution of Au over TiO_2 nanoparticles could be observed at high resolution.

© 2023 The Author(s). Published by the Royal Society of Chemistry

Open Access Article. Published on 17 February 2023. Downloaded on 5/3/2023 8:01:09 AM.
This article is licensed under a Creative Commons Attribution-NonCommercial 3.0 Unported Licence.

Fig. 5 panels follow the expected trend In their distribution. However, in the case of Au (yellow), a very fine and homogeneous dispersion of Au on TiO_2 particles was observed. It is to be noted that the atomic weight of gold is more than four times that of titanium, and gold content in terms of the atomic percent is about 0.12–0.14% in 0.5Au@TiO_2. Although many earlier studies have reported Au@TiO_2 such a fine distribution has not been shown; uniform distribution is shown, probably, for the first time, with a photo deposition method. It is to be noted that the zeta potential of TiO_2 P25 is positive, and hence negatively charged metal-ion precursor could be loaded over TiO_2. During nitrogen purging in the dark, the negative charge $[AuCl_4]^{-1}$ is expected to be uniformly deposited over TiO_2 upon UV irradiation, and $[AuCl_4]^{-1}$ gets reduced to Au with uniform dispersion.[53] We also speculate the oxygen vacancies on the titania surface could be a possible driving force for a very high distribution. Under irradiation conditions, pre-deposited gold precursor ions get homogenously reduced over TiO_2. Indeed this leads to a highly integrated *x*Au@TiO_2. The lower the amount of gold deposited, the better the distribution observed. The low atom percent of Au and its high dispersion on titania are the reasons that its features could not be detected in XRD, while UV-Vis absorption shows the characteristic SPR feature. The specific surface area of Au on TiO_2 is likely to be higher, which results in high hydrogen production as well as glycerol conversion to VAPs. A number of earlier studies indicated the electronic and structural integration of the catalyst components leading to a facile charge transfer between semiconductors and the metal towards efficient photocatalytic activity, which was also analyzed by XPS and discussed in the next section.

X-ray photoelectron spectroscopy studies

XPS provides information on the electronic interaction between various components as well as the surface composition of composite materials. To understand the electronic interaction between TiO_2 and Au, XPS studies were carried out and the results are shown in Fig. 6. The deconvolution of Ti 2p core level shows that Ti was present in two different states for Ti^{3+} (457.45 ± 0.05 eV) and Ti^{4+}(458.6 ± 0.05 eV); however, Ti^{4+} was predominantly available (92%), while only 8% of Ti^{3+} was available on the virgin TiO_2 surface.[54] However, with 0.5Au@TiO_2, there was a decrease in the Ti^{3+} content by 50% (to 4%) as that of pristine TiO_2, and this is attributed to the deposition/integration of gold with those sites. As metal atoms are known to be electrophilic, there is a driving force to deposit gold in Ti^{3+} or oxygen vacancy sites. This integration also leads to charge transfer from TiO_2 to Au and makes the composite electronically integrated. In Fig. 6b, O 1s spectra of TiO_2 and 0.5Au@TiO_2 are shown. Three different oxygen species observed at 529.75 ± 0.05 eV (red trace), 530.45 ± 0.05 eV (blue trace), ~531.8 eV (green trace) are attributed to lattice oxygen of TiO_2, oxygen associated with Ti^{3+}, and the hydroxyl group, respectively. While there was no change in the hydroxyl group intensity was observed before and after Au-integration, the percentage of oxygen associated with Ti^{3+} decreased marginally in the O 1s spectra. This reiterates that gold cluster deposition occurs selectively at the defect sites.

Fig. 7 shows the Au 4f spectrum of 0.5Au@TiO_2. Generally, bulk and metallic gold species appear at 84 ± 0.1 eV for the Au $4f_{7/2}$ core level in the XPS spectrum.[54–56] However, interestingly, there was a large negative shift of 0.9 eV was observed with the Au 4f core levels of 0.5Au@TiO_2. Almost 1 eV shift to low BE suggests a large charge transfer from titania to gold. This observation could be possibly due to a combination of the following reasons. (a) As mentioned in the discussion of Ti 2p and O 1s, Au species gets integrated into the defect site of TiO_2, which is fully supported by the observation of a 50% decrease in Ti^{3+} content in 0.5Au@TiO_2, compared to that in virgin TiO_2. These XPS results also point toward an electronic integration between Au and TiO_2, and helping to create metal-semiconductor nano-Schottky or heterojunctions. Such junctions are essential for electron–hole pair separation, which in turn increase the utilization of the charge carriers through redox reactions. (b) Small clusters of gold are expected to behave differently than nanoclusters or bulk gold. Elemental mapping indicates the extensive distribution of small gold clusters. Due to the small size of such clusters, gold is likely deposited uniformly on the interior and exterior surfaces of the pores of titania. (c) Small clusters are expected to be electrophilic and prefer to bind at sites richer in electrons. This leads to a preferential interaction between defect sites of titania and small gold clusters. Combining the above factors makes the gold cluster behave more like anionic gold. However, a significant reduction in BE shift was observed with 1Au@TiO_2 (0.6 eV at 83.4 eV compared to that with metallic gold at 84 eV) and shows a reduction in anionic character compared to that with 0.5Au@TiO_2 (Fig. 7b). Although the gold content was doubled, hydrogen generation was observed to be marginally lower, suggesting that the state of gold does matter for the best performance. This synergy between the metal and semiconductor helps toward the charge separation, which in turn helps high photocatalytic glycerol oxidation to VAPS and hydrogen evolution.

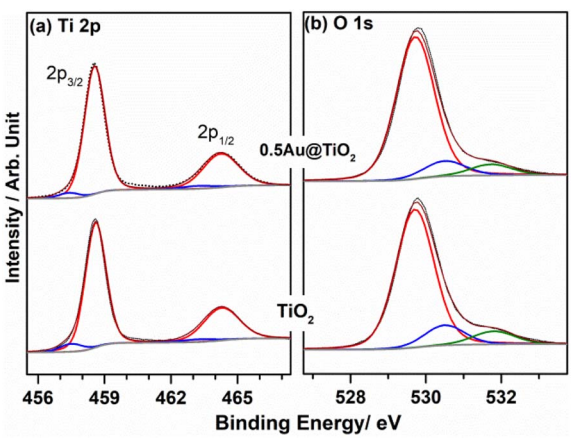


Fig. 6 (a) Ti 2p, and (b) O 1s core level spectra of TiO_2 P25 and 0.5Au@TiO_2. Ti^{3+} and Ti^{4+} are given in blue and red traces, respectively. Red, blue, and green traces in O 1s corresponds to TiO_2 lattice oxygen, O-associated with Ti^{3+} and OH group, respectively.

Open Access Article. Published on 17 February 2023. Downloaded on 5/3/2023 8:01:09 AM.
This article is licensed under a Creative Commons Attribution-NonCommercial 3.0 Unported Licence.

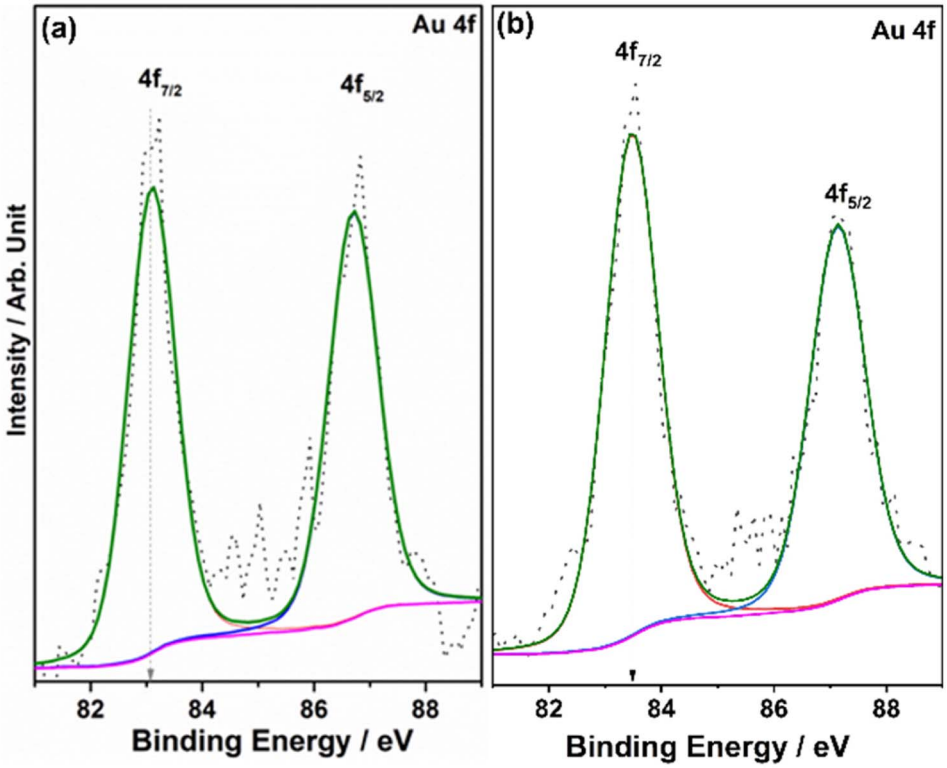


Fig. 7 XPS spectra for Au 4f core levels for (a) 0.5Au@TiO_2 and (b) 1Au@TiO_2. Compared to the standard metallic gold $4f_{7/2}$ feature at 84.0 eV, the appearance of the same at 83.1 and 83.4 eV for 0.5Au@TiO_2 and 1Au@TiO_2, respectively, underscores the difference in electronic integration between Au and TiO_2, and the extent of the anionic character of gold.

Mechanism

The integration of the plasmonic metal with semiconductors can lead to efficient photocatalytic activity. Based on the experimental data obtained from various studies and discussed in the earlier sections for Au@TiO_2, a possible reaction mechanism is proposed in Fig. 8. TiO_2 exhibits a bandgap of 3.2 eV, which absorb only 4–5% of the UV light present in the solar spectrum, the electron and hole separation is, indeed, one of the main issues for the low efficiency of photocatalytic activity with virgin TiO_2. Small and highly-dispersed gold cluster integration enhanced its light absorption capacity to the visible region, amplifying its electron–hole generation *via* the LSPR

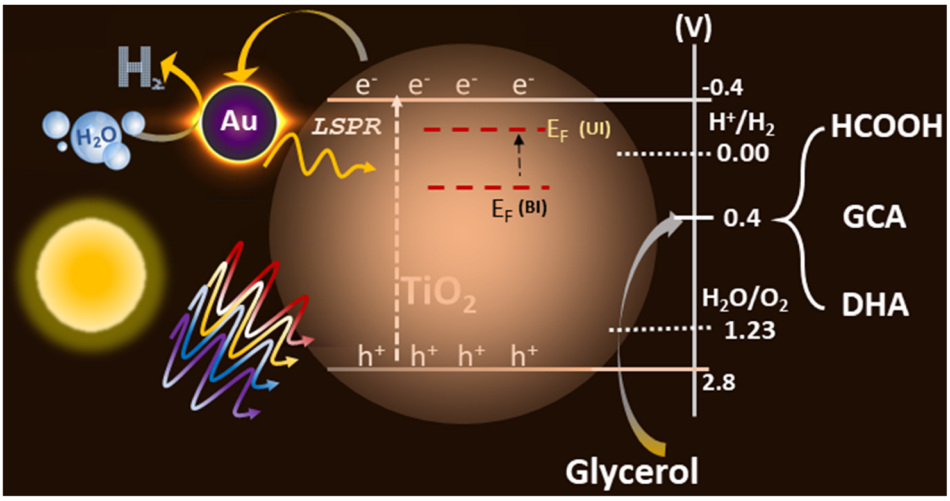


Fig. 8 Possible mechanism for plasmon-induced Au@TiO_2 toward photocatalytic hydrogen generation and glycerol oxidation towards the value-added products. E_F levels shown are indicative and not to the scale; however, an upward shift under illumination occurs due to electron storage in gold clusters. Abbreviations: E_F(UI) Fermi level under illumination, E_F(BI) Fermi level before illumination or fresh catalyst, GCA (glycolaldehyde), DHA (dihydroxyacetone).

© 2023 The Author(s). Published by the Royal Society of Chemistry

Open Access Article. Published on 17 February 2023. Downloaded on 5/3/2023 8:01:09 AM.
This article is licensed under a Creative Commons Attribution-NonCommercial 3.0 Unported Licence.

effect of gold particles, which is evident from the UV-Vis spectra. Also, the electronically integrated anionic Au-clusters with TiO_2 suggest a negative shift of the Fermi level of the composite, which is more facile for charge separation and enhances hydrogen generation 20 times, compared to that in virgin TiO_2.[57,58]

Photocatalysis involves both photophysical and photochemical processes. It is well-known that the time scale of photophysical ($\leq$ ns) and photochemical ($\geq$ μs) processes are very different and it is necessary to address this issue.[6] By selectively storing electrons in gold, utilization of holes, which are also known as the minority charge carriers, for oxidation increases to a large extent. Basically, the charge separation enhances both the reduction and oxidation aspects of the photocatalysis and hence an overall increase in the activity is observed. Further, the integration of Au helps in the photophysical process *via* the LSPR effect and as an electron sink for efficient charge separation, this leads to an enhanced redox process and underscores the dual functional character of the gold clusters with light absorption as well as catalysis. XPS results show that gold is present as anionic gold, which also proves the electron transfer is occurring from TiO_2 to gold, where water reduction is taking place. However, the oxidation process occurs *via* holes present in the valence band of TiO_2, from glycerol to VAPs (Fig. S7†). Glycerol and glucose require low oxidation potential (0.4 V *vs.* RHE with Pt/C and 0.4 *vs.* RHE with Au, respectively) than water,[59,60] while VB of TiO_2 is around 2.7 V with high oxidation potential. The potential required for both reduction and oxidation is met with the above arrangement, which helps in the large utilization of holes, resulting in low charge recombination and high photocatalytic activity. The large dispersion of atom-like gold clusters observed in STEM results (Fig. 5) supports the effective charge carrier separation as well as its utilization. Further, by depositing gold at the oxygen vacancy sites, not only electronic integration was achieved, but charge recombination was also minimized. These factors increased the charge utilization and improved the redox activity towards H_2 and VAP formation. A significantly high formic acid formation underscores the high potential associated with holes and helps achieve C–C cleavage of glycerol components. This particular aspect should be utilized to tackle other biomass components too.

Conclusions

We synthesized xAu@TiO_2 ($x = 0.1$, 0.5, and 1 wt%) composites *via* facile photo-deposition, with small Au clusters uniformly deposited and electronically integrated on TiO_2. 0.5Au@TiO_2 exhibits maximum hydrogen yield in direct sunlight with glycerol as a sacrificial agent compared to other biomass components. This study focused on two aspects; (1) novel integration of gold with TiO_2 and its large distribution due to small clusters, which increases the effective charge transfer between semiconductor to metal and reduces the electron–hole recombination. (2) Glycerol is not only a promising sacrificial reagent but could be oxidized to value-added products under aerobic conditions. This aspect helps in the utilization of photogenerated electrons and holes to hydrogen and value-added products of glycerol, respectively. Glucose and cellulose were also shown to exhibit hydrogen generation activity, and it is suggested to explore them more with different catalyst systems to find a potential solution for hydrogen and value-added products. We believe the low activity with glucose/cellulose, compared to glycerol, is due to the consumption of charge carriers in breaking C–C bonds in the initial hours. Hence, prolonging the reaction for a longer time in sunlight is expected to produce VAPs and more hydrogen. Alternately, 1.5 and 2 sun conditions could be employed to perform the glycerol and glucose oxidation reactions, which is expected to increase the temperature further, in addition to light power. More work in this direction is likely to improve the activity in the desired direction of the biomass components to VAPS and hydrogen.

The preparation method can be utilized to prepare different noble metal integrated TiO_2 composites, a combination of SPR active metal and another transition metal in the form of alloy or bimetal co-catalysts is likely to provide more options for tuning the redox potential and hence the possibility of selectively producing one value-added product at a time and hence product separation step could be avoided. A combination of such co-catalysts with different semiconductors could also be evaluated for partial oxidation of biomass components by photocatalysis.[61] With an ideal catalyst, one may be able to achieve maximum C–C cleavage towards making 100% of C1-oxygenates, such as formic acid and formaldehyde. For maximum light absorption, thin-film and powder form with proper dispersion have the potential for large-scale application.[6,47,62] Recent work by Domen *et al.* on a 100 m^2 photocatalyst panel for water splitting in sunlight indicates the possibility to circulate a thin layer of suspension over large area devices for the maximum absorption of sunlight to maximize the reactivity.[63] Less expensive system should be more practical and sustainable for large-scale synthesis, but earlier literature reports did not address the identification and quantification of the oxidized VAPs produced during hydrogen evolution. In fact, we suggest the practitioners of photocatalysis move from employing a mere sacrificial agent to generating VAPs, as this makes an attractive proposition.

It has been 50 years since the announcement of the first proof of concept of water splitting by Fujishima and Honda;[5] however, photocatalytic hydrogen evolution research and technology is still at the infantry level. We believe that a small step suggested in the present manuscript could significantly impact these strategies and can potentially make the photocatalytic hydrogen evolution and glycerol oxidation process by photocatalysis attractive.

Conflicts of interest

There are no conflicts or competing interests to declare.

Acknowledgements

HB and NBM thank UGC, New Delhi for research fellowships; IC and KNS thank INSPIRE and Maharashtra state government for

Open Access Article. Published on 17 February 2023. Downloaded on 5/3/2023 8:01:09 AM. This article is licensed under a Creative Commons Attribution-NonCommercial 3.0 Unported Licence.

research fellowships, respectively. We acknowledge the financial support from CSIR, New Delhi, through the HCP-44 project.

References

1 J. Gong, C. Li and M. R. Wasielewski, *Chem. Soc. Rev.*, 2019, **48**, 1862–1864.
2 S. Rajaambal, K. Sivaranjani and C. S. Gopinath, *J. Chem. Sci.*, 2015, **127**, 33–47.
3 M. R. Shaner, H. A. Atwater, N. S. Lewis and E. W. McFarland, *Energy Environ. Sci.*, 2016, **9**, 2354–2371.
4 M. G. Walter, E. L. Warren, J. R. McKone, S. W. Boettcher, Q. Mi, E. A. Santori and N. S. Lewis, *Chem. Rev.*, 2010, **110**, 6446–6473.
5 A. Fujishima and K. Honda, *Nature*, 1972, **238**, 37–38.
6 (*a*) C. S. Gopinath and N. Nalajala, *J. Mater. Chem. A*, 2021, **9**, 1353–1371; (*b*) S. Rajaambal, K. Sivaranjani and C. S. Gopinath, *Dalton Trans.*, 2014, **43**, 12546–12554.
7 K. K. Patra, P. A. Bharad, V. Jain and C. S. Gopinath, *J. Mater. Chem. A*, 2019, **7**, 3179–3189.
8 N. Fajrina and M. Tahir, *Int. J. Hydrogen Energy*, 2019, **44**, 540–577.
9 M. R. Karimi Estahbanati, M. Feilizadeh, F. Attar and M. C. Iliuta, *React. Chem. Eng.*, 2021, **6**, 197–219.
10 D. Lv, Y. Lei, D. Zhang, X. Song, Y.-W. Li, J. W. H. Niemantsverdriet, W. Hao, Y. Deng and R. Su, *J. Phys. Chem. C*, 2020, **124**, 20320–20327.
11 R. Deas, S. Pearce, K. Goss, Q. Wang, W.-T. Chen and G. I. N. Waterhouse, *Appl. Catal., A*, 2020, **602**, 117706.
12 G. Dodekatos and H. Tüysüz, *Catal. Sci. Technol.*, 2016, **6**, 7307–7315.
13 H. Sakurai, M. Kiuchi, C. Heck and T. Jin, *Chem. Commun.*, 2016, **52**, 13612–13615.
14 G. Dodekatos, S. Schünemann and H. Tüysüz, *ACS Catal.*, 2018, **8**, 6301–6333.
15 B.-H. Wu, W.-T. Liu, T.-Y. Chen, T.-P. Perng, J.-H. Huang and L.-J. Chen, *Nano Energy*, 2016, **27**, 412–419.
16 A. A. Melvin, K. Illath, T. Das, T. Raja, S. Bhattacharyya and C. S. Gopinath, *Nanoscale*, 2015, **7**, 13477–13488.
17 (*a*) P. Devaraji and C. S. Gopinath, *Int. J. Hydrogen Energy*, 2018, **43**, 601–613; (*b*) P. Devaraji, N. K. Sathu and C. S. Gopinath, *ACS Catal.*, 2014, **4**, 2844–2853.
18 (*a*) K. K. Patra and C. S. Gopinath, *J. Phys. Chem. C*, 2018, **122**, 1206–1214; (*b*) K. K. Patra, B. Bhuskute and C. S. Gopinath, *Sci. Rep.*, 2017, **7**, 6515; (*c*) K. K. Patra and C. S. Gopinath, *ChemCatChem*, 2016, **8**, 3294–3301.
19 F. J. Méndez, A. González-Millán and J. A. García-Macedo, *Int. J. Hydrogen Energy*, 2019, **44**, 14945–14954.
20 X. Shi, Z. Lou, P. Zhang, M. Fujitsuka and T. Majima, *ACS Appl. Mater. Interfaces*, 2016, **8**, 31738–31745.
21 R. Fiorenza, M. Bellardita, L. D'Urso, G. Compagnini, L. Palmisano and S. Scirè, *Catalysts*, 2016, **6**, 121.
22 (*a*) J. B. Priebe, J. Radnik, A. J. J. Lennox, M.-M. Pohl, M. Karnahl, D. Hollmann, K. Grabow, U. Bentrup, H. Junge, M. Beller and A. Brückner, *ACS Catal.*, 2015, **5**, 2137–2148; (*b*) P. A. Bharad, K. Sivaranjani and C. S. Gopinath, *Nanoscale*, 2015, **7**, 11206–11215.
23 H. Bajpai, K. K. Patra, R. Ranjan, N. Nalajala, K. P. Reddy and C. S. Gopinath, *ACS Appl. Mater. Interfaces*, 2020, **12**, 30420–30430.
24 A. Villa, G. M. Veith and L. Prati, *Angew. Chem., Int. Ed.*, 2010, **49**, 4499–4502.
25 A. V. Puga, A. Forneli, H. García and A. Corma, *Adv. Funct. Mater.*, 2014, **24**, 241–248.
26 (*a*) E. Taboada, I. Angurell and J. Llorca, *J. Photochem. Photobiol., A*, 2014, **281**, 35–39; (*b*) N. K. Sathu, P. Devaraji and C. S. Gopinath, *J. Nanosci. Nanotechnol.*, 2016, **16**, 9203–9208.
27 B. Zhou, J. Song, Z. Zhang, Z. Jiang, P. Zhang and B. Han, *Green Chem.*, 2017, **19**, 1075–1081.
28 X. Zhang, L. Luo, R. Yun, M. Pu, B. Zhang and X. Xiang, *ACS Sustainable Chem. Eng.*, 2019, **7**, 13856–13864.
29 C. Wang, X. Cai, Y. Chen, Z. Cheng, X. Luo, S. Mo, L. Jia, R. Shu, P. Lin, Z. Yang, S. Sun, E. Pu and Y. Shen, *Int. J. Hydrogen Energy*, 2017, **42**, 17063–17074.
30 T. N. Q. Trang, L. T. N. Tu, T. V. Man, M. Mathesh, N. D. Nam and V. T. H. Thu, *Composites, Part B*, 2019, **174**, 106969.
31 T. Montini, V. Gombac, L. Sordelli, J. J. Delgado, X. Chen, G. Adami and P. Fornasiero, *ChemCatChem*, 2011, **3**, 574–577.
32 Y. Yang, F. Li, J. Chen, J. Fan and Q. Xiang, *ChemSusChem*, 2020, **13**, 1979–1985.
33 L. S. Al-Mazroai, M. Bowker, P. Davies, A. Dickinson, J. Greaves, D. James and L. Millard, *Catal. Today*, 2007, **122**, 46–50.
34 N. Strataki, V. Bekiari, D. I. Kondarides and P. Lianos, *Appl. Catal., B*, 2007, **77**, 184–189.
35 Y. Li, G. Lu and S. Li, *Appl. Catal., A*, 2001, **214**, 179–185.
36 H. Hu, D. Qian, P. Lin, Z. Ding and C. Cui, *Int. J. Hydrogen Energy*, 2020, **45**, 629–639.
37 A. G. Dosado, W.-T. Chen, A. Chan, D. Sun-Waterhouse and G. I. N. Waterhouse, *J. Catal.*, 2015, **330**, 238–254.
38 W.-T. Chen, A. Chan, D. Sun-Waterhouse, J. Llorca, H. Idriss and G. I. N. Waterhouse, *J. Catal.*, 2018, **367**, 27–42.
39 P. Jiménez-Calvo, V. Caps, M. N. Ghazzal, C. Colbeau-Justin and V. Keller, *Nano Energy*, 2020, **75**, 104888.
40 S. A. Balsamo, S. Sciré, M. Condorelli and R. Fiorenza, *J. Interdiscip. Multidiscip. Res.*, 2022, **5**, 92–104.
41 A. K. R. Police, S. V. P. Vattikuti, K. K. Mandari, M. Chennaiahgari, P. S. M. Venkata, D. K. Valluri and C. Byon, *Ceram. Int.*, 2018, **44**, 11783–11791.
42 M. O. Segovia-Guzmán, M. Román-Aguirre, J. Y. Verde-Gomez, V. H. Collins-Martínez, G. Zaragoza-Galán and V. H. Ramos-Sánchez, *Catal. Today*, 2020, **349**, 88–97.
43 I. Majeed, M. A. Nadeem, A. Badshah, F. K. Kanodarwala, H. Ali, M. A. Khan, J. A. Stride and M. A. Nadeem, *Catal. Sci. Technol.*, 2017, **7**, 677–686.
44 M. Jung, J. N. Hart, D. Boensch, J. Scott, Y. H. Ng and R. Amal, *Appl. Catal., A*, 2016, **518**, 221–230.
45 M. Imizcoz and A. V. Puga, *Catal. Sci. Technol.*, 2019, **9**, 1098–1102.
46 M. R. Karimi Estahbanati, N. Mahinpey, M. Feilizadeh, F. Attar and M. C. Iliuta, *Int. J. Hydrogen Energy*, 2019, **44**, 32030–32041.

 © 2023 The Author(s). Published by the Royal Society of Chemistry

Open Access Article. Published on 17 February 2023. Downloaded on 5/3/2023 8:01:09 AM.
This article is licensed under a Creative Commons Attribution-NonCommercial 3.0 Unported Licence.

47 N. Nalajala, K. K. Patra, P. A. Bharad and C. S. Gopinath, *RSC Adv.*, 2019, **9**, 6094–6100.
48 B. Tudu, N. Nalajala, K. P. Reddy, P. Saikia and C. S. Gopinath, *ACS Sustainable Chem. Eng.*, 2021, **9**, 13915–13925.
49 B. Tudu, N. Nalajala, P. Saikia and C. S. Gopinath, *Sol. RRL*, 2020, **4**, 1900557.
50 B. Tudu, N. Nalajala, K. P. Reddy, P. Saikia and C. S. Gopinath, *ACS Appl. Mater. Interfaces*, 2019, **11**, 32869–32878.
51 H. Kasap, D. S. Achilleos, A. Huang and E. Reisner, *J. Am. Chem. Soc.*, 2018, **140**, 11604–11607.
52 D. W. Wakerley, M. F. Kuehnel, K. L. Orchard, K. H. Ly, T. E. Rosser and E. Reisner, *Nat. Energy*, 2017, **2**, 17021.
53 H. Wu, W. Jiang, L. Shi, R. Li, L. Huang and C. Li, *iScience*, 2022, **25**, 103572.
54 K. Sivaranjani and C. S. Gopinath, *J. Mater. Chem.*, 2011, **21**, 2639–2647.
55 K. Roy, C. P. Vinod and C. S. Gopinath, *J. Phys. Chem. C*, 2013, **117**, 4717–4726.
56 A. A. Melvin, P. A. Bharad, K. Illath, M. P. Lawrence and C. S. Gopinath, *ChemistrySelect*, 2016, **1**, 917–923.
57 L. Cheng, D. Zhang, Y. Liao, F. Li, H. Zhang and Q. Xiang, *J. Colloid Interface Sci.*, 2019, **555**, 94–103.
58 V. Subramanian, E. E. Wolf and P. V. Kamat, *J. Am. Chem. Soc.*, 2004, **126**, 4943–4950.
59 M. Simões, S. Baranton and C. Coutanceau, *Appl. Catal., B*, 2010, **93**, 354–362.
60 N. Schloegel, G. K. H. Wiberg and M. Arenz, *Electrochim. Acta*, 2022, **410**, 140023.
61 J. Ran, J. Zhang, J. Yu, M. Jaroniec and S. Z. Qiao, *Chem. Soc. Rev.*, 2014, **43**, 7787–7812.
62 N. Nalajala, K. N. Salgaonkar, I. Chauhan, S. P. Mekala and C. S. Gopinath, *ACS Appl. Energy Mater.*, 2021, **4**, 13347–13360.
63 H. Nishiyama, T. Yamada, M. Nakabayashi, Y. Maehara, M. Yamaguchi, Y. Kuromiya, Y. Nagatsuma, H. Tokudome, S. Akiyama, T. Watanabe, R. Narushima, S. Okunaka, N. Shibata, T. Takata, T. Hisatomi and K. Domen, *Nature*, 2021, **598**, 304–307.

© 2023 The Author(s). Published by the Royal Society of Chemistry

ACS APPLIED MATERIALS & INTERFACES

www.acsami.org

Research Article

Can Half-a-Monolayer of Pt Simulate Activity Like That of Bulk Pt? Solar Hydrogen Activity Demonstration with Quasi-artificial Leaf Device

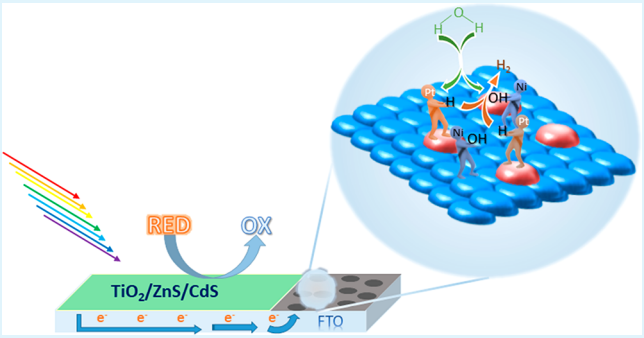
Himanshu Bajpai, Kshirodra Kumar Patra, Ravi Ranjan, Naresh Nalajala, Kasala Prabhakar Reddy, and Chinnakonda S. Gopinath*

Cite This: *ACS Appl. Mater. Interfaces* 2020, 12, 30420−30430

Read Online

ACCESS | Metrics & More | Article Recommendations | Supporting Information

ABSTRACT: Pt is the best cocatalyst for hydrogen production. It is also well-known that the surface atomic layer is critical for catalysis. To minimize the Pt content as cocatalyst, herein we report on half-a-monolayer of Pt ($0.5\theta_{Pt}$) decorated on earth-abundant Ni−Cu cocatalyst, which is integrated with a quasi-artificial leaf (QuAL) device (TiO_2/ZnS/CdS) and demonstrated for efficient solar hydrogen production. For the QuAL, TiO_2 is sensitized with ZnS and CdS quantum dots by the SILAR method. The $0.5\theta_{Pt}$-decorated Ni−Cu shows an onset potential of 0.05 V vs reversible hydrogen electrode for the hydrogen evolution reaction, which is almost similar to that of commercial Pt/C. Photoactivity of the present QuAL device with either bulk Pt or $0.5\theta_{Pt}$-coated Ni−Cu cocatalyst is, surprisingly, equal. Our findings underscore that a fraction of a monolayer of Pt can enhance the activity of the cocatalyst, and it is worth exploring further for the high activity associated with atomic Pt and other noble metals.



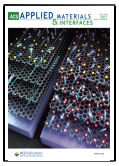
KEYWORDS: *Platinum, solar hydrogen, artificial leaf, photocatalysis, nickel−copper*

INTRODUCTION

Global energy demand is increasing rapidly, and a huge amount of energy comes from limited nonrenewable fossil fuels at present. With the consumption of more carbon-based fuels, we are also changing the equilibrium of our environment due to the daily addition of CO_2 and other greenhouse gases.[1] To fullfil the world's energy demands while decreasing the carbon footprint, solar energy is one of the best possible alternatives to fossil fuels. Nonetheless, the conversion of solar energy into chemical energy is challenging, and much more concerted research is required in this area.[2−5]

The conversion of solar energy into chemical energy is one of the keys to a sustainable energy future. It is well-known that hydrogen from water splitting is a clean fuel source compared to carbon-based fuel.[6] However, it is impossible that any single photocatalyst material (such as TiO_2, CdS) can help to achieve solar water splitting.[7,8] Conversely, a combination of more than one semiconductor with appropriate bandgaps and band edges and their integration into a photoanode device for photocatalytic solar water splitting is a promising strategy.[9−11] A photocatalyst device should fulfill the following requirements: (i) the photoanode device should absorb light from UV, visible, and possibly near IR (NIR) ranges (that are available in sunlight) to generate the maximum number of electron−hole pairs; (ii) efficient separation of electron and hole, and diffusion of them toward the redox sites; (iii) effective utilization of electron and hole for reduction and oxidation, respectively, of water at relevant cocatalyst sites.[12−16] It is desirable to employ quantum dots (QDs), especially of surface plasmon material, to increase the light absorption.[17] High-quality heterojunction between quantum dots and semiconductor can separate the electron and hole efficiently and minimize recombination.[18] Utilization of charge carriers can be fulfilled by cocatalysts, which will work as an active site for hydrogen and oxygen evolution.[19,20] While hydrogen evolution is a two-electron process, its counterpart, oxygen evolution, is a four-electron process; the latter part is the rate-determining step due to sluggish kinetics and lowers the overall rate of the reaction. However, by using holes for the oxidation of a sacrificial reagent, H_2 evolution can be made kinetically fast.[18]

Received: April 22, 2020
Accepted: June 12, 2020
Published: June 12, 2020



Downloaded via NATL CHEMICAL LABORATORY on May 3, 2023 at 07:00:12 (UTC).
See https://pubs.acs.org/sharingguidelines for options on how to legitimately share published articles.

© 2020 American Chemical Society

https://dx.doi.org/10.1021/acsami.0c07431
ACS Appl. Mater. Interfaces 2020, 12, 30420−30430

Nature does the water splitting in photosynthesis in a very efficient way with limited light absorption. The porous network of the chloroplast in the leaf absorbs the light, and the water molecules are oxidized and reduced in photosystems II and I, respectively. While oxygen escapes into the atmosphere, hydrogen is stored in NADPH. Many efforts have been carried out to mimic natural leaf functions. Herein the porous network of TiO_2 is sensitized by ZnS and CdS quantum dots. Light absorption by different components leads to charge carrier generation, and their utilization occurs to reduce water to produce H_2 and oxidize the sacrificial reagent; this is why it is termed as quasi-artificial leaf (QuAL).[9] To utilize the electron at the active site for hydrogen evolution, Pt is by far the best cocatalyst; but for large scale production, we need to find an alternative to Pt, due to its high cost and low abundance. For a less expensive substitute for Pt, many studies have been made with earth-abundant metal catalysts; however, in terms of activity and stability, they are significantly inferior to Pt. In the present study, we explored the possibility of simulating the activity of bulk Pt with just half-a-monoloayer of Pt ($0.5\theta_{Pt}$) integrated on another earth-abundant cocatalyst and demonstrating the same through the QuAL device.

QDs are promising materials, and due to their morphology, size, and cross-section, the optical properties are also proven to be different from their bulk counterparts and favorable for light harvesting.[14,17,21,22] By sensitizing such QDs with porous TiO_2, light absorption can be increased; heterojunction between QD and TiO_2 significantly increases the charge separation and diffusion. TiO_2 also absorbs 4−5% of UV light available from sunlight.[23,24] In view of the above facts, we prepared a QD-sensitized photoanode (TiO_2/ZnS/CdS) by successive ionic layer adsorption and reaction (SILAR).[25] We used an additional ZnS layer as a passivation layer after the CdS deposition. Several control photoanodes were also made to clarify the mechanism of the photoanode function. Our best photoanode (TiO_2/ZnS/CdS) shows hydrogen generation activity of 4 mL/h from a 1 cm^2 size device.

The $0.5\theta_{Pt}$ corresponding to about 10^{14} atoms/cm^2 is integrated with reasonably active, economically viable, and earth-abundant Ni−Cu bimetal cocatalyst, which has the potential to work as a better cocatalyst for large scale solar hydrogen production.[26−28] Hydrogen evolution takes place on the surface of the cocatalyst; hence, by limiting the platinum on the surface, we could achieve the activity like that of platinum.[29] Here we report on QuAL of TiO_2/ZnS/CdS as a photoanode and platinum half-monolayer-integrated NiCu alloy nanoparticle for photocatalytic hydrogen production.

EXPERIMENTAL METHODS

Ni−Cu Alloy Nanoparticles. NiCu alloy was prepared by following the procedure reported by Patra et al.[27] A 25 mL amount of oleylamine was taken in a 100 mL three-neck RBF (round-bottom flask) and kept at 120 °C for 10 min to remove any water from the oleylamine. Then $Ni(NO_3)_2{\cdot}6H_2O$ and $Cu(CH_3COO)_2$ were added in a 5:2.5 molar ratio. The temperature was increased to 220 °C, and the reaction mixture was kept under the above conditions for 1 h under stirring to form nanoparticles. After this, the reaction mixture was allowed to cool to room temperature (RT). $Ni_5Cu_{2.5}$ (NiCu) alloy nanoparticles were washed repeatedly and finally centrifuged with ethanol to remove the catalyst. A more detailed procedure is available in ref 27.

Half-Monolayer Pt-Integrated Ni−Cu ($0.5\theta_{Pt}$-NC) Bimetallic Nanoparticles. Synthesis of $0.5\theta_{Pt}$-NC was carried out in two stages, and they are described in the following. NiCu alloy nanoparticles were dispersed in 30 mL of ethanol in a RBF, and $NaBH_4$ was added in a 1:4 (NiCu:$NaBH_4$) weight ratio and stirred for 30 min; the solution was further sonicated for 30 min followed by refluxing at 80 °C for 1 h. Then it was cooled to RT, washed, and centrifuged with ethanol. This is referred to as NiCu@H^-, as the NiCu alloy surface is fully covered with hydride ions.

To prepare half-monolayer (0.5θ) Pt-covered on NiCu alloy nanoparticles, NiCu@H^- was dispersed in 30 mL of ethanol in RBF and then K_2PtCl_4 was added in a 8:1 (NiCu@H^-:Pt) weight ratio. It was sonicated for 30 min and then refluxed at 74 °C for 12 h. After cooling to room temperature, it was washed and centrifuged with ethanol. It is referred to as $0.5\theta_{Pt}$-NC. The main idea behind this procedure is to populate the NiCu alloy surface with hydride ions in the first step and then treat the same with Pt^{2+} ions. Two hydride ions are required to reduce one Pt^{2+} ion, and a perfect reduction is expected to provide a 0.5 ML Pt-covered NiCu alloy surface. As hydride ions are available only on the surface, no bulk reduction of platinum is possible with this current procedure. Pt is expected to be present in the atomic state. Despite our best efforts, we are unable to observe atomic Pt on single particles of $0.5\theta_{Pt}$-NC by structural/microscopy methods such as XRD or HRTEM. However, TEM-EDS (TEM-energy dispersive X-ray spectroscopy) measurements made on clusters were helpful to observe the elemental mapping, including Pt, and its content. Electrochemical measurements also fully support the presence of atomic Pt.

Fabrication of the Photochemical Device. The QD-sensitized QuAL device was prepared by the doctor blade method followed by the SILAR method, which were reported by Trevisan et al.[9] and Patra et al.[25,27] Briefly, FTO (fluorine-doped tin oxide) was cleaned and washed with soap solution, deionized water, and ethanol, in the above sequential order. After $TiCl_3$ treatment (to increase the adhesion and homogeneity of the TiO_2 film on FTO), P25-TiO_2 paste was applied on a 1 × 1 cm^2 area of cleaned FTO by the doctor blade method followed by calcination at 450 °C for 30 min. CdS and ZnS QDs were assembled in the pores of the titania film by the SILAR method described below: The precoated TiO_2 film on FTO was immersed (a) in an aqueous solution of 0.1 M $Zn(CH_3COO)_2$ for 1 min, (b) washed with deionized (DI) water, followed by (c) immersion in a 0.1 M solution (1:1 water: methanol) of Na_2S for 1 min, and (d) finally washed with DI water. This is for one full SILAR cycle of assembly of ZnS QDs in the titania pores. Intermediate washing with DI water removes any ions that are not chemisorbed or bonded to the surface, and hence one full SILAR cycle leads to the maximum of a monolayer of a chalcogenide. In a similar process five CdS SILAR cycles were carried out with an aqueous solution of $Cd(NO_3)_2$ and Na_2S sequentially. Finally, two SILAR cycles of ZnS coating were carried out to make a TiO_2/ZnS/CdS photoanode with top ZnS layers as passivating layers. For the solar to hydrogen measurement, the cocatalyst was drop-casted alongside the photoanode on FTO.

Catalyst materials and devices made were thoroughly characterized by various analytical methods. Diffuse reflectance UV−vis measurement was carried with a Shimadzu spectrophotometer (model-UV2550) using spectral grade $BaSO_4$ as a reference material. Photoelectrochemical and electrochemical measurements were carried out using a Gamry potentiostat (model 3000) in a three-electrode system with Ag/AgCl as the reference electrode and Pt foil as counter electrode under one sun conditions (Newport Instruments 300 W xenon arc lamp fitted with an AM 1.5 filter). Powder X-ray diffraction (XRD) data were collected with a Pan Analytic X'pert pro dual goniometer diffractometer using Cu−Kα (1.5418 Å) radiation with a Ni filter. Field emission scanning electron microscopy (FESEM) and energy dispersive X-ray spectroscopy (EDX) were performed on an FESEM system (FEI NOVA NANOSEM 450) equipped with EDX. HRTEM and EDS analysis of the materials was conducted on a JEOL JEM F-200 HRTEM operating at 200 kV. Raman spectra were recorded with a Horiba JY LabRAM HR 800 Raman spectrometer with a 633 nm excitation source. X-ray photoelectron spectroscopy (XPS) analysis was carried out with a Thermo Fisher Scientific Instruments, equipped with Al K_α (monochromatic) X-ray radiation source and operated at 6 mA beam current and 12 kV.

https://dx.doi.org/10.1021/acsami.0c07431
ACS Appl. Mater. Interfaces 2020, 12, 30420−30430

Solar Hydrogen Production Measurement. Hydrogen production was measured at zero potential in the wireless configuration using one sun conditions. For hydrogen production measurements, 30 mL of 0.25 M Na_2S and 0.35 M Na_2SO_3 as a sacrificial hole scavenger in a three-neck quartz RBF was taken and purged with N_2 for 10 min, and then the photoelectrode was immersed into the solution and irradiated with light (100 mW cm^{-2} with a 450 W Newport solar simulator with an AM1.5 filter). Hydrogen was the only product in the gas phase, and it was confirmed by using GC (gas chromatography, Agilent 7890A) measurements. For hydrogen quantification, the inverted buret method[25] was employed; one of the RBF necks was connected to an inverted burette, and the volume of displaced liquid due to H_2 collection was noted periodically.

RESULTS AND DISCUSSION

UV−Visible Absorption Spectroscopy. For any visible-light-driven photocatalyst material to be successful, it should show good absorption of light in a wide range of UV−visible regions. Indeed this is the first critical requirement for a material to be considered for evaluation. Optical properties of TiO_2, TiO_2/CdS, and TiO_2/ZnS/CdS were evaluated by UV−visible spectroscopy, and the optical band gap was calculated by TAUC plot which is shown in Figure 1, parts a and b, respectively. The

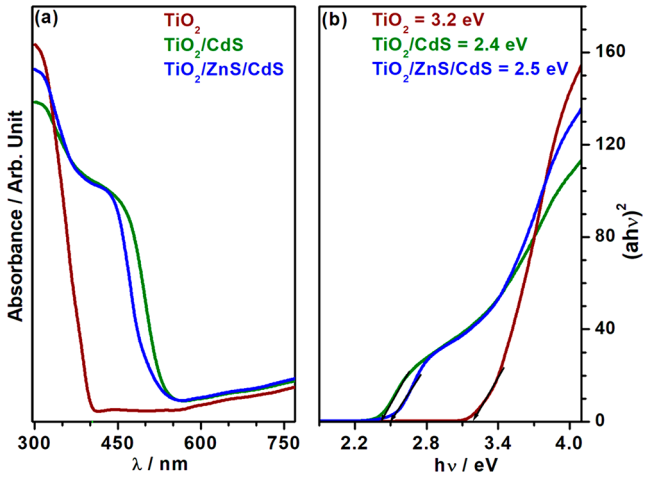


Figure 1. (a) UV−visible absorption spectra of TiO_2, TiO_2/CdS, TiO_2/ZnS/CdS; the latter two photoanodes are deposited with two ZnS protective layers. (b) Tauc plot of TiO_2, TiO_2/CdS, and TiO_2/ZnS/CdS for their respective band gap indicated by arrows.

pristine TiO_2 film shows an absorption onset at 385 nm, which corresponds to a bandgap of 3.2 eV. Upon sensitizing titania with CdS quantum dots, a strong redshift is observed without a break in absorption and exhibits an absorption up to about 510 nm with an optical band gap of 2.4 eV (Figure 1a). It is to be noted that the SILAR method allows the in situ assembly of CdS QDs into the mesopores of titania,[25] through the diffusion of Cd^{2+} and S^{2-} ions. This is the specialty of the SILAR method which provides a route for in situ assembly of QDs, which no other method offers. QD formation in the pores ensures the heterostructure formation and hence electronic integration between titania and CdS. When the ZnS seed layer was introduced before CdS integration with titania, a small but finite blue-shift was observed, and the optical band gap also increased to 2.5 eV (Figure 1b). In fact this observation is in contrast to that of a red shift observed by Lee et al.[30] Nonetheless, high current density and solar cell efficiency observed by Lee et al.[30] and more hydrogen generation observed in the present work with seed ZnS layers are in agreement with each other. Similar to our earlier work on the TiO_2/CdS/PbS system,[25] high absorption of light in the present system (Figure 1) is expected to lead to 20% IPCE up to 520 nm. It is to be underscored that ZnS and CdS possesses Wurtzite crystal structure with a hexagonal crystal system. A solid solution is highly possible between CdS and ZnS; according to Vegard's law, the bandgap of such a solid solution is expected to vary between them (CdS (2.4 eV) to ZnS (3.6 eV)), depending on the composition;[31−33] however, due to the limited amount of ZnS, a marginal, but definite, blue shift of 0.1 eV was observed in the present photoanode.

Photocatalytic Hydrogen Production. Solar to hydrogen production was measured under one sun conditions. Hydrogen evolution was evaluated in a systematic way, using TiO_2, TiO_2/CdS, and TiO_2/ZnS/CdS with a different cocatalyst (Pt, NiCu alloy, and 0.5θ_{Pt}-NC). The final layer of ZnS is the protective layer, which is also transparent to sunlight and prevents corrosion; however, it will not be mentioned hereafter, as it is part of all QuAL devices.[9] A photoanode with 1 × 1 cm^2 area was used for all measurements. TiO_2-only coated photoelectrode did not show any measurable hydrogen evolution with any of the cocatalysts. Expectedly, TiO_2 absorbs only UV light, which is only 4% of the whole solar spectrum; further charge carrier recombination is high, and hence no hydrogen generation was observed with pure titania. Solar to hydrogen conversion was carried out with TiO_2/ZnS/CdS and Ti_2O/CdS photoanodes using Pt, NiCu alloy, and 0.5θ_{Pt}-NC as cocatalysts, and the results are shown in Figure 2. Hydrogen generation as a function

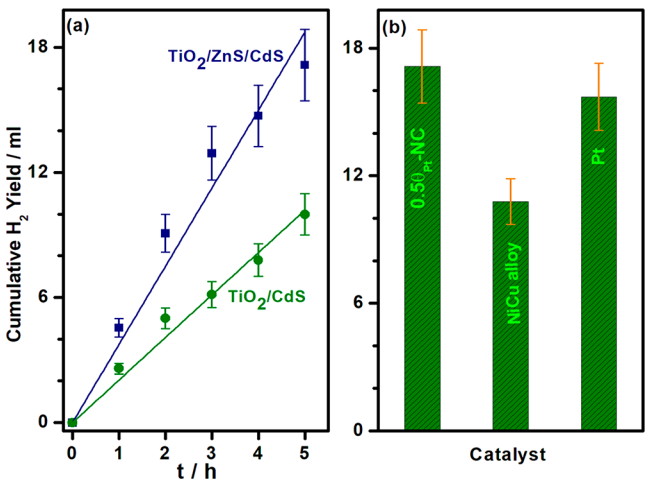


Figure 2. (a) Photocatalytic hydrogen production from TiO_2/ZnS/CdS and TiO_2/CdS photoanodes with 0.5θ_{Pt}-NC as a cocatalyst. (b) Photocatalytic hydrogen production from TiO_2/ZnS/CdS with 0.5θ_{Pt}-NC, NiCu alloy, or Pt as a cocatalyst for 5 h under one sun conditions.

of irradiation time is shown in Figure 2a for TiO_2/ZnS/CdS and Ti_2O/CdS photoanodes measured with 0.5θ_{Pt}-NC as a cocatalyst. Hydrogen production was observed to be 4−4.5 and 2.2−2.5 mL/h with TiO_2/ZnS/CdS and TiO_2/CdS photoanodes, respectively. A careful look at the near-linear increase in hydrogen generation with time indicates constant activity with time, and no decrease in activity was observed. This indicates the robustness of the photoanode device. Indeed the activity measurements shown in Figure 2a,b have been repeated with the same photoanode for at least five cycles, and it remained the same. Solar to hydrogen production was also evaluated with

https://dx.doi.org/10.1021/acsami.0c07431
ACS Appl. Mater. Interfaces 2020, 12, 30420−30430

different cocatalysts. Amounts of 16, 11, and 17 mL of hydrogen were produced in 5 h by using Pt, NiCu alloy, and 0.5θ_{Pt}-NC as cocatalyst, respectively, with the TiO_2/ZnS/CdS photoanode (Figure 2b). Within an error margin of 10%, both Pt and 0.5θ_{Pt}-NC cocatalysts show the same activity, which is very intriguing. It is also confirmed from several characterization experiments that there is no bulk Pt with the latter cocatalyst.

Hydrogen production observed with the TiO_2/ZnS/CdS (4−4.5 mL/h) device is about 2-fold that of TiO_2/CdS (2.2−2.5 mL/h) with the same 0.5θ_{Pt}-NC cocatalyst. See the short movie provided in video V1 (see Figure S1 for a video grab of video V1) for hydrogen evolution with TiO_2/ZnS/CdS and 0.5θ_{Pt}-NC as a cocatalyst. In the case of both photoelectrodes, they absorb light in the visible region to a similar extent, and charge carrier recombination is also expected to be similar, due to similar heterostructures (except for the seed ZnS layer in the latter device), which prevents electron−hole recombination. In the case of TiO_2/ZnS/CdS, by introducing a single layer of ZnS, a higher solar to hydrogen yield was observed, indicating that it could be because of significantly lower electron−hole recombination,[30] which is further supported by PEC. As indicated in the previous section, an interface made of a solid solution of CdS+ZnS between titania and CdS enhances the charge separation. This aspect will be discussed later.

The photoanode with 0.5θ_{Pt}-NC cocatalyst generates 17 mL of hydrogen in 5 h, which is similar to that for Pt itself or marginally higher; at best, the hydrogen generation capacity is equal for Pt and 0.5θ_{Pt}-NC, within the error limit. Here the underlying important concept is that by decreasing the Pt amount to the bare minimum in the monolayer (or less) and keeping it on the surface of another earth abundant cocatalyst, hydrogen generation activity should be retained like that of Pt or close to that. The 0.5θ_{Pt}-NC nanoparticles fit the above concept very well and were evaluated for hydrogen evolution with the TiO_2/ZnS/CdS photoanode. With the same photoanode, NiCu alloy and Pt were used as the cocatalyst, and the activity evaluation shows 11 ± 1 mL and 16 ± 1.6 mL, respectively, in 5 h. At least five batches of 0.5θPt-NC and NiCu alloy cocatalysts were prepared and evaluated for activity; results are reproducible within an error limit of 10%. It should be noted that the absolute amount of Pt employed in Pt is much higher than Pt in 0.5θ_{Pt}-NC. Due to the synergistic effect of Ni and Pt and their spatial close proximity on the surface of the 0.5θ_{Pt}-NC cocatalyst, solar hydrogen production is similar to that of bulk Pt but by using a tiny fraction of Pt. More detailed studies would be required to distinguish the activity difference in a quantitative manner. It should be underscored that Ni and Pt belong to the same group (group VIIIB) in the periodic table with unfilled d-orbitals. Both elements would be activated simultaneously and in a similar way, especially for hydrogen generation, which produces a multiplication effect (rather than a simple additive effect), and enhances the activity of the cocatalyst. This is supported by the similar onset potential for Pt and 0.5θ_{Pt}-NC, which will be discussed later.

For the stability, initially, hydrogen evolution activity was evaluated for 5 h with the TiO_2/ZnS/CdS photoanode and 0.5θ_{Pt}-NC cocatalyst. However, after 5 h of activity evaluation, a decrease in activity was found and the simultaneous observation of cocatalyst dislodging from the device was observed. When hydrogen bubbles are evolving over the cocatalyst surface, after about 5 h, slow dislodging of cocatalyst particles was observed along with hydrogen bubbles. This indicates the unsatisfactory adherence of cocatalyst on the FTO plates, and we devised a method to make the cocatalyst stay on the FTO plate for a longer period, as described below. Among the few commercial binders evaluated, nafion and cocatalyst were found to mix and bind well. This mixture also adheres to the FTO plate well, and longer times for experiments were carried out. As the volume of nafion (Nph) increases from 1 to 10 μL for a fixed amount of 1 mg of cocatalyst, the activity decreases, mainly due to the lower amount of cocatalyst in it. In view of this, part of the nafion was replaced with graphite. By keeping stability and activity in mind, we used graphite and nafion with different percentages of 0.5θ_{Pt}-NC. We prepared 1, 10, and 15 wt % of 0.5θ_{pt}-NC cocatalyst mixed with graphite for the remaining amount. This is denoted as *X*% 0.5θ_{Pt}-NC@C. For the deposition on FTO, we took 1 mg of *X*% 0.5θ_{Pt}-NC@C dispersed in 500 μL of ethanol and 1 μL of nafion by 30 min sonication, in which 10% 0.5θ_{Pt}-NC@C/Nph shows the best activity (Figure 3a) and stability up to an

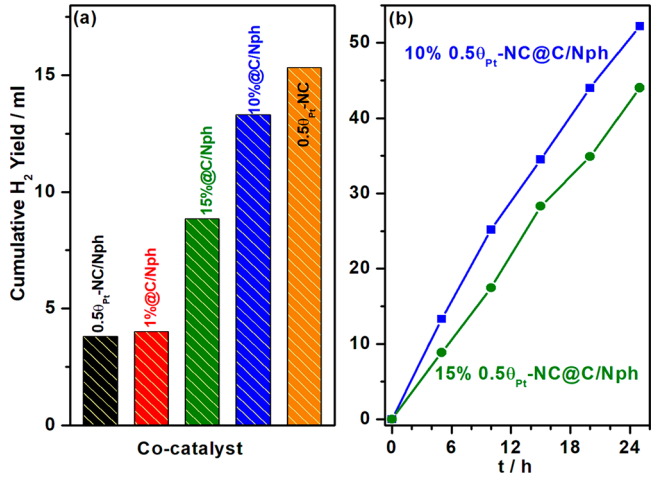


Figure 3. (a) Photocatalytic hydrogen production of the TiO_2/ZnS/CdS photoanode with pure 0.5θ_{Pt}-NC cocatalyst, 0.5θ_{Pt}-NC/Nph (cocatalyst with 1 μL of naphion), 1%, 10%, and 15% of 0.5θ_{Pt}-NC cocatalyst mixed with 99%, 90%, and 85% of graphite and mixed with 1 μL of naphion (namely 1%@C/Nph, 10%@C/Nph, and 15%@C/Nph). (b) Stability of the TiO_2/ZnS/CdS photoanode with 10% and 15% 0.5θ_{Pt}-NC@C/Nph under one sun conditions. It is to be underscored that just 10% of 0.5θ_{Pt}-NC cocatalyst mixed with 90% graphite in 1 μL of naphion produced activity comparable to that of virgin 0.5θ_{Pt}-NC. This reiterates that the inherent activity of 0.5θ_{Pt}-NC cocatalyst is likely to be much higher than the value reported in this manuscript.

evaluation time of 25 h (Figure 3b). Even though the cocatalyst amount is low, better dispersion leads to high activity and similar activity to that of bare 0.5θ_{Pt}-NC. This result suggests the inherent activity of 0.5θ_{Pt}-NC should be much higher than the values reported in the current manuscript. It is also to be noted that Patra et al.[27] has reported 10.5 mL/h hydrogen production with a TiO_2/Mn-doped CdS photoanode and NiCu alloy cocatalyst. Hence, it is very important to investigate the highly efficient photoanode along with cocatalyst optimization. We also plan to improve stability so that it can replace Pt as a cocatalyst for large scale H_2 production.

Elemental Mapping and Textural Properties of the Photoanode. Figure 4 shows the representative SEM and elemental mapping from the vertical cross-section of the fractured TiO_2/ZnS/CdS device for Ti, Cd, Zn, and S elements. Thickness of the film is found to be around 11 μm (Figure 4a). The average thickness of the photoanode was measured by SEM

https://dx.doi.org/10.1021/acsami.0c07431
ACS Appl. Mater. Interfaces 2020, 12, 30420−30430

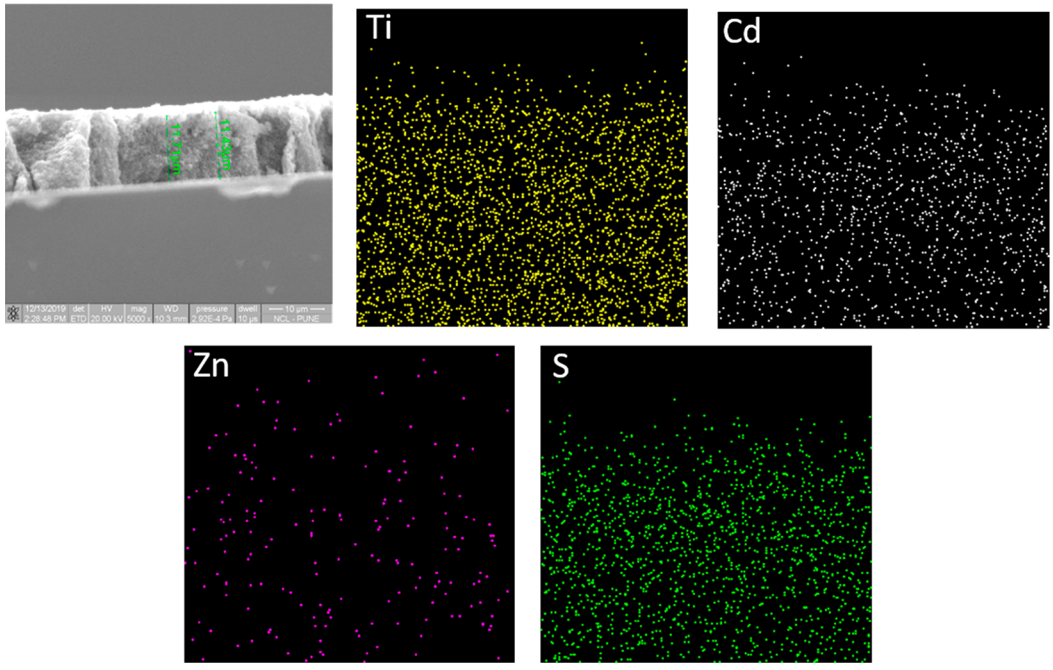


Figure 4. FESEM (top-left) and EDX elemental mapping of the TiO_2/ZnS/CdS photoanode for Ti, Cd, Zn, and S. Elemental mapping was measured only on the photoanode area; the FTO and glass areas were carefully avoided, to show the low concentration of Zn distribution.

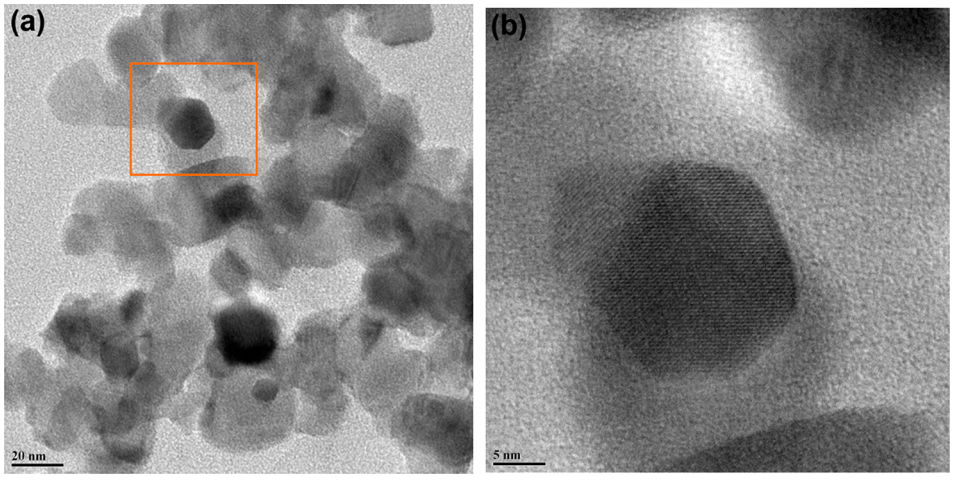


Figure 5. TEM images recorded for the TiO_2/ZnS/CdS photoanode. The square area shown in panel a is recorded at high resolution and shown in panel b. Hexagonal particles observed are due to CdS and confirmed from a (110) interplanar *d*-spacing of 0.210 nm. Heterojunctions between CdS and TiO_2 particles are directly observed in TEM images.

and the surface profilometer at different spots on the photoanode, and a representative result is shown in Figure S2. The average thickness was found to be 9 μm, which is shown in Figure S2b. At the edge of the photoanode, the thickness was found to be 12 μm for all films; this is likely due to the application of the doctor blade method to make titania film. From the following EDX elemental mapping, it is evident that Cd and S are uniformly distributed in the TiO_2 porous thin film from the top to the bottom layers. The TiO_2 film made by the doctor blade method gives a porous network of TiO_2 channels, which is suitable for Cd, S, and Zn ions to diffuse into the mesopores of TiO_2 and make abundant heterostructure between TiO_2, CdS, and ZnS. Heterostructure between TiO_2 and CdS is necessary for efficient electron transfer. It is also to be noted that Zn ions are found to be minimal throughout the film uniformly. The heterostructure between TiO_2 and a solid solution of ZnS +CdS is to prevent the electron−hole recombination. From elemental mapping, it is evident that the heterojunctions between TiO_2 and CdS/ZnS are helping to improve the overall electron transfer and hence photocatalytic performance. The most important observation is the dispersion of CdS components throughout the film from top to bottom layers, underscoring that there are no layers of CdS observed, rather the uniformly distributed QDs. X-ray diffraction was recorded for P25-TiO_2, TiO_2/ZnS/CdS, and TiO_2/CdS photoanodes, and the results are shown in Figure S3. Predominant anatase (75%) with 25% rutile titania for all three photoanodes were observed; no new diffraction feature due to CdS or ZnS was observed for either of the photoanodes. Chemical analysis carried out by ICP shows 2.10 wt % CdS and 0.42 wt % ZnS, and the rest is titania for the photoanodes; an intermediate ZnS layer in the TiO_2/ZnS/CdS photoanode did not change the value significantly.

https://dx.doi.org/10.1021/acsami.0c07431
ACS Appl. Mater. Interfaces 2020, 12, 30420−30430

Indeed, the weight measurements made for the FTO plate, before and after SILAR cycles, also indicate that a 2.5 wt % of chalcogenides was incorporated in the titania layers. ICP analysis and weight difference measurements are observed to be in good agreement with each other.

The heterojunction between CdS and TiO_2 was further explored by TEM studies, and the results are shown in Figure 5. Photoanode material was carefully removed from the FTO plate, and a small amount was sonicated and coated on the TEM grid to study the microstructure. The uniform distribution of CdS and TiO_2 nanoparticles can be clearly seen in Figure 5a. CdS particles could be easily identified with hexagonal Wurtzite structure and characteristic *d*-values. One such CdS particle imaged at high resolution is shown in Figure 5b, which shows the (110) plane with a *d*-value of 0.210 nm. A careful analysis of TEM images indicates that the CdS particles are surrounded by TiO_2 nanoparticles and suggests the formation of CdS in the pores of TiO_2, due to the SILAR preparation method. The particle size for TiO_2 was found to be 20 ± 2 nm. The lattice spacing for TiO_2 was measured to be 0.35 nm for the (101) plane.

Photoelectrochemical Measurement. Photoelectrochemical performance of the TiO_2/ZnS/CdS photoanode was evaluated in the three-electrode system with Pt as a counter electrode and Ag/AgCl as a reference electrode using an aqueous solution of Na_2S/Na_2SO_3. From the chronoamperometry measurement, photoresponse and maximum current density and stability measurements were carried out with a 1 × 1 cm^2 film, and the results are shown in Figure 6.

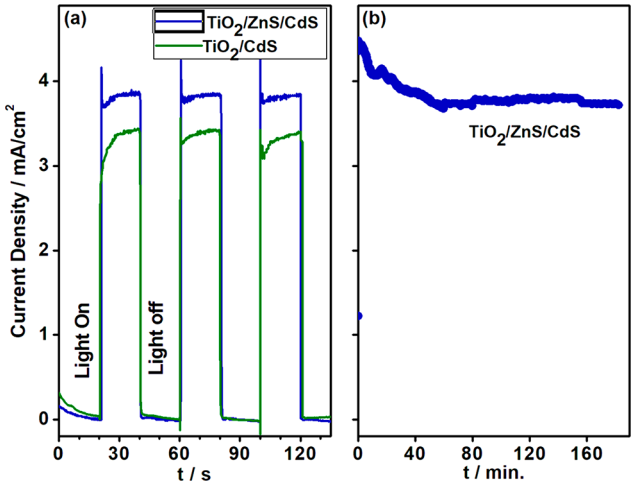


Figure 6. (a) Chronoamperometry measurement at 0 V under one sun conditions. (b) Photoelectrochemical stability of the photoanode for 3 h under one sun conditions by chronoamperometry.

TiO_2/ZnS/CdS shows a current density of 3.8 mA/cm^2 compared to TiO_2/CdS, which exhibits a 3.4 mA/cm^2 current density at zero applied potential. Photoresponse at 0 V was measured to clarify the stability and photoresponse, and the result is shown in Figure 6a. Better current density and photoresponse (than TiO_2/CdS) suggests that TiO_2/ZnS/CdS has improved heterostructure, which gives better electron transfer to TiO_2 compared to TiO_2/CdS; indeed, similar differences in photocatalytic activity of photoanodes were observed (Figure 2). Chronoamperometry measurement was also made for 3 h under one sun conditions (1.5 AM), which is shown in Figure 5b, to evaluate the stability of the TiO_2/ZnS/CdS photoanode. Current density decreases from initial 4.5 mA/cm^2 to stable 4 ± 0.1 mA/cm^2 in 1 h, and thereafter it remains constant within the error bar. Photocurrent density values observed in the continuous light-on mode (Figure 6b) is comparable to the value observed in light on/off measurements (Figure 6a). Stable photocatalytic activity observed for several hours suggests that there is no degradation of the photoanode. Indeed, the stable photocurrent density values and the constant hydrogen generation values observed in Figures 2 and 3 are in good correspondence.

Structural and Microscopy Analysis of Cocatalysts. To understand the structural aspects of NiCu alloy in different forms, XRD, TEM, and HRTEM measurements were made and compared. Figure 7a shows the X-ray diffraction pattern recorded for NiCu@bimetal, NC@H^-, NiCu alloy, and 0.5θ_{Pt}-NC. Figure 7b,c and d,e shows TEM images of NiCu alloy and 0.5θ_{Pt}-NC, respectively; the inset shows the HRTEM image of 0.5θ_{Pt}-NC. We have synthesized two forms of the Ni−Cu nanoparticle, one is an alloy and the other is a bimetal[27] for the reference. NiCu alloy shows the typical alloy features corresponding to JCPDS no. 47-1406. NiCu@bimetal shows the diffraction pattern of Cu and Ni corresponding to JCPDS no. 04-0836 and JCPDS no. 04-0850, respectively; indeed, it is easy to distinguish the bimetal by observing individual metal peaks, while in the alloy it merges into one. In a previous report by Patra et. al,[27] it was shown that NiCu in alloy form shows better activity for hydrogen evolution. Hence, NiCu alloy was chosen for the present studies. The XRD pattern of NiCu@H^- shows a diffraction pattern identical to that of the bimetal form of NiCu. When NiCu@H^- is treated with Pt(II), the intensity of the diffraction pattern drastically changes because of the reduction in particle size, which is also reflected in HRTEM of 0.5θ_{Pt}-NC (Figure 7e). The diffraction pattern shifted to lower 2θ and was broadened. TEM images shown in Figure 7b,c for NiCu alloy display a particle size in the range of 25 and 40 nm with an average size of 34 nm. However, a severe reduction in particle size to about 4−5 nm was observed after Pt deposition. An approximate spherical shape particle is observed before and after Pt deposition on NiCu alloy. The HRTEM image shown for 0.5θ_{Pt}-NC displays well resolved lattice fringes for the (200) facet of NiCu alloy.[34] Similar images were observed for NiCu alloy also.

The principle adopted for Pt deposition in our synthesis method was expected to lead to half-a-monolayer of Pt on NiCu alloy. A careful analysis by TEM-EDS was attempted to evaluate the spatial distribution of all elements, particularly Pt, on 0.5θ_{Pt}-NC particles, and the results observed are shown in Figure 8. Figure 8a shows the TEM image of a cluster of 0.5θ_{Pt}-NC particles, and it was evaluated for all elements present on it (Figure 8b−e). Ni and Cu were observed uniformly all over the cocatalyst surface, supporting the alloy (bimetal) nature of the cocatalyst. The atom % ratio of Ni:Cu is observed to be 2.3:1, indicating a marginal Ni enrichment. Apart from Ni and Cu, a significant amount of oxygen and a small amount of Pt were also observed. The presence of oxygen is attributed to the surface oxidation of Ni and Cu, and it is supported by XPS measurements and discussed later (Figure 9). It is to be noted that the distribution of Pt is uniform on the surface of 0.5θ_{Pt}-NC, and it is as expected from the preparation method employed. Unlike Ni and Cu, no clustering of Pt is observed, which supports the above conclusion. A 1.18 atom % (4.67 wt %) Pt was measured from the EDS analysis. In fact, more detailed and high resolution studies would be required to understand the

https://dx.doi.org/10.1021/acsami.0c07431
ACS Appl. Mater. Interfaces 2020, 12, 30420−30430

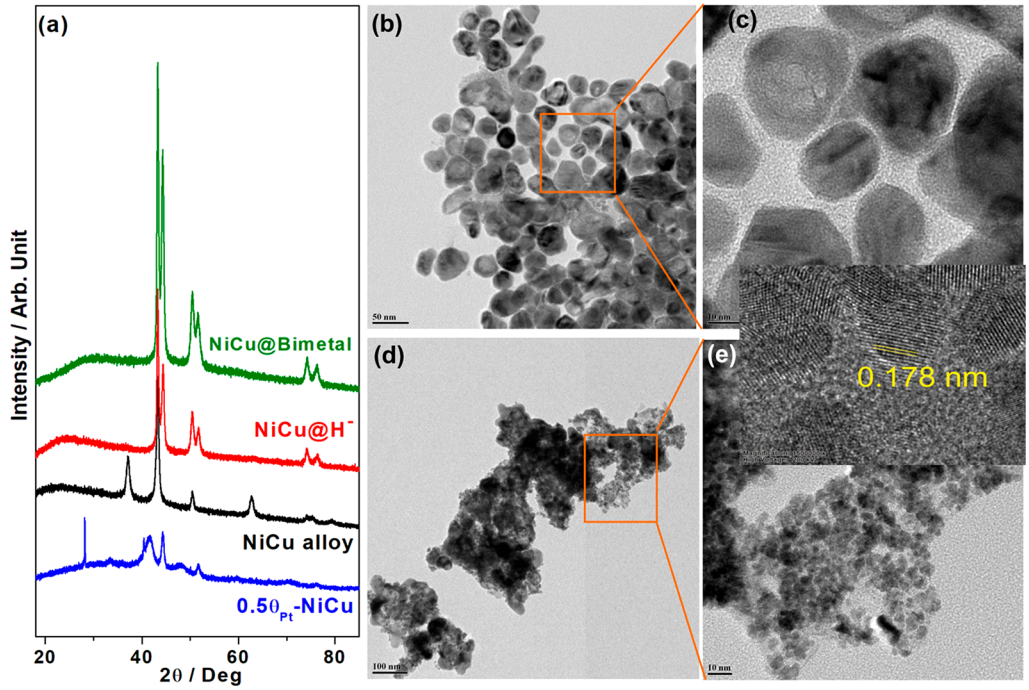
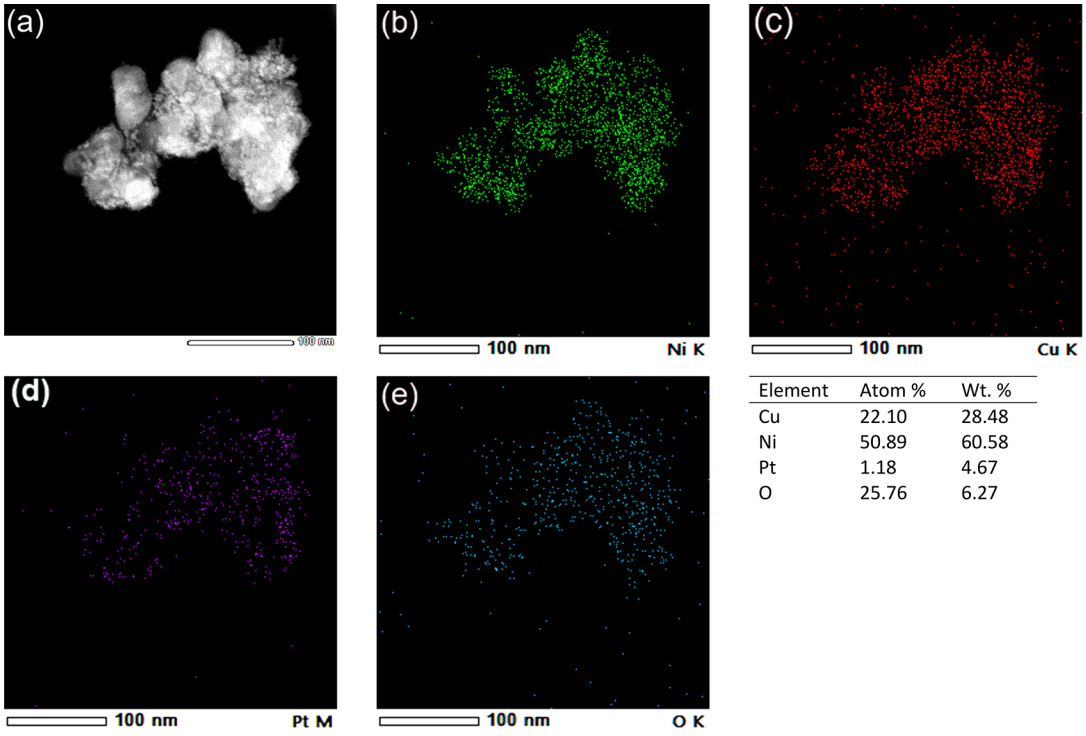


Figure 7. (a) X-ray diffraction pattern NC@bimetal, NiCu alloy, NiCu@H^-, and 0.5θ_{Pt}-NC. HRTEM images observed for (b and c) NiCu alloy, and (d and e) 0.5θ_{Pt}-NC. A decrease in particle size from NiCu alloy (25−40 nm) to 0.5θ_{Pt}-NC (4−5 nm) in panels c and e, respectively, is noted. The inset shown for HRTEM of 0.5θ_{Pt}-NC displays the abundant (200) facet of NiCu alloy.



Element	Atom %	Wt. %
Cu	22.10	28.48
Ni	50.89	60.58
Pt	1.18	4.67
O	25.76	6.27

Figure 8. (a) TEM and EDS images recorded 0.5θ_{Pt}-NC for distribution of (b) Ni, (c) Cu, (d) Pt, and (e) O elements. Atom and weight percent of elements are also given for quantitative information. It is to be noted that oxygen arises due to surface oxidation.

distribution of Pt, possibly by controlling the Pt content to less than 0.5 ML. Interestingly, oxygen was also observed to be distributed uniformly and without any clustering, despite 25.76 atom % (6.27 wt %).

XPS. XPS analysis was performed as well to explore the effect of surface composition of materials on the possible oxidation aspects of Ni and Cu. It is well-known that both Ni and Cu are pyrophoric in nature, and even with careful storage and handling, surface oxidation of them cannot be avoided due to some exposure to air while preparing the sample for XPS analysis and their introduction into the XPS chamber. Figure 9a shows Ni $2p_{3/2}$ spectra of NiCu alloy and 0.5θ_{Pt}-NC cocatalysts. NiCu

https://dx.doi.org/10.1021/acsami.0c07431
ACS Appl. Mater. Interfaces 2020, 12, 30420−30430

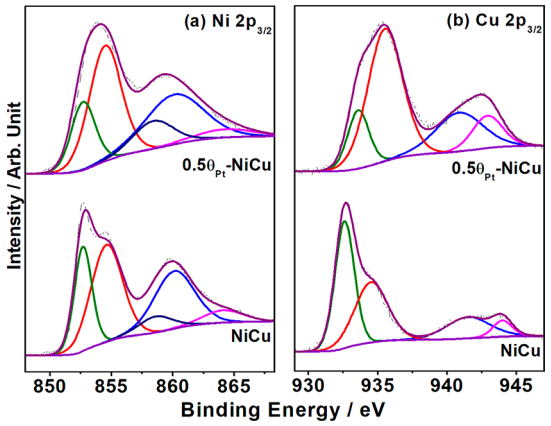


Figure 9. XPS of (a) Ni $2p_{3/2}$ and (b) Cu $2p_{3/2}$ core levels of NiCu alloy and $0.5\theta_{Pt}$-NC. Green colored peaks correspond to metallic Ni or Cu while red colored peaks are attributed to a mixture of oxidized Ni (NiO and $Ni(OH)_2$) and Cu (CuO) species. The satellite feature is fitted with blue and pink colored peaks.

alloy exhibits the characteristic peaks for Ni metal (852.7 eV) and oxidized Ni species (NiO and $Ni(OH)_2$) at 855.5 eV. Although XPS explores about 10 nm depth, a mixture of metallic Ni and oxidized Ni species are possible within the probing depth.[35] However, we attribute the oxidized Ni species (observed before and after Pt deposition) due to atmospheric degradation and not due to preparation method. After hydride treatment and half-a-monolayer platinum deposition, the amount of metallic Ni is marginally decreased on the surface, which is clearly visible from the Ni-metal peak intensity. With the metallic Ni feature, the NiO feature also decreases and the $Ni(OH)_2$ feature increases on the surface. This is fully supported by the shift in the satellite feature to higher BE, compared to that of NiCu alloy. It is also to be reiterated that XRD does not show any oxide or hydroxide features in Figure 7a. In addition, excess borohydride added in the preparation of NiCu@H^- is expected to reduce any oxidized Ni and Cu species on NiCu alloy. In view of these facts, cocatalysts prepared and employed for the activity studies are metallic in nature, and the surface contaminations observed with Ni and Cu 2p levels are due to atmospheric degradation.

The Cu $2p_{3/2}$ feature (Figure 9b) in NiCu alloy shows Cu (932.5 eV) and Cu(II) features at 934.5 eV along with a satellite feature between 939 and 945 eV.[36,37] The narrow line width of 932.5 eV supports the oxidation state to be zero. In the case of NiCu alloy, the Cu feature is supported by the deconvolution of Cu $2p_{3/2}$ spectra. Metallic Cu intensity decreases upon Pt deposition on $0.5\theta_{Pt}$-NC, as in the Ni case while Cu(II) content increases which is also confirmed by an increase in the intensity of satellite features. Indeed, Ni and Cu are equally vulnerable to surface oxidation and hence show significant amounts of oxidized species on the surface. We would like to indicate the possibility of galvanic displacement during Pt deposition, which may change the surface composition. As mentioneded previously, the initial average particle size of NiCu alloy is 34 nm, and upon Pt deposition, the particle size decreased drastically to about 4−5 nm. Although the particle size reduction would be helpful to improve the activity due to significantly increased surface area, the reasons behind size reduction are yet to be determined and this will be addressed in future publications.

Electrochemical Measurement. Electrochemical measurement was carried out using a three-electrode system using platinum and Ag/AgCl as a counter and reference electrode, respectively, in 0.5 M H_2SO_4. The catalyst paste was coated on a glassy carbon electrode with a total catalyst amount of 5 μg. The electrochemically active surface area (ECSA) of the catalysts was estimated from the double-layer capacitance,[38,39] which was determined using the cyclic voltammogram recorded at different scan rates in the non-Faradaic region in 0.5 M H_2SO_4 solution, and the result is shown in Figure S5. The ratio of the double layer capacitance to the specific capacitance provides ECSA values.[40] Details of the ECSA calculation and specific capacitance values are available in refs 38−40. From the fitted capacitances shown in Figure S5, the active surface area of NiCu (62.5 cm^2) was found to be larger than that of $0.5\theta_{Pt}$-NC (35.4 cm^2). Contrary to the expectations, larger ECSA was observed with NiCu than with $0.5\theta_{Pt}$-NC, despite the smaller particle size of the latter. The corresponding ECSA-corrected LSV and Tafel plots of NiCu and $0.5\theta_{Pt}$-NC are shown in Figure 10a,b. The polarization curve

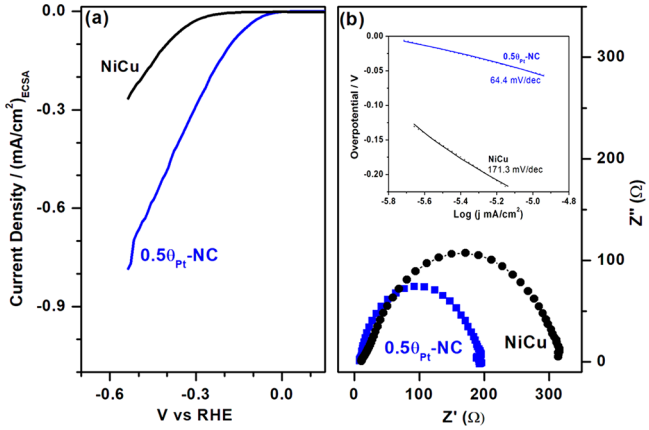


Figure 10. (a) ECSA-corrected LSV and (b) Nyquist plots obtained from electrochemical impedance measurement which provides charge transfer resistance of NiCu alloy and $0.5\theta_{Pt}$-NC catalysts. Inset in panel b shows Tafel slopes with linear fitting for both catalysts.

of NiCu (Figure 10a) alloy shows the onset potential at 0.2 V vs RHE; however, when NiCu alloy is integrated with half-a-monolayer of Pt, the onset potential dramatically decreased to 0.05 V. This observation highlights that the facile electron transfer is dramatically enhanced due to synergistic effect of 0.5 ML of Pt with NC. It is evident from the present measurements that a fraction of ML of platinum on the surface of NiCu alloy can enhance the HER activity drastically, despite the low ECSA. Results shown in Figure 10a also indicate that there is no bulk Pt deposited on the cocatalyst.

To understand the charge transfer resistance at the catalyst−electrolyte interface, we performed the electrochemical impedance measurement, and the result is shown in Figure 10b. The radius of the semicircle represents the charge transfer resistance at the interface, suggesting facile electron transfer in $0.5\theta_{Pt}$-NC as compared to NiCu alloy (Figure 10b). This observation demonstrates that $0.5\theta_{Pt}$-NC has a less resistive pathway; further, due to the synergistic effect of Ni and Pt, it enhances the HER activity. Tafel slopes are measured to be 171.32 and 64.4 mV·dec^{-1} for NiCu and $0.5\theta_{Pt}$-NC, respectively (Figure 10b inset). The smaller Tafel slope also suggests a higher HER activity with $0.5\theta_{Pt}$-NC catalyst.

https://dx.doi.org/10.1021/acsami.0c07431
ACS Appl. Mater. Interfaces 2020, 12, 30420−30430

Mechanism. A combination of two or more semiconductors with desired bandgaps and band-edge potentials with an efficient cocatalyst can lead to an efficient photocatalytic water splitting system, which might be scalable. The system reported in this manuscript has this type of potential. Herein with the detailed characterization studies and the activity evaluation carried out, a possible mechanism of solar to chemical conversion is given in Figure 11. CdS with a bandgap 2.4 eV can absorb light up to 522 nm, which covers about 44% of the visible light part of the solar spectrum. TiO_2 can absorb 4−5% of UV light present in the solar spectrum and can add efficiency to the device. Upon light absorption, electrons are excited to the conduction band (CB) of CdS QDs; thereafter these electrons are transferred to the CB of TiO_2. The heterojunction observed between titania and CdS helps for this electron transfer. This facilitates the electrons to reach the $0.5\theta_{Pt}$-NC cocatalyst, which is coated adjacent to the photoanode on the FTO plate. These electrons are utilized to reduce water. Sensitization of TiO_2 first with a monolayer of wide band gap ZnS reduces the electron−hole recombination and enhances the charge separation and utilization at the cocatalyst sites. UV−vis absorption by the TiO_2/ZnS/CdS photoanode shows a marginal increase in the bandgap to 2.5 eV (compared to 2.4 eV with the TiO_2/CdS photoanode), indicating a formation of a solid solution of ZnS and CdS to CdZnS.[32,33] This leads to a different interface between titania and CdS with the TiO_2/ZnS/CdS photoanode, compared to no such interface in the TiO_2/CdS photoanode. Indeed a pure ZnS layer, without forming a solid solution, would actually hinder the electron transfer from CdS to titania,[12,31−33] due to the high energy of the CB edge of ZnS. Larger amounts of photocatalytic hydrogen production observed with TiO_2/ZnS/CdS (Figure 2) compared to TiO_2/CdS demonstrates this. Increase in the photoelectron current density (Figure 5) and the TEM results (Figure 6) also support a better quality heterostructure with TiO_2/ZnS/CdS. The SILAR method employed for assembling CdS and ZnS QDs inside the pores of titania should be underscored. Due to layer-by-layer construction of the chalcogenides because of diffusion of ionic precursors (Cd^{2+}, Zn^{2+}, and S^{2-}), the QDs are assembled inside the pores in situ. This method allows the formation of heterostructure between the semiconductors in the best possible way and helps to enhance the charge separation and utilization. It is also to be noted that electron transfer occurs from CdS to TiO_2, and the hole-transfer happens in the exact reverse direction. It is an added advantage for effective electron transfer toward the cocatalyst sites, and it mimics the electron-transfer from photosystem II to photosystem I in the natural leaf. In the case of the cocatalyst part, $0.5\theta_{Pt}$-NC shows an onset potential similar to that of Pt/C. This fact further demonstrates that hydrogen evolution is enhanced due to the atomic Pt layer available on the surface.

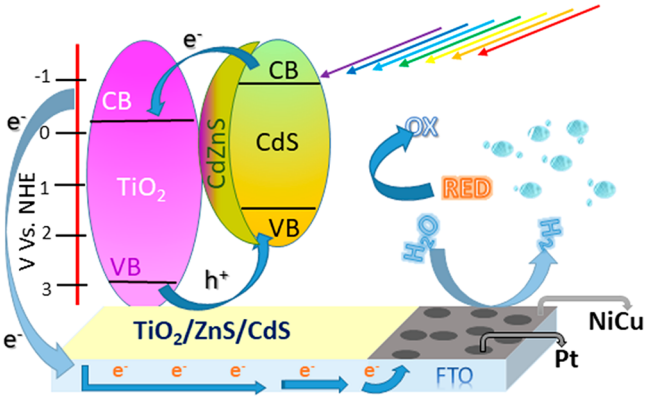


Figure 11. A possible mechanism for the solar to hydrogen production over the TiO_2/ZnS/CdS photoanode; blue lines show the transfer of the electron and holes. Gray and black dots represent NiCu alloy and 0.5 ML Pt integrated, respectively (only for the representation). The first layer of ZnS interacts with CdS to form a CdZnS solid-solution interface between titania and CdS, which helps for effective charge separation and conduction.

CONCLUSION

In summary, we developed a QuAL device with a TiO_2 film sensitized with ZnS and CdS quantum dots (QDs) and integrated it with half-a-monolayer of Pt covered on Ni−Cu ($0.5\theta_{Pt}$-NC) alloy nanoparticles. The critical novelty of the present work is to successfully demonstrate the activity of bulk Pt from a mere half-a-monolayer of Pt coated on the surface of NiCu alloy. However, it is to be demonstrated on other metal and metallic surfaces. The preparation method described can also be extended to other noble metals. The QuAL device with $0.5\theta_{Pt}$-NC cocatalyst was demonstrated to show solar hydrogen production at a rate of 4 mL h^{-1}, and the photoanode shows a current density of 4 ± 0.1 mA cm^{-2} at zero applied potential. An innovative ZnS seed layer integration with CdS QDs leads to a solid solution of the CdS+ZnS interface, and this increased the charge carrier separation, resulting in high current density and solar hydrogen generation under one sun conditions. Hence, a proper band alignment among the semiconductor components could lead to better solar to H_2 conversion with low charge carrier recombination. On the other hand, for the cocatalyst part, $0.5\theta_{Pt}$-NC shows low overpotential compared to NiCu alloy due to the synergistic effect between Ni and Pt on the surface, which enhances the H_2 evolution on the surface of the cocatalyst. As we indicated in the manuscript, inherent activity of $0.5\theta_{Pt}$-NC is likely to be higher, and a correct combination of binders is likely to bring out the best possible activity.

Over the last two decades, a large amount of work has been reported in the field of photocatalytic water splitting; however, there is no great breakthrough yet in this area of research. We believe there is alot of potential associated with QuAL and artificial leaf devices, and more work in this direction is desired. Simulation of bulk Pt activity with half-a-monolayer of Pt would lower the cost of the device, so more effort is required in this direction. Economically viable and different metallic cocatalysts should also be evaluated with an atomic platinum layer.

ASSOCIATED CONTENT

Supporting Information

The Supporting Information is available free of charge at https://pubs.acs.org/doi/10.1021/acsami.0c07431.

Hydrogen generation video (S1), cross-section and surface profile of photoanode (S2), X-ray diffraction profiles (S3), and cyclic voltammetry results (S4) (PDF)
Video V1 (AVI)

AUTHOR INFORMATION

Corresponding Author

Chinnakonda S. Gopinath − *Catalysis and Inorganic Chemistry Division and Academy of Scientific and Innovative Research (AcSIR), CSIR-National Chemical Laboratory, Pune 411 008,*

https://dx.doi.org/10.1021/acsami.0c07431
ACS Appl. Mater. Interfaces 2020, 12, 30420−30430

India; orcid.org/0000-0002-4525-3912;
Email: cs.gopinath@ncl.res.in

Authors

Himanshu Bajpai − *Catalysis and Inorganic Chemistry Division and Academy of Scientific and Innovative Research (AcSIR), CSIR-National Chemical Laboratory, Pune 411 008, India*

Kshirodra Kumar Patra − *Catalysis and Inorganic Chemistry Division, CSIR-National Chemical Laboratory, Pune 411 008, India*

Ravi Ranjan − *Catalysis and Inorganic Chemistry Division and Academy of Scientific and Innovative Research (AcSIR), CSIR-National Chemical Laboratory, Pune 411 008, India*

Naresh Nalajala − *Catalysis and Inorganic Chemistry Division, CSIR-National Chemical Laboratory, Pune 411 008, India*

Kasala Prabhakar Reddy − *Catalysis and Inorganic Chemistry Division, CSIR-National Chemical Laboratory, Pune 411 008, India*

Complete contact information is available at:
https://pubs.acs.org/10.1021/acsami.0c07431

Notes

The authors declare no competing financial interest.

■ ACKNOWLEDGMENTS

We acknowledge the financial support from CSIR, New Delhi, through MLP034526 (Niche creating project). H.B. and R.R. thank UGC, New Delhi, and INSPIRE-DST, respectively, for research fellowships.

■ DEDICATION

We dedicate this manuscript to Dr. Subramanian Sivasanker, for his immense contributions to industrial catalysis, petroleum refining, and petrochemical production areas.

■ REFERENCES

(1) Armaroli, N.; Balzani, V. The Future of Energy Supply: Challenges and Opportunities. *Angew. Chem., Int. Ed.* **2007**, *46*, 52−66.

(2) She, H.; Zhou, H.; Li, L.; Zhao, Z.; Jiang, M.; Huang, J.; Wang, L.; Wang, Q. Construction of a Two-Dimensional Composite Derived from TiO_2 and SnS_2 for Enhanced Photocatalytic Reduction of CO_2 into CH_4. *ACS Sustainable Chem. Eng.* **2019**, *7*, 650−659.

(3) Lewis, N. S.; Nocera, D. G. Powering the planet: Chemical Challenges in Solar Energy Utilization. *Proc. Natl. Acad. Sci. U. S. A.* **2006**, *103*, 15729−15735.

(4) Wang, Z.; Li, C.; Domen, K. Recent Developments in Heterogeneous Photocatalysts for Solar-Driven Overall Water Splitting. *Chem. Soc. Rev.* **2019**, *48*, 2109−2125.

(5) Turner, J. A. Sustainable Hydrogen Production. *Science* **2004**, *305*, 972−974.

(6) Nocera, D. G. The Artificial Leaf. *Acc. Chem. Res.* **2012**, *45*, 767−776.

(7) Bharad, P. A.; Sivaranjani, K.; Gopinath, C. S. A Rational Approach Towards Enhancing Solar Water Splitting: A Case Study of Au−RGO/N-RGO−TiO_2. *Nanoscale* **2015**, *7*, 11206−11215.

(8) Tudu, B.; Nalajala, N.; Reddy, K. P.; Saikia, P.; Gopinath, C. S. Electronic Integration and Thin Film Aspects of Au−Pd/rGO/TiO_2 for Improved Solar Hydrogen Generation. *ACS Appl. Mater. Interfaces* **2019**, *11*, 32869−32878.

(9) Trevisan, R.; Rodenas, P.; Gonzalez-Pedro, V.; Sima, C.; Sanchez, R. S.; Barea, E. M.; Mora-Sero, I.; Fabregat-Santiago, F.; Gimenez, S. Harnessing Infrared Photons for Photoelectrochemical Hydrogen Generation. A PbS Quantum Dot Based "Quasi-Artificial Leaf. *J. Phys. Chem. Lett.* **2013**, *4*, 141−146.

(10) Maeda, K.; Mallouk, T. E. Two-Dimensional Metal Oxide Nanosheets as Building Blocks for Artificial Photosynthetic Assemblies. *Bull. Chem. Soc. Jpn.* **2019**, *92*, 38−54.

(11) Roy, N.; Suzuki, N.; Terashima, C.; Fujishima, A. Recent Improvements in the Production of Solar Fuels: From CO_2 Reduction to Water Splitting and Artificial Photosynthesis. *Bull. Chem. Soc. Jpn.* **2019**, *92*, 178−192.

(12) Rajaambal, S.; Sivaranjani, K.; Gopinath, C. S. Recent Developments in Solar H_2 Generation from Water Splitting. *J. Chem. Sci.* **2015**, *127*, 33−47.

(13) Zou, Z.; Ye, J.; Sayama, K.; Arakawa, H. Direct Splitting of Water under Visible Light Irradiation with an Oxide Semiconductor Photocatalyst. *Nature* **2001**, *414*, 625−627.

(14) Sivaranjani, K.; Agarkar, S.; Ogale, S. B.; Gopinath, C. S. Toward a Quantitative Correlation between Microstructure and DSSC Efficiency: A Case Study of $TiO_{2-x}N_x$ Nanoparticles in a Disordered Mesoporous Framework. *J. Phys. Chem. C* **2012**, *116*, 2581−2587.

(15) Patra, K. K.; Gopinath, C. S. Bimetallic and Plasmonic Ag−Au on TiO_2 for Solar Water Splitting: An Active Nanocomposite for Entire Visible-Light-Region Absorption. *ChemCatChem* **2016**, *8*, 3294−3311.

(16) Melvin, A. A.; Illath, K.; Das, T.; Raja, T.; Bhattacharyya, S.; Gopinath, C. S. M−Au/TiO_2 (M = Ag, Pd, and Pt) Nanophotocatalyst for Overall Solar Water Splitting: Role of Interfaces. *Nanoscale* **2015**, *7*, 13477−13488.

(17) Patra, K. K.; Ghosalya, M. K.; Bajpai, H.; Raj, S.; Gopinath, C. S. Oxidative Disproportionation of MoS_2/GO to MoS_2/MoO_{3-x}/RGO: Integrated and Plasmonic 2D-Multifunctional Nanocomposite for Solar Hydrogen Generation From NIR and Visible Regions. *J. Phys. Chem. C* **2019**, *123*, 21685−21693.

(18) Rajaambal, S.; Mapa, M.; Gopinath, C. S. $In_{1-x}Ga_xN$@ZnO: A Rationally Designed and Quantum Dot Integrated Material for Water Splitting and Solar Harvesting Applications. *Dalton Trans.* **2014**, *43*, 12546−12554.

(19) Yang, J.; Wang, D.; Han, H.; Li, C. Roles of Cocatalysts in Photocatalysis and Photoelectrocatalysis. *Acc. Chem. Res.* **2013**, *46*, 1900−1909.

(20) Zhang, S.; Liu, Z.; Chen, D.; Guo, Z.; Ruan, M. Oxygen Vacancies Engineering in TiO_2 Homojunction/ZnFe-LDH for Enhanced Photoelectrochemical Water Oxidation. *Chem. Eng. J.* **2020**, *395*, 125101.

(21) Alivisatos, A. P. Semiconductor Clusters, Nanocrystals, and Quantum Dots. *Science* **1996**, *271*, 933−937.

(22) Brus, L. Quantum Crystallites and Nonlinear Optics. *Appl. Phys. A: Solids Surf.* **1991**, *53*, 465−474.

(23) Preethi, L. K.; Mathews, T.; Nand, M.; Jha, S. N.; Gopinath, C. S.; Dash, S. Band Alignment and Charge Transfer Pathway in Three Phase Anatase-Rutile-Brookite TiO_2 Nanotubes: An Efficient Photocatalyst for Water Splitting. *Appl. Catal., B* **2017**, *218*, 9−19.

(24) Nalajala, N.; Patra, K. K.; Bharad, P. A.; Gopinath, C. S. Why the Thin Film form of a Photocatalyst is Better than the Particulate form for Direct Solar-to-Hydrogen Conversion: A Poor Man's Approach. *RSC Adv.* **2019**, *9*, 6094−6100.

(25) Patra, K. K.; Bhuskute, B. D.; Gopinath, C. S. Possibly Scalable Solar Hydrogen Generation with Quasi-Artificial Leaf Approach. *Sci. Rep.* **2017**, *7*, 6515.

(26) Du, P.; Eisenberg, R. Catalysts made of Earth-Abundant Elements (Co, Ni, Fe) for Water Splitting: Recent Progress and Future Challenges. *Energy Environ. Sci.* **2012**, *5*, 6012−6021.

(27) Patra, K. K.; Bharad, P. A.; Jain, V.; Gopinath, C. S. Direct Solar-to-Hydrogen Generation by Quasi-Artificial Leaf Approach: Possibly Scalable and Economical Device. *J. Mater. Chem. A* **2019**, *7*, 3179−3189.

(28) Ran, J.; Zhang, J.; Yu, J.; Jaroniec, M.; Qiao, S. Z. Earth-Abundant Cocatalysts for Semiconductor-Based Photocatalytic Water Splitting. *Chem. Soc. Rev.* **2014**, *43*, 7787−7812.

(29) Nalajala, N.; Gooty Saleha, W. F.; Ladewig, B. P.; Neergat, M. Sodium Borohydride Treatment: A Simple and Effective Process for The Removal of Stabilizer and Capping Agents from Shape-Controlled Palladium Nanoparticles. *Chem. Commun.* **2014**, *50*, 9365−9368.

(30) Lee, Y.-S.; Gopi, C. V. V. M.; Venkata-Haritha, M.; Kim, H.-J. Recombination Control in High-Performance Quantum Dot-Sensitized Solar Cells with a Novel TiO_2/ZnS/CdS/ZnS Heterostructure. *Dalton Trans.* **2016**, *45*, 12914−12923.
(31) Maitri, M.; Sivaranjani, K.; Bhange, D. S.; Saha, B.; Chakraborty, P.; Viswanath, A. K.; Gopinath, C. S. Structure, Electronic Structure, Optical and Dehydrogenation Catalytic study of $(Zn_{1-z}In_z)(O_{1-x}N_x)$ Solid Solution. *Chem. Mater.* **2010**, *22*, 565−578.
(32) Maitri, M.; Thushara, K. S.; Saha, B.; Chakraborty, P.; Janet, C. M.; Viswanath, R. P.; Madhavan Nair, C.; Murti, K. V. G. K.; Gopinath, C. S. Electronic Structure and Catalytic Studies of Solid Solution of GaN in ZnO. *Chem. Mater.* **2009**, *21*, 2973−2979.
(33) Yu, J.; Zhang, J.; Jaroniec, M. Preparation and Enhanced Visible-light Photocatalytic H_2-Production Activity of CdS quantum dots-sensitized $Zn_{1-x}Cd_xS$ solid Solution. *Green Chem.* **2010**, *12*, 1611−1614.
(34) Argueta-Figueroa, L.; Morales-Luckie, R. A.; Scougall-Vilchis, R. J.; Olea-Mejía, O. F. Synthesis, Characterization and Antibacterial Activity of Copper, Nickel and Bimetallic Cu−Ni Nanoparticles for Potential use in Dental Materials. *Prog. Nat. Sci.* **2014**, *24*, 321−328.
(35) Velu, S.; Suzuki, K.; Vijayaraj, M.; Barman, S.; Gopinath, C. S. In Situ XPS Investigations of $Cu_{1-x}Ni_xZn$Al-Mixed Metal Oxide Catalysts used in the Oxidative Steam Reforming of Bio-Ethanol. *Appl. Catal., B* **2005**, *55*, 287−299.
(36) Gnanakumar, E. S.; Naik, J. M.; Manikandan, M.; Raja, T.; Gopinath, C. S. Role of Nanointerfaces in Cu- and Cu + Au-Based Near-Ambient-Temperature CO Oxidation Catalysts. *ChemCatChem* **2014**, *6*, 3116−3124.
(37) Roy, K.; Gopinath, C. S. UV Photoelectron Spectroscopy at Near Ambient Pressures: Mapping Valence Band Electronic Structure Changes from Cu to CuO. *Anal. Chem.* **2014**, *86*, 3683−3687.
(38) Gao, M. Y.; Yang, C.; Zhang, Q. B.; Yu, Y. W.; Hua, Y. X.; Li, Y.; Dong, P. Electrochemical fabrication of porous Ni-Cu alloy nanosheets with high catalytic activity for hydrogen evolution. *Electrochim. Acta* **2016**, *215*, 609−616.
(39) Deng, H.; Zhang, C.; Xie, Y.; Tumlin, T.; Giri, L.; Karna, S. P.; Lin, J. Laser Induced MoS_2/Carbon Hybrids for Hydrogen Evolution Reaction Catalysts. *J. Mater. Chem. A* **2016**, *4*, 6824−6830.
(40) McCrory, C. C. L.; Jung, S.; Peters, J. C.; Jaramillo, T. F. Benchmarking heterogeneous electrocatalysts for the oxygen evolution reaction. *J. Am. Chem. Soc.* **2013**, *135*, 16977−16987.

https://dx.doi.org/10.1021/acsami.0c07431
ACS Appl. Mater. Interfaces 2020, 12, 30420−30430

ACS APPLIED MATERIALS & INTERFACES

www.acsami.org

Addition/Correction

Correction to "Can Half-a-Monolayer of Pt Simulate Activity Like That of Bulk Pt? Solar Hydrogen Activity Demonstration with Quasi-artificial Leaf Device"

Himanshu Bajpai, Kshirodra Kumar Patra, Ravi Ranjan, Naresh Nalajala, Kasala Prabhakar Reddy, and Chinnakonda S. Gopinath*

ACS Appl. Mater. Interfaces **2020**, *12* (27), 30420−30430. DOI: 10.1021/acsami.0c07431

Cite This: *ACS Appl. Mater. Interfaces* 2022, 14, 32771−32771

Read Online

ACCESS | Metrics & More | Article Recommendations

In the original version of this article, there is a mix-up in the address of the affiliated institutes. AcSIR's address is shown to be a part of the National Chemical Laboratory, which is purely a mistake and incorrect. Corrected affiliations are reflected with the authorship of this Correction.

AUTHOR INFORMATION

Corresponding Author

Chinnakonda S. Gopinath − *Catalysis and Inorganic Chemistry Division, CSIR-National Chemical Laboratory, Pune 411 008, India; Academy of Scientific and Innovative Research (AcSIR), Ghaziabad 201 002, India;* orcid.org/0000-0002-4525-3912; Email: cs.gopinath@ncl.res.in

Authors

Himanshu Bajpai − *Catalysis and Inorganic Chemistry Division, CSIR-National Chemical Laboratory, Pune 411 008, India; Academy of Scientific and Innovative Research (AcSIR), Ghaziabad 201 002, India*

Kshirodra Kumar Patra − *Catalysis and Inorganic Chemistry Division, CSIR-National Chemical Laboratory, Pune 411 008, India*

Ravi Ranjan − *Catalysis and Inorganic Chemistry Division, CSIR-National Chemical Laboratory, Pune 411 008, India; Academy of Scientific and Innovative Research (AcSIR), Ghaziabad 201 002, India*

Naresh Nalajala − *Catalysis and Inorganic Chemistry Division, CSIR-National Chemical Laboratory, Pune 411 008, India*

Kasala Prabhakar Reddy − *Catalysis and Inorganic Chemistry Division, CSIR-National Chemical Laboratory, Pune 411 008, India*

Complete contact information is available at: https://pubs.acs.org/10.1021/acsami.2c10019

Published: July 8, 2022



Downloaded via NATL CHEMICAL LABORATORY on May 3, 2023 at 11:13:33 (UTC).
See https://pubs.acs.org/sharingguidelines for options on how to legitimately share published articles.

ACS Publications

© 2022 American Chemical Society